

**Effects of Needle Injuries
and Simulated Repetitive
Lifting on Lumbar Spinal
Segments Mechanics and
Annulus Fibrosus Structure**

By

Tirad Sulaiman Alsharari

B.Eng. (Biomedical), M.Eng. (Biomedical)

Principal Supervisor: Assoc. Prof. John Costi

Co-Supervisor: Dr. Rami Al-Dirini

Adjunct Supervisor: Dr. Javad Tavakoli

Thesis Submitted to Flinders University for the degree of

Doctor of Philosophy

College of Science and Engineering

11th November 2024

Table of Contents

<i>Table of Contents</i>	<i>i</i>
<i>List of Figures</i>	<i>viii</i>
<i>List of Tables</i>	<i>xxiii</i>
<i>List of Abbreviations</i>	<i>xxvi</i>
<i>Abstract</i>	<i>xxvii</i>
<i>Declaration</i>	<i>xxx</i>
<i>Acknowledgements</i>	<i>xxxiv</i>
<i>Conference Presentations</i>	<i>37</i>
<i>Awards & Prizes</i>	<i>38</i>
Chapter 1 Introduction	39
1.1 Motivation	39
1.2 Aims	41
1.3 Significance	41
1.4 Thesis Outline	42
Chapter 2 Literature Review	44
2.1 Anatomy of the Functional Spinal Unit	44
2.1.1 Intervertebral Disc.....	44
2.1.1.1 Nucleus Pulposus.....	45
2.1.1.2 Annulus Fibrous	46
2.1.1.3 Cartilaginous Endplates.....	46
2.1.2 Lumbar Vertebrae	47
2.2 Techniques and Measurements for Visualising Disc	
Microstructure	47
2.2.1 Optical	48
2.2.2 Non-Optical	53
2.2.2.1 Magnetic Resonance Imaging	53

2.2.2.2	Ultrasound	54
2.2.2.3	Micro-CT	55
2.3	Annular Lesions and Disc Degeneration.....	57
2.3.1	Concentric Tears	57
2.3.2	Radial Tears	58
2.3.3	Rim Lesions.....	59
2.3.4	Comparison of Lesion Types and Association with Age	59
2.3.5	Disc Herniation	59
2.4	Effects of Repetitive Lifting on the Disc	61
2.4.1	Key Mechanical and Viscoelastic Parameters	61
2.4.2	One-Axis Repetitive Loading.....	64
2.4.3	Multi Axes Repetitive Loading.....	66
2.5	Needle Sizes and Use in Clinical Treatment.....	69
2.6	Effects of Needle Injuries on the Disc	71
2.6.1	Structural Effects.....	71
2.6.2	Mechanical Effects	72
2.6.2.1	Effects of Needle Injuries on Disc Pressurisation and Stability..	72
2.6.2.2	Effects of Needle Diameter on Disc Mechanical Properties.....	74
2.7	Conclusion	80
Chapter 3	<i>Methods</i>.....	81
3.1	Overview and Sample Size.....	81
3.2	FSU Preparation	84
3.2.1	Dissection and Potting.....	84
3.2.2	Measurements and Hydration	86
3.3	Creation of Disc Needle Injury	89
3.3.1	Reproducibility of Needle Insertion	92
3.3.1.1	Data-Image Analysis	94
3.4	Mechanical Testing.....	97
3.4.1	Flinders Hexapod Robot	97

3.4.2	6DOF Testing and Repetitive Loading	98
3.4.2.1	6DOF Testing.....	99
3.4.2.2	Repetitive Loading.....	100
3.4.3	Calculations of Stiffness and Phase Angle	101
3.5	Structural Analysis.....	102
3.5.1	Injury Sectioning and Imaging.....	102
3.5.2	Quantifying Needle Injury	105
3.5.2.1	Injury Length and Area.....	106
3.5.2.1.1	Reproducibility of Manual Interventions	107
3.5.2.1.1.1Method	107
3.5.2.1.1.2Data Analysis	110
3.5.2.2	Injury Solidity and Aspect Ratio.....	111
 Chapter 4 Impact of Repetitive Lifting on Lumbar Disc Mechanics: Immediate and Post-Recovery Changes in 6DOF Stiffness and Phase Angle of Ovine FSUs..... 112		
4.1	Abstract.....	112
4.2	Introduction.....	113
4.3	Materials and Methods	115
4.3.1	FSU Preparation.....	115
4.3.2	Mechanical Testing.....	116
4.3.3	Data Analysis.....	118
4.4	Results	119
4.4.1	Stiffness and Phase Angle	123
4.4.1.1	Translational and Shear DOFs	123
4.4.1.2	Rotational and Bending DOFs	127
4.5	Discussion.....	129
4.6	Conclusion.....	133

Chapter 5	<i>Assessing the Combined Impact of Needle Injuries and Repetitive Lifting on Lumbar Disc Mechanics: Immediate and Post-Recovery Changes in 6DOF Stiffness and Phase Angle of Ovine FSUs ..</i>	135
5.1	Abstract.....	135
5.2	Introduction.....	136
5.3	Materials and Methods	138
5.3.1	FSU Preparation.....	138
5.3.2	Creation of Needle Injury	138
5.3.3	Mechanical Testing.....	139
5.3.4	Data Analysis.....	141
5.4	Results.....	141
5.4.1	Stiffness and Phase Angle	144
5.4.1.1	Translational and Shear DOFs	144
5.4.1.2	Rotational and Bending DOFs	148
5.5	Discussion.....	151
5.6	Conclusion.....	156
Chapter 6	<i>Does Repetitive Lifting Increase Annulus Fibrosus Structural Disruption After Needle Insertion Injury?.....</i>	158
6.1	Abstract.....	158
6.2	Introduction.....	159
6.3	Materials and Methods	161
6.3.1	FSU Preparation.....	161
6.3.2	Needle Injury Sectioning	162
6.3.3	Injury Quantification and Data Analysis	163
6.4	Results.....	166
6.5	Discussion.....	169
6.6	Conclusion.....	175
Chapter 7	<i>Concluding Insights and Future Directions</i>	177

7.1	Overview of Key Findings.....	177
7.1.1	Repetitive Lifting Irreversibly Alters FSU Flexion Stiffness and Viscoelastic Properties	177
7.1.2	Immediately after Lifting, the Combined Effects of Needle Injuries and Repetitive Lifting on FSU Stiffness Trigger a Compensatory Response in the Disc	178
7.1.3	Different Forms of Needle Injuries in the Annulus Fibrosus May Exhibit Different Morphological Responses to Repetitive Lifting: Preliminary Analysis.....	179
7.2	Significance.....	180
7.3	Future Directions	180
7.4	Conclusion.....	182
Chapter 8	References.....	183
Appendices.....		200
	Appendix A	200
A.1	Excluded stiffness and phase angle measurements from the mechanical testing of chapter 4	200
A.1.1	Noisy signal at the last compression cycle.....	200
A.1.1.1	Before (pre-) repetitive lifting.....	200
A.1.1.2	After (post-) repetitive lifting.....	201
A.1.2	Outlier measurements based on statistical analysis.....	203
A.1.2.1	Before (pre-) repetitive lifting.....	203
A.1.2.2	After (post-) repetitive lifting	205
A.1.2.3	After recovering period	206
	Appendix B	207
B.1	Excluded stiffness and phase angle measurements from the mechanical testing of Chapter 5	207
B.1.1	Noisy signal at the last compression cycle.....	207
B.1.1.1	Before (pre-) repetitive lifting.....	207
B.1.1.2	After (post-) repetitive lifting	208
B.1.1.3	After recovery period	209

B.1.2	Outlier measurements based on statistical analysis.....	211
B.1.2.1	Before (pre-) repetitive lifting.....	211
B.1.2.2	After (post-) repetitive lifting	212
B.1.2.3	After recovery period	213
Appendix C	215
C.1	Original and processed images of control and mechanical needle injuries with segmentation and measurements of area, length, solidity, and aspect ratio across slices 1 through 5.....	215
C.1.1	Injury slice 1.....	216
C.1.1.1	Original images.....	216
C.1.1.2	Segmentation and area measurements	217
C.1.1.3	Length measurements	218
C.1.1.4	Solidity measurements	219
C.1.1.5	Aspect ratio measurements	220
C.1.2	Injury slice 2.....	221
C.1.2.1	Original images.....	221
C.1.2.2	Segmentation and area measurements	222
C.1.2.3	Length measurements	223
C.1.2.4	Solidity measurements	224
C.1.2.5	Aspect ratio measurements	225
C.1.3	Injury slice 3.....	226
C.1.3.1	Original images.....	226
C.1.3.2	Segmentation and area measurements	227
C.1.3.3	Length measurements	228
C.1.3.4	Solidity measurements	229
C.1.3.5	Aspect ratio measurements	230
C.1.4	Injury slice 4.....	231
C.1.4.1	Original images.....	231
C.1.4.2	Segmentation and area measurements	232
C.1.4.3	Length measurements	233
C.1.4.4	Solidity measurements	234
C.1.4.5	Aspect ratio measurements	235

C.1.5	Injury slice 5.....	236
C.1.5.1	Original images.....	236
C.1.5.2	Segmentation and area measurements	237
C.1.5.3	Length measurements	238
C.1.5.4	Solidity measurements	239
C.1.5.5	Aspect ratio measurements	240
C.2	Tables of measurements and mean values for each injury parameter (area, length, solidity, and aspect ratio) of control and mechanical injury groups.....	241
C.2.1	Area (μm^2).....	241
C.2.2	Length (μm).....	242
C.2.3	Solidity (unitless).....	243
C.2.4	Aspect ratio (unitless).....	244
	Appendix D	246
D.1	Original images of control and mechanical groups with predominant unsuccessful sectioning across slices 1 through 5	246
D.1.1	Control injuries	246
D.1.2	Mechanical injuries.....	247

List of Figures

Figure 2.1 Left lateral view of the FSU with all surrounding ligaments (Newell et al., 2017).....	44
Figure 2.2 Two views of intervertebral disc (a) coronal and (b) transverse planes of the disc with (c) illustration of the alternating fibres in adjacent lamellae. AF: annulus fibrosus; CEP: cartilaginous endplate; BEP: bony endplate; NP: nucleus pulposus (Newell et al., 2017).	45
Figure 2.3 Oblique section view (a) of the nucleus-inner annulus junction with transverse lines of tensile loading in the boxed region. Higher magnification of the boxed region of the image (a) with the dark transverse line of tension ‘x’ (b). Insertion nodes with deep attachments of the NP into the cartilaginous endplate (CEP), which in turn is attached to vertebral endplate (c).	50
Figure 2.4 Oblique section view (a) of the disc anterior annulus showcasing a 30° angle. Microtome cutting to a thickness of 30µm along the cutting plane, marked by an asterisk (*) is detailed (b). The image displays the IP (in-plane) and CS (cross-section) lamellae within adjacent intra-lamellar and the ILM (inter-lamellar matrix) regions (Tavakoli et al., 2017).	50
Figure 2.5 Low magnification view of the lamellae featuring the CB (denoted by *), which provides trans-lamellar connection (Schollum et al., 2009).....	51
Figure 2.6 High magnification view of (a and b) ILM and CB while stretching and fixing the annulus 100% radially, displaying IP and CS arrays separated by a junction (J) that implies inhomogeneous interlamellar connectivity with discrete anchoring mechanism and (c) the merging of cross-bridges and lamellae (denoted by *) suggesting their structural integration (Tavakoli et al., 2016, Pezowicz et al., 2006, Schollum et al., 2009)	52
Figure 2.7 Two example images (a and b) illustrating imaged annulus structures using three imaging modalities: polarised light microscopy, MRI, and ultrasound. The third image in each example superimposes the images of the three modalities (Langlais et al., 2019).	55

Figure 2.8 Common types of annular lesions as observed in histology specimens, featuring left column: sagittal view, and right column: cross-sectional view; (a) concentric tear, (b) radial tears, (c) rim lesion. Top (right) and lateral (left) view of a specimen indicating tissue disruption (Cheung and Luk, 2019). 57

Figure 2.9 Load-displacement curve for a functional spinal unit (FSU) under uniaxial compression. Adapted from Newell et al. (2017), originally based on findings from Asano et al. (1992) and Koeller et al. (1986). Modifications include highlighting the loading and unloading curves to illustrate the material's viscoelastic behaviour and highlighting the linear section of the curve in red as the stiffness calculation region to reflect the initial elastic response. This graph illustrates the typical load-displacement relationship, emphasising the disc's viscoelastic properties. Note: The graph is not to scale and has been adjusted for visual clarity. 61

Figure 2.10 Load-displacement curve illustrating energy loss due to hysteresis in a Functional Spinal Unit (FSU) during uniaxial compression (a), adapted from Newell et al. (2017), originally based on findings from Asano et al. (1992) and Koeller et al. (1986), with modifications to include a filled 'Energy Loss' area. This graph highlights the energy dissipated due to the viscoelastic properties of the disc. Part (b) is an original creation depicting phase angle variations over time, correlating with the mechanical load-displacement curve shown in part (a). Note: the graphs are not to scale and adjusted for visual clarity. 63

Figure 2.11 Five stages of gradual disc prolapse (Adams and Hutton, 1985)... 65

Figure 2.12 Hypothesised model proposing high compression potential to rupture the endplate cartilage, the posterior annulus or both, allowing the NP to be eventually pressed out (Berger-Roscher et al., 2017). 68

Figure 2.13 Model for the mechanism of the disc herniation irrelevant to the endplate failure, suggesting failure mechanism to be limited to the disc (Amin et al., 2020). 69

Figure 2.14 Needle gauges and their corresponding outer diameters. 70

Figure 3.1 An overview of the linkage of sample size and methods of this chapter to the project main studies (**Chapter 4, 5, and 6**). The methods include

the preparation of FSUs, reproducibility testing for needle insertion, mechanical testing to examine repetitive lifting effects, and structural analysis to investigate the combined impact of needle injury and repetitive lifting on lumbar disc mechanics..... 83

Figure 3.2 The custom-built alignment rig and the main stages of potting the FSU. The process begins with potting the inferior vertebra (a), followed by the superior vertebra (b). The completed FSU with both vertebrae potted is also shown (c)..... 86

Figure 3.3 Illustration of offset measurements for the disc's axis of rotation in relation to the hexapod robot's global coordinate system. The calculated offsets: the red arrow for X offset (lateral distance to the potting cup), the green arrow for Y offset (anterior distance to the potting cup), and the blue arrow for Z offset (vertical distance to the hexapod load cell). Note: Arrows not to scale. 88

Figure 3.4 Multi views of the needle insertion apparatus and FSU alignment. An oblique top perspective of the apparatus, featuring a needle holder with an integrated stopper to prevent over-insertion, adjustable screws for FSU height alignment, and a belt for securing the FSU, ready for mounting (a). A further close-up view of the needle securely locked in the needle holder with the bevel facing upward during needle insertion into the disc (b). A posterolateral view of the mounted FSU, highlighting the alignment of the disc above the mid-height for needle insertion (c). 90

Figure 3.5 Anterolateral view radiographs displaying three repeated needle insertions for one FSU..... 93

Figure 3.6 Illustration of needle insertion level and depth measured from a radiograph..... 93

Figure 3.7 The Flinders hexapod robot used for 6DOF mechanical testing (a) with an FSU placed in stainless steel cups, submerged in a water bath, and positioned between the stable base and the moving top plate of the hexapod (b). 97

Figure 3.8 Illustration of the 6DOF testing sequence with corresponding magnitudes (a) and the directional movements applied to the intervertebral disc (b)..... 99

Figure 3.9 An example plot of the last cycle showing the pattern of dynamic testing in anterior shear at 0.1 Hz with the loading portion (red fit) from which stiffness is calculated..... 101

Figure 3.10 Top view of the intervertebral disc showing the extracted segment of the annulus containing the needle injury (white). The segment is cry-sectioned, and five consecutive slices perpendicular to the injury axis, each with a thickness of 60 μm , are obtained. The region of interest where the slices are collected is at 1200 μm depth from the annulus edge (yellow). Note: Drawing not to scale..... 102

Figure 3.11 Top view of a formalin-fixed disc after the removal of the upper vertebra. The remaining disc-bottom vertebra is seamlessly repositioned into the apparatus used earlier for the creation of needle injury. The depiction concludes with the integration of a specially designed angled U-shaped attachment. This setup facilitates a precise vertical cutting to extract the annulus segment containing the needle injury..... 104

Figure 3.12 Illustration of the vertical cut made by a trimming feather blade perpendicular to the injury axis (a). The figure further displays the removal of the annular segment enclosing the needle injury (b). The extracted segment, with its flat base, is shown embedded in an OCT compound, ready for sectioning perpendicular to the injury axis (c)..... 105

Figure 3.13 Analysis with ImageJ software of original image of a needle (a), undergoing segmented injury contours (b), before injury mask generated (c)... 106

Figure 3.14 Demonstration of the elongated axis identification of a needle injury using the 'Ridge Detection' plugin in ImageJ, applied to the created mask of the injury. 107

Figure 3.15 Six images were randomly chosen for reproducibility assessment, each derived from three injuries. For each injury, two images were randomly selected from its respective set of five..... 108

Figure 3.16 Illustration of MATLAB plotting of the convex injury area (in white) and its convex hull (outlined in green) for injury solidity calculation (a), and the principal major (in red) and minor (in blue) axes for aspect ratio calculation (b).
..... 111

Figure 4.1 An overview of the mechanical testing sequence for FSU. The sequence comprises an overnight hydration period, followed by 6DOF mechanical testing before (pre-) and after (post-) simulating repetitive lifting. A final 6DOF test was conducted to assess disc recovery from repetitive lifting after 7 hours, representative of rest or sleep..... 117

Figure 4.2 Load-displacement curves for averaged shear (pre-repetitive lifting, N=20; post-repetitive lifting, N=19; repetitive lifting recovery, N=20) and compression (pre-repetitive lifting, N=19; post-repetitive lifting, N=17; repetitive lifting recovery, N=20) loading during pre-repetitive lifting (blue), post-repetitive lifting (red), and repetitive lifting recovery (green). Dotted lines indicate the 95% confidence interval (CI). 121

Figure 4.3 Load-displacement curves for all rotational loading directions before (pre-) repetitive lifting (blue, N=20), after (post-) repetitive lifting (red, N=19), and following recovery from repetitive lifting (green, N=20). The dotted lines represent the 95% confidence interval (CI). 122

Figure 4.4 Averaged stiffness (N/mm) and phase angle (°), each with their corresponding 95% confidence intervals in compression (Comp). For stiffness, the data represents states before (pre-) repetitive lifting (blue, N=19), after (post-) repetitive lifting (red, N=17), and following recovery period (green, N=20). Similarly, for phase angle, the data is labelled for states before (pre-) repetitive lifting (blue, N=18), after (post-) repetitive lifting (red, N=18), and following recovery period (green, N=20). Error bars indicate the range of the 95% confidence interval, and an asterisk (*) denotes significance (p<0.05). 124

Figure 4.5 Average stiffness and phase angle with a 95% CI for pre-repetitive lifting (N=20), post- repetitive lifting (N=19), and repetitive lifting recovery (N=20) in shear directions: right and left lateral shear (RLS, LLS, respectively), anterior shear (AS), and posterior shear (PS). * Denotes significance (p<0.05). 124

Figure 4.8 Average stiffness and phase angle with a 95% CI for pre- repetitive lifting (N=20), post- repetitive lifting (N=19), and repetitive lifting recovery (N=20) of all rotational directions including extension (EXT), flexion (FLEX), left and right axial rotation (LAR, RAR), along with left and right lateral bending (LLB, RLB). Significant findings are marked with an asterisk (*), indicating $p < 0.05$ 128

Figure 5.1 An overview of the mechanical testing sequence for each FSU, following the recovery period from the previous day's repetitive lifting. Two randomly assigned groups, 'Control' (N=10) and 'Injury' (N=10), with the 'Injury' group undergoing needle injury creation, while both groups proceeded to overnight hydration. The sequence advanced with 6DOF testing both before (pre-) and after (post-) simulated repetitive lifting, concluding with a final 6DOF test following the recovery period after the repetitive lifting. 140

Figure 5.2 Load-displacement curves for averaged shear and compression tests. Solid lines represent the control group, whereas dashed lines represent the injury group. Both groups were subjected to mechanical testing at three different loading stages: before (pre-, in blue) repetitive lifting, after (post-, in red) repetitive lifting, and following repetitive lifting recovery (in green). 142

Figure 5.3 Averaged load-displacement curves for rotational loading directions. Solid lines represent the control group, whereas dashed lines represent the injury group. Both groups were subjected to mechanical testing at three different loading stages: before (pre-, in blue) repetitive lifting, after (post-, in red) repetitive lifting, and following repetitive lifting recovery (in green). 143

Figure 5.4 Averaged stiffness (N/mm) and phase angle ($^{\circ}$) with a 95% CI for compression (Comp). Solid bars represent the control group, while patterned bars indicate the injury group. Both groups underwent mechanical testing at three stages: before (pre-, in blue), after (post-, in red), and following (in green) repetitive lifting. Significant findings, marked with an asterisk (*), indicate $p < 0.05$, suggesting statistical significance between the groups within each loading stage. Sample sizes: control - pre-repetitive lifting (stiffness=9, phase=9), post-repetitive lifting (stiffness=8, phase=8), recovery (stiffness=8, phase=8). Injury - consistent counts of 10 for stiffness and phase across all stages. 146

Figure 5.5 Averaged stiffness (N/mm) and phase angle (°) with a 95% CI for all shear directions, including right and left lateral shear (RLS, LLS, respectively), anterior shear (AS), and posterior shear (PS). Solid bars represent the control group, while patterned bars indicate the injury group. Both groups underwent mechanical testing at three stages: before (pre-, in blue), after (post-, in red), and following (in green) repetitive lifting. Significant findings, marked with an asterisk (*), indicate $p < 0.05$, suggesting statistical significance between the groups under all loading conditions. Sample sizes: control - pre-repetitive lifting (stiffness=10, phase=10), post-repetitive lifting (stiffness=9, phase=9), recovery (stiffness=10, phase=10). Injury - consistent counts of 10 for stiffness and phase across all stages. 147

Figure 5.6 Averaged stiffness (N/mm) and phase angle (°) with a 95% CI for all rotational directions including extension (EXT), flexion (FLEX), left and right axial rotation (LAR, RAR), and left and right lateral bending (LLB, RLB). Solid bars represent the control group, while dashed bars indicate the injury group. Both groups underwent mechanical testing at three stages: before (pre-, in blue), after (post-, in red), and following (in green) repetitive lifting. Significant findings, marked with an asterisk (*), indicate $p < 0.05$. Sample sizes: control - pre-repetitive lifting (stiffness=10, phase=10), post-repetitive lifting (stiffness=9, phase=9), recovery (stiffness=10, phase=10). Injury - consistent counts of 10 for stiffness and phase across all stages..... 150

Figure 5.7 Diagram illustrating the mechanistic theory of an intervertebral disc's response to simulated repetitive lifting, considering a pre-existing irreversible decrease in flexion stiffness before injury (Chapter 4) (a). This initial state is compounded with a posterolateral needle injury to the left side, with no change in lateral bending stiffness observed (b). The subsequent compensatory biomechanical response immediately following the simulated repetitive lifting is characterised by an increase in right lateral bending stiffness on the side contralateral to the injury (c), serving to balance bending movements and potentially prevent further injury or stress on the left side. This increased stiffness was shown to be reversible, diminishing after a recovery period (d),

which indicates the disc's inherent resilience and ability to recover from such biomechanical stress..... 153

Figure 6.1 Representative injury images from each group, organised by sequential injury slices (1-5) along the rows, with each slice being 60 μm thick. Columns 1 and 2 display original brightfield images from the control and mechanical groups both with green ink outlines marking the injuries. Columns 3 and 4 show these images processed using ImageJ for injury segmentation..... 164

Figure 6.2 Injury masks of the representative injuries of each group (**Figure 6.1**), organised by sequential injury slices (1-5) along the rows. Columns 1 and 2 display injury mask images from the control and mechanical groups, both highlighting injury lengths using ImageJ. Columns 3 and 4 show these images with the convex hull area (green), and principal major (red) and minor (blue) axes plotted by MATLAB for aspect ratio calculations..... 165

Figure 6.3 Mean values for the control group (blue, n=3) and the mechanical injury group (red, n=3) for all measured parameters: area (μm^2), length (μm), solidity (unitless), and aspect ratio (unitless). Each bar represents the group mean, calculated by averaging the mean values of the three injuries in the respective group. The error bars signify the 95% confidence intervals..... 168

Figure 6.4 Comparison of 25G needle injuries in adjacent annulus layers as observed in the current (a, c) and previous (b, d) studies (van Heeswijk, 2017), each illustrating distinct forms of injuries. Parallel injuries from both studies appeared within annular layers in images (a) and (b). Notably, in the counter-oblique adjacent layers (c and d), the higher Brightfield magnification (200 μm scale bar) from the current study reveals a hybrid (parallel and cross) form injury (c). In contrast, the previous study, using lower DIC magnification (1 mm scale bar), the injury manifested in cross form (d)..... 171

Figure 6.5 Comparison of parallel and hybrid injury forms in two consecutive slices. The parallel and hybrid injury forms are within a single annular layer, presented in two consecutive slices: the top slice and the bottom slice with each slice shown in both control and mechanical injuries..... 173

Figure A- 1 Noisy signal at the last compression cycle before (pre-) repetitive lifting leading to the omission of the stiffness measurement from this cycle (FSU 08ID50).....	200
Figure A- 2 Noisy signal at the last compression cycle after (post-) repetitive lifting leading to the omission of the stiffness measurement from this cycle (FSU 10ID20).....	201
Figure A- 3 Noisy signal at the last compression cycle after (post-) repetitive lifting leading to the omission of the stiffness measurement from this cycle (FSU 12ID24).....	202
Figure A- 4 Outlier of one compression phase angle measurement before (pre-repetitive lifting) leading to the omission of this measurement (FSU ID50).....	203
Figure A- 5 Outlier of one compression phase angle measurement before (pre-repetitive lifting) leading to the omission of this measurement (FSU ID24).....	204
Figure A- 6 Outlier of one compression phase angle measurement after (post-repetitive lifting) leading to the omission of this measurement (FSU ID24).....	205
Figure A- 7 Outlier of one compression phase angle measurement following recovery period leading to the omission of this measurement (FSU ID24).....	206
Figure B- 1 Noisy signal at the last compression cycle before (pre-)repetitive lifting leading to the omission of the stiffness measurement from this cycle in the control group data (FSU 12ID24).....	207
Figure B- 2 Noisy signal at the last compression cycle after (post-)repetitive lifting leading to the omission of the stiffness measurement from this cycle in the control group data (FSU 12ID24).....	208
Figure B- 3 Noisy signal at the last compression cycle after recovery period leading to the omission of the stiffness measurement from this cycle in the control group data (FSU 11ID12).....	209
Figure B- 4 Noisy signal at the last compression cycle after recovery period leading to the omission of the stiffness measurement from this cycle in the control group data (FSU 12ID24).....	210
Figure B- 5 Outlier of one compression phase angle measurement before (Pre-Repetitive Lifting) leading to the omission of this measurement in the control group data (FSU 12ID24).....	211

Figure B- 6 Outlier of one compression phase angle measurement after (post-) Repetitive Lifting) leading to the omission of this measurement in the control group data (FSU 12ID24). 212

Figure B- 7 Outlier of one compression phase angle measurement after recovery period leading to the omission of this measurement in the control group data (FSU 11ID12). 213

Figure B- 8 Outlier of one compression phase angle measurement following recovery period leading to the omission of this measurement (FSU ID24)..... 214

Figure C- 1 Original images of needle injuries in Slice 1. Each image is annotated with labels indicating control or mechanical injuries, along with the slice number and specific injury IDs. The top row displays control injuries, labelled as ID17, ID25, and ID56, respectively. The bottom row shows mechanical injuries, with labels ID10, ID26, and ID44, respectively. 216

Figure C- 2 Segmentation of needle injuries in slice 1. Each image is annotated with labels indicating control or mechanical injuries, along with the slice number and specific injury IDs, each with its respective area measurement. The top row displays control injuries, labelled as ID17, ID25, and ID56, respectively. The bottom row shows mechanical injuries, with labels ID10, ID26, and ID44, respectively. 217

Figure C- 3 Length of needle injuries in slice 1. Each image is annotated with labels indicating control or mechanical injuries, along with the slice number and specific injury IDs, each with its respective length measurement. The top row displays control injuries, labelled as ID17, ID25, and ID56, respectively. The bottom row shows mechanical injuries, with labels ID10, ID26, and ID44, respectively. 218

Figure C- 4 Solidity of needle injuries in slice 1. Each image is annotated with labels indicating control or mechanical injuries, along with the slice number and specific injury IDs, each with its respective solidity measurement. The top row displays control injuries, labelled as ID17, ID25, and ID56, respectively. The bottom row shows mechanical injuries, with labels ID10, ID26, and ID44, respectively. 219

Figure C- 5 Aspect ratio of needle injuries in slice 1. Each image is annotated with labels indicating control or mechanical injuries, along with the slice number and specific injury IDs, each with its respective aspect ratio measurement. The top row displays control injuries, labelled as ID17, ID25, and ID56, respectively. The bottom row shows mechanical injuries, with labels ID10, ID26, and ID44, respectively. 220

Figure C- 6 Original images of needle injuries in slice 2. Each image is annotated with labels indicating control or mechanical injuries, along with the slice number and specific injury IDs. The top row displays control injuries, labelled as ID17, ID25, and ID56, respectively. The bottom row shows mechanical injuries, with labels ID10, ID26, and ID44, respectively. 221

Figure C- 7 Segmentation of needle injuries in slice 2. Each image is annotated with labels indicating control or mechanical injuries, along with the slice number and specific injury IDs, each with its respective area measurement. The top row displays control injuries, labelled as ID17, ID25, and ID56, respectively. The bottom row shows mechanical injuries, with labels ID10, ID26, and ID44, respectively. 222

Figure C- 8 Length of needle injuries in slice 2. Each image is annotated with labels indicating control or mechanical injuries, along with the slice number and specific injury IDs, each with its respective length measurement. The top row displays control injuries, labelled as ID17, ID25, and ID56, respectively. The bottom row shows mechanical injuries, with labels ID10, ID26, and ID44, respectively. 223

Figure C- 9 Solidity of needle injuries in slice 2. Each image is annotated with labels indicating control or mechanical injuries, along with the slice number and specific injury IDs, each with its respective solidity measurement. The top row displays control injuries, labelled as ID17, ID25, and ID56, respectively. The bottom row shows mechanical injuries, with labels ID10, ID26, and ID44, respectively. 224

Figure C- 10 Aspect ratio of needle injuries in slice 2. Each image is annotated with labels indicating control or mechanical injuries, along with the slice number and specific injury IDs, each with its respective aspect ratio measurement. The

top row displays control injuries, labelled as ID17, ID25, and ID56, respectively. The bottom row shows mechanical injuries, with labels ID10, ID26, and ID44, respectively. 225

Figure C- 11 Original images of needle injuries in slice 3. Each image is annotated with labels indicating control or mechanical injuries, along with the slice number and specific injury IDs. The top row displays control injuries, labelled as ID17, ID25, and ID56, respectively. 226

Figure C- 12 Segmentation of needle injuries in slice 3. Each image is annotated with labels indicating control or mechanical injuries, along with the slice number and specific injury IDs, each with its respective area measurement. The top row displays control injuries, labelled as ID17, ID25, and ID56, respectively. The bottom row shows mechanical injuries, with labels ID10, ID26, and ID44, respectively. 227

Figure C- 13 Length of needle injuries in slice 3. Each image is annotated with labels indicating control or mechanical injuries, along with the slice number and specific injury IDs, each with its respective length measurement. The top row displays control injuries, labelled as ID17, ID25, and ID56, respectively. The bottom row shows mechanical injuries, with labels ID10, ID26, and ID44, respectively. 228

Figure C- 14 Solidity of needle injuries in slice 3. Each image is annotated with labels indicating control or mechanical injuries, along with the slice number and specific injury IDs, each with its respective solidity measurement. The top row displays control injuries, labelled as ID17, ID25, and ID56, respectively. The bottom row shows mechanical injuries, with labels ID10, ID26, and ID44, respectively. 229

Figure C- 15 Aspect ratio of needle injuries in slice 3. Each image is annotated with labels indicating control or mechanical injuries, along with the slice number and specific injury IDs, each with its respective aspect ratio measurement. The top row displays control injuries, labelled as ID17, ID25, and ID56, respectively. The bottom row shows mechanical injuries, with labels ID10, ID26, and ID44, respectively. 230

Figure C- 16 Original images of needle injuries in slice 4. Each image is annotated with labels indicating control or mechanical injuries, along with the slice number and specific injury IDs. The top row displays control injuries, labelled as ID17, ID25, and ID56, respectively. The bottom row shows mechanical injuries, with labels ID10, ID26, and ID44, respectively. 231

Figure C- 17 Segmentation of needle injuries in slice 4. Each image is annotated with labels indicating control or mechanical injuries, along with the slice number and specific injury IDs, each with its respective area measurement. The top row displays control injuries, labelled as ID17, ID25, and ID56, respectively. The bottom row shows mechanical injuries, with labels ID10, ID26, and ID44, respectively. 232

Figure C- 18 Length of needle injuries in slice 4. Each image is annotated with labels indicating control or mechanical injuries, along with the slice number and specific injury IDs, each with its respective length measurement. The top row displays control injuries, labelled as ID17, ID25, and ID56, respectively. The bottom row shows mechanical injuries, with labels ID10, ID26, and ID44, respectively. 233

Figure C- 19 Solidity of needle injuries in slice 4. Each image is annotated with labels indicating control or mechanical injuries, along with the slice number and specific injury IDs, each with its respective solidity measurement. The top row displays control injuries, labelled as ID17, ID25, and ID56, respectively. The bottom row shows mechanical injuries, with labels ID10, ID26, and ID44, respectively. 234

Figure C- 20 Aspect ratio of needle injuries in slice 4. Each image is annotated with labels indicating control or mechanical injuries, along with the slice number and specific injury IDs, each with its respective aspect ratio measurement. The top row displays control injuries, labelled as ID17, ID25, and ID56, respectively. The bottom row shows mechanical injuries, with labels ID10, ID26, and ID44, respectively. 235

Figure C- 21 Original images of needle injuries in slice 5. Each image is annotated with labels indicating control or mechanical injuries, along with the slice number and specific injury IDs. The top row displays control injuries,

labelled as ID17, ID25, and ID56, respectively. The bottom row shows mechanical injuries, with labels ID10, ID26, and ID44, respectively. 236

Figure C- 22 Segmentation of needle injuries in slice 5. Each image is annotated with labels indicating control or mechanical injuries, along with the slice number and specific injury IDs, each with its respective area measurement. The top row displays control injuries, labelled as ID17, ID25, and ID56, respectively. The bottom row shows mechanical injuries, with labels ID10, ID26, and ID44, respectively. 237

Figure C- 23 Length of needle injuries in slice 5. Each image is annotated with labels indicating control or mechanical injuries, along with the slice number and specific injury IDs, each with its respective length measurement. The top row displays control injuries, labelled as ID17, ID25, and ID56, respectively. The bottom row shows mechanical injuries, with labels ID10, ID26, and ID44, respectively. 238

Figure C- 24 Solidity of needle injuries in slice 5. Each image is annotated with labels indicating control or mechanical injuries, along with the slice number and specific injury IDs, each with its respective solidity measurement. The top row displays control injuries, labelled as ID17, ID25, and ID56, respectively. The bottom row shows mechanical injuries, with labels ID10, ID26, and ID44, respectively. 239

Figure C- 25 Aspect ratio of needle injuries in slice 5. Each image is annotated with labels indicating control or mechanical injuries, along with the slice number and specific injury IDs, each with its respective aspect ratio measurement. The top row displays control injuries, labelled as ID17, ID25, and ID56, respectively. The bottom row shows mechanical injuries, with labels ID10, ID26, and ID44, respectively. 240

Figure C- 26 Mean values for each injury in the control (blue, n=3) and mechanical injury (red, n=3) groups for four measured parameters, as labelled above each chart: area (μm^2), length (μm), density (unitless), and aspect ratio (unitless). Each of the three bars per colour represents the average of measurements from the five slices for the respective injury. 245

Figure D- 1 Original images of control group with predominant unsuccessful sectioning across slices 1 through 5. Columns correspond to the respective slices, and rows represent individual injuries. "X" marks indicate instances where sectioning was entirely unsuccessful, resulting in no slices being collected for imaging..... 246

Figure D- 2 Original images of mechanical group with predominant unsuccessful sectioning across slices 1 through 5. Columns correspond to the respective slices, and rows represent individual injuries. "X" marks indicate instances where sectioning was entirely unsuccessful, resulting in no slices being collected for imaging..... 247

List of Tables

Table 2-1 Combinations of repetitive movements flexion (Flex), axial rotation (AR) and lateral bending (LB) with or without fixed/repetitive compression (Comp) studied previously.....	67
Table 2-2 Review of Needle: Disc Height Ratios used across different disc species previously.....	76
Table 2-3 Summary of reviewed in vitro studies investigating the effects of disc needle injuries. studies are organised by specimen and testing mode, ratio of needle diameter to disc height and resultant mechanical and structural influence.....	78
Table 3-1 and Table 3-2 Measurements of the needle insertion level and depth taken during needle insertion repeats for four FSUs. For each FSU (disc height and width mean in mm, respectively), three separate measurements are presented for each insertion repeat, alongside the calculated mean. Table 3-1 (left) presents the needle insertion level (mm) into the disc, while Table 3-2 (right) indicates the needle insertion depth (mm) relative to the top edge of the disc. An 'x' in the tables signifies missing data due to an experimental error. ...	95
Table 3-3 and Table 3-4 Results from the reproducibility assessment, based on the ImageJ analysis procedure. These tables capture the measurements for both the area and length of the injuries across all six images in five separate test repeats.....	110
Table 4-1 Percent differences (%) and p-values (P) for averaged changes in stiffness and phase angle after (post-) repetitive lifting and following repetitive lifting recovery compared to the condition before (pre-) repetitive lifting across different directions: compression (Comp), right lateral shear (RLS), left lateral shear (LLS), anterior shear (AS), and posterior shear (PS). Significance values ($P < 0.05$) are in bold and underlined.	124
Table 4-2 Percent differences (%) and p-values (P) for averaged changes in stiffness and phase angle after (post-) repetitive lifting and following repetitive lifting recovery compared to the condition before (pre-) repetitive lifting across	

different directions: extension (EXT), flexion (FLEX), left axial rotation (LAR), right axial rotation (RAR), left lateral bending (LLB), and right lateral bending (RLB). Significance values ($P < 0.05$) are in bold and underlined..... 127

Table 5-1 Percent differences (%) and p-values (P) for averaged changes in stiffness and phase angle in the injury group compared to the control group across different directions: compression (Comp), right lateral shear (RLS), left lateral shear (LLS), anterior shear (AS), and posterior shear (PS). Values indicating significance ($P < 0.05$) are highlighted in bold and underlined. The table includes data from mechanical testing conducted before (pre-) repetitive, after (post-) repetitive lifting, and following repetitive lifting recovery..... 145

Table 5-2 Percent differences (%) and p-values (P) for averaged changes in stiffness and phase angle in the injury group compared to the control group in extension (EXT), flexion (FLEX), left axial rotation (LAR), right axial rotation (RAR), left lateral bending (LLB), and right lateral bending (RLB). Values with significance ($P < 0.05$) are highlighted in bold and underlined. This comparative analysis includes mechanical testing conducted before (pre-) repetitive lifting, after (post-) repetitive lifting, and following repetitive lifting recovery..... 149

Table 6-1 'T-test p-value' of independent t-test. '95% Confidence Interval' presents the range of values for the difference between control and mechanical groups. 'Hedges' g' shows the effect size, with the negative sign suggesting that the mechanical group has a lower mean than the control group for the respective parameters, and a positive value indicates the opposite. 'Effect Size Interpretation' provides a general interpretation of the magnitude of the effect size (Small for $0.2 < |Hedges' g| < 0.5$, Medium for $0.5 \leq |Hedges' g| < 0.8$, and Large for $|Hedges' g| \geq 0.8$)..... 169

Table 6-2 (Left) and **Table 6-3** (Right) quantify changes in injury area, length, solidity, and aspect ratio within a single annular layer for the parallel and hybrid injury forms in both the control (cont) and mechanical (mech) injuries (**Figure 6.5**). Table 6-2 quantifies changes in the parameters in the mechanical group, averaging across slices and comparing each injury form to its respective

control. Table 6-3 quantifies changes in injury parameters across the consecutive slices, comparing the bottom slice to the top. 174

Table C- 1 Area measurements (μm^2) across five slices for each injury within control and mechanical groups along with the mean values. 241

Table C- 2 Length measurements (μm) across five slices for each injury within control and mechanical groups along with the mean values. 242

Table C- 3 Solidity measurements (unitless) across five slices for each injury within control and mechanical groups along with the mean values. 243

Table C- 4 Aspect ratio (unitless) across five slices for each injury within control and mechanical groups along with the mean values. 244

List of Abbreviations

6DOF	Six degrees of freedom
AP	Anterior posterior
BEP	Bony endplate
CEP	Cartilaginous endplate
CPSD	Cross power spectral density
CT	Computed tomography
DVC	Digital volume correlation
FSU	Functional spinal units
ICC	Intraclass correlation coefficient
LAT	Lateral side
LBP	Low back pain
NATA	National Association of Testing Authorities
NP	Nucleus pulposus
OCT	Optimal cutting temperature
PBS	Phosphate-buffered saline
SAHMRI	South Australian Health and Medical Research Institute
SWS	Shear wave speed

Abstract

Despite the intervertebral disc's ability to withstand considerable loading, its resilience is critical in the context of widespread back disorders, such as low back pain (LBP), which impose significant global health and economic challenges. These challenges are exacerbated by factors like repetitive lifting, further complicating the disc's vulnerability not only to occurrences like annular tears but also to artificial interventions, including clinical needle punctures used in diagnosing and treating spinal issues. Although prior *in vitro* studies have examined the mechanical impact of needle injuries on intervertebral discs, they have not considered simulated *in vivo* mechanical loading conditions reflective of repetitive lifting, which is closely associated with these injuries. Moreover, there has been a lack of investigation into the development and potential morphological changes in the annulus fibrosus due to needle-induced rupture under conditions that mimic repetitive lifting. Bridging this gap requires an examination of the individual mechanical effects of repetitive lifting on functional spinal units (FSUs), incorporating more realistic conditions that include inter-day disc recovery. Consequently, this thesis aims to assess the mechanical influence of simulated repetitive lifting on ovine FSUs immediately after lifting and following a recovery period, both independently and in conjunction with disc needle injuries. It also seeks to quantify the morphological changes in needle-induced ruptures within the annulus fibrosus after exposure to simulated repetitive lifting.

To fulfil the aims of the research, the sole mechanical effects of repetitive lifting were first evaluated. Twenty ovine FSUs underwent six degrees of freedom (6DOF) testing at 0.1 Hz for five cycles, followed by simulated repetitive lifting to replicate a day of lifting. This simulation involved 1000 cycles combining compression (1.1 MPa)—equivalent to lifting an intermediate weight of 20 kg, within safe manual handling limits—and flexion (13°). Subsequently, two additional 6DOF tests were conducted: one immediately after the lifting session and the other after a recovery period, allowing the discs to reach fluid equilibrium similar to that during sleep. Once these FSUs were adapted to the

recovery state, further investigation was performed on the combined effects of needle injuries and simulated repetitive lifting. The FSUs were divided into control and injury groups, each comprising 10 FSUs. The injury group received 25G needle injuries in the posterolateral regions of the discs before repeating the simulated repetitive lifting and testing protocol on both groups. Microtome sections were successfully collected from some of these injuries, perpendicular to the injury axis, where microscope images were obtained, and the morphologies of these injuries were quantified.

The sole mechanical effects of repetitive lifting were found to cause significant biomechanical changes in flexion, a primary direction applied to the load. The changes appeared as a decrease in stiffness (77.2%, $P < 0.001$) and an increase in the phase angle (89%, $P < 0.001$) immediately following the simulated repetitive lifting. After a period applied for disc recovery to allow for fluid equilibrium, the observed changes in flexion persisted. Specifically, there was a continued reduction in stiffness (71.2%, $P < 0.001$) and an increased phase angle (63.8%, $P < 0.001$). These findings suggested that the recovery period was insufficient to fully moderate the biomechanical damage induced by repetitive lifting, likely in the disc's microstructure.

Assessments of FSU mechanics by combined needle injuries and repetitive lifting demonstrated an increase in stiffness in right lateral bending (27.27%, $P = 0.01$) immediately following the lifting, suggesting a compensatory mechanism for a compromised left posterolateral side due to a needle injury. This increase in stiffness response might relate to a permanent reduction in flexion stiffness caused by the previous repetitive lifting prior to needle injury, considering that an intrinsic aspect of forward bending relates to lateral bending. Furthermore, the vulnerability of the left side annulus to needle injuries could be due to disruption likely in the inner annulus as a consequence of cumulative damage from repetitive lifting. The right side's increased stiffness during lateral bending, previously not present, suggested a distinctive biomechanical response of the disc to counteract the reduced flexion stiffness, thereby maintaining equilibrium in bending movements and potentially preventing further injury or stress to the

injured left side. The increase in stiffness was temporary since it diminished after a recovery period.

Exploration of how repetitive lifting impacts the morphology of needle injuries in the annulus was insufficient to draw definitive conclusions due to encountered variability in the measurements. This variability might be linked to the different forms of needle injury inherent when inflicted into the annulus. The present research emphasised this variability further by identifying, for the first time, a hybrid injury form—a combination of the known parallel and cross forms. These forms naturally occur and intrinsically manifest, aligning with or intersecting the oblique fibres of the annulus, respectively. Preliminary analysis, conducted by taking morphological measurements on limited data with consistent injury forms, may encourage future studies to investigate the potential for differential responses to repetitive lifting among needle injuries based on their form.

The findings of this thesis on the biomechanical effects of repetitive lifting can contribute to the development of safety guidelines for workers engaged in repetitive lifting tasks. Furthermore, investigating the interplay between repetitive lifting and disc needle injuries sets a foundation for future research to improve diagnosis and treatment strategies for disc issues.

Declaration

I certify that this thesis does not incorporate without acknowledgement any material previously submitted for a degree or diploma in any university and that, to the best of my knowledge and belief, it does not contain any material previously published or written by another person except where due reference is made in the text.

﴿ وَيَسْأَلُونَكَ عَنِ الرُّوحِ قُلِ الرُّوحُ مِنْ أَمْرِ رَبِّي وَمَا أُوتِيتُمْ مِنَ الْعِلْمِ إِلَّا قَلِيلًا ﴾

And they ask you 'O Muhammad' about the soul. Say,
"The soul is of the affair of my Lord, and you 'O humanity'
have not been given of knowledge except a little."

[Quran 17:85]

Acknowledgements

Ál-Ḥamdu lillāh (Praise be to God). This PhD journey would not have been possible without the support of Allah (God) Almighty and His blessings in the form of unlimited favours. I am grateful to Allah for my wonderful parents, family, supervisors, colleagues, and the opportunities that have been part of my journey. "He who has not thanked people has not thanked Allah" (Prophet Muhammad, peace and blessings be upon him). Thus, I extend my thanks to many, without whom my journey would not have been successful.

I would like to express my gratitude to my principal supervisor, John Costi, for his outstanding supervision. Having been part of his team during both my master's and PhD studies, I have directly benefited from his extensive expertise and deep knowledge in the field. His patient guidance, accurate and timely feedback, and unwavering encouragement have been invaluable, especially through the challenges encountered in my research project during the unprecedented period of the COVID-19 pandemic. I acknowledge the significant amount of time and dedication he has devoted to me, and I am deeply grateful for the profound influence I have gained from his mentorship. I am beyond grateful to John, and I promise to pass on what I have learned from him, as long as I am capable.

I would also like to extend my gratitude to my associate supervisors, Rami Al-Dirini and Javad Tavakoli. Their exceptional expertise, critique, and feedback have significantly contributed to the success of my PhD research. The critical comments from our many inspiring meeting discussions have fuelled my motivation to push my research forward. I cannot imagine the success of my PhD without their support and guidance. My words fall short of expressing my gratitude for their patience and the effort and time they have dedicated to my research despite their busy schedules.

Special thanks to my fellow PhD candidate, Michael Russo, whom I've known since my master's studies. Since then, Michael has been of tremendous support to me, always easy to reach and consistently uplifting with his high spirit during

difficult times. His input in our invaluable discussions and his assistance with the Flinders hexapod have been essential to my research. I'm very thankful to Michael for his countless assistance.

I am also grateful to Mark Taylor and Egon Perilli for being continuous assessors throughout the annual milestones of my research, providing invaluable feedback that has considerably contributed to the progress of my PhD. I also extend my thanks to statistical consultant Pawel Skuza for the many meetings we've had, offering advice on the statistics of my research. Sincere thanks go to the engineering services, particularly to Richard Stanley and Tim Hodge for their technical support; many thanks also go to the Flinders Microscopy team, including Nicholas Eyre and Pat Vilimas, for their support and technical advice on the histological aspect of my research.

I sincerely thank Jouf University in Saudi Arabia for the financial support provided for my PhD studies. I also appreciate the extension granted, considering the significant impact caused by the COVID-19 pandemic. My gratitude extends to a wide circle of individuals who have contributed to my excitement and well-being throughout this journey, creating a nurturing environment through their support and positive engagement. Special thanks go to Omar Shakar, Ghassan Al-Nuaimi, David Hobbs, Robert Trott, Atefa Rezwani, Ushmita Reebye, Mohsen Feyzi, Parham Foroutan, Tyra Lange, Rebecca Caddy, Kishor Regmi and Francesca Bucci.

I dedicate this thesis to my mother, Latifah, and father, Sulaiman, for their love, prayers, sacrifices, and patience. I would also like to sincerely thank my brothers, Aziz, Majed, Hamdan, and Waleed, and my sister, Majedah, for all their encouragement and support. May Allah reward them for it. To my mother, you are a source of strength and blessings in my life with your unconditional love and continued sincere prayers in my difficult moments. May Allah assist me in giving back a fraction of what you have given to me, and grant you strength, health, and happiness in this life, and the highest level in Paradise (Firdaws Al-'Alaa) in the hereafter. To my great and wise father, a doctor in life, though he

never had the chance to attend school. You passed away when I was 12 years old (may Allah bless your soul). I am amazed by the continuous impact your teachings have had, not only on me but also on the lives of your sons, despite your absence from such an early age. I always cherish the lessons you imparted and the generous rewards for our achievements in primary school. Your foresight in confidently telling others that they would see among your children an engineer and a doctor was incredibly impressive. Indeed, Father, you were right. Today, as I stand on the threshold of achieving what once seemed like a distant dream, and with engineers among your sons, I can see it all clearly. I am carrying forward not just the knowledge and skills I have gained but also the values and vision you instilled in us. I aspire to pass this wisdom on to my children and future generations. May Allah reward you for all you've done for us, grant you the highest level in Paradise, and assist me in keeping you in my prayers until the end of my life.

To my loving wife, Shatha, mere words of gratitude and appreciation are not enough. Shatha, to whom I am deeply indebted, I could not have completed this journey without your support. You have been patient by my side abroad for years, and now, you endure almost a year-long wait, taking care of our children while I am away focusing on completing my studies. Thank you very much Shatha, from the bottom of my heart. I love you and may Allah reward you abundantly for all you've done for me. To my daughter Lamar and my son Jassar, thank you for your love and the joy you bring into my life. I love you; may Allah bless you. I guess I can finally say I've done my homework and will be flying back home soon, Insha'Allah (by Allah's will).

Conference Presentations

- T. Alsharari, J. Costi, R. Al-Dirini, J. Tavakoli (2021) – Effects of Needle Injuries on the Structure and Mechanics of the Lumbar Disc. Seminar Presentation at the Engineered Systems Research Section, College of Science and Engineering, Flinders University, Adelaide, South Australia, Oct. 2021
- T. Alsharari, J. Costi, R. Al-Dirini, J. Tavakoli (2021) – Effects of Needle Injuries on the Structure and Mechanics of the Lumbar Disc. Podium Presentation at the Engineered Systems Research Section, Higher Degree by Research Conference, College of Science and Engineering, Flinders University, Adelaide, South Australia, Dec. 2021.
- T. Alsharari, J. Costi, R. Al-Dirini, J. Tavakoli (2021) – Effects of Needle Injuries on the Structure and Mechanics of the Lumbar Disc. Online Presentation in the Medical and Health Sciences category at the 6th Saudi Scientific Symposium in Australia, Sydney, Dec. 2021

Awards & Prizes

- Third Place Award for Best Presentation at the Engineered Systems Research Section, Higher Degree by Research Conference, College of Science and Engineering, Flinders University, Adelaide, South Australia, Dec. 2021.
- First Place Award for Best Presentation in the Medical and Health Sciences category at the 6th Saudi Scientific Symposium, Sydney, Dec. 2021.
- Award of Most Outstanding Research Image, Medical Devices Research Institute, Flinders University, Adelaide, South Australia, Dec. 2021.

Chapter 1 Introduction

1.1 Motivation

Back disorders, including low back pain (LBP), are a common global health issue, causing significant disability ([Hartvigsen et al., 2018](#), [Vos et al., 2017](#)). They impose a substantial economic burden, costing over 605 million AUD annually in Australia ([Penm et al., 2006](#)) and exceeding 50 billion USD in the United States ([AIHW, 2023](#), [Davis, 2012](#)). The Australian National Health Survey reported LBP as the second leading cause of disease burden overall in 2015, and 16% of Australians experienced LBP in 2017–18 ([Health and Welfare, 2019](#)). LBP is attributed to abnormalities in the lumbar spine, such as degenerative changes or unusual mechanical loading exerted on the intervertebral disc. Mechanical loading includes a sudden overload resulting from falls, car accidents, or repetitive lifting practices involved in some manual labour ([Adams, 2004](#), [Riihimäki, 1991](#)). These loading modes can lead to structural failure in the form of disc herniation ([Adams and Hutton, 1982](#), [Galante, 1967](#))—extrusion of the disc centre outward—commonly present with chronic LBP ([Ali et al., 2013](#)).

The intervertebral disc contains the nucleus pulposus (NP), rich in water and collagen, to make the disc resilient and resistant to axial compression. Its proteoglycan content allows it to effectively handle these stresses, which radiate outward towards the tough collagenous annulus fibrosis (AF) ([Greenwald et al., 1978](#)). Annular tears naturally appear in degenerating discs. However, minor annular disruptions created by needle punctures are used as a pathway for treating back disorders. Despite conflicting results from cohort studies regarding needle use in discography and its link to disc herniation, there is a consensus ([Carragee et al., 2009](#), [Hur et al., 2016](#)) about its association with disc degeneration. Nonetheless, discography remains the gold standard for diagnosing discogenic pain ([Chen and Gao, 2023](#)) and continues to be an acceptable intervention by professional spine societies ([Hunt et al., 2019](#), [Centerville et al., 2018](#), [Bogduk, 2004](#), [Gilbert et al.](#)). Additionally, needles are

increasingly recognised for their role in administering biological treatments for disc degeneration (Buckley et al., 2018, Cho et al., 2013, Ren et al., 2013, Tam et al., 2014).

Previous studies have provided insights into the impact of needle injuries on the intervertebral disc's mechanics (Elliott et al., 2008, Torre et al., 2019, Michalek et al., 2010b, Michalek et al., 2012) and structure (Michalek and Iatridis, 2012, van Heeswijk et al., 2018, Michalek et al., 2010a) testing functional spinal units (FSUs). However, these studies primarily focused on such injuries in isolation without considering the combined effects of repetitive lifting. In occupational settings, an individual can potentially perform repetitive lifting a scenario is likely to lead to conditions that necessitate disc diagnosis or treatment through needle interventions. This potential is substantiated by findings from a 10-year cohort clinical study, which linked disc herniation to needle injuries, with subjects found to be from lifting occupations that included heavy weight (Carragee et al., 2009). Additionally, it remains unclear how needle-induced rupture in the annulus fibrosus develops and potentially changes in morphology under the combined repetitive lifting. Addressing this gap is critical for the health and safety of workers engaging in repetitive lifting and vulnerable to needle injuries, as these conditions are prevalent and can have a long-term impact on disc health.

To comprehend the effect of needle injuries under combined lifting conditions, understanding the sole mechanical effect of repetitive lifting is essential. While prior research has replicated repetitive lifting scenarios effectively, studies examining the mechanical responses of FSUs to prolonged simulated lifting of durations approximating a week (Drake et al., 2005), a year (Amin, 2019a), or even longer (Gordon et al., 1991) have not considered the factor of inter-day disc recovery, such as fluid re-equilibration that occurs during sleep. The duration of disc fluid equilibrium is critical as it influences disc height (Lu et al., 1996, Natarajan and Andersson, 1999) and stiffness (Costi et al., 2002).

1.2 Aims

Therefore, using ovine FSUs and simulating repetitive lifting, the project was designed with the following aims:

- **Method development:**
 - **Aim 1:** Develop and validate a method for creating reproducible needle insertion into the posterolateral region of the intervertebral disc.
- **Mechanical assessment:**
 - **Aim 2:** Focus on assessing the effects of repetitive lifting on the six degrees of freedom (6DOF) stiffness and phase angle (viscoelastic measure) of the FSUs.
 - **Aim 3:** Evaluate the combined impact of needle injuries and repetitive lifting on these mechanical properties (6DOF stiffness and phase angle). Both Aims 2 and 3 concentrate on observing changes immediately after lifting and following a period of disc recovery.
- **Structural assessment:**
 - **Aim 4:** Investigate the impact of repetitive lifting on the morphology of needle injuries created in annulus fibrosis. The morphology quantified in terms of injury area, length, aspect ratio, and solidity (the ratio of the injury area to its convex hull, the smallest convex polygon containing the injury).

Simulated repetitive lifting was characterised by applying a compression of 1.1 MPa to the FSU, equivalent to lifting an intermediate weight of 20 kg (within safe manual handling limits), combined with a 13° flexion, and executed for 1000 cycles to simulate an achievable magnitude in a day's duration.

1.3 Significance

This research will present novel insights into the impact of repetitive lifting on FSU mechanics, examining the impact independently and in combination with

disc needle injury. The research will present an understanding of the effect of repetitive lifting on the morphology of needle-induced annulus disruptions in the disc. While the outcomes of this thesis offer valuable contributions to the evidence base needed for developing safety guidelines for workers involved in repetitive lifting tasks, they should be interpreted with caution given the study's use of an animal model. These findings can guide future clinical research focused on developing diagnostic and treatment strategies for the intervertebral disc. Moreover, the findings may serve as a foundation for developing more specific preventative measures and rehabilitation protocols customised for individuals, specifically those with needle injuries to their discs.

1.4 Thesis Outline

The thesis is outlined as follows:

- **Chapter 1** introduces the thesis, outlining the project's motivation, aims, and significance.
- **Chapter 2** presents a review of the literature focusing on the structural and mechanical effects of repetitive lifting and needle injuries on the intervertebral discs.
- **Chapter 3** described the method developed and validated for creating reproducible needle insertion into the intervertebral disc (*Aim 1*), along with details of the methods used throughout the project.
- **Chapter 4** assessed the impact of repetitive lifting on lumbar 6DOF disc mechanics immediately after simulated repetitive lifting and following a period of disc recovery (*Aim 2*).
- **Chapter 5** examined the combined impact of needle injuries and repetitive lifting on lumbar disc mechanics. The assessment occurred immediately after simulated repetitive lifting and following disc recovery (*Aim 3*).
- **Chapter 6** investigated the impacts of repetitive lifting on the morphology of needle injuries in the disc annulus fibrosus (*Aim 4*).
- **Chapter 7** provides the concluding insights and future directions.

- **Appendix A** excluded data and outliers in **Chapter 4**.
- **Appendix B** excluded data and outliers in mechanical testing of **Chapter 5**.
- **Appendix C** original and processed images of needle injuries and related morphological measurements, tables, and charts – **Chapter 6**.
- **Appendix D** images of needle injuries with predominant unsuccessful sectioning – **Chapter 6**.

Chapter 2 Literature Review

2.1 Anatomy of the Functional Spinal Unit

The functional spinal unit (FSU), also known as the spinal motion segment, is the smallest unit used in biomechanical testing to represent the six degrees of freedom (6DOF) physiological motion of the spine. It consists of two adjacent vertebrae: the intervening disc and the facet joints with all the surrounding ligaments and posterior elements (**Figure 2.1**).

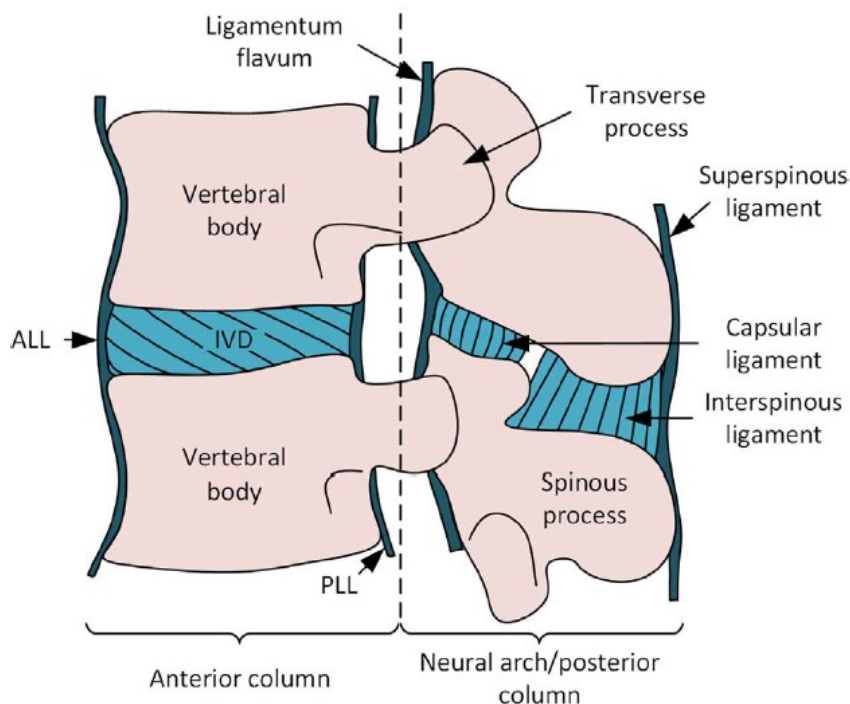


Figure 2.1 Left lateral view of the FSU with all surrounding ligaments (Newell et al., 2017).

2.1.1 Intervertebral Disc

The disc comprises a complex structure that bears loads within the body. At its core lies the gel-like nucleus pulposus (NP), encircled by the collagen-rich annulus fibrosus. Both parts are firmly connected to the neighbouring vertebral bodies above and below through the cartilaginous endplates (CEPs) (**Figure 2.2**).

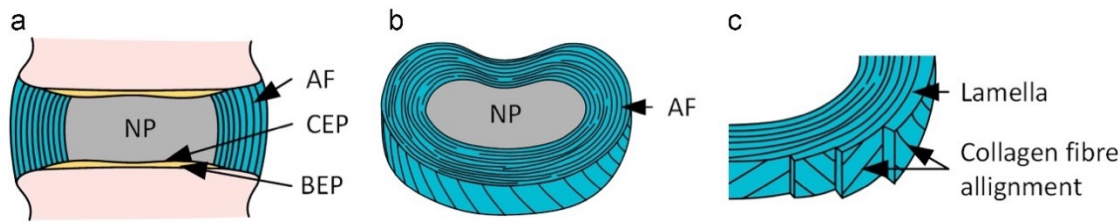


Figure 2.2 Two views of intervertebral disc (a) coronal and (b) transverse planes of the disc with (c) illustration of the alternating fibres in adjacent lamellae. AF: annulus fibrosus; CEP: cartilaginous endplate; BEP: bony endplate; NP: nucleus pulposus (Newell et al., 2017).

The disc mechanically functions as a cushion and shock absorber, enabling the transmission and distribution of loads placed on the spinal column while maintaining spine flexibility and stability. The disc can endure heavy loads and difficult physiological conditions. Understanding the structure and functional properties of the disc is a crucial factor in evaluating various spine disorders, such as low back pain (LBP), which results from changes in the disc structure due to aging or injury (Urban and Roberts, 2003b).

2.1.1.1 Nucleus Pulposus

The NP is a gel-like tissue with an abundant matrix primarily composed of collagen II, approximately 20% dry weight (Inoue and Takeda, 1975), proteoglycans, approximately 40% dry weight (Adams and Muir, 1976) and water, which constitutes about 80% of disc weight (Iatridis et al., 1996, Antoniou et al., 1996). This tissue is enclosed by the annulus fibrosus, consisting of tough concentric layers called the lamellae. These layers provide support to the NP, allowing it to behave like a pressurised fluid (Adams et al., 1996). Its high water content enables it to exert hydrostatic pressure, which varies significantly depending on the subject's age, degeneration level and loading mode (Adams and Hutton, 1983, Kraemer et al., 1985). Within the NP, proteoglycans contribute to the disc's resilience and resistance to compressive force, permitting it to radially bulge towards the resisting lamellae of the annulus, whereas collagens mainly enhance disc tensile strength (Greenwald et al., 1978). Damage to proteoglycans and collagens has been found to be strongly associated with the growth of disc degeneration over time (Sivan et al., 2014).

2.1.1.2 Annulus Fibrous

The annulus fibrosus comprises 15–25 alternate lamellae (collagen sheets) encircling the NP (Marchand and Ahmed, 1990). The fibres within the lamellae are aligned in parallel at 30° from each other, with each lamella containing 20–60 collagen fibre bundles with a 0.22-mm inter-bundle space and 10-µm bundle thickness (Marchand and Ahmed, 1990, Adams and Roughley, 2006a). From the centre of the disc outwards, the composition of collagen type II decreases progressively while collagen type I increases. This transition enhances the tensile strength of the disc, making it highly resistant to compressive load applied to the NP (Kerr et al., 2017, Ashton-Miller and Schultz, 1997). Located between the lamellae, the inter-lamellar matrix (ILM) consists of cross-bridges and elastic fibres. These cross-bridges refer to fibrous connections that traverse radially across multiple annulus layers of the disc (Tavakoli et al., 2016). The ILM measures approximately 20 µm in thickness (Vergari et al., 2016b).

2.1.1.3 Cartilaginous Endplates

The CEPs comprise thin layers of hyaline cartilage consisting predominantly of collagen II fibres, along with proteoglycans and water (Roberts et al., 1989). They separate the NP at the superior and inferior interfaces of the disc from adjacent cancellous bone (Huang et al., 2014). They are enclosed by the ring apophysis which covers the annulus more than NP (Vital et al., 2020). At the periphery with the collagen fibres of the CEPs, the lamellae are continuously connected, whereas the integration with the NP is quite complex (Roberts et al., 1989, Wade et al., 2011). The CEPs provide nutrients to the avascular disc via diffusion into peripheral and adjacent blood vessels (Huang et al., 2014). At the bony interface, the CEPs integrate with a layer of cortical bone known as the bony endplate (BEP) (Figure 2.2). However, the CEPs' connection with the NP shows actual structural integration (Wade et al., 2011, Wade et al., 2012a) while being a dominant source of mechanical strength and flexibility in the spine (Rodrigues et al., 2017).

2.1.2 Lumbar Vertebrae

The lumbar vertebrae are the largest bony structure and the load-bearing portions of the spine, withstanding a very high compressive load (Adams and Hutton, 1982). They consist of the vertebral body and the posterior elements (Rawls and Fisher, 2018). The spinous process sits posteriorly at the junction of the paired laminae, which also projects anteriorly to join the paired pedicles, forming the arch of the vertebra. At both sides of the vertebra, the transverse process extends laterally from the fusion of the pedicle and lamina to provide sites for muscle attachment (Ankel-Simons, 2010, Adams et al., 2002, Ferguson and Steffen, 2003). The articulation of the superior and inferior articular processes between two vertebrae makes up the facet joint (zygapophysial joint). The facet joint contributes to the stability of the spine by preventing excessive shear and axial rotation (Adams and Dolan, 1995). During spine flexion, the articular processes of superior and inferior vertebrae glide against each other, separating the articular surfaces at the lower edge of the joint (Hadley, 1961). When the spine is compressed during an upright standing posture, 80% of the load is carried by the lumbar vertebrae and discs while 20% is resisted by the facet joints under normal conditions (Adams and Dolan, 1995).

2.2 Techniques and Measurements for Visualising Disc Microstructure

Generally, imaging methods used for characterising structures of soft tissues are based on energy of varying wavelengths within the electromagnetic spectrum. For instance, the energy of a photon in visible light microscopy is approximately 1000 times lower than that of a photon used for X-ray imaging, which uses this higher energy to yield body images with much higher diffraction-limited resolution compared to light microscopy (Mizutani et al., 2008). Energy types for imaging include ionising radiation (X-ray & gamma-ray), magnetic resonance, visible light, and infrared radiation. However, each type of energy-based imaging uses different principles to construct images. For example, imaging using

ionising radiation is based on the passage of X-rays or detection of gamma-ray emission through the body.

Imaging modalities can be divided into optical-based or non-optical-based. The former uses visible light, while the latter includes contemporary systems of magnetic imaging resonance (MRI), ultrasound and computed tomography (CT) (Pansare et al., 2012). Regardless of the level of invasiveness of an imaging technique, dynamic changes (e.g., loading, hydration and temperature) can affect the structural and mechanical properties of specimen tissues. Hence, throughout the imaging process, it is important to maintain these changes to a level that simulates those that occur *in vivo*.

2.2.1 Optical

The optical sectioning technique has been employed primarily for the 2D micro-visualisation of soft tissues, specifically the disc using confocal, light and stereo microscopy (Goth et al., 2016, Bruehlmann et al., 2004a, Cassidy et al., 1989, Marchand and Ahmed, 1990). The disc is an anisotropic, multi-layered structure with non-linear viscoelastic properties. It is strong and integrated at high loads and rates of loading while remaining flexible at low loads (Tavakoli and Costi, 2018a, Costi et al., 2008a, Race et al., 2000). The optical technique has provided insights into the micro-level disc environment, contributing to the integrity of disc structure and mechanics. For instance, it depicts the interplay between the annulus fibrosus residual stress that supports the safe distribution of NP pressure (Michalek et al., 2012), and the ultrastructural organisation and distribution of the elastic fibre network in the intra- and inter-lamellar regions and the boundaries between collagen bundles (Tavakoli and Costi, 2018b, Tavakoli et al., 2017). The technique has been used in micro-level strain analysis where strain is found to align with the structure of fibre bundles (Vergari et al., 2016b, Michalek et al., 2009, Bruehlmann et al., 2004a). This approach has also been localised to create a network compared to elastic fibres (Tavakoli and Costi, 2018b, Tavakoli et al., 2017).

To investigate disc micro-deformation, segments of the annulus fibrosus are imaged under tension using optical confocal microscopy (Vergari et al., 2016b, Michalek et al., 2009, Bruehlmann et al., 2004b). Studies have been consistent in observing the stretching of collagen fibrils as bundles re-orient and slide relative to each other. However, no consensus has been reached on whether lamellae slip at the lamellae boundaries (Bruehlmann et al., 2004a) or not (Vergari et al., 2016b, Michalek et al., 2009). One study reporting the slipping of the lamellae attributes this finding to large motions of cells in the ILM. Nevertheless, a study's findings contradict the slipping of lamellae (Disney et al., 2019). In the study, non-optical 3D imaging in synchrotron tomography is applied, and the result confirms no slipping action at the lamellae boundaries (Disney et al., 2019).

One limitation of optical techniques is that they present 2D images in which visual information is limited to the imaging plane. Imaged tissue samples are mechanically anisotropic and non-linear viscoelastic with residual stress or strain. Hence, they should be investigated within the integrity of the surrounding environment. The removal of tissues from their intact environment can alter the native mechanical behaviour. An example of this alteration is the transverse shrinkage that occurs when the annulus fibrosus is disconnected from the adjacent endplate (Vergari et al., 2016b) and the non-physiological behaviour of NP when relieved from hydrostatic pressure (Disney et al., 2019).

Furthermore, a light-based microscopy technique known as Differential Interference Contrast (DIC) has been used to visualise unstained samples of bovine (Pezowicz et al., 2006) and ovine discs (Schollum et al., 2010, Schollum et al., 2008, Schollum et al., 2009, Wade et al., 2012b, Sapiee et al., 2019). This technique confirms a structural analogy of ovine discs with that of human (Schollum et al., 2010, Schollum et al., 2008, Schollum et al., 2009, Wade et al., 2012b). As well as providing a detailed view of the disc interior and exterior junctions within an FSU, it demonstrates the intersections of cartilaginous-vertebral endplate junction where annular bundles of fibrils, cartilage and bone interweave together (Sapiee et al., 2019) as well as the connectivity of the NP

fibres with the inner annulus and with the endplate ([Wade et al., 2012b](#)) (**Figure 2.3**).

'This image has been removed due to copyright restriction. Available online from [Wade et al., 2012b](#)'

Figure 2.3 Oblique section view (a) of the nucleus-inner annulus junction with transverse lines of tensile loading in the boxed region. Higher magnification of the boxed region of the image (a) with the dark transverse line of tension 'x' (b). Insertion nodes with deep attachments of the NP into the cartilaginous endplate (CEP), which in turn is attached to vertebral endplate (c).

Within 100% radially stretched and fixed ovine annulus, DIC images are taken of lamella collagen bundles that are obliquely sectioned and identified relative to the cutting plane as in-plane (IP) parallel or cross-plane (CP) perpendicular lamellae ([Pezowicz et al., 2006](#), [Schollum et al., 2009](#)) (**Figure 2.4**). The cross-bridges (CB) appear among the lamellae under low magnification (500 μm) ([Schollum et al., 2009](#)) (**Figure 2.5**).

'This image has been removed due to copyright restriction. Available online from [Tavakoli et al., 2017](#)'

Figure 2.4 Oblique section view (a) of the disc anterior annulus showcasing a 30° angle. Microtome cutting to a thickness of 30 μm along the cutting plane, marked by an asterisk (*) is detailed (b). The image displays the IP (in-plane) and CS (cross-section) lamellae within adjacent intra-lamellar and the ILM (inter-lamellar matrix) regions ([Tavakoli et al., 2017](#)).

'This image has been removed due to copyright restriction. Available online from [Schollum et al., 2009](#)'

Figure 2.5 Low magnification view of the lamellae featuring the CB (denoted by *), which provides trans-lamellar connection ([Schollum et al., 2009](#)).

Images of higher magnification (50-60 μ m scale bar) show further details of the CB and different junction mechanisms (J1, J2, and J3) that split the IP and CS lamellae. The collagenous CBs seem to merge and integrate with the lamellae ([Schollum et al., 2009](#)) with the capability to recover when subjected to radial tensile strain ([Pezowicz et al., 2006](#)), whereas the junction mechanisms confer separation between the IP and CS lamellae implying localised but inhomogeneous interlamellar connectivity with discrete anchoring (**Figure 2.6**) ([Schollum et al., 2009](#), [Tavakoli et al., 2016](#)).

'This image has been removed due to copyright restriction. Available online from [Tavakoli et al., 2016](#) and [Schollum et al., 2009](#)'

Figure 2.6 High magnification view of (a and b) ILM and CB while stretching and fixing the annulus 100% radially, displaying IP and CS arrays separated by a junction (J) that implies inhomogeneous interlamellar connectivity with discrete anchoring mechanism and (c) the merging of cross-bridges and lamellae (denoted by *) suggesting their structural integration ([Tavakoli et al., 2016](#), [Pezowicz et al., 2006](#), [Schollum et al., 2009](#))

More information is extracted from the analysis of IDC images. ILM is roughly eight times thinner than a lamella containing elastic fibres that anchor into the IP lamellae to form transverse clefts ([Pezowicz et al., 2006](#)). ILM exhibits cohesion even under radial stretching ([Pezowicz et al., 2006](#)). Its failure may initiate disc herniation ([Schollum et al., 2008](#)) as it connects lamellae through a convoluted pyramid of interconnecting fibres at the ILM-lamella boundary ([Pezowicz et al., 2006](#))

2.2.2 Non-Optical

2.2.2.1 Magnetic Resonance Imaging

Magnetic resonance imaging is a non-invasive technique capable of providing a detailed picture of disc morphology and hydration, while also offering insights into the collagen network arrangement (Wu et al., 2019, Watanabe et al., 2007, Thompson et al., 1990). However, this imaging technology exhibits limitations in its maximum achievable resolution ($\sim 200\ \mu\text{m}$) when it is used to map strain on the multi-layered annulus at the microstructural level (O'Connell et al., 2007, Chan and Neu, 2014). Nonetheless, recent advancements using ultra-high field MRI at a magnetic field strength of 11.7 T successfully visualise the 3D microstructure of ovine discs at a resolution of approximately $100\ \mu\text{m}$ (Sharabi et al., 2018).

As tissue microstructure reflects underlying mechanical properties, which is the goal of tissue imaging technology, MRI can be used alongside elastography—a method for imaging soft tissue stiffness—in a context known as magnetic resonance elastography (MRE). This enhanced method facilitates spatial quantification of the shear stiffness or shear modulus of tissue microstructure composition and constituents when they are displaced by propagating shear waves generated from a vibration source at the surface of the tissue. Over the years, MRE has been applied *in vivo* with great success to evaluate microstructures of liver (Yin et al., 2019), muscle (Nelissen et al., 2019), brain (Strasser et al., 2019) and disc (Walter et al., 2017). The technique has been developed *in vitro* to characterise the mechanical properties of a disc, drawing attention as a biomarker candidate for diagnosing disc degeneration (Streitberger et al., 2015, Cortes et al., 2014, Ben-Abraham et al., 2017). In *in vivo* studies have used MRE to quantify the stiffness increase in a disc at higher degeneration grades (Walter et al., 2017). However, its weak signal makes it more sensitive to noise, and its applications have been limited to the more hydrated and less stiff NP rather than the AF. Recent advancements have overcome these limitations by adapting a high-frequency needle MRE to

investigate the shear modulus of both the NP and annulus fibrosus using a bovine disc (Beauchemin et al., 2018).

2.2.2.2 *Ultrasound*

Ultrasound is a form of acoustic vibration that can propagate through most of the soft tissues within the human body. It has been used clinically to examine tissues of the breast, liver, kidney and eye (Faverly et al., 2001). Recent advances in ultrasound techniques have rendered it a viable option for imaging the 3D microstructure of soft tissues. However, thus far, only one recent study has applied it to a disc *in vivo*, and this application is limited to the annulus fibrosus (Langlais et al., 2019). The average pixel size used in the study was 92 μm , and the average imaging time was 5 minutes. The study imaged the annulus fibrosus successfully by placing the ultrasound probe on the anterior abdominal wall of adolescents. By tilting it slowly, the probe was aligned with the disc plane to avoid ultrasound wave reflection from surrounding tissues such as vertebrae. As a result, lamellar concentric structures were visible, and the ultrasound technique was validated by imaging cow tail discs *in vitro*, where it showed consistency of previous images obtained by MRI and polarised light microscopy. Moreover, the study confirmed the results of previous MRI imaging that viewed the lamellae as alternate bright and dark layers (**Figure 2.7**) (Wright et al., 2016). It also demonstrated limitations in the resolution of the MRI and ultrasound modalities, which showed the lamellae but not the fibre layers within them.

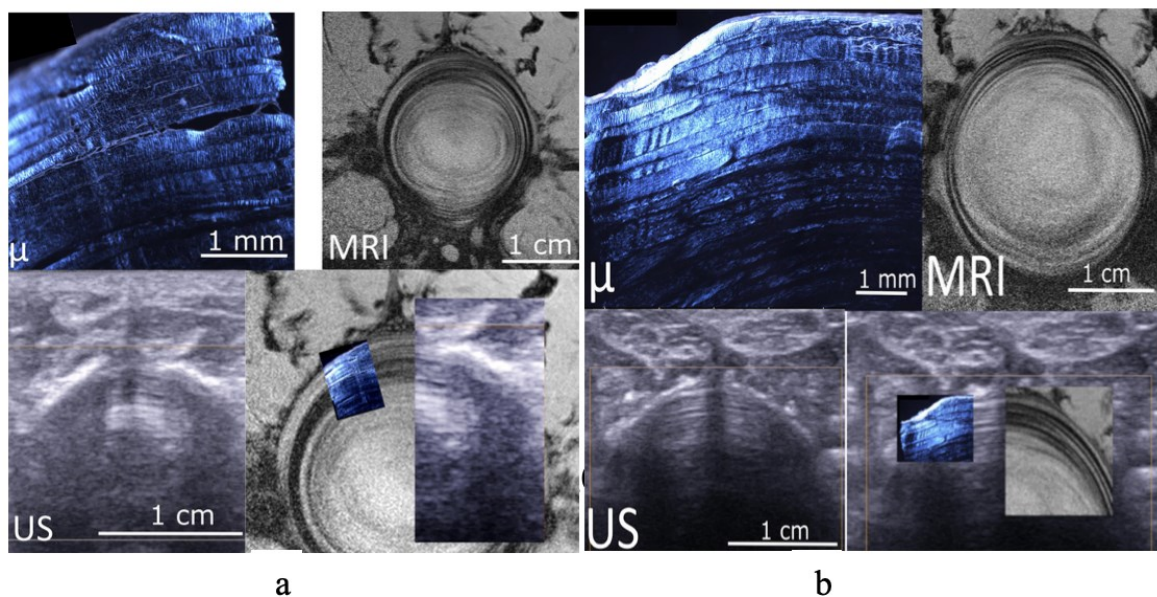


Figure 2.7 Two example images (a and b) illustrating imaged annulus structures using three imaging modalities: polarised light microscopy, MRI, and ultrasound. The third image in each example superimposes the images of the three modalities (Langlais et al., 2019).

Furthermore, when integrated with elastography, the ultrasound imaging system contributes to an innovative diagnostic modality known as ultrasound shear wave elastography. It detects the propagation shear wave speed (SWS) of tissue, which depends on its mechanical properties. The technique has become of interest recently for evaluating various soft tissues such as liver (Iijima et al., 2019), muscle (Koppenhaver et al., 2019), prostate (Ji et al., 2019) and breast (Xiang et al., 2019). With this approach, measurement using SWS has been feasible in the annulus fibrosus both *in vitro* and *in vivo* (Vergari et al., 2014a, Vergari et al., 2014b, Vergari et al., 2016a).

2.2.2.3 Micro-CT

Micro-computed-tomography (micro-CT) is a micro-focus 3D imaging technique used extensively to improve the visibility of biological tissues such as the brain, bone, muscles and disc (Lombardi et al., 2019, e Silva et al., 2017, Disney et al., 2019, Dall’Ara et al., 2017). Unlike 2D microscopic imaging techniques on specimens under invasive procedures (Vergari et al., 2016a, Michalek et al., 2009, Bruehlmann et al., 2004b), micro-CT evaluates the microstructural

deformation of intact specimens without affecting the tissue's mechanical properties (e.g., residual stress state).

Micro-CT has been used with digital volumetric correlation (DVC), which measures internal 3D strain fields by comparing image voxels before and after tissue deformation ([Dall'Ara et al., 2017](#)). The technique has proven feasible for visualising the microstructure of hard tissues, such as bone, due to their higher X-ray transmission contrast. However, it has not had as much success with soft tissues, such as the intervertebral disc, which exhibit low X-ray transmission contrast, making it challenging to visualise their microstructure. This limitation in conventional micro-CT persisted for soft tissues until synchrotron-based X-ray micro-CT emerged, which uses synchrotron generated X-rays to achieve phase-contrast imaging. The high-flux radiation source of synchrotrons overcomes some limitations associated with the use of contrast agents and micro-CT. However, synchrotron X-ray-based imaging can still involve scan durations long enough for soft tissues to exhibit stress relaxation, potentially resulting in microstructural movement. While synchrotron imaging offers higher flux and resolution, careful management of scan durations is still important to minimise the effects of tissue movement during imaging ([Maerz et al., 2014](#), [Margaritondo and Hwu, 2021](#)).

Disney et al. (2019) used in-line phase contrast produced by synchrotron micro-CT (of $\sim 5\text{--}6\ \mu\text{m}$ resolution) to achieve structural edge of the tissue microstructure through the occurrence of Fresnel fringes—the interference between a direct beam and a beam reflected from the edges of tissues due to variation in the X-ray refractive index. Along with the use of DVC, the microstructural deformation of the annulus fibrosus was directly quantified within intact discs in rats. The study findings are consistent with the elastic network described previously ([Tavakoli and Costi, 2018b](#), [Tavakoli et al., 2017](#)), with some heterogeneous zones and alignment of the maximum strain direction with the bundle orientation, indicating bundle stretching and sliding.

2.3 Annular Lesions and Disc Degeneration

Annular lesions have been associated with disc degeneration and LBP (Andersson, 1999, Hoy, 2010, Livshits et al., 2011, Vos et al., 2017). Annular lesions are failure patterns of the annulus and are classified into three distinct forms of fissure: rim (peripheral) lesions, radial tears and circumferential (concentric) tears (**Figure 2.8**). Such lesions are commonly present after 10 years (Adams and Roughley, 2006b), and their incidence is interpreted as evidence of disc degeneration (Haefeli et al., 2006, Sharma et al., 2009, Vernon-Roberts et al., 2007).

‘This image has been removed due to copyright restriction. Available online from [Cheung and Luk, 2019](#)’

Figure 2.8 Common types of annular lesions as observed in histology specimens, featuring left column: sagittal view, and right column: cross-sectional view; (a) concentric tear, (b) radial tears, (c) rim lesion. Top (right) and lateral (left) view of a specimen indicating tissue disruption ([Cheung and Luk, 2019](#)).

2.3.1 Concentric Tears

Concentric tears are crescent-shaped detachments between the annulus lamellae that result from injury or trauma. This type of lesion is more pronounced at the lumbar spinal level L2/L3 (Osti et al., 1990) and is usually more visible in normal discs than are other tears such as rim lesions, which are observed in degenerative discs (Frymoyer and Wiesel, 2004). Concentric tears are reported to

be the most common type of tear, with a higher chance (74%) of appearing than radial tears and rim lesions (Vernon-Roberts et al., 1997) and with similar incidence anteriorly (47%) and posteriorly (56%) to the disc. These tears can be seen in discs as early as 30 years of age (Vernon-Roberts et al., 1997). Some studies suggest that concentric tears may be a consequence of degenerative progression initiated by radial tears (Osti et al., 1990). However, this is contradictory to another study which found no direct correlation between concentric and radial tears (Vernon-Roberts et al., 1997). This discrepancy may arise from differences in study design and methodology. Vernon-Roberts et al (1997) examined human intervertebral discs and reported the independent evolution of concentric and radial tears, while Osti et al. (1990) used an animal model, which may exhibit different degeneration mechanics. Additionally, Osti et al.'s (1990) findings were based on induced annular injuries, which may not fully replicate natural degenerative processes in humans. However, the induction of concentric tears has been found to thicken the anterior lamellae and increase the bone fraction of vertebrae over time (Fazzalari et al., 2001a).

2.3.2 Radial Tears

Radial tears are radial fissures extending from the NP towards the AF—posteriorly or posterolaterally (Hirsch and Schajowicz, 1952, Osti et al., 1990). They are irregular and graded on a scale of 0–5, and their extent is used as a measure of how far the NP moves through layers of the annulus fibrosus (Raj, 2008). However, old radial tears do not permit the NP to escape easily (Adams and Dolan, 1995). These tears usually appear in the posterior portion of the disc (91% chance) and have a higher prevalence with age (Ernst et al., 2005), which can progress the degeneration of the annulus and nucleus (Osti et al., 1990). This category of tears has been reported to be apparent between 11 and 16 years (Boos et al., 2002) and caused by cyclic bending or compression (Raj, 2008).

2.3.3 Rim Lesions

Rim lesions refer to the gap between the vertebral rim and outer fibres of the anterior annulus, running parallel to the endplate and near the junction with apophyseal rings (Hilton et al., 1976, Osti et al., 1990, Schmorl, 1959). The separation is usually initiated through traumatic injury, bone spurs or high-shear strains such as those resulting from repetitive flexion (Adams and Roughley, 2006a, Osti et al., 1992, Tanaka, 2018). Rim lesions are frequently observed at human spinal level T12/L1, with 69% occurring on the anterior portion of the disc (Osti et al., 1992).

2.3.4 Comparison of Lesion Types and Association with Age

Radial and concentric tears are more pronounced at level L4/L5 and show an equal rate of occurrence (Hilton et al., 1976, Thompson et al., 2000). Annular lesions are associated not only with disc degeneration but also with disc age (Osti et al., 1992, Boos et al., 2002): they progress as age increases. Moreover, discs in advanced age (35–50 years) are more likely (73%) to display annular lesions than discs in earlier age (17–35 years) (50%). Each type of annular lesion tends to show more at one level of disc degeneration than at another level. This tendency has been verified with the Thompson Grading Scale, a common clinical system used to assess FSUs in relation to the severity of disc degeneration. This scale categorises the morphological gross appearance of the disc into five grades: Grade I (normal), Grade II/III (moderate), and Grade IV/V (severe) (Thompson et al., 1990).

2.3.5 Disc Herniation

Disc herniation is the displacement of the NP through clefts and fissures in the annulus wall (Tampier et al., 2007). This displacement can be the cause of degeneration in discs undergoing significant trauma (Schwan et al., 2019). It can also be a consequence of non-uniform load distribution following a loss of proteoglycans and collagen (Adams et al., 1996) or of cumulative or acute loading

conditions (Adams et al., 2000, Veres et al., 2009, Veres et al., 2010). The extent of disc herniation morphology can be classified as a protrusion (NP migration contained by AF), extrusion (NP extrusion through ruptured AF) or sequestration (extruded NP released from its disc attachment) into the spinal canal (Adams and Hutton, 1982, Jordan et al., 2011). In disc protrusion and extrusion, the displaced NP material commonly impinges upon surrounding nerve roots, causing pain radiating to the extremities and radiculopathy, which is characterised by pain along with potential motor and sensory impairments following the path of the affected nerve root (Deyo and Mirza, 2016). Under extensive mechanical loading (e.g., flexion and compression), two factors are hypothesised to contribute to the incidence of disc herniation: They include stretched and weakened annulus fibrosus and hydrostatic NP rupturing through the annulus. These factors can be identified by the degeneration level of the disc or loading mechanisms, such as sudden flexion and compression or axial rotation, or both (Chao et al., 2010, Torg et al., 2002).

While disc herniation may lead to disc degeneration (Lama et al., 2013, Schwan et al., 2019), it is usually preceded and predicted by the level of disc degeneration. At mild degeneration levels, the potential coexistence of annular tears and dehydration of the NP justifies the prominence of disc herniation in response to a sudden overload (Adams and Hutton, 1982, Galante, 1967) or repetitive loading (Schmidt et al., 2007). Moreover, a suggested mechanism attributes the initiation of disc herniation solely to the dehydration level of the NP. That is, the dehydration of the NP is accompanied by a loss of disc height and a cumulative lateral compressive force built up on the inner annulus, causing minor radial tears. These micro-level tears can eventually result in annular delamination and disruption from inner to outer lamellae (Veres et al., 2010, Yamaguchi and Hsu, 2019) with a higher chance of disc herniation in mild degeneration (low fibrous NP) and a lower chance in severely degenerated discs (high fibrous NP). The loading mechanism can also play a pivotal role in disc herniation. For instance, axial rotation develops disc herniation when applied alone (Tampier et al., 2007) or combined with repetitive flexion (Drake et al., 2005, Marshall and McGill, 2010, Schmidt et al., 2007) by weakening the ILM of

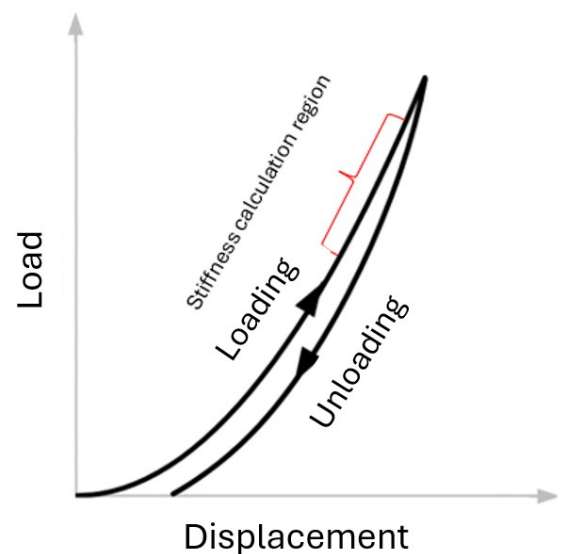
the disc and facilitating the migration of the NP via the clefts within it (Harvey-Burgess and Gregory, 2019).

2.4 Effects of Repetitive Lifting on the Disc

2.4.1 Key Mechanical and Viscoelastic Parameters

The effects of repetitive lifting on the intervertebral disc have been measured using key mechanical and viscoelastic parameters to understand their response to such loading (Gordon et al., 1991, Amin, 2019a, Drake et al., 2005). In viscoelastic materials like the intervertebral disc, unique mechanical behaviour results in different paths for loading and unloading curves, indicating both viscous and elastic properties. In such materials, the overall mechanical resistance is assessed by measuring stiffness, which is calculated by examining the slope of the linear portion of the load-displacement curve, similar to how it is determined when functional spinal units (FSUs) are subjected to uniaxial compression. This measure of stiffness provides insight into the disc's immediate elastic response to applied loads, highlighting its ability to store energy elastically while dissipating it viscously (Gadd and Shepherd, 2011, Newell et al., 2017, Koeller et al., 1986, Asano et al., 1992) (Figure 2.9).

Figure 2.9 Load-displacement curve for a functional spinal unit (FSU) under uniaxial compression. Adapted from Newell et al. (2017), originally based on findings from Asano et al. (1992) and Koeller et al. (1986). Modifications include highlighting the loading and unloading curves to illustrate the material's viscoelastic behaviour and highlighting the linear section of the curve in red as the stiffness calculation region to reflect the initial elastic response. This graph illustrates the typical load-displacement relationship, emphasising the disc's viscoelastic properties. Note: The graph is not to scale and has been adjusted for visual clarity.



However, in viscoelastic materials, measuring stiffness alone does not fully capture their mechanical behaviour under dynamic conditions, as it only reflects the immediate elastic resistance to deformation. Viscoelasticity refers to the dual nature of materials that exhibit both elastic and viscous behaviours, characterised by their gradual response over time when exposed to a steady load or deformation (Cohen et al., 1998). This means that intervertebral discs not only store energy like elastic materials but also dissipate energy over time, similar to viscous fluids (Kazarian and Kaleps, 1979). Consequently, further viscoelastic parameters, such as hysteresis, which includes the associated energy loss, and phase angle, have been utilised in previous studies to provide a more comprehensive understanding of how the disc responds to repetitive loading (Gordon et al., 1991, Amin, 2019a, Drake et al., 2005). Although these concepts are closely related, with each characterising the viscoelastic properties of a material, they describe different aspects of material behaviour. Hysteresis quantifies the energy lost during each loading cycle, reflecting the disc's ability to absorb shocks and dissipate energy as internal friction. Energy loss refers to the total dissipation of mechanical energy, highlighting the disc's damping capacity and ability to withstand prolonged loading. The phase angle measures the lag or phase difference between load and displacement, indicating the balance between elastic energy storage and viscous energy dissipation (Gadd and Shepherd, 2011) (Figure 2.10).

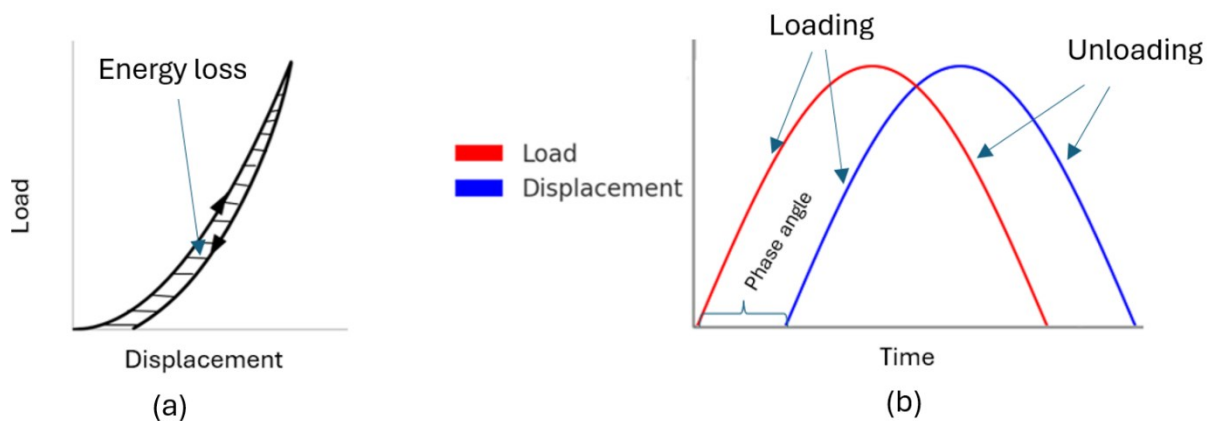


Figure 2.10 Load-displacement curve illustrating energy loss due to hysteresis in a Functional Spinal Unit (FSU) during uniaxial compression (a), adapted from Newell et al. (2017), originally based on findings from Asano et al. (1992) and Koeller et al. (1986), with modifications to include a filled 'Energy Loss' area. This graph highlights the energy dissipated due to the viscoelastic properties of the disc. Part (b) is an original creation depicting phase angle variations over time, correlating with the mechanical load-displacement curve shown in part (a). Note: the graphs are not to scale and adjusted for visual clarity.

Despite hysteresis and phase angle being independent of loading frequencies when loading the intervertebral disc (Costi et al., 2008a, Koeller et al., 1984, Costi et al., 2008b), the phase angle remains advantageous in contexts where understanding the stiffness of a viscoelastic material of the disc is crucial, and a comprehensive grasp of its behaviour is needed. This advantage arises from the phase angle's ability to provide insights into the equilibrium between the elastic and viscous components of a material's response, which directly relates to its stiffness—a property found to increase with the increase in loading frequency (Costi et al., 2008a). A smaller phase angle typically indicates a more elastic, or stiffer, response, valuable for assessing a material's ability to resist deformation under load. Specifically, a phase angle of 0° would indicate a purely elastic material, while a phase angle of 90° would indicate a purely viscous material (Gadd and Shepherd, 2011). The relationship between stiffness and loading frequency, along with its quantitative link to the phase angle, highlights the importance of both measures in replicating repetitive lifting scenarios. This approach provides valuable insights into how repetitive loading affects disc mechanics and viscoelastic properties. This is particularly important because

repetitive lifting, as performed in occupational settings with variable loading frequencies, has been replicated in the literature (Gordon et al., 1991, Amin, 2019a, Drake et al., 2005). Such measures, like stiffness and phase angle, allow for meaningful comparisons across these studies, thereby enhancing our understanding of the effects of repetitive loading on the intervertebral disc.

2.4.2 One-Axis Repetitive Loading

Previous studies have assessed the effects of repetitive loading on the intervertebral disc when applied along a single axis. Such application, when applied 6000 cycles at 1 Hz in flexion-extension using porcine FSU, shows no change in disc stiffness, while it does increase hysteresis (Drake et al., 2005). However, in compression combined with flexion (37,260 cycles at 1.5 Hz) applied on human FSUs, it leads to a decrease in disc stiffness but an increase in disc energy loss (Gordon et al., 1991). Further, the structural effects of repetitive lifting, which have been found to produce disc prolapse under compression (until failure at 0.67 Hz), have been investigated on human FSUs (Adams and Hutton, 1985). The investigation theorised that 21% disc prolapse to transition gradually via five important stages. The stages commence with disc self-selection (stage 1), followed by lamellae distortion (stage 2), NP penetration (stage 3), NP extrusion (stage 4) and annular rupture (stage 5) (**Figure 2.11**) (Adams and Hutton, 1985).

'This image has been removed due to copyright restriction. Available online from [Adams and Hutton, 1985](#)'

Figure 2.11 Five stages of gradual disc prolapse ([Adams and Hutton, 1985](#)).

The mechanical behaviour of FSUs under repetitive loading supports the theory of disc herniation, as the mechanical responses observed are consistent with the progression towards disc herniation. Studies have shown that human FSUs undergo structural changes under repetitive flexion, rather than repetitive compression. For instance, repetitive compression yields 21% chance of disc prolapse ([Adams and Hutton, 1985](#)), whereas repetitive flexion results in 100% (71% protrusion, 29% extrusion) with annular ruptures in the posterolateral region ([Gordon et al., 1991](#)). This notable difference in the incidence of disc herniation can be attributed to the different distributions of intradiscal pressure induced by each loading type. Specifically, compression generates internal radial forces that are distributed evenly around the annulus, yielding less force on each portion of the annulus. This relatively small force is less likely to cause disc herniation compared to the large force induced by flexion through which uneven pressure distribution tends to compress the anterior annulus while decompressing the posterior annulus and facet joints ([Adams et al., 2002](#)). Additional observations have been made when loading the porcine FSUs with

repetitive flexion-extension (86,400 cycles at 1 Hz); the disc's annulus delaminated, accompanied by the circumferential movement of the NP towards the posterior and posterolateral portions of the disc (Callaghan and McGill, 2001). These findings suggest that under certain loading conditions, FSUs become structurally compromised, which aligns with the theorised stages of disc prolapse outlined by Adams and Hutton (1985). While these findings support the theory, the correlation between repetitive flexion and disc herniation does not necessarily establish direct causality but rather suggests a strong possibility that certain loading conditions may significantly increase the risk of disc herniation by, for example, potentially exacerbating internal pressure imbalances within the disc.

2.4.3 Multi Axes Repetitive Loading

Advancement of equipment has provided recent studies with capabilities towards a more clinical approach to disc behaviours. Hence, the multi-axis devices simultaneously apply repetitive loading of the disc and provide a more physiological representation of human disc loading. A study's findings, using human FSUs, suggest that applying repetitive lifting, which combines compression, flexion, and right axial rotation (20,000 cycles at 1 Hz), causes a decrease in disc stiffness in flexion and lateral shear, while stiffness increases during extension (Amin, 2019a). Further effects are found in the disc phase angle during flexion and additionally during compression, left axial rotation, and posterior shear (Amin, 2019a). These mechanical changes from repetitive lifting not only decrease internal disc strain but also result in a 73% incidence of disc injury, manifesting as either endplate failure or disc herniation in humans (Amin et al., 2020). However, the disc failure mechanism has been further examined in the ovine model under different testing protocols: (1,000 cycles at 2 Hz) by Berger-Roscher et al. (2017) and (1200 cycles at 0.5 Hz) by Wilke et al. (2016). Additionally, the effects of combinations of two or three repetitive movements (flexion, axial rotation, and lateral bending) with or without compression, applied as either fixed or cyclic, have been investigated (Berger-Roscher et al., 2017, Wilke et al., 2016) (Table 2-1).

Table 2-1 Combinations of repetitive movements flexion (Flex), axial rotation (AR) and lateral bending (LB) with or without fixed/repetitive compression (Comp) studied previously.

Combination Group #	Combinations of Repetitive Loading	Study
1	Comp + Flex + AR +/- LB	(Wilke et al., 2016)
2	Comp + Flex + AR + LB	(Berger-Roscher et al., 2017).
3	Comp + Flex + AR	(Berger-Roscher et al., 2017).
4	Comp + AR + LB	(Berger-Roscher et al., 2017).
5	Comp + Flex + LB	(Berger-Roscher et al., 2017).
6	Comp + Flex + AR	(Amin et al., 2020)

The conclusions of these combinations expose the failure of the disc and endplate junction. The frequent failure of the endplate junction (76%) and disc annulus (24%) has been observed, but the exact association with disc herniation remains uncertain (Berger-Roscher et al., 2017). The risk of endplate junction failure is highest at the combination of repetitive compression, flexion, axial rotation, and lateral bending though it is lowest wherein flexion and lateral bending are not combined (Berger-Roscher et al., 2017). The association of disc herniation and endplate damage is essentially induced in groups 1 and 2 (Table 2-1), leading to hypothesis of potential mechanistic role played by compression in the two groups (Berger-Roscher et al., 2017, Wilke et al., 2016). The hypothesis proposes that high compression perhaps ruptures the endplate cartilage, the posterior annulus, or both, allowing the NP to be eventually pressed out (Berger-Roscher et al., 2017) (Figure 2.12).

‘This image has been removed due to copyright restriction. Available online from Berger-Roscher et al., 2017’

Figure 2.12 Hypothesised model proposing high compression potential to rupture the endplate cartilage, the posterior annulus or both, allowing the NP to be eventually pressed out (Berger-Roscher et al., 2017).

However, the more recent study applying repetitive lifting in compression, flexion, and right axial rotation using human FSUs (Amin et al., 2020) theorises a mechanism of disc herniation irrelevant to the endplate failure where it suggests failure mechanism limited to the disc (Figure 2.13).

‘This image has been removed due to copyright restriction. Available online from [Amin et al., 2020](#)’

Figure 2.13 Model for the mechanism of the disc herniation irrelevant to the endplate failure, suggesting failure mechanism to be limited to the disc ([Amin et al., 2020](#)).

According to this mechanism the herniation process begins with the inward buckling of the AF, particularly on the side opposite to the applied rotation. It progresses as the NP migrates to the posterolateral region, leading to a compaction of annular lamellae. With cumulative damage, the annulus fibrosus tears, allowing the nucleus to extrude—a mechanism that aligns with Adams' theory of gradual prolapse (**Figure 2.13**) ([Adams and Hutton, 1985](#)).

2.5 Needle Sizes and Use in Clinical Treatment

Needle size, a critical factor in clinical treatments, is measured in gauges—where a lower gauge number corresponds to a larger needle diameter. The various sizes are matched following standardised measurements (ISO 2016). Needles are commonly used in procedures such as discography, which is considered the gold standard for diagnosing discogenic pain—pain originating from damaged intervertebral discs (Chen and Gao, 2023). In this procedure,

needles typically range from 14G to 27G, with outer diameters from 2.15 mm to 0.42 mm (**Figure 2.14**).











Needle Size	Gauge (G)	Outer Diameter (mm)
	14	2.15
	15	1.90
	16	1.69
	18	1.30
	20	0.92
	21	0.83
	22	0.73
	23	0.67
	25	0.53
	27	0.42

Figure 2.14 Needle gauges and their corresponding outer diameters.

Discography is widely accepted by professional spine societies ([Hunt et al., 2019](#), [Centerville et al., 2018](#), [Bogduk, 2004](#), [Gilbert et al.](#)) and involves inserting needles through the annulus fibrosus (AF) to inject a radiopaque medium into the nucleus pulposus (NP). This allows for tracking leakage, which can indicate annular defects. Cohort studies have suggested a potential link between discography and disc degeneration ([Carragee et al., 2009](#), [Hur et al., 2016](#)) . Needles of 25G and 22G, commonly used in this procedure, are introduced into the posterolateral region of the disc and correspond to approximately 4.7% and 6.5% of the average human disc height (mean 11.3 mm), respectively ([Carragee et al., 2009](#), [O'Connell et al., 2007](#)).

2.6 Effects of Needle Injuries on the Disc

Annular injuries caused by needles induce a slow and progressive pattern of disc degeneration that is more relevant than injuries from a blade or scalpel (Masuda et al., 2005, Sobajima et al., 2005a, Zhang et al., 2009). Needle diameter is positively associated with the severity of disc degeneration using *in vivo* animal models (Kim et al., 2005, Fazzalari et al., 2001a, Keorochana et al., 2010, Cunha et al., 2017, Elliott et al., 2008) and is associated with biomechanical deterioration (Hsieh et al., 2009, Michalek et al., 2010b, Keorochana et al., 2010). Even when it is not penetrating the NP, needle injuries result in upregulation of NP gene expression (Anderson et al., 2003). The indirect degenerative influence of annular needle injuries on the NP suggests that degenerate changes are driven mechanically following the structural initiation of needle injuries (Sobajima et al., 2005b, Korecki et al., 2008). Further details of the structural and mechanical effects of needle injuries are provided in subsequent sections.

2.6.1 Structural Effects

Needle injuries cause structural breakage of disc fibres, which potentially affects the disc's mechanical properties at the micro (Michalek et al., 2010a) and macro levels (Michalek et al., 2010b, Michalek and Iatridis, 2012). This impact may occur immediately or over time following biological processes such as inflammation (Michalek et al., 2010b, Kaigle et al., 1997, Martin et al., 2013, Hsieh et al., 2009, Elliott et al., 2008). Such microstructural failure seems to initiate and propagate to the macro-level (Iatridis and ap Gwynn, 2004), accelerating the risk of disc herniation (Rajasekaran et al., 2013).

Research conducted in *in vivo* rat (Cunha et al., 2017, Keorochana et al., 2010) and rabbit (Kim et al., 2005) models, along with *in vitro* ovine models (van Heeswijk et al., 2018), demonstrates a proportional relationship between needle diameter (ranging from 26G to 18G) and the occurrence of disc herniation. This relationship is also linked to the amount of NP passing through the injury pathway, leading to biochemical and biomechanical deterioration and progressive disc degeneration. Needle diameters of 23G and 18G produce disc

herniation *in vivo* in rabbits (Kim et al., 2005), while only 18G needles produce disc herniation in both rats *in vivo* (Hsieh et al., 2009) and ovine *in vitro* (van Heeswijk et al., 2018).

Unlike disc degeneration in rats (Hsieh et al., 2009, Han et al., 2008) and humans (Urban and Roberts, 2003a), large needle (18G) injuries in rats *in vivo* studies result in a more pronounced decrease in disc proteoglycans and aggrecans over time compared to small injuries (22G and 20G) (Keorochana et al., 2010). Such decline is assessed by Alcian blue staining reduction in total disc area, assuming consequent aggrecan accumulation at the inner annulus fibrosus and a productive pattern of proteoglycan compensation (Masuda et al., 2006, Zhang et al., 2009).

2.6.2 Mechanical Effects

2.6.2.1 Effects of Needle Injuries on Disc

Pressurisation and Stability

Although needle injuries are less mechanically effective at causing large-scale tissue disruption than major injuries (e.g., scalpel incisions), they are highly effective when the ratio of needle diameter to disc height is greater than 40% (Elliott et al., 2008, Yang et al., 2016, van Heeswijk et al., 2018). A rat disc model shows that the immediate mechanical influence of needle injuries persisted over time despite changes in disc composition (Martin et al., 2013). Needle injuries depressurise the NP, leading to disc instability (Yang et al., 2016). The same observation has been reported in the presence of naturally occurring annular tears in mildly degenerated discs (Kirkaldy-Willis and Farfan, 1982). This release of residual stress affects the toe region more than the linear region (Torre et al., 2019). It exerts stronger effects in terms of circumferential hoop-stresses, NP pressurization, and outward bulging (Torre et al., 2019, Michalek and Iatridis, 2012).

In an organ culture model of a bovine disc with the endplate removed, needle injuries impose biological and mechanical alterations on the disc consistent with

those observed clinically (Korecki et al., 2008, Carragee et al., 2009). Needles of 25G and 14G induced in the culture produce approximately 16% and 20% decreases in dynamic compressive modulus after 1 hour of loading and 39% and 51% increase of creep during the loading, respectively, with the local appearance of cell death as in the rat model (Cunha et al., 2017) and near needle injuries (Korecki et al., 2008). Injuries from needles of 29G and 26G influence the creep response of rat discs *in vivo*. However, at 8 weeks, the degenerate changes are different from those in humans. Nonetheless, 26G-needle injuries produce a rapid and increasing creep response (Martin et al., 2013).

In an *in vitro* ovine model, in conjunction with finite element simulation, a 16G needle significantly increases axial stress while reducing disc strain range, intradiscal pressure and fluid loss (Khalaf et al., 2017). Nevertheless, while appearing to have no significant effects on the macro-scale elastic modulus, 26G and 21G needle injuries exhibit local mechanical effects on micromechanical properties in bovine discs, including altering the shear strain distribution within the annulus fibrosus wherein needle injury propagates up until cycle 2 of 10 cycles of shear strain (Michalek et al., 2010a). However, a second-cycle tensile strain does not significantly change the annulus elastic modulus, but a modest change in the shearing between fibre bundles is evident without significant changes to the linear strain within and between bundles (Vergari et al., 2017). Needle injuries have been hypothesised to alter fluid flow transport patterns based on permeability studies and the amount of hydrostatic pressurisation expected by different loading modes (Hsieh et al., 2009, Michalek and Iatridis, 2011, Michalek et al., 2010b, Michalek and Iatridis, 2012). They affect the biphasic response in ovine discs by reducing the aggregate modulus. However, the combination with fatigue loading increases aggregate modulus but decreases permeability (Nikkhoo et al., 2019).

2.6.2.2 Effects of Needle Diameter on Disc Mechanical Properties

In studies examining the effects of various needle diameters on disc mechanical properties, a clear relationship between needle size and its impact on both compressive and torsional stiffness has emerged. Needle sizes such as 22G and 26G generally do not affect the compressive properties of rat discs. However, other needle sizes, such as 30G, 25G, and 21G, result in a 20% reduction in compressive stiffness, although this reduction disappears under conditions of compressive overload (Michalek et al., 2010b). As the needle size increases, such as with 18G needles, the compressive effects become more pronounced, especially when combined with annulus fibre tension. In these cases, the reduction in compressive stiffness is also accompanied by a loss of torsional stiffness, indicating a proportional relationship between injury size and its effects on both torsional and compressive properties (Michalek et al., 2010b).

The threshold for significant mechanical disruption appears to correlate with a needle size that constitutes approximately 80% of the disc height (Martin et al., 2013). This suggests that the ratio of needle diameter to disc height plays a key role in determining the extent of mechanical impact. Larger needles, such as 18G, induce more substantial mechanical changes and are associated with herniation in ovine discs, whereas smaller needles, such as 25G, show less sensitivity to failure loading and do not typically cause herniation (van Heeswijk et al., 2018). These findings suggest that needle injuries impact disc mechanics differently depending on the size of the needle, the ratio of needle diameter to disc height, and the associated loading conditions (Torre et al., 2019, Michalek and Iatridis, 2012).

However, the overall effects of needle injuries have been studied using uneven ratios of needle diameter to disc height in different animal species (Table 2-2). For example, in rat models, larger needles exceeding 100% of the disc height have been shown to cause structural damage beyond the disc, affecting surrounding tissues such as bone (Hsieh et al., 2009). This variability

underlines the complexity of translating findings from animal studies to clinical settings, as a substantial scale mismatch may lead to misleading interpretations of needle injury effects.

Table 2-2 Review of Needle: Disc Height Ratios used across different disc species previously.

Needle Gauge G (Diameter mm)	Human (11.3 mm)	Bovine (6.90 mm)	Ovine (3.93 mm)	Porcine (8 mm)	Rabbit (1.42 mm)	Rat (0.94 mm)
30G (0.32)						34%
26G (0.47)		7%				50%
25G (0.53)	5%	8%	13%			56%
24G (0.58)				7%		
23G (0.67)		10%			47%	
22G (0.73)	6%	11%		9%		78%
21G (0.83)		12%			58%	88%
20G (0.92)				12%		98%
19G (1.1)		16%				
18G (1.3)			33%	16%	92%	138%
16G (1.69)			43%			
14G (2.15)		31%				

Note: Disc height measurements are adapted from measurements by O’Connell et al. (2007), whereas needle diameters are modified by the International Organization for Standardization (ISO) 2016

A crucial comparison lies in evaluating the effects of needle injuries in combination with fluid injection, as is usually undertaken clinically for treatment and experimentally for therapeutic testing. For instance, the presence of disc herniation caused by 22G (6% disc height) or 25G (5% disc height) needles in humans, with injections administered during discography as reported by Carragee et al. (2009), contrasts with rat disc herniation triggered by individual 21G and 25G needle injuries without injection (Cunha et al., 2017). This discrepancy may be explained by the injection's influence on changes observed in ovine discs *in vivo*, where needle injuries combined with saline pressurised injection resemble concentric-like tears of annulus fibrosus delamination, distinct from injuries caused by individual needles (Fazzalari et al., 2001b). Therefore, in humans, the NP material may move concentrically between lamellar layers without exiting via needle injuries. Furthermore, the diameter of the needle demonstrates another prominent role in the same context. Small (26G) needle injuries do not cause leakage of internal pressurising gel injected into porcine discs longitudinally via one of the adjacent vertebrae, while larger (18G, 20G, 22G, 24G) needle injuries do so in a study where needle rupture pressure is inversely correlated with needle diameter (Yang et al., 2016). As needle diameter increases from 24G to 18G (7% to 18% of disc height, respectively), the pressure drops by 75%. Compared with needles of 24, 22G, 20G and 18G, there is a reduction in failure pressure (initial leakage pressure) by 53%, 37%, and 17%, respectively.

In summary, studies on the effects of needle injuries on intervertebral discs, conducted *in vitro* across various scales and animal species—from microscale annulus explant tests to whole-disc assessments and full FSU tests in bovine, ovine, and rat models—reveal a complex and diverse range of outcomes. Moreover, these investigations highlight the extensive variability in effects, influenced by a range of loading conditions such as compression, flexion-extension, torsion, and lateral bending. This variability suggests that the effects of needle injuries may depend on mechanical loading conditions, needle diameter relative to disc height, testing scales, and species (Table 2-3).

Table 2-3 Summary of reviewed in vitro studies investigating the effects of disc needle injuries. studies are organised by specimen and testing mode, ratio of needle diameter to disc height and resultant mechanical and structural influence.

Specimen & Testing Mode	Ratio of Needle Diameter to disc height (%)	Mechanical Influence	Structural Influence
Annulus Explants			
10 cycles of dynamic shear strain on bovine (Michalek et al., 2010a)	7, 12	Changed the distribution of shear strains.	Repeated loading did not cause further growth of the disruption beyond the second cycle.
2 cycles dynamic tensile strain on bovine (Vergari et al., 2017)	10, 11, 12,16	No significant effect on annulus elastic modulus.	Decrease in intra-bundle shear is observed; however, despite these alterations in fibre bundles, the linear strain between bundles and intra-bundle shear remained consistent.
Isolated Disc			
Static & 1 hour-long Dynamic Compression of bovine (Korecki et al., 2008)	8, 31	A decrease in dynamic modulus & increase in creep.	Immediate and lasting changes in disc height, stiffness, and viscoelastic properties (e.g., reduced dynamic modulus and increased creep, with no recovery observed) occur; however, only minor changes in fibre bundle shearing are noted.

Specimen & Testing Mode	Ratio of Needle Diameter to disc height (%)	Mechanical Influence	Structural Influence
FSU			
5 cycles and 10 cycles dynamic compression & torsion on rat (Michalek et al., 2010b)	34, 56, 88	20% decrease in compressive elastic stiffness was noted yet eliminated by compressive overload. Torsional parameters related to tension vary proportionally with needle size.	
10 cycles of dynamic compression, flexion-extension, lateral bending, and torsion on bovine (Michalek and Iatridis, 2012)	12	No effects on stiffness and phase angle	No effect on disc height
Sudden overload of ovine (van Heeswijk et al., 2018)	13, 33		Lateral inner annulus disruption was observed in 12 of the 16 discs tested.
20 cycles of axial and torsional loading on rat (Torre et al., 2019)	50	In torsion, stiffness decreased, but neutral zone length and hysteresis remained unaffected.	

2.7 Conclusion

In *vitro* assessments of needle injuries have employed a multi-scale approach, incorporating both microscale structural and mechanical testing on annulus explants, performing macroscale testing on whole isolated discs and FSUs, and examining the effects under various loading directions. The variability in methodologies, in addition to the wide range of needle diameter to disc height ratios used, has predictably led to less consistent findings across these studies. Additionally, evaluations of needle injury effects were previously conducted in isolation, without mimicking repetitive lifting, a task that is highly relevant. Such simulation is critical, given that repetitive lifting is a common activity for many individuals, and it has been linked to disc herniation, as well as a reduction in FSU stiffness and an increase in phase angle, a measure of viscoelasticity. However, the mechanical effects of repetitive lifting over prolonged durations were assessed using testing protocols that inadequately simulated daily disc recovery, which is a significant factor.

To fully capture the influence of needle injuries on FSU mechanics, it is essential to use more realistic and physiologically relevant testing protocols, including the use of entire FSU and mimicking *in vivo* conditions under repetitive lifting. By adopting this approach, not only can the effects of needle injuries be more accurately assessed, but an opportunity is also opened to explore the morphological changes induced in the annulus fibrosus by needle rupture under such combined loading from repetitive lifting—a topic that has yet to be thoroughly investigated. Overall, understanding the mechanical effects of needle injuries on the FSUs and their potential for morphological development is crucial in shaping safety guidelines and effective rehabilitation protocols for individuals with disc needle injuries.

Chapter 3 Methods

3.1 Overview and Sample Size

Thirty-one functional spinal units (FSUs) were prepared from twenty-four ovine lumbar spines (**Figure 3.1**) (**Section 3.2**), from which four were used to test the reproducibility of needle insertion (**Section 3.3**), twenty for mechanical testing (**Section 0**) to assess the impact of simulated repetitive lifting on disc mechanics, before (**Chapter 4**) and after (**Chapter 5**) needle injury creation, and the remaining seven used as controls to assess the effect of simulated repetitive lifting on the morphology of annulus fibrosus rupture induced by needle injury (**Chapter 6**). The structural analysis group was specifically designed to investigate the effects of repetitive lifting on needle-induced injuries. The focus was on comparing the extent of structural disruption between needle injuries subjected to repetitive lifting and those that were not. Although including a non-needle injury control would have provided additional comparative data, this was outside the scope of the analysis.

The limited availability of mature ovine spines was a major factor in determining the sample size for the tests in the current project. However, efforts were made to ensure that the reliability of the results remained within acceptable limits. The sample size required for the mechanical testing was verified based on previous measurements of the 6DOF mechanical effects of 25G needle injuries using ovine FSUs, which were part of a Bachelor of Engineering (Biomedical) (Honours) project ([Russo, 2017](#)), and were taken as pilot data for the current project. The pilot measurements of anterior shear stiffness, affected by the 25G needle injury compared to a control group, were used as the primary measure, with stiffness means of 218 N/mm and 194 N/mm, and standard deviations of 22 N/mm and 25 N/mm for the control and 25G needle groups, respectively. Based on these measurements, a priori power analysis using G*Power software (version 3.1.9.7) with a one-tailed test indicated that a minimum sample size of 13 per group was required to detect the mechanical effects of 25G needle injuries with a power of 80% and a significance level (α) of 0.05. The recommended sample size

of 13 per group was reasonably higher than the available sample size of 10 FSUs per group. For reproducibility testing of needle insertion (**Section 3.3**), three repeats of needle insertion were performed on each of the available four specimens to closely approximate the 10 insertions performed during the mechanical testing.

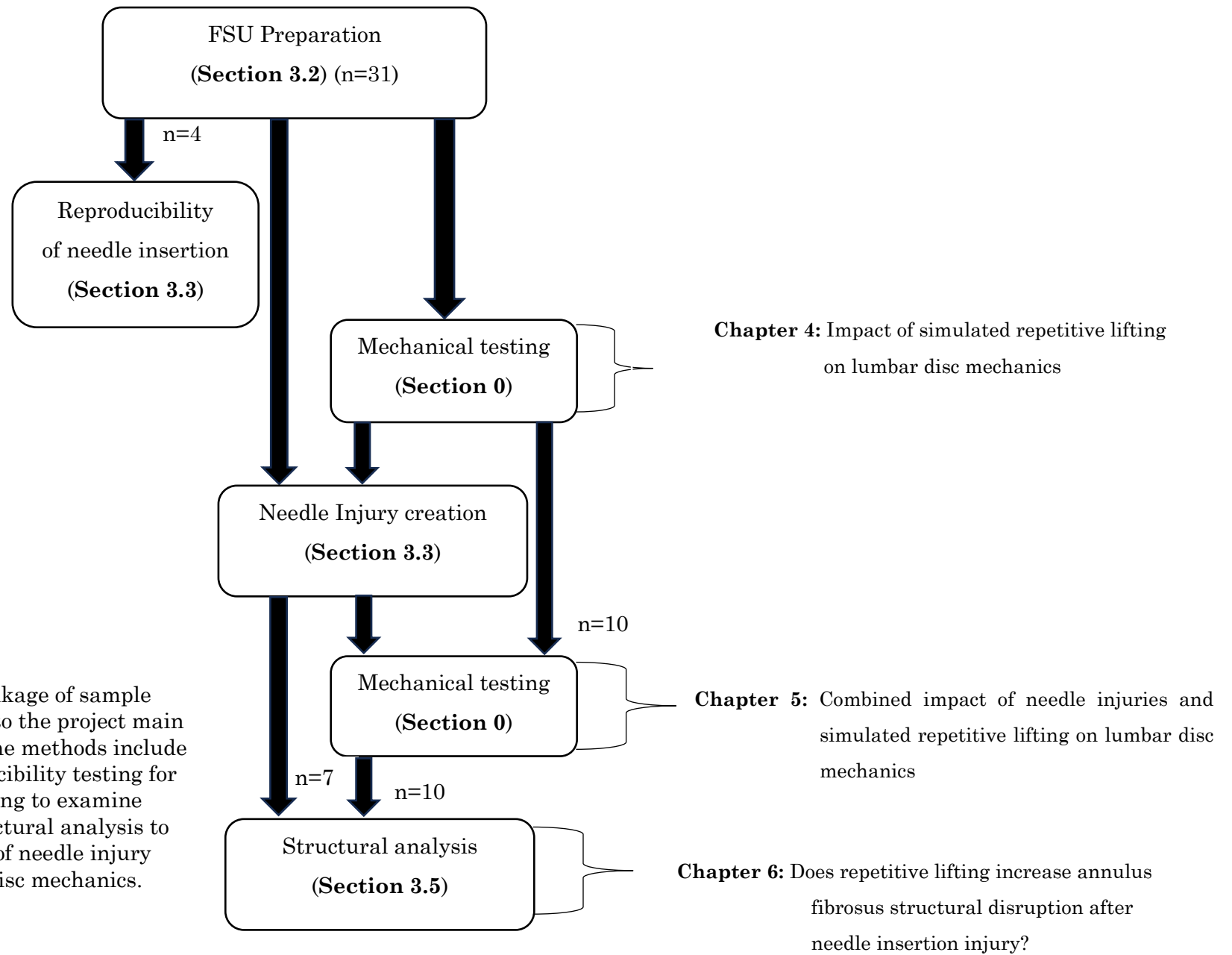


Figure 3.1 An overview of the linkage of sample size and methods of this chapter to the project main studies (**Chapter 4, 5, and 6**). The methods include the preparation of FSUs, reproducibility testing for needle insertion, mechanical testing to examine repetitive lifting effects, and structural analysis to investigate the combined impact of needle injury and repetitive lifting on lumbar disc mechanics.

3.2 FSU Preparation

All animal care procedures and experimental activities adhered to the guidelines established by the South Australian Health and Medical Research Institute (SAHMRI) in Adelaide, South Australia (Amin et al., 2016a). Merino ovine lumbar spines aged 3-5 years were obtained post-mortem from SAHMRI. Ovine spines were chosen for this project as an optimal alternative for research studies, primarily due to the challenge of sourcing human spines, which were often limited in supply. Ovine spines were chosen for this project since their structural and biomechanical properties closely reflect those of humans (Wilke et al., 1997, Fazzalari et al., 2001a, Veres et al., 2008). The spines were frozen within 30-60 minutes post-mortem according to SAHMRI protocols. They were packed in plastic bags with labels and delivered in insulated foam containers with ice packs to the laboratory of this research in a frozen state, where they were immediately stored at -20°C. The maximum duration of frozen storage was 23 months. For experimental testing, they were allowed to thaw at room temperature for up to 3 hours to ensure the disc tissue was sufficiently thawed for mechanical and structural testing. After that, the FSUs of these spines were subjected to specific procedures, including dissection, potting, dimensional measurements, and overnight hydration. Throughout the preparation process, consistent hydration of the discs was maintained to preserve their integrity. This step was achieved by periodically spraying them with saline approximately every five minutes and by continuously wrapping the discs in paper towels moistened with saline, ensuring they remained adequately hydrated at all times (Veres et al., 2008).

3.2.1 Dissection and Potting

The L4/5 FSUs selected due to their anatomical and biomechanical parallels to human FSUs (Wilke et al., 1997, Fazzalari et al., 2001b, Veres et al., 2008) were carefully isolated from their spines. The procedure commenced with the use of a scalpel and forceps to remove surrounding soft tissues. This task was made more feasible by working with the spines in a semi-frozen state, thereby ensuring the preservation of the FSU structure and all intervertebral ligaments. A band saw

was then used to cut the vertebrae parallel to the disc's mid-transverse plane, effectively separating the FSUs from the rest of the spinal column. The cuts were made at the junctions of the L3/4 and L5/6 vertebrae, ensuring that the L4/5 FSU, including their endplates, were not affected.

To ensure the superior and inferior vertebrae were securely fixed in stainless steel cups for the mechanical testing phase, the preparation protocol for the dissected FSUs included a potting process using dental cement, which hardens through a chemical reaction (**Figure 3.2c**). The cement, a blend of polymethyl methacrylate powder and monomer liquid mixed at a ratio of 1.7 ml of powder to 1 ml of liquid, was carefully poured into each cup to quickly solidify, forming a robust bond around each vertebra within a period of 15-20 minutes. To ensure the vertebrae were perfectly aligned during this process, a custom-designed rig was used consisting of a base platform with screws to hold the cups in place. The alignment rig also includes a vertical guide to maintain the correct positioning of the vertebrae while the cement hardens (**Figure 3.2**). The process began with potting the inferior vertebra after proper alignment of the FSU (**Figure 3-2a**). The alignment involved positioning the FSU's transverse process with the vertical guide of the rig while the pedicles aligned with the two notches of the cup, which were oriented perpendicularly to the vertical guide of the rig. The cement was then poured into the cup and allowed to harden, forming a secure bond around the inferior vertebra.

Once the inferior vertebra was potted, it was detached with its cup from the rig base and secured upside down to the top of the rig. This allowed the cup to slide down through the rig's vertical guide into another cup for potting the superior vertebra. The superior vertebra cup consisted of a steel base with Kapton tape around its edge for holding cement around the superior vertebra while hardening (**Figure 3-2b**).

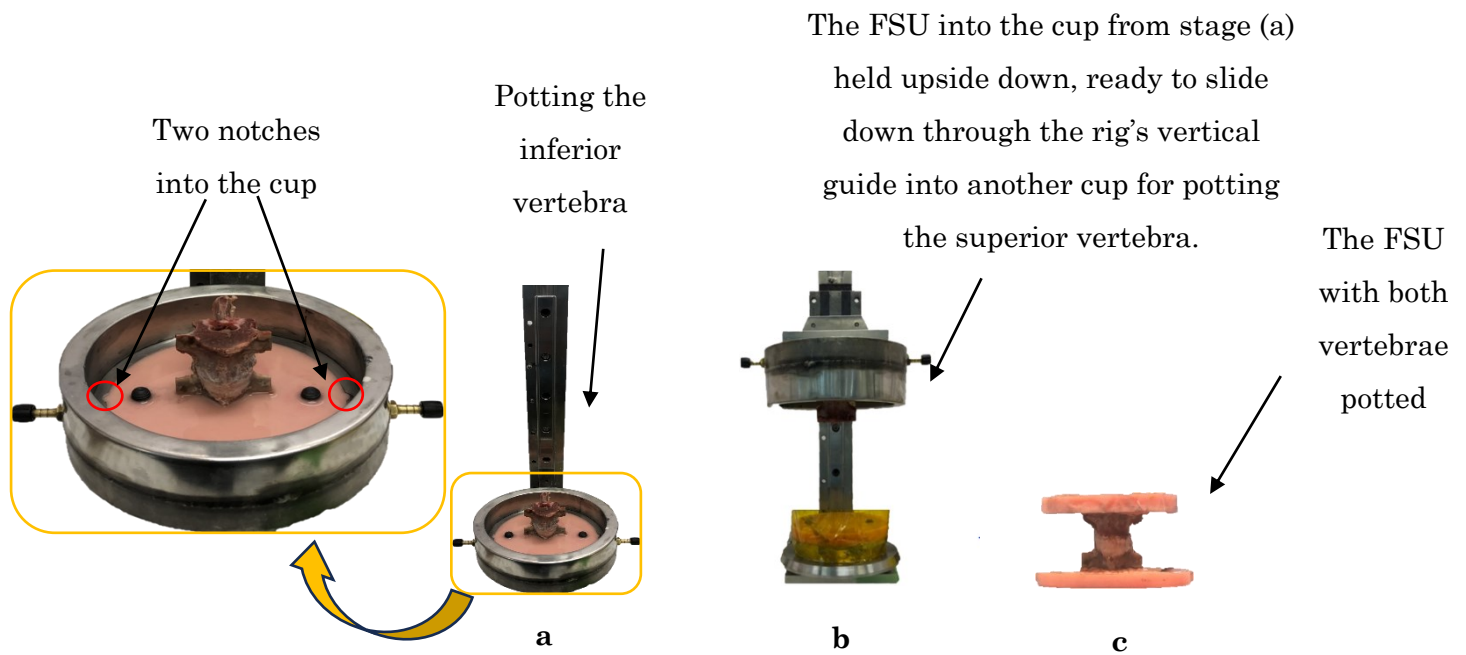


Figure 3.2 The custom-built alignment rig and the main stages of potting the FSU. The process begins with potting the inferior vertebra (a), followed by the superior vertebra (b). The completed FSU with both vertebrae potted is also shown (c).

3.2.2 Measurements and Hydration

To replicate the physiological conditions of *in vivo* FSUs during mechanical testing and accurately maintain overnight hydration of the disc, applying a compressive load of equivalent magnitude to that experienced during sleep was critical. This replication necessitated precise measurements of the discs and vertebrae dimensions on the day of potting and testing to estimate the required load.

Prior to potting each FSU, a vernier caliper was used to estimate the lateral (LAT) and anterior-posterior (AP) disc widths by measuring at the top of the upper vertebra and the bottom of the lower vertebra, where these approximate measurements correspond to the disc between the vertebrae. These measurements were then used to calculate the disc area using the formula: disc area = $0.84 \times AP \times LAT$ (Nachemson and Morris, 1964). For every FSU, each measurement was conducted three times to ensure precision, with the average values being recorded.

The derived area (A) was then used to estimate the intradiscal pressure (P), which correlates with the external load (F), and the stress (σ_{ext}) as illustrated by the following formula:

$$P = 1.5 \sigma_{ext}$$

$$P = \frac{1.5F}{A}$$

$$F = \frac{PA}{1.5}$$

For compressive loading, a negative sign was assigned to the pressure value to indicate its direction.

Immediately after potting the inferior vertebra for each FSU, additional measurements involved determining the X, Y, and Z offsets between the disc's axis of rotation (**Figure 3.3**) and the centre of the global coordinate system (GCS) of the hexapod robot used for mechanical testing (Ding et al., 2014; Lawless et al., 2014) (**Section 3.4.1**). The disc centre was approximated as the centre of the outer region corresponding to the disc of the superior vertebra. In this region, a vernier calliper was used to measure the midpoint between the anterior and posterior edges in the anterior-posterior (AP) direction and the midpoint between the left and right edges in the lateral (LAT) direction. The X, Y, and Z offsets represent the distances from the disc's centre to the potting cup's lateral (X offset) and anterior edges (Y offset) and vertically to the hexapod load cell (Z offset).

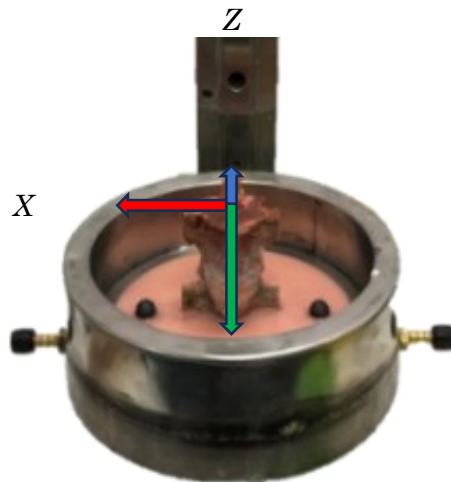


Figure 3.3 Illustration of offset measurements for the disc's axis of rotation in relation to the hexapod robot's global coordinate system. The calculated offsets: the red arrow for X offset (lateral distance to the potting cup), the green arrow for Y offset (anterior distance to the potting cup), and the blue arrow for Z offset (vertical distance to the hexapod load cell). Note: Arrows not to scale.

Once FSU potting was completed, radiographic images were initially acquired to determine the disc height which was essential for measuring the FSU height. This measurement was critical to precisely align the hexapod's end effector with the FSUs during mechanical testing, ensuring that the applied loads accurately replicated physiological conditions (**Section 3.2.2**).

The human intervertebral disc exhibits viscoelastic properties that enable it, during daily activities, to undergo fluctuating high intradiscal pressures caused by varying mechanical loading. This variation resulted in a diurnal cycle of fluid reduction and a decrease in disc height. Conversely, during night-time rest, the disc underwent recovery, regaining fluid and height, while the intradiscal pressure diminished due to the reduced external vertical load acting on the disc during sleep (Lu et al., 1996, Natarajan and Andersson, 1999). Thus, before embarking on mechanical testing, the *in vivo* physiological state of disc hydration and pressure for each FSU needed to be mimicked. Each FSU disc was soaked overnight for approximately 13 hours in a 0.15 M phosphate-buffered saline (PBS) solution at room temperature, with a compressive preload applied (Costi et al., 2008a). An intradiscal pressure of 0.1 MPa, indicative of a resting disc state, was targeted as the recovery preload (Wilke et al., 1999b). Achieving this pressure involved exerting a specific compressive load on the disc.

The magnitude of this load (F) was calculated using the previously derived disc area (A) and the formula $F = PA / 1.5$, where P is the targeted intradiscal pressure. This resulted in a compressive force of magnitude $0.1 * A / 1.5$ being applied to each disc overnight to simulate the resting state.

3.3 Creation of Disc Needle Injury

This study aimed to establish a consistent methodology for creating reproducible needle injury in each disc. While previous studies used various ratios of needle diameters and disc height (**Table 2-2**), this project used a 25G needle due to its clinical relevance. Further This option provided a 12.8% ratio of needle diameter (0.5 mm) to ovine disc height (mean 3.9 mm) (O'Connell et al., 2007). A 25G needle with a 0.5 mm diameter was selected to replicate the needle-to-disc height ratio observed in humans, achieving a 12.8% ratio relative to the average ovine disc height (3.9 mm) (O'Connell et al., 2007). This ratio closely approximates the human scale, where an 18G needle (1.3 mm) corresponds to a 11.5% ratio against the average human disc height (11.3 mm) (O'Connell et al., 2007).

O'Connell et al. (2007) measured ovine disc height from a lateral radiographic image by normalising the disc height, dividing the disc space area by the AP width. Since in the current project, each FSU was tested weekly, with each FSU prepared, radiographed, and its disc height measured all on the day of testing, it was impractical to use a mean disc height calculated from all FSUs. The mean disc height could only be determined after all FSUs were ready for testing, which wasn't feasible given the staggered testing schedule. Therefore, a consistent mean disc height from the literature was used to ensure uniformity and comparability across all FSUs tested sequentially each week. Additionally, a custom-engineered, 3D-printed apparatus was designed primarily to facilitate reproducible needle insertion into the posterolateral region of the disc and, secondarily, to assist in extracting the injury track for later microtome sectioning (**Figure 3.4**).

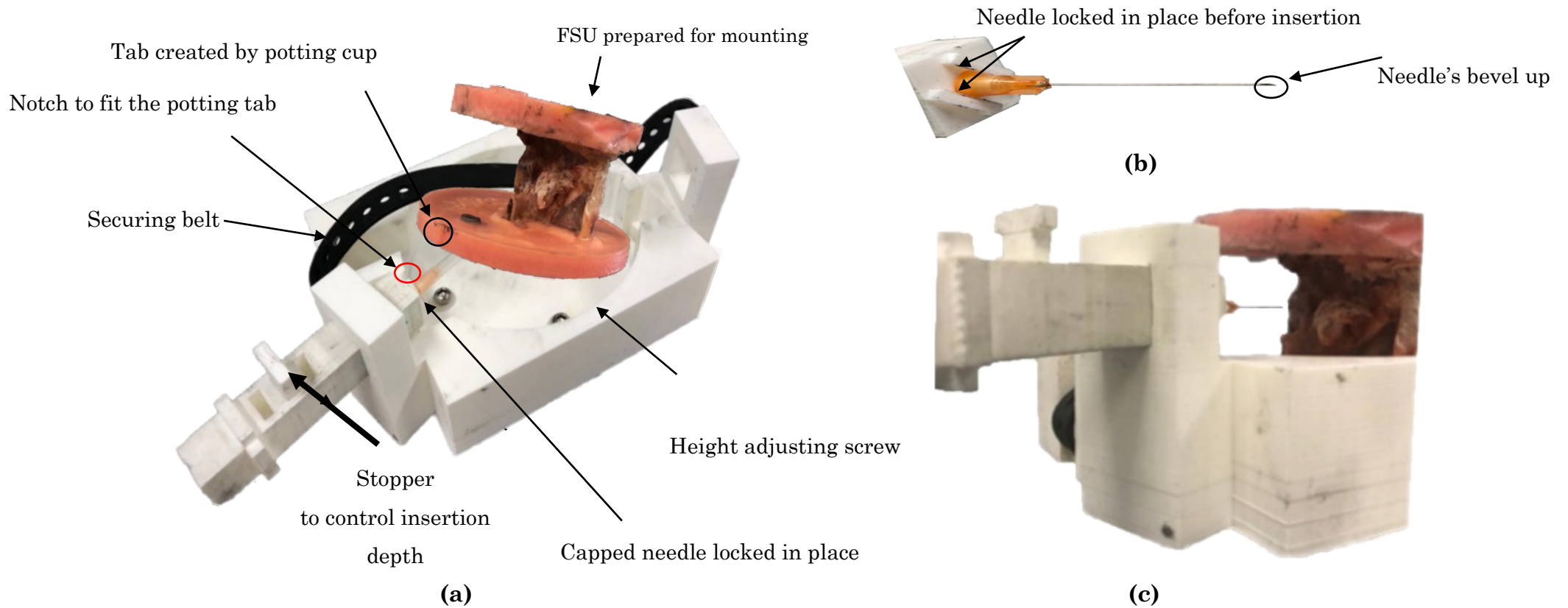


Figure 3.4 Multi views of the needle insertion apparatus and FSU alignment. An oblique top perspective of the apparatus, featuring a needle holder with an integrated stopper to prevent over-insertion, adjustable screws for FSU height alignment, and a belt for securing the FSU, ready for mounting (a). A further close-up view of the needle securely locked in the needle holder with the bevel facing upward during needle insertion into the disc (b). A posterolateral view of the mounted FSU, highlighting the alignment of the disc above the mid-height for needle insertion (c).

The apparatus ensured accurate and controlled insertion of the needle into the disc. The needle holder of the apparatus was designed to grip the needle securely and guide its consistent movement through an angled slot, which was specifically crafted to direct the needle's movement horizontally, ensuring the injury was confined to the posterolateral region of the disc. Moreover, the needle holder was equipped with an integrated stopper, calibrated using a calliper to set a boundary that prevented the needle from inserting beyond a predetermined depth into the disc. This depth, accurately measured and set at approximately 17 mm from the annulus edge into the disc, ensured that the needle fully penetrated the annulus.

The injury creation protocol began with a careful measurement of the disc's total height, from the top edge to the bottom edge, using a calliper to accurately determine and mark the top quarter of the disc's height for the needle's entry point. This location, positioned above the mid-height towards the convex top vertebra, was chosen to facilitate needle insertion without the risk of hitting the concave bottom vertebra. After marking this entry point, the FSU was placed into the apparatus by snugly fitting the two tabs previously created by the two notches from the potting cup (**Figure 3-2a, Section 3.2**) into corresponding notches in the apparatus. These notches, which align with the FSU pedicles, were used as a reference to position the angled slot for the needle holder, guiding the needle's posterolateral insertion into the disc. The needle was then inserted into the needle holder, with its bevel facing upwards (**Figure 3.4b**). The alignment of the needle was adjusted through the four screws beneath the FSU, ensuring that the needle axis aligned with the marked quarter-height point on the disc (**Figure 3.4c**). Once aligned, the needle was marked using a water-safe green marker (Staedtler Lumocolor 317 Permanent M). During insertion, the marker ink was transferred from the needle to the annulus, making the injury visible under subsequent microscopic imaging and structural analysis (**Section 3.5**). The efficacy of this injury creation protocol, implemented using the custom-built apparatus to ensure reproducibility, was assessed, and the results were presented in the following subsection.

3.3.1 Reproducibility of Needle Insertion

The reproducibility of needle insertion was evaluated using the protocol and apparatus described above. This evaluation was crucial to ensure that any observed effects or outcomes were attributable to the effects of needle injuries instead of the variations in the procedure. Four ovine lumbar FSUs (3 L4-5 and 1 L5-6), not included in the primary project FSUs, were used for this purpose. Each FSU was prepared (**Section 3.2**) before being subject to three repeats of needle insertion. After every insertion, the needle was withdrawn, and then the FSU was dismounted from the apparatus and remounted. Following each repeat, an anterolateral radiograph was captured to visualise the posterolateral position of the inserted needle (**Figure 3.5**). Reproducibility was evaluated based on the level of the needle's insertion and the insertion depth. The level of the needle's insertion referred to the vertical distance from the top edge of the disc (used as the datum) to the tip of the needle. In contrast, the insertion depth was the horizontal distance from the edge of the annulus to the tip of the inserted needle (**Figure 3.6**).

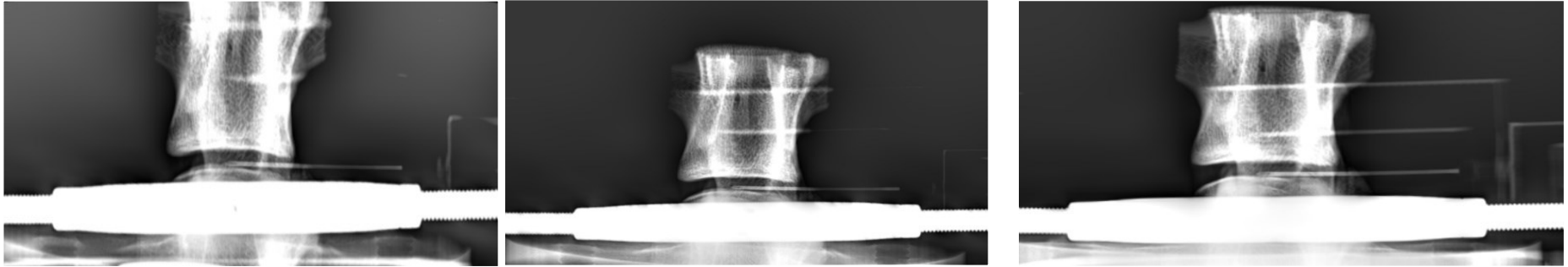


Figure 3.5 Anterolateral view radiographs displaying three repeated needle insertions for one FSU.

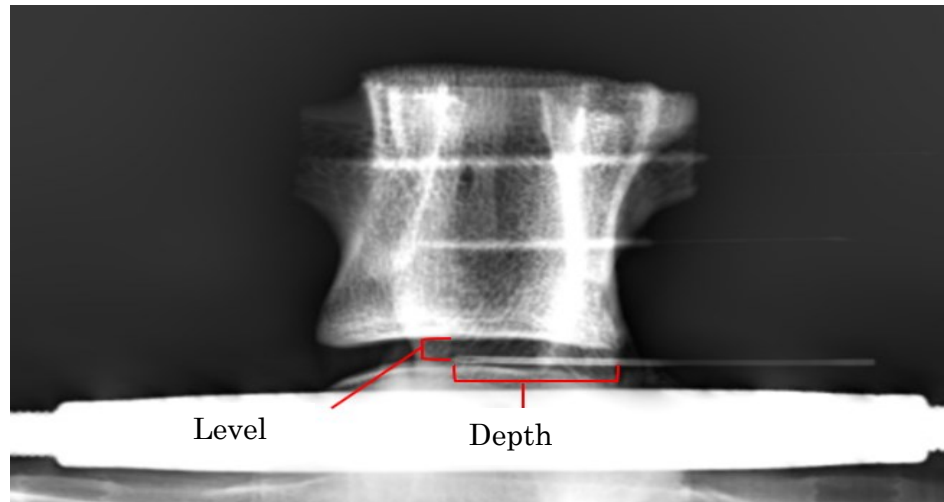


Figure 3.6 Illustration of needle insertion level and depth measured from a radiograph.

3.3.1.1 Data-Image Analysis

The collected radiographs were imported into ImageJ software (version 1.53s), where pixel values were calibrated to physical dimensions using a standard reference of known dimensions included during radiograph acquisition. This calibration was uniformly applied across all radiographs to enable reliable measurements. For each needle insertion repeat, three measurements were taken for both needle level and depth into the disc. Averages for these measurements were then calculated (**Table 3-1** for level and **Table 3-2** for depth). Notably, one of the needle insertion repetitions from one FSU encountered an error, resulting in missing data denoted by an 'x' in the relevant tables.

Table 3-1 and **Table 3-2** Measurements of the needle insertion level and depth taken during needle insertion repeats for four FSUs. For each FSU (disc height and width mean in mm, respectively), three separate measurements are presented for each insertion repeat, alongside the calculated mean. Table 3-1 (left) presents the needle insertion level (mm) into the disc, while Table 3-2 (right) indicates the needle insertion depth (mm) relative to the top edge of the disc. An 'x' in the tables signifies missing data due to an experimental error.

Needle Insertion Level						Needle Insertion Depth					
FSU ID (Disc height, mm)	Insertion Repeat	Measurement 1	Measurement 2	Measurement 3	Mean	FSU ID (Disc width, mm)	Insertion Repeat	Measurement 1	Measurement 2	Measurement 3	Mean
5L45 (3.14)	1	1.39	1.39	1.34	1.37	5L45 (30.5)	1	17.41	17.25	17.33	17.33
	2	1.51	1.4	1.57	1.49		2	17.43	17.46	17.57	17.49
	3	1.7	1.74	1.74	1.73		3	17.75	17.88	17.81	17.81
7L45 (3.84)	1	2.57	2.51	2.57	2.55	7L45 (31.3)	1	17.81	17.85	17.87	17.84
	2	2.55	2.54	2.57	2.55		2	18.83	18.74	18.44	18.67
	3	2.59	2.56	2.56	2.57		3	17.96	18.1	18.43	18.16
9L45 (3.51)	1	x	x	x	x	9L45 (30.53)	1	x	x	x	x
	2	1.76	1.79	1.79	1.78		2	15.74	15.5	15.81	15.68
	3	2.1	2.01	2.06	2.06		3	16.1	15.8	16.1	16
12L56 (3.85)	1	2.42	2.48	2.37	2.42	12L56 (32.47)	1	17.26	17.44	16.99	17.23
	2	2.52	2.52	2.59	2.54		2	16.81	16.72	16.81	16.78
	3	1.61	1.61	1.61	1.61		3	17.09	17.09	17.08	17.09

As previously discussed earlier, a 25G needle was selected to replicate the needle-to-disc height ratio observed in humans, which approximates a 12.8% ratio relative to the ovine disc height. This closely reflects the 11.5% ratio used for human disc height, which aligns the experimental model with the human scale. To further evaluate the accuracy of these measurements, a previous study reported a mean ovine disc height of 3.93 mm (O'Connell et al., 2007), while the mean disc height calculated from the FSUs in this study was 3.59 mm. The difference of 0.34 mm, with a standard deviation (SD) of 1.19 mm, falls within the range of expected variability and aligns with prior findings.

In light of these disc height variations, the differences in needle insertion levels between certain FSUs can also be explained by their respective disc heights. Specifically, the difference between the insertion levels of FSUs 7L45 and 5L45 may be attributed to their disc heights. FSU 7L45 has a disc height of 3.84 mm, consistent with its higher insertion level, while FSU 5L45 has a disc height of 3.14 mm. These findings underline the influence of disc height on insertion level and highlight the importance of considering disc height variability when interpreting the results.

The Intraclass Correlation Coefficient (ICC), an indicator of the reliability of ratings or measurements, was derived using IBM SPSS Statistics (version 25.0.0.2). Given that multiple measurements were averaged in the analysis, the average-measures reliability is the more relevant approach. An ICC value of 0 represents random measurements, while a value of 1 indicates impeccable consistency between measurements. Typically, ICC values less than 0.5 represent poor reliability, those between 0.5 and 0.75 indicate moderate reliability, those between 0.75 and 0.9 suggest good reliability, and values greater than 0.9 demonstrate excellent reliability (Koo and Li, 2016).

Regarding the level of needle insertion, the ICC value for average-measures reliability was 0.877, indicating good reliability. As for the depth of needle insertion, the ICC value for average-measures reliability was 0.909, also reflecting good reliability. The obtained ICC values emphasised a strong level of

reliability for both needle insertion level and depth using the apparatus. These findings underscored the method's dependability, offering a robust foundation for its application in the present project.

3.4 Mechanical Testing

3.4.1 Flinders Hexapod Robot

The uniquely designed Flinders hexapod is a Stewart-based platform integrated with six-ball screw actuators that facilitate precise six-degrees of freedom (6DOF) movement in both displacement and rotation. By connecting a movable top plate through six legs to a fixed base plate, the hexapod offers a platform where FSUs placed in stainless steel cups and submerged in a water bath can be securely mounted (**Figure 3.7**).

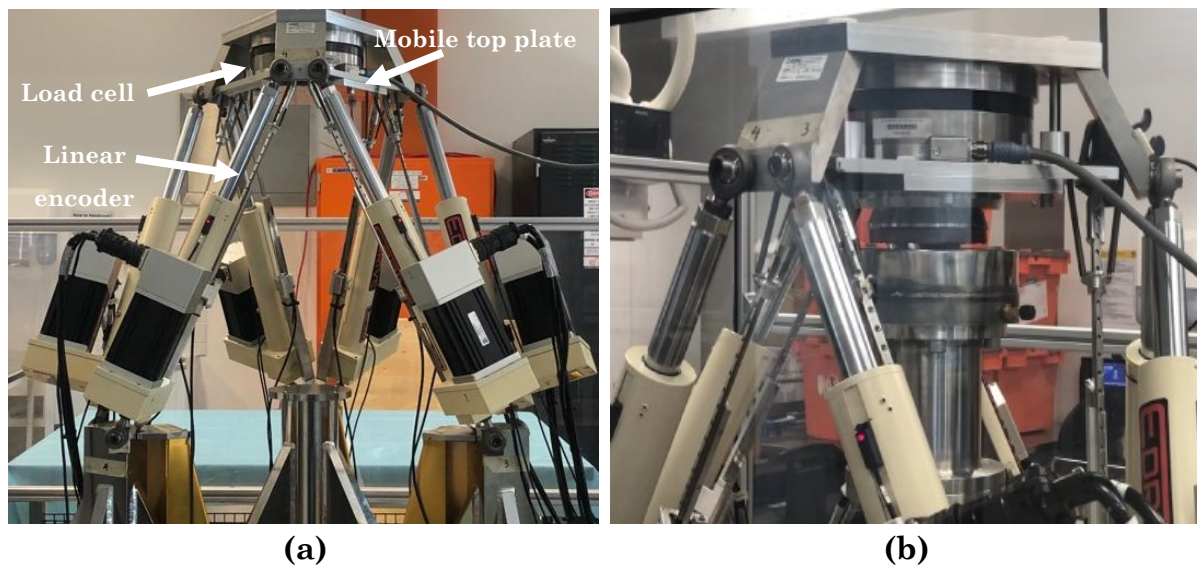


Figure 3.7 The Flinders hexapod robot used for 6DOF mechanical testing (a) with an FSU placed in stainless steel cups, submerged in a water bath, and positioned between the stable base and the moving top plate of the hexapod (b).

This design allows the hexapod to accurately mimic the complex movements of various biological tissues, from bones and muscles to joints such as intervertebral discs, while simultaneously measuring their real-time displacement, rotation, and load dynamics (Lawless et al., 2014).

The hexapod secures the FSU by bolting it between the base plate and a coupling plate positioned above. This coupling plate is then attached to the hexapod's

movable top plate. The hexapod's six actuators have demonstrated precision based on validation tests by the National Association of Testing Authorities (NATA), ensuring a displacement accuracy of ± 0.01 mm and an angular rotation accuracy of $\pm 0.006^\circ$. Each actuator is accompanied by an optical linear encoder (Model: B366784180185, LDM54 from MicroE Systems Inc., Brillerica, MA) is placed, capable of length measurements with a resolution of $0.5 \mu\text{m}$. A load cell for the hexapod (Model: MC3A-6-1000, AMTI, Watertown, MA) is situated above the top plate. This load cell offers a measurement range of 4,400 N for axial compression and 110-Nm for axial torque, providing accuracies of ± 9 N and ± 0.2 Nm, respectively, as validated by the NATA (Ding et al., 2011). The hexapod's operation offers flexibility: It can be driven using ramp or cyclic loading and can function in three distinct control modes: 'position', 'load', and 'hybrid' modes. In the 'position' mode, the hexapod operates under displacement control for a single selected DOF. Conversely, the 'load' mode drives the hexapod with load control across all 6DOF simultaneously. The 'hybrid' mode combines the two modes, typically by limiting position control to a single DOF (the primary test objective) while using load control to neutralise off-axis loads.

3.4.2 6DOF Testing and Repetitive Loading

To evaluate the 6DOF mechanical effects of simulated repetitive lifting on the FSU, the project used two primary testing protocols. Initially, the 6DOF test was conducted to assess the FSU's mechanical response under a range of movements, establishing a mechanical profile of the FSU before applying simulated repetitive lifting. Following the 6DOF Testing, the repetitive loading protocol was applied to simulate the specific loading exerted on the FSU during extensive repetitive lifting tasks. After completing the repetitive loading, the 6DOF test was performed again to identify any mechanical changes in the FSU's mechanical behaviour, thereby allowing for a direct comparison of the FSU's mechanical condition before and after experiencing simulated repetitive lifting.

3.4.2.1 6DOF Testing

The 6DOF Testing was conducted across six motion axes to account for the disc's structural anisotropy and to realistically simulate FSU movements. The testing applied mechanical loading to the FSU, driven by load control or position control, to mimic *in vivo* mechanical conditions assumed during routine slow movements, like those in office work, with loading at a frequency of 0.1 Hz. Additionally, it incorporated the application of a preload and a follower preload on the FSU to simulate physiological intradiscal pressures of 0.1 MPa at rest and 0.5 MPa, representing body weight during standing, respectively (Wilke et al., 1999b), using corresponding equations (Section 3.2.2). Due to the disc's biphasic nature, fluid flow within it depended on the sequence of the 6DOF Testing. For instance, fluid flow was expected to be more pronounced during compression and bending than in shear. Therefore, the 6DOF testing, which lasted nearly 40 minutes, followed a predetermined sequence of directions (Figure 3.8) (Costi et al., 2008a, Amin et al., 2016b).

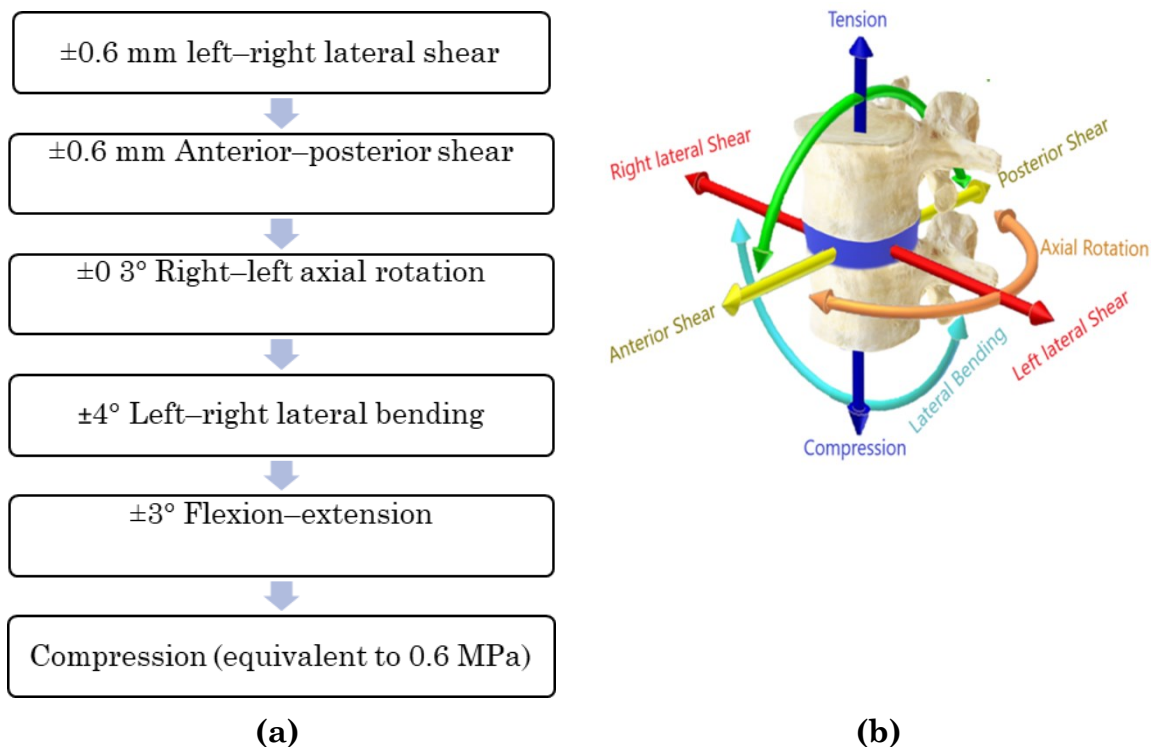


Figure 3.8 Illustration of the 6DOF testing sequence with corresponding magnitudes (a) and the directional movements applied to the intervertebral disc (b).

The 6DOF testing sequence commenced with lateral and anterior-posterior shears of ± 0.6 mm, then progressed to axial rotation of $\pm 3^\circ$, lateral bending of $\pm 4^\circ$, and flexion-extension of $\pm 3^\circ$, and ended with a compression corresponding to an intradiscal pressure of 0.6 MPa. The testing sequence was consistent with the physiological range of motion (Lu et al., 2005, Costi et al., 2008a). For the compression test, an initial follower preload was applied to achieve a calculated nucleus pressure of 0.5 MPa. An additional load was then applied to increase the calculated nucleus pressure by another 0.1 MPa, to result in a total disc nucleus pressure of 0.6 MPa, and thus simulating the pressure experienced by an individual standing (Wilke et al., 1999b). For each DOF, dynamic movement was executed in a haversine waveform over five cycles. However, compression was exceptionally subjected to a load-controlled cycle. For the remaining DOFs, a hybrid control mode was employed, combining position control with the reduction of off-axis coupling forces and moments to zero in load control. After each DOF test, FSU were allowed a 10-minute recovery period.

3.4.2.2 Repetitive Loading

A simulated repetitive lifting was conducted to mimic the condition an individual might experience during a day. The simulation focused on repetitive loading by integrating lifting weight with FSU flexion, and a specified number of lifting cycles. Specifically, the loading was applied under a combined compressive load of 1.1 MPa nucleus pressure, equivalent to lifting an intermediate weight of 20 kg, within safe manual handling limits (Cooper, 2018, Wilke et al., 1999a), and a 13° flexion (Pearcy and Tibrewal, 1984, Adams and Hutton, 1983, Stokes and Frymoyer, 1987) for 1000 cycles (Hansson et al., 1987, Zehr and Callaghan, 2023, Berger-Roscher et al., 2017). This simulated repetitive lifting was conducted at a frequency of 1 Hz (Callaghan and McGill, 2001, Drake et al., 2005, Amin, 2019a) using a haversine waveform.

3.4.3 Calculations of Stiffness and Phase Angle

The 6DOF testing assessed the mechanical condition of FSU. The collected data was recorded in two text files: one containing translations and rotations and the other documenting the forces and moments. To represent FSU displacement accurately, the displacement data underwent transformation via LabVIEW (National Instruments, USA) to compensate for the X and Y offsets between the FSU and hexapod actuators. MATLAB software (R2018b, MathWorks, USA) was then used to analyse the data. The stiffness of each DOF was determined by calculating the linear regression slope of the loading portion from the last dynamic cycle (fifth cycle). This computation was performed using polyfit and polyval MATLAB functions (**Figure 3.9**).

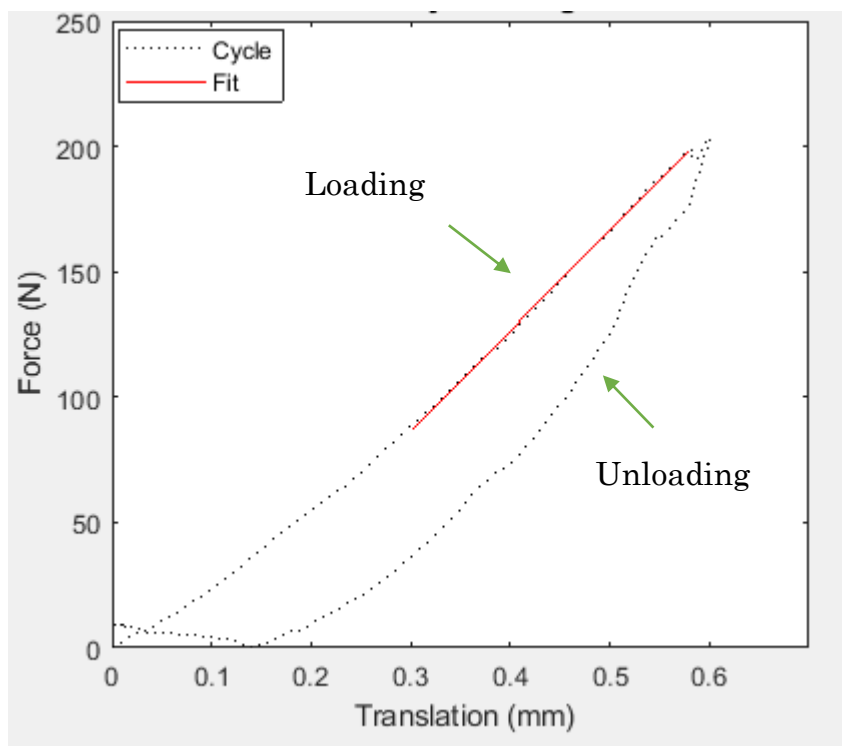


Figure 3.9 An example plot of the last cycle showing the pattern of dynamic testing in anterior shear at 0.1 Hz with the loading portion (red fit) from which stiffness is calculated.

The viscoelastic measure of phase angle, which signified the shift in time between an applied load and resultant displacement, was calculated through

dynamic testing spanning four cycles. This calculation was performed using the estimate function in MATLAB's cross power spectral density (CPSD). In other words, it represented the difference between peaks of loading and displacement.

3.5 Structural Analysis

3.5.1 Injury Sectioning and Imaging

A methodical approach was undertaken to achieve proper sectioning of the injury and understand the injury's characteristics to ensure precise results. It was imperative to understand the aim of the approach in the broader context of the entire disc (**Figure 3.10**). Continuous sectioning using microtome started at the annular edge, creating slices of 60 μm thickness. This slicing continued until reaching a depth of 1200 μm into the annulus, from which five slices perpendicular to the injury axis were collected. Subsequently, each slice was imaged at 10X magnification using a Brightfield BX50 light microscope from Olympus, Japan.

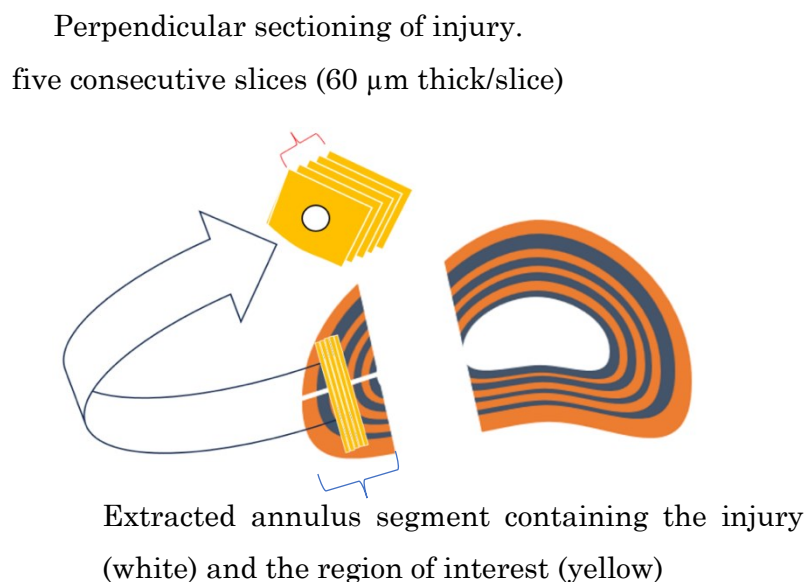


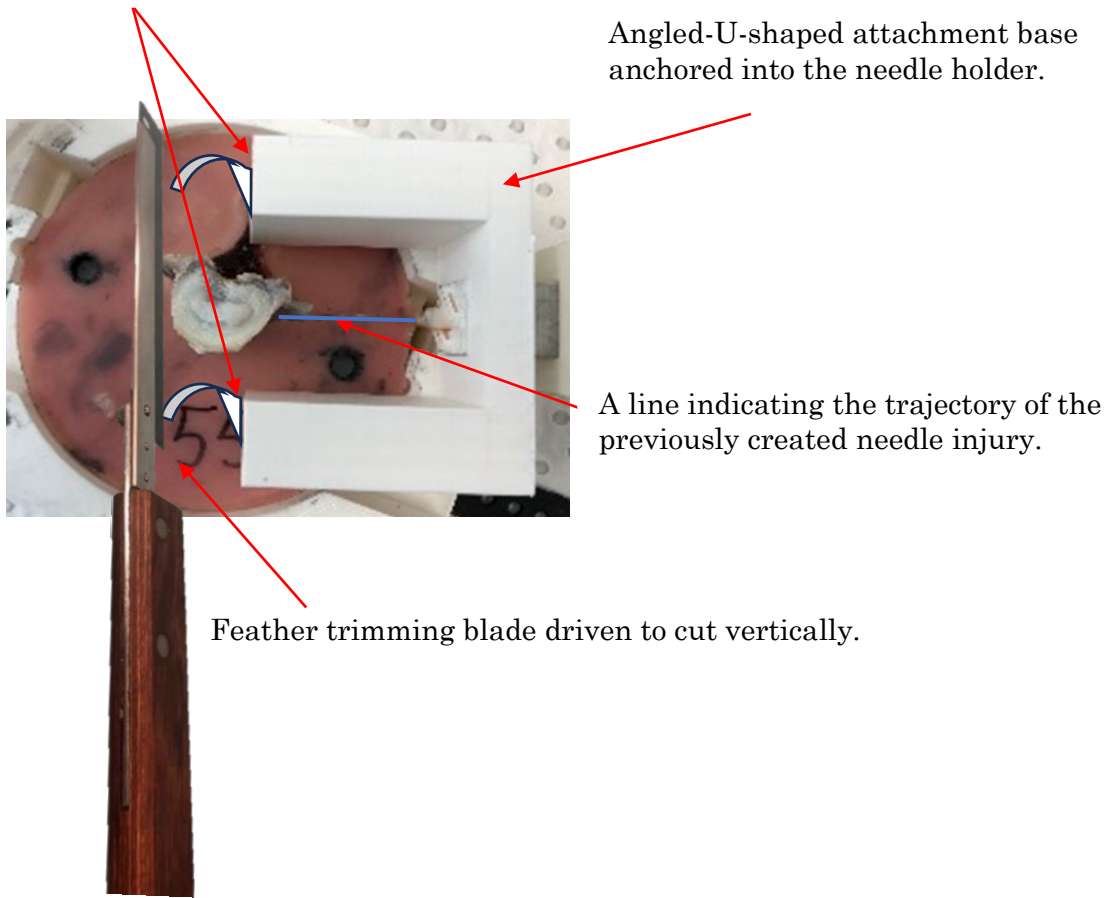
Figure 3.10 Top view of the intervertebral disc showing the extracted segment of the annulus containing the needle injury (white). The segment is cry-sectioned, and five consecutive slices perpendicular to the injury axis, each with a thickness of 60 μm , are obtained. The region of interest where the slices are collected is at 1200 μm depth from the annulus edge (yellow). Note: Drawing not to scale.

The method commenced by surgically removing the upper vertebra of each FSU through an incision made at the upper disc-endplate junction, ensuring maximum preservation of the disc tissue. The upper vertebra was removed prior to formalin fixation to allow optimal penetration of the formalin solution and thus enhance fixation quality. This step ensured thorough preservation of the disc structure. Each FSU was then placed in a 10% buffered formalin solution for 3 days. This intermediate fixation duration was selected to bridge the differences observed in the literature between shorter durations of 24 to 48 hours (Shu et al., 2017, Pelle et al., 2014) and the longer period of one week for fixing intervertebral disc tissues (van Heeswijk et al., 2018). After the fixation period, the remaining part of the FSU (disc-bottom vertebra) was repositioned into the apparatus previously used to create the needle injury (**Section 3.3**). An angled U-shaped attachment specifically designed for the apparatus was incorporated. The base of this attachment secured itself to the needle holder while its arms ran parallel to the needle holder's axis, aligning with the trajectory of the induced injury. A feather-sharp blade was then introduced, sliding vertically from top to bottom along the flat surface of the open side of the angled U-shaped guide (**Figure 3.11**).

Following the initiation of a perpendicular incision at the nucleus-annulus interface along the injury axis (**Figure 3.12a**), the annular segment containing the needle injury was isolated at the lower disc endplate junction with care to maximise disc tissue preservation. As a result, the annular segment encompassing the injury was efficiently removed (**Figure 3.12b**). This method ensured the segment had a flat base, ideal for embedding in the optimal cutting temperature (OCT) compound. The segment was subsequently frozen below -20°C until it solidified. Once this preparation phase was completed, the segment was set for sectioning perpendicular to the injury axis using a microtome (Leica Biosystems, CM3050, Germany) (**Figure 3.12c**).

Open end of the attachment arms with flat surface to guide the vertical cutting of the blade

Angled-U-shaped attachment base anchored into the needle holder.



A line indicating the trajectory of the previously created needle injury.

Feather trimming blade driven to cut vertically.

Figure 3.11 Top view of a formalin-fixed disc after the removal of the upper vertebra. The remaining disc-bottom vertebra is seamlessly repositioned into the apparatus used earlier for the creation of needle injury. The depiction concludes with the integration of a specially designed angled U-shaped attachment. This setup facilitates a precise vertical cutting to extract the annulus segment containing the needle injury.

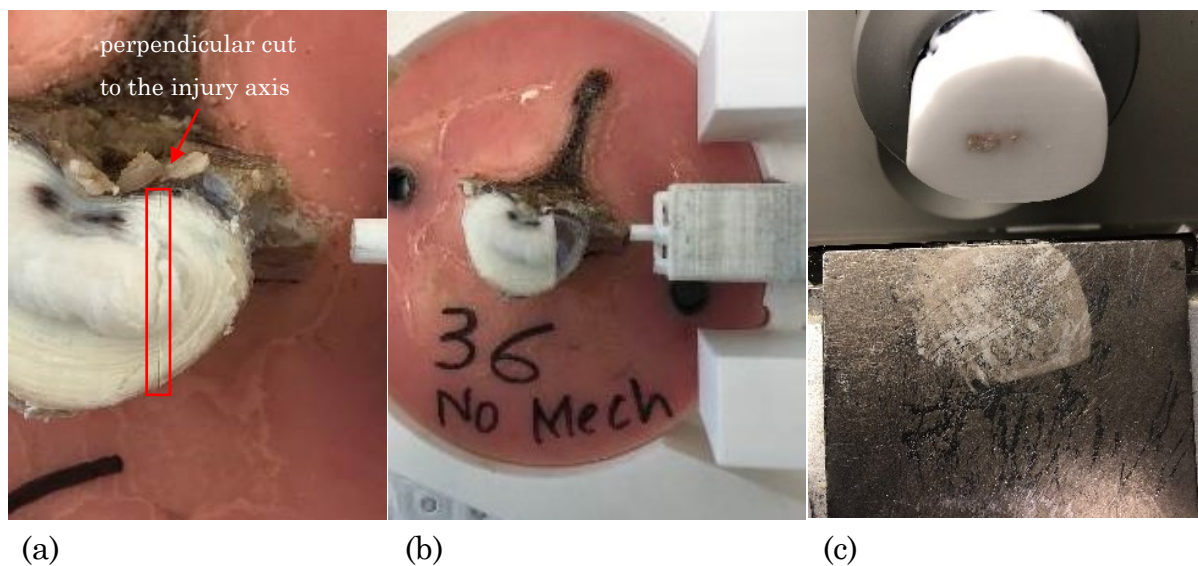


Figure 3.12 Illustration of the vertical cut made by a trimming feather blade perpendicular to the injury axis (a). The figure further displays the removal of the annular segment enclosing the needle injury (b). The extracted segment, with its flat base, is shown embedded in an OCT compound, ready for sectioning perpendicular to the injury axis (c).

3.5.2 Quantifying Needle Injury

To quantitatively analyse injury parameters, the five consecutive slices collected from each injury (**Section 3.5.1**) were assumed to be similar and were treated as replicates. The location of the needle injury in each slice was identified by the water-proof green marker ink previously used (**Section 3.3**) that transferred from the needle to the annulus during insertion. This ink provided a clear, visible mark under microscopic imaging. The measurements derived from these slices were then averaged to obtain a mean value for or the injury length, area, solidity, and aspect ratio. The relevance of assessing these parameters arises from their potential to offer key details regarding the severity and characteristics of the injury. Injury length and area provide a measure of the extent of damage, with length describing how far the injury extends through the annular tissue and area capturing the total surface affected. Larger injury length or area generally indicates more extensive damage, suggesting that the disc's structural integrity has been compromised. However, quantifying injury solidity and aspect ratio offers additional insights into the injury's shape and distribution. Solidity

represents how compact or dense the injury is, with higher solidity indicating a more localised injury, while lower solidity suggests a more irregular and spread-out injury. Aspect ratio reflects the shape of the injury, with a higher aspect ratio indicating an elongated injury and a lower ratio suggesting a more rounded and centralised injury. Further, in the context of disc injuries in FSUs undergoing mechanical loading, lower solidity, larger length, larger area, or a higher aspect ratio could correlate with greater tissue disruption and potentially more significant biomechanical consequences. Additionally, while elongated injuries might imply significant disruption to the annular tissue, this disruption could be exacerbated if the elongation aligns with the direction of loading, such as the flexion direction when applying repetitive loading combined with compression on FSUs.

3.5.2.1 Injury Length and Area

ImageJ software (version 1.53s) was employed to import each image as originally acquired and analyse the injury parameters (**Figure 3.13a**). The 'Find Edges' command was applied to highlight the injury contours, and then the injury boundaries were segmented (**Figure 3.13b**) using the software's integrated wand tool. This process generated a mask specific to each injury (**Figure 3.13c**).

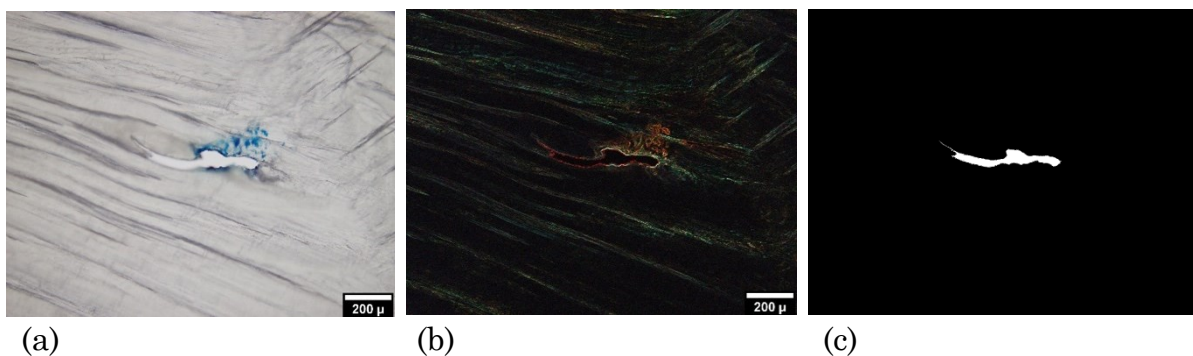


Figure 3.13 Analysis with ImageJ software of original image of a needle (a), undergoing segmented injury contours (b), before injury mask generated (c).

From the created mask of each injury, the injury area was computed using the built-in 'Measure' function of the software. However, for identifying and quantifying the elongated axis of every injury (**Figure 3.14**), the 'Ridge

Detection' plugin in ImageJ was employed—a technique that has earned widespread use in research (Li et al., 2020, Möller and Schattat, 2019, González et al., 2020, Betegón-Putze et al., 2019).

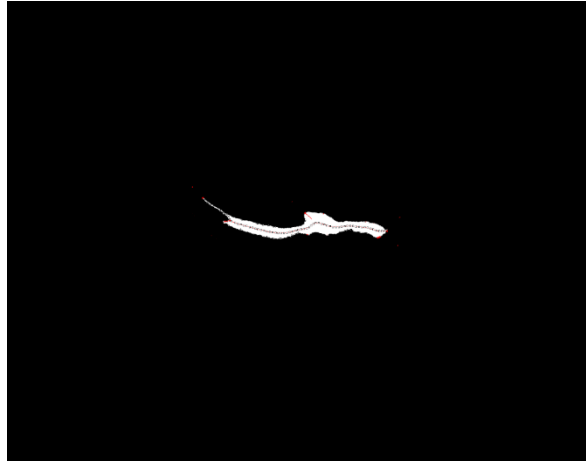


Figure 3.14 Demonstration of the elongated axis identification of a needle injury using the 'Ridge Detection' plugin in ImageJ, applied to the created mask of the injury.

3.5.2.1.1 Reproducibility of Manual Interventions

While the tools used in ImageJ software – such as the 'Find Edges' and 'Measure' commands for measuring area or the 'Ridge Detection' plugin for detecting length – were automated, the act of defining injury boundaries with the wand tool, among other steps, relied heavily on the operator's discretion and judgment. These manual steps might introduce variability in measurements, influenced by subjective interpretation or human errors. Therefore, conducting the reproducibility test was essential to ensure that the manual interventions made were consistent across different measurements and that any potential variability introduced due to the manual processes did not significantly alter the outcomes. This testing aimed to strengthen the reliability of the measurements and confirm that the results were not excessively influenced by inadvertent biases or inconsistencies in the manual steps.

3.5.2.1.1.1 Method

This section describes the reproducibility assessment methodology with the aim of expanding upon the foundational ImageJ analysis procedure outlined earlier. Images were randomly sourced from needle injuries inflicted on FSUs that had

been subjected to simulated repetitive lifting before the injuries (**Chapter 4**) and additional lifting after the injuries were inflicted (**Chapter 5**). For the reproducibility test, two injury images were randomly selected from a set image of five sectioned slices of each respective injury. This process was applied to each of the three injuries, resulting in a total of six images chosen for reproducibility assessment (**Figure 3.15**).

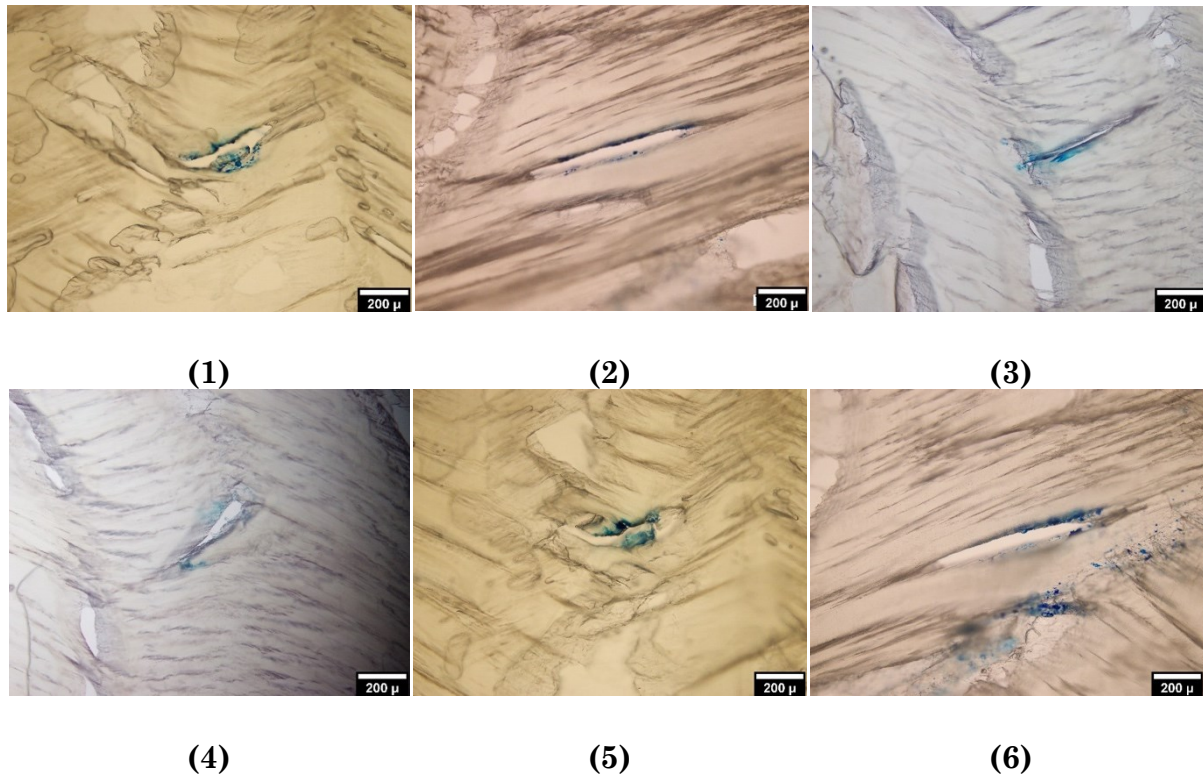


Figure 3.15 Six images were randomly chosen for reproducibility assessment, each derived from three injuries. For each injury, two images were randomly selected from its respective set of five.

Once the six images were randomly selected from five sections across the three injuries, reproducibility measurements were performed with five separate repeats. The same six images were used for each of the five repeats, with measurements of the injuries' area and length taken during each repeat. To further ensure impartiality, the images were analysed in a randomised sequence each day:

- Day 1 (repeat 1): Injury images 1, 2, 3, 4, 5, 6
- Day 2 (repeat 2): Injury images 2, 4, 1, 6, 3, 5
- Day 3 (repeat 3): Injury images 4, 3, 2, 5, 1, 6
- Day 4 (repeat 4): Injury images 2, 4, 6, 1, 5, 3
- Day 5 (repeat 5): Injury images 6, 5, 1, 3, 2, 4

The repeats were conducted with a minimum of 24 hours between each session. This randomised order was implemented to prevent any image from consistently benefiting or suffering from its sequence during the analysis. Moreover, conducting each repeat on a different day was crucial to maintaining impartiality, reducing recall bias, and preventing prior sessions from inadvertently influencing subsequent measurements.

3.5.2.1.1.2 Data Analysis

A comprehensive test was undertaken to establish the reproducibility of the ImageJ-based analysis, as detailed in the previous section. The test results, encompassing five separate repeats and measurements from six distinct injury images, are presented in **Table 3-3** and **Table 3.4** with measurements of the injury's length and area, respectively.

Table 3-3 and **Table 3-4** Results from the reproducibility assessment, based on the ImageJ analysis procedure. These tables capture the measurements for both the area and length of the injuries across all six images in five separate test repeats.

Injury Length (μm)					
Injury Image	Repeat 1	Repeat 2	Repeat 3	Repeat 4	Repeat 5
1	450	442.4	444.7	446.4	446.8
2	667.8	666.3	664.3	664.2	665
3	361.5	352.6	359.2	357.4	357.1
4	259.8	257.3	255	259.3	257.2
5	406.4	394	390.1	399.4	387.3
6	742.2	748.1	740.6	746	752.3

Injury Area (μm^2)					
Injury Image	Repeat 1	Repeat 2	Repeat 3	Repeat 4	Repeat 5
1	14906.5	14668.7	14611.7	14764.3	14634
2	26433.8	26325.3	26652.6	26701.5	26669.7
3	1978.1	1998.1	2048.5	1980.5	1903.9
4	7150.5	7268.5	7294.6	7303.7	7293.7
5	8041.9	7967.7	7483.9	8009	7259.9
6	32504.2	32601.7	32397.6	32662.5	32205.9

Based on the ICC values obtained using SPSS, the absolute agreement for both injury length and injury area was determined to be 1. This perfect score across the five testing sessions underscored the reliability of the ImageJ software method and the consistent precision of the operator. Thus, employing the methods in the current project ensured a high degree of reliability and precision for quantifying the area and length of needle injuries.

3.5.2.2 Injury Solidity and Aspect Ratio

Injury solidity and aspect ratio were calculated using MATLAB R2018b. The solidity of an injury, a measure of its density, was defined as the ratio of the injury's area to the area of its convex hull—the smallest convex polygon that could encompass the injury (Wirth, 2004). The convex hull was computed using MATLAB's 'convhull' function (Figure 3.16a). For aspect ratio, the injury was first smoothed by fitting a cubic spline curve to it using MATLAB's 'cscvn' function, treating the injury as a singular shape. Subsequently, Principal Component Analysis (PCA) was executed using MATLAB's 'pca' function, which obtained the lengths of the major and minor principal axes of the injury (Figure 3.16b). The aspect ratio was then derived by comparing these two lengths.

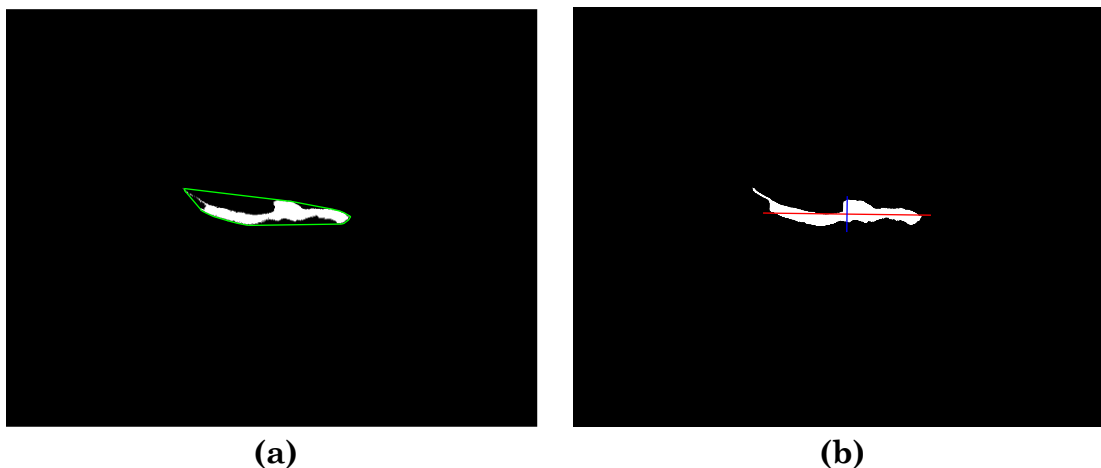


Figure 3.16 Illustration of MATLAB plotting of the convex injury area (in white) and its convex hull (outlined in green) for injury solidity calculation (a), and the principal major (in red) and minor (in blue) axes for aspect ratio calculation (b).

Chapter 4 Impact of Repetitive Lifting on Lumbar Disc Mechanics: Immediate and Post-Recovery Changes in 6DOF Stiffness and Phase Angle of Ovine FSUs

4.1 Abstract

Previous studies have assessed the mechanical effects of repetitive lifting on the intervertebral disc. However, no study has evaluated these effects by simulating repetitive lifting within a single day while accounting for the disc's inter-day recovery, such as fluid re-equilibration during sleep. Therefore, this study aimed to evaluate the six degrees of freedom (6DOF) mechanical effects of repetitive lifting on functional spinal unit (FSU) stiffness and phase angle under a more realistic simulation, which incorporated a duration achievable within a working day, using an ovine model. Twenty ovine FSUs underwent 6DOF testing at 0.1 Hz for five cycles, followed by simulated repetitive lifting under combined compression (1.1 MPa) and flexion (13°) for 1000 cycles. Two additional 6DOF tests were conducted immediately after the lifting and after a recovery period, a requirement sufficient for the disc to achieve fluid equilibrium. The study found significant biomechanical changes, particularly in flexion, including reduced stiffness (77.2%, $P < 0.001$) and increased phase angle (89%, $P < 0.001$) immediately after lifting. Following the recovery period, the observed changes in flexion persisted, with reduced stiffness (71.2%, $P < 0.001$) and an increased phase angle (63.8%, $P < 0.001$), suggesting that even a recovery period allowing for fluid equilibrium was insufficient to fully alleviate the biomechanical damage induced by repetitive lifting. The findings provide a foundation for future research into the biomechanical effects of repetitive lifting, employing a more realistic simulation approach to the intervertebral disc. They also offer insights into the moderating role of adequate recovery periods in workplaces.

4.2 Introduction

Risk factors for low back pain (LBP) are relevant for workers involved in manual handling tasks, who are often required to perform repetitive lifting—a notable activity that has been identified as a contributing factor to LBP (Marras et al., 1995, Punnett et al., 1991, Heneweer et al., 2011, Straker, 1999). Repetitive lifting can lead to disc herniation (Kelsey, 1975, Kelsey et al., 1984, Mundt et al., 1993), especially in discs with mild degeneration characterised by annular tears and dehydration of the nucleus pulposus (NP) (Schmidt et al., 2007).

In vitro studies have demonstrated an increased risk of disc failure with repetitive lifting applied to FSUs in the directions of compression (Adams and Hutton, 1985) and flexion (Gordon et al., 1991) in humans, as well as flexion combined with extension in porcine models (Callaghan and McGill, 2001). Additional research has reported disc failure under more complex scenarios, simulating the combined impact of flexion, axial rotation, and lateral bending in ovine models (Wilke et al., 2016, Berger-Roscher et al., 2017). Moreover, one study found that a 73% incidence of disc injury occurred in the form of endplate failure or disc herniation in humans (Amin et al., 2020), with the latter theorised to proceed through a sequential progression that involved stages of lamellar distortion, NP penetration, NP extrusion, and finally, annular rupture (Gordon et al., 1991). Further, the direction of the applied repetitive loading also correlated directly to the incidence of disc herniation. For instance, repetitive compression of the human FSU resulted in a 24% incidence of disc herniation (Adams and Hutton, 1985), while repetitive flexion caused a 100% incidence. Of the latter percent, 71% were annular protrusions, and 29% were NP extrusions with associated annular ruptures in the posterolateral region (Gordon et al., 1991). Some *in vitro* studies examined the mechanical effects of repetitive lifting under conditions of compression combined with axial rotation (Amin, 2019a) and flexion alone (Gordon et al., 1991) in human FSUs, as well as flexion combined with extension in porcine models (Drake et al., 2005). The impact of repetitive lifting in these loading conditions exhibited a decrease in disc stiffness in compression (Gordon et al., 1991, Amin, 2019a), flexion, and lateral shear with

an increase in extension while causing an increase in disc phase angle in compression, left axial rotation, and posterior shear with a decrease in extension (Amin, 2019a). These results were also accompanied by an increase in energy loss (Gordon et al., 1991) and internal strain within the disc (Amin et al., 2019b). However, the stiffness of flexion-extension combined showed no change, while an increase in hysteresis was evident (Drake et al., 2005).

Previous studies have provided insights into the disc behaviour under simulated repetitive lifting, mimicking real-life scenarios. However, the mechanical responses of the FSU during prolonged durations of simulated repetitive lifting equivalent to a week (Drake et al., 2005), a year (Amin, 2019a) or more (Gordon et al., 1991)—did not consider the inter-day recovery of the disc, such as that which occurs during sleep when fluid re-equilibration takes place. The duration of disc fluid equilibrium is a significant factor that potentially affects disc height (Lu et al., 1996, Natarajan and Andersson, 1999) and stiffness (Costi et al., 2002). Therefore, using an ovine model, this study aimed to assess the mechanical influence of simulated repetitive lifting performed for 1000 cycles (Hansson et al., 1987, Zehr and Callaghan, 2023, Berger-Roscher et al., 2017), likely to occur during a working day, on the FSU stiffness and its phase angle. In addition to assessing the immediate effects of repetitive lifting, the study aimed to evaluate the outcomes after 7 hours, a recovery period considered adequate for the disc to reach a state of fluid equilibrium (Costi et al., 2002). It is hypothesised that FSU 6DOF stiffness will increase while the phase angle decreases immediately following the lifting. This hypothesis is based on the disc experiencing compression and fluid extrusion during repetitive loading, which leads to reduced height and internal pressure, thereby decreasing stiffness and increasing the phase angle. However, after a recovery period, these mechanical properties will return to their baseline values, with stiffness increasing and the phase angle decreasing as fluid re-equilibration occurs, restoring the disc's height, internal pressure, and viscoelastic behaviour.

4.3 Materials and Methods

The procedures used in this section share similarities with those described in Chapter 3, with a brief reiteration and cross-referencing to the related sections in Chapter 3 for more details. While Chapter 3 provides comprehensive details on the tools and methods used, this section offers a concise overview, emphasising the key steps and sequence during the mechanical testing day. Additionally, this section differentiates itself by including details on the data analysis methods used for analysing the results presented in the subsequent section of this chapter.

4.3.1 FSU Preparation

Twenty mature ovine lumbar spines, aged between 3 and 5 years, were obtained from the South Australian Health and Medical Research Institute (SAHMRI). The spines were frozen within 30-60 minutes post-mortem according to SAHMRI protocols. They were packed in plastic bags with labels and delivered in insulated foam containers with ice packs to the laboratory of this study in a frozen state, where they were immediately stored at -20°C. Ovine spines were selected for their anatomical and mechanical similarities to those of humans (Wilke et al., 1997, Fazzalari et al., 2001a, Veres et al., 2008). Prior to mechanical testing, FSUs were prepared (**Section 3.2**); briefly, the spines were thawed at room temperature and dissected to isolate the L4-L5 level FSUs. During the dissection, soft tissues were removed, and vertebrae were sectioned in alignment with the disc's mid-transverse plane, ensuring all ligaments remained intact and the FSUs were then re-frozen until the scheduled day of mechanical testing. On the day of mechanical testing, a vernier calliper was used to measure the widths of the discs' lateral (LAT) and anterior-posterior (AP) dimensions at the outer regions of the vertebrae that correspond to the disc. The measurements taken at the superior and inferior sides of each FSU aimed to calculate the disc area for determining the magnitude of compressive load to be applied. Each measurement was conducted three times for every FSU to ensure precision, and the average values were taken. The vertebrae were then potted in

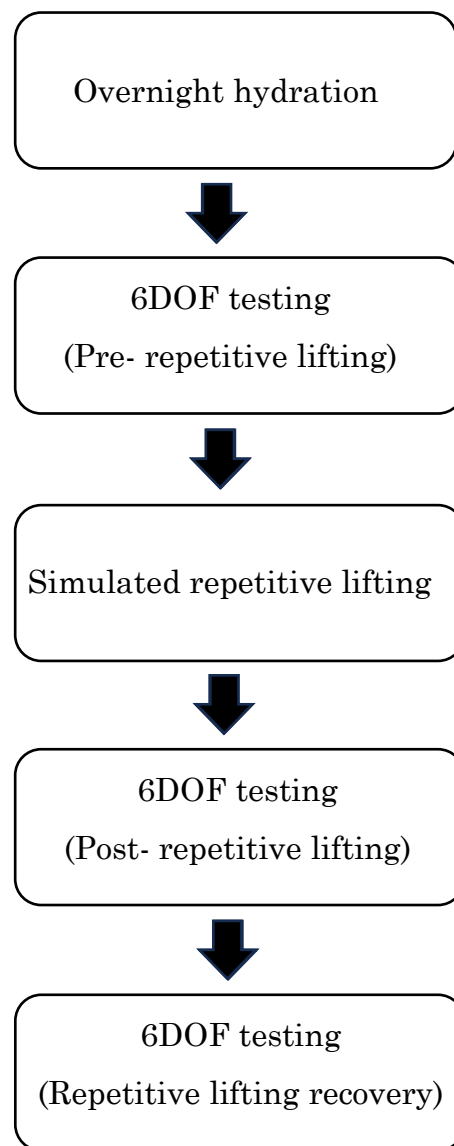
metal cups using polymethyl methacrylate (PMMA), aided by an alignment rig to ensure parallel alignment with the disc's mid-transverse plane. The instantaneous axis of rotation for the disc (Pearcy and Bogduk, 1988) was measured with a vernier calliper relative to the cups. These cups served as the rotation centre for the mechanical testing, which was conducted using a custom-developed 6DOF hexapod robot (Ding et al., 2014, Lawless et al., 2014) (Section 3.4.1). Once potting was completed radiographs were taken to determine disc height to properly position the FSU within the hexapod. Additionally, Throughout preparation, the FSU discs were regularly hydrated with saline spray and wrapped in paper towels moistened with saline to maintain their moisture and integrity.

4.3.2 Mechanical Testing

Before embarking on mechanical testing, it was necessary to mimic the *in vivo* physiological state of disc hydration and pressure. Therefore, each potted FSU was securely installed into the hexapod, wherein each FSU disc was soaked overnight in a 0.15 M phosphate-buffered saline (PBS) solution and preloaded in compression to a level that produced 0.1 MPa intradiscal pressure, simulating the unloading condition during sleep (Wilke et al., 1999b). Intradiscal pressure was determined by considering the linear relationship between the applied compressive stress on the FSU and the resultant increase in nucleus pressure, with the latter being approximately 1.5 times greater. (Edwards et al., 2001). This assessment required calculating the disc area with the formula $0.84 \times \text{LAT} \times \text{AP}$, using the lateral (LAT) and anterior-posterior (AP) widths previously measured (Nachemson and Morris, 1964). For mechanical testing (Figure 4.1), each FSU first underwent 6DOF mechanical assessment at 0.1 Hz, reflecting activity such as during office work (Costi et al., 2008a). The testing protocol was designed to minimise the disc's biphasic behaviour by reducing fluid flow through the use of a specific loading sequence. The sequence began with shear and axial rotation, proceeded to lateral bending, then to flexion and extension, and concluded with compression. Imposed displacements were ± 0.6 mm for shear and rotations of $\pm 3^\circ$ for axial rotation, $\pm 4^\circ$

for lateral bending, and $\pm 3^\circ$ for flexion-extension, with final compression creating 0.6 MPa intradiscal pressure (Costi et al., 2008a, Amin et al., 2016a). Except for compression, which was driven by load control, each DOF underwent five haversine testing cycles using a hybrid control mode. The hybrid mode conducted the testing using position control while minimising off-axis coupling forces and moments to zero through load control. A ten-minute recovery period under a 0.1 MPa compressive load followed each DOF test. Following the 6DOF mechanical testing, each FSU underwent a simulated repetitive lifting simulation characterised by applying a combined compression of 1.1 MPa, equivalent to lifting an intermediate weight of 20 kg within safe manual handling limits (Cooper, 2018, Wilke et al., 1999a) and a 13° flexion (Pearcy and Tibrewal, 1984, Adams and Hutton, 1983, Stokes and Frymoyer, 1987) for 1000 cycles (Hansson et al., 1987, Zehr and Callaghan, 2023, Berger-Roscher et al., 2017), which could potentially be achieved in a working day. The simulated repetitive lifting was performed at a 1 Hz frequency (Callaghan and McGill, 2001, Drake et al., 2005, Amin, 2019a) with a haversine waveform. A final 6DOF test was then conducted to assess disc recovery from repetitive lifting after 7 hours, representative of rest or sleep (Section 3.4).

Figure 4.1 An overview of the mechanical testing sequence for FSU. The sequence comprises an overnight hydration period, followed by 6DOF mechanical testing before (pre-) and after (post-) simulating repetitive lifting. A final 6DOF test was conducted to assess disc recovery from repetitive lifting after 7 hours, representative of rest or sleep.



4.3.3 Data Analysis

A first-order polynomial was fitted to the load-displacement data from the final cycle for each DOF using the POLYFIT.m function in MATLAB (R2018b, The Mathworks Inc.). Stiffness was then calculated by taking the derivative of the fitted polynomial, effectively deriving it from the slope of the loading portion through linear regression. Stiffness was calculated with ranges from 0.3–0.58 mm for shear, 3.5°–4.9° for flexion, 1.5°–2.9° for lateral bending, 1.25°–1.85° for extension, 1°–1.9° for axial rotation, to 0.75–1.7 MPa for compression. These ranges were selected to capture the linear portion of the loading segment of the load-displacement curve, thus ensuring that stiffness values are reliable and

consistent, and not influenced by the initial and final non-linear regions of the loading segment (Amin et al., 2016b). Phase angle, an indicator of viscoelastic behaviour that represents the time lag between the magnitudes of applied load and resultant displacement, was determined over the last four cycles using MATLAB's CPSD function (Section 3.4.3).

The General Linear Model (GLM) with repeated measures ANOVA (RM-ANOVA), as implemented in IBM SPSS Statistics (version 25.0.0.2), was employed to analyse stiffness and phase angle. Separate RM-ANOVAs were conducted for each DOF in all loading directions for both stiffness and phase angle measures. The measures during stages before (pre-), after (post-), and following repetitive lifting recovery were treated as within-subject factors in the model, specifically including comparisons of stiffness and phase angle after (post-) repetitive lifting and following repetitive lifting recovery, with pre-repetitive lifting serving as the baseline to identify any significant changes. A significance threshold was set at an alpha level of 0.05. Post-hoc pairwise comparisons between the three stages for both stiffness and phase angle variables were performed, and the p-values were adjusted using the Bonferroni correction method to control for multiple comparisons.

4.4 Results

Twenty FSUs successfully underwent mechanical testing. However, one 6DOF test following repetitive lifting was excluded due to testing errors related to improper data output. Additionally, noisy signals at the last loading cycle led to the omission of one compression stiffness measurement before and two after repetitive lifting. Furthermore, IBM SPSS Statistics (version 25.0.0.2) analysis using the 'EXAMINE' command identified outliers in the compression phase angle measurements: two before repetitive lifting, one after repetitive lifting, and another following the recovery period (Appendix A).

Load-displacement curves across all loading directions before repetitive lifting, after repetitive lifting, and following the recovery period exhibited comparable mechanical characteristics (Figure 4.2 and Figure 4.3). Yet, a noticeable

variation in flexion response was observed when comparing post-repetitive lifting and repetitive lifting recovery to the pre-repetitive lifting baseline (**Figure 4.3**).

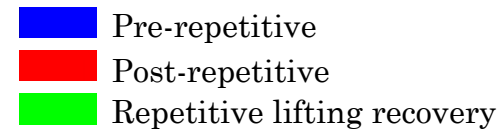
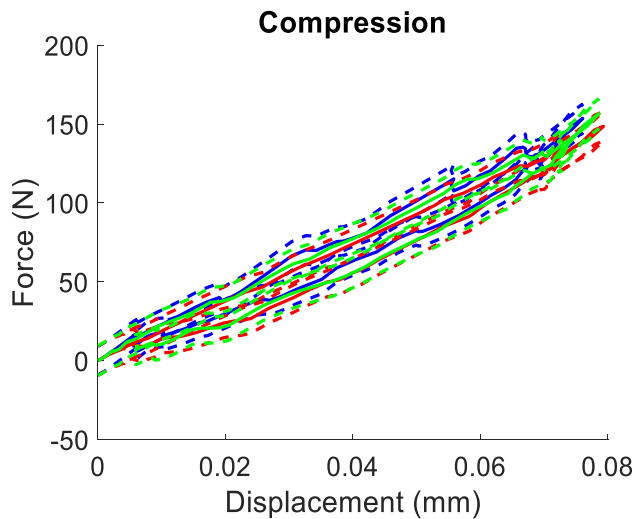
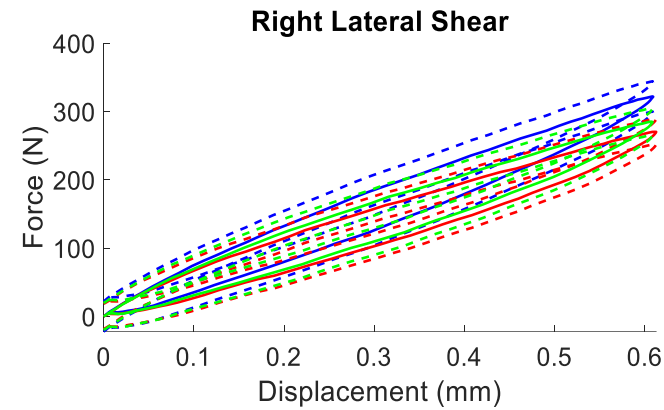
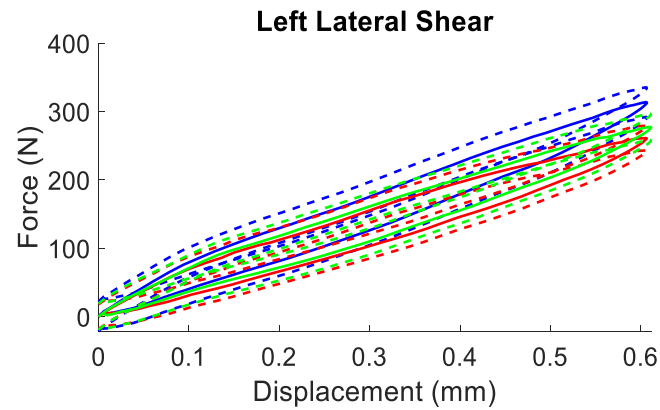
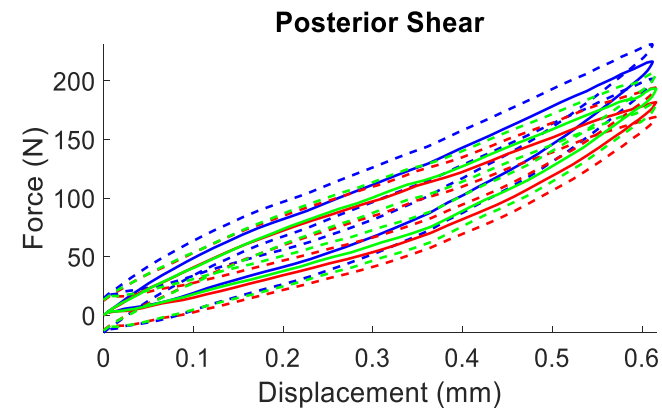
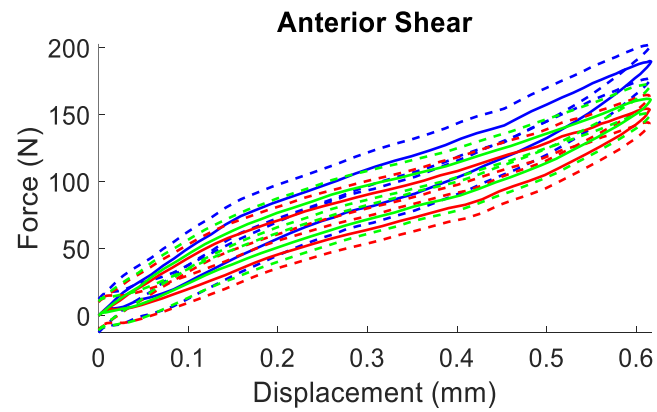


Figure 4.2 Load-displacement curves for averaged shear (pre-repetitive lifting, N=20; post-repetitive lifting, N=19; repetitive lifting recovery, N=20) and compression (pre-repetitive lifting, N=19; post-repetitive lifting, N=17; repetitive lifting recovery, N=20) loading during pre-repetitive lifting (blue), post-repetitive lifting (red), and repetitive lifting recovery (green). Dotted lines indicate the 95% confidence interval (CI).

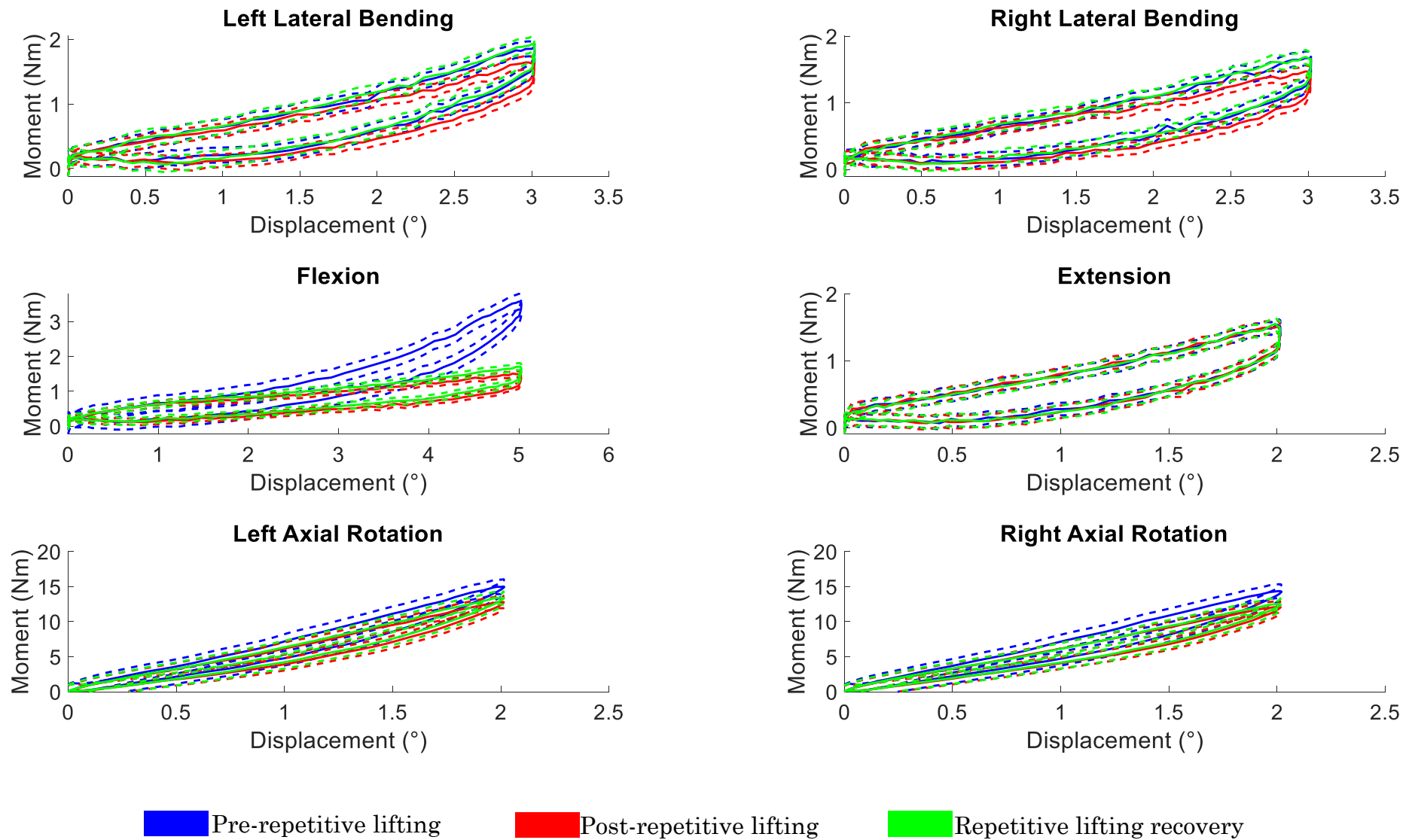


Figure 4.3 Load-displacement curves for all rotational loading directions before (pre-) repetitive lifting (blue, N=20), after (post-) repetitive lifting (red, N=19), and following recovery from repetitive lifting (green, N=20). The dotted lines represent the 95% confidence interval (CI).

4.4.1 Stiffness and Phase Angle

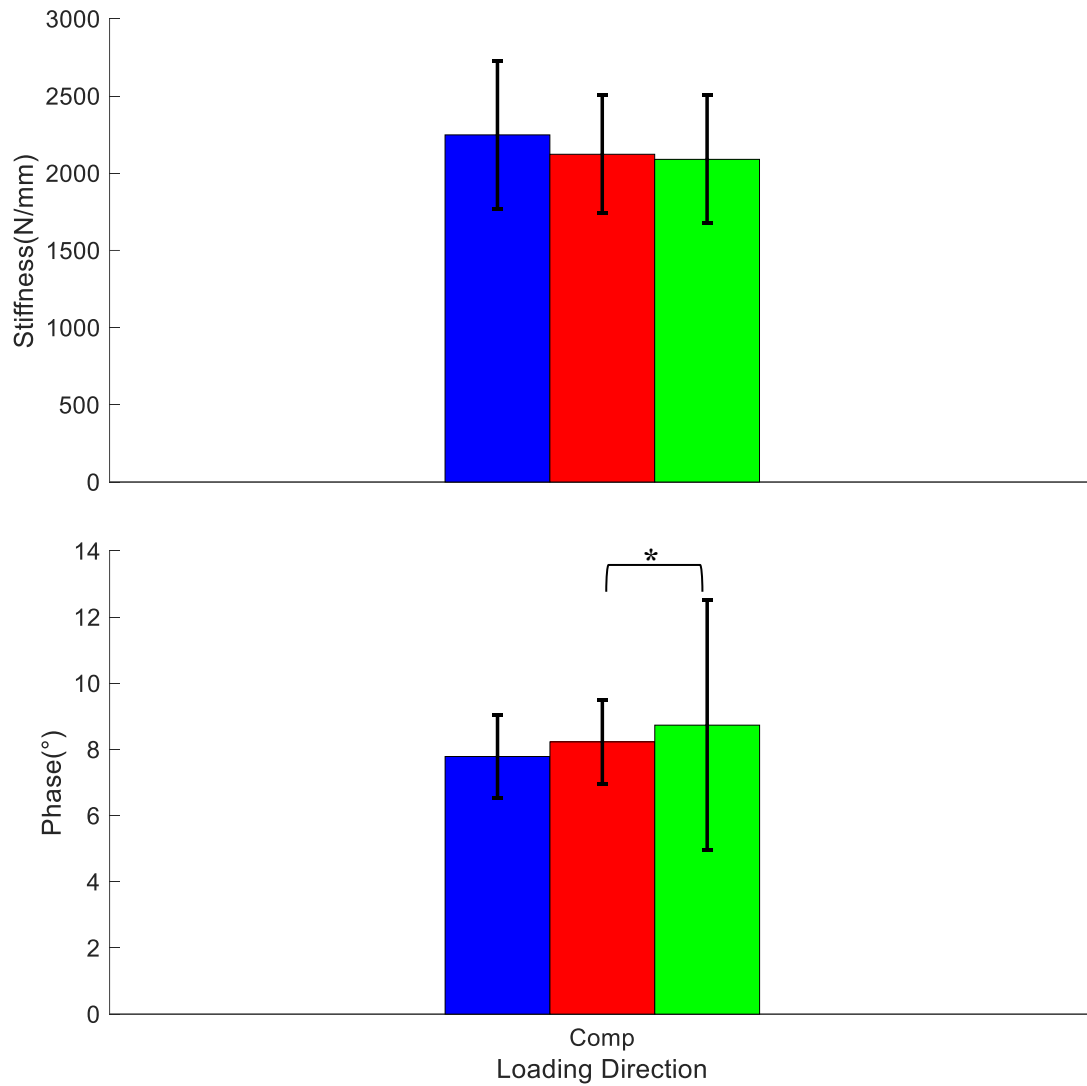
This section provides a thorough overview of the analysis, presenting the initial data prior to refining it by applying a conservative threshold that considers only changes of 25% or more as significant. The discussion section of this chapter elaborates on the rationale behind this threshold, where the refined data is analysed after its application.

4.4.1.1 Translational and Shear DOFs

Most translational and shear directions were significantly affected immediately after repetitive lifting ($p < 0.05$), with a decrease in stiffness (18.3% - 23.9%) and an increase in phase angle (10.6% - 14.2%), except for compression. Compression showed a relatively minor stiffness decrease (4.9%) and phase angle increase (5.7%), which were not significant ($P = 0.738$ and $P = 0.873$, respectively). Following the recovery period, similar significant decreases in stiffness ($p < 0.05$) (13.5% - 21.9%) and increases in phase angle ($p < 0.05$) (13.5% - 21.9%) were observed in most directions, except for compression ($p < 0.05$), which exhibited a relatively minor stiffness decrease (8.4%) and phase angle increase (7.5%) ($P = 0.282$ and $P = 0.540$, respectively). However, fewer directions experienced an increase in phase angle compared to the immediate state after repetitive lifting, particularly only posterior shear maintained a significant increase ($P < 0.001$, 10.6%) in phase angle (**Table 4-1**) (**Figure 4.4** and **Figure 4.5**).

Table 4-1 Percent differences (%) and p-values (P) for averaged changes in stiffness and phase angle after (post-) repetitive lifting and following repetitive lifting recovery compared to the condition before (pre-) repetitive lifting across different directions: compression (Comp), right lateral shear (RLS), left lateral shear (LLS), anterior shear (AS), and posterior shear (PS). Significance values ($P < 0.05$) are in bold and underlined.

DOF	Post- repetitive lifting				Repetitive lifting recovery			
	Stiffness		Phase		Stiffness		Phase	
	(%)	P	(%)	P	(%)	P	(%)	P
Comp	-4.9	0.738	5.7	0.873	-8.4	0.282	-7.5	0.540
AS	-22.7	<0.001	10.6	0.008	-21.9	<0.001	2.2	>0.999
PS	-19.3	<0.001	14.2	<0.001	-15.5	<0.001	10.6	<0.001
RLS	-18.3	<0.001	13.1	0.230	-13.5	0.005	7.0	0.973
LLS	-23.9	<0.001	13.4	0.005	-16.6	0.007	7.7	0.275



■ Pre-repetitive lifting
 ■ Post-repetitive
 ■ Repetitive lifting recovery

Figure 4.4 Averaged stiffness (N/mm) and phase angle (°), each with their corresponding 95% confidence intervals in compression (Comp). For stiffness, the data represents states before (pre-) repetitive lifting (blue, N=19), after (post-) repetitive lifting (red, N=17), and following recovery period (green, N=20). Similarly, for phase angle, the data is labelled for states before (pre-) repetitive lifting (blue, N=18), after (post-) repetitive lifting (red, N=18), and following recovery period (green, N=20). Error bars indicate the range of the 95% confidence interval, and an asterisk (*) denotes significance ($p < 0.05$).

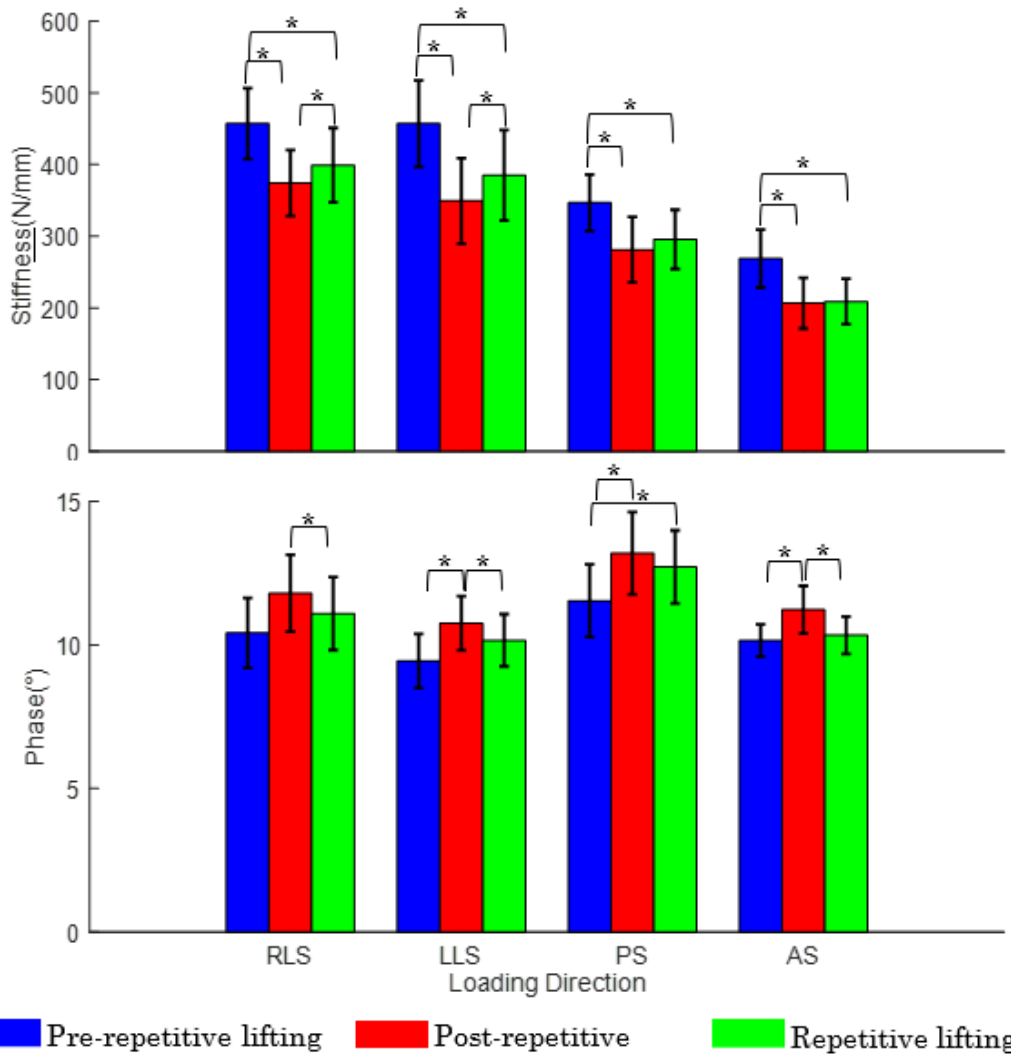


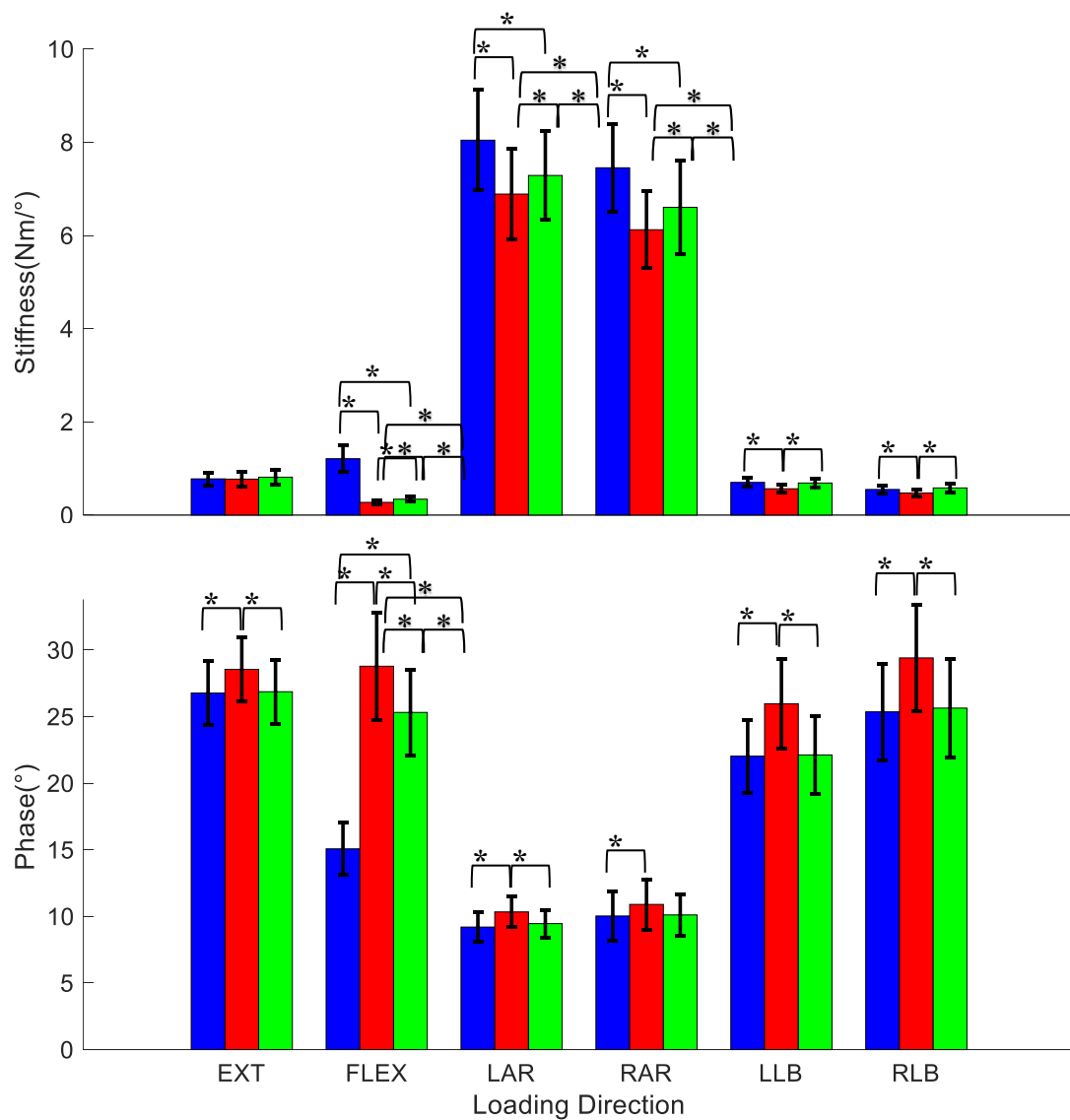
Figure 4.5 Average stiffness and phase angle with a 95% CI for pre-repetitive lifting (N=20), post-repetitive lifting (N=19), and repetitive lifting recovery (N=20) in shear directions: right and left lateral shear (RLS, LLS, respectively), anterior shear (AS), and posterior shear (PS). * Denotes significance (p<0.05).

4.4.1.2 Rotational and Bending DOFs

Immediately after repetitive lifting, the most significant changes across all rotational and bending directions were observed in flexion, with a decrease in stiffness (77.2%, $p < 0.001$) and an increase in phase angle (89.0%, $p < 0.001$). Similarly, after recovery from repetitive lifting, flexion showed a decrease in stiffness (71.2%, $p < 0.001$) and an increase in phase angle (63.8%, $p < 0.001$). Apart from extension, significant changes were observed immediately after repetitive lifting across all directions of axial rotation and lateral bending ($p < 0.05$), with decreases in stiffness (12.9% - 20.1%) and increases in phase angle (7.4% - 18.5%). However, after the recovery period, fewer directions maintained similar changes (**Table 4-2** and **Figure 4.6**).

Table 4-2 Percent differences (%) and p-values (P) for averaged changes in stiffness and phase angle after (post-) repetitive lifting and following repetitive lifting recovery compared to the condition before (pre-) repetitive lifting across different directions: extension (EXT), flexion (FLEX), left axial rotation (LAR), right axial rotation (RAR), left lateral bending (LLB), and right lateral bending (RLB). Significance values ($P < 0.05$) are in bold and underlined.

DOF	Post- repetitive lifting				Repetitive lifting recovery			
	Stiffness		Phase		Stiffness		Phase	
	(%)	P	(%)	P	(%)	P	(%)	P
EXT	1.3	>0.999	7.1	<u>0.028</u>	9.1	0.532	-0.6	>0.999
FLEX	77.2	<u><0.001</u>	89	<u><0.001</u>	71.2	<u><0.001</u>	63.8	<u><0.001</u>
LAR	12.9	<u><0.001</u>	10.7	<u>0.001</u>	-9.3	<u>0.001</u>	1.6	>0.999
RAR	16.1	<u><0.001</u>	7.4	<u>0.009</u>	12.5	<u>0.004</u>	0.9	>0.999
LLB	20.1	<u>0.001</u>	18.5	<u><0.001</u>	-1.2	>0.999	0.2	>0.999
RLB	-14	<u>0.038</u>	16.7	<u><0.001</u>	6.7	0.964	1.4	>0.999



■ Pre-repetitive lifting
 ■ Post-repetitive
 ■ Repetitive lifting recovery

Figure 4.6 Average stiffness and phase angle with a 95% CI for pre- repetitive lifting (N=20), post- repetitive lifting (N=19), and repetitive lifting recovery (N=20) of all rotational directions including extension (EXT), flexion (FLEX), left and right axial rotation (LAR, RAR), along with left and right lateral bending (LLB, RLB). Significant findings are marked with an asterisk (*), indicating $p < 0.05$.

4.5 Discussion

This study investigated the effects of simulated repetitive lifting on the 6DOF stiffness and phase angle of ovine FSUs, assessing these parameters immediately after the lifting and following a recovery period. When interpreting such statistically significant changes, it was imperative to evaluate the biomechanical implications by considering the statistical significance of the observed changes and their practical significance within the context of biological variability and the potential for systematic error in experimental measurements. Previous research suggested that approximately 20% of the systematic variation in FSU mechanical properties could be accounted for by factors such as biological variation, potting medium and experimental techniques (Amin et al., 2016a). Consequently, a conservative threshold has been adopted in this study, considering changes below a 25% difference as potentially within the margin attributable to inherent variability and systematic error in the laboratory setting. Subsequent analysis aimed to focus on changes in stiffness and phase angle that met or surpassed the 25% threshold. Moreover, in making comparisons with previous studies, this study aimed to concentrate on findings that exhibited changes exceeding this threshold, ensuring a consistent and rigorous comparison of significant biomechanical alterations. This approach enhances the robustness of the findings and, however, reduces type I errors (false positives).

It was hypothesised that FSU 6DOF stiffness would increase while the phase angle decreases immediately following the lifting. However, after a recovery period, these mechanical properties were hypothesised to return to their baseline values, with stiffness increasing and the phase angle decreasing as fluid re-equilibration was expected. The results, however, showed a differential response in stiffness and phase angle across different DOFs after repetitive lifting and following recovery. Stiffness significantly decreased after repetitive lifting in all directions, except for extension and compression, while it did not recover to pre-lifting levels for most directions, with the exceptions of extension, lateral bending, and compression. Yet, the phase angle increased significantly after

repetitive lifting for all directions except for compression and right lateral shear. Similar to stiffness, phase angle did not return to its pre-lifting level for most directions apart from compression, anterior shear, and right lateral shear.

Accordingly, immediately following repetitive lifting, a significant biomechanical impact was evidenced in flexion, with a decrease in stiffness by 77.2% and an increase in phase angle by 89% when compared to the pre-repetitive lifting baseline measurements. This decrease in flexion stiffness closely aligned with an approximately 66% reduction in stiffness observed in human FSUs, although it did not accompany any change in phase angle (Amin, 2019a). Such a decrease in stiffness might be attributed to the deformation of the anterior annulus (Amin, 2019a) and was consistent with the expanded range of motion in flexion in the lumbar spine during repetitive lifting (Mehta et al., 2014, Dolan and Adams, 1998). This decrease in flexion stiffness differed from the result of a previous study, where repetitive lifting applied to porcine FSUs increased flexion-extension stiffness while increasing hysteresis (Drake et al., 2005).

It is important to note that while hysteresis and phase angle describe different aspects of viscoelastic behaviour, they both similarly reflect changes in the viscoelastic properties of the material (Section 2.4.1). For instance, an increase in either hysteresis or phase angle indicates greater energy dissipation and a more dominant viscous component in the disc's response. In this context, the increase in phase angle observed in the current study is consistent with the increase in hysteresis observed by Drake et al. (2005) in that they both indicate altered viscoelastic properties and a shift towards a more viscous response of the disc.

This study, for the first time, also incorporated a substantial recovery period (Costi et al., 2002, Bezci et al., 2015) following repetitive lifting to mimic fluid re-equilibration in a real-life scenario after repetitive lifting. Upon recovery, there was a persistent reduction in flexion stiffness by 71.2%, and an elevated phase angle by 63.8% underlined the enduring biomechanical alterations to the disc tissue. The alterations significantly exceeded the 25% threshold set for

substantial biomechanical change, suggesting that the recovery state, even with a steady state of fluid equilibrium, was not entirely sufficient to reverse the damage from repetitive lifting. Since the testing protocol replicated the human lumbar FSU's flexion limit of 13° (Pearcy and Tibrewal, 1984, Pearcy, 1985), it could be inferred that disc damage resulted from the extreme flexion angle, particularly under the strain of 1000 cycles of repetitive loading.

The changes in stiffness and phase angle observed in this study have important biomechanical and occupational implications. As stiffness is a key measure of the disc's ability to bear loads and resist deformation, a decrease in stiffness, particularly in flexion, indicates a diminished capacity for structural support after repetitive lifting. This reduction could compromise FSU stability, which may increase the risk of disc injury, especially in occupations involving repetitive lifting. In contrast, the phase angle, which reflects the disc's behaviour in balancing both elastic energy storage and viscous dissipation, was found to increase in this study. The shift towards greater energy dissipation suggests microstructural damage within the disc tissues. Over time, this altered behaviour can reduce the disc's ability to recover, contributing to cumulative disc fatigue and potentially leading to more severe degenerative changes.

The lasting effects on the FSU's flexion, despite rest and recovery periods, could be inferred as microstructural alterations within the disc tissues, which significantly altered the disc's viscoelastic properties, leading to reduced stiffness and an increased phase angle. Such alterations might be associated with increased internal strain (Amin et al., 2019b) and disc injury caused by repetitive lifting in previous studies (Callaghan and McGill, 2001, Drake et al., 2005, Adams and Hutton, 1985, Wilke et al., 2016, Amin et al., 2020). They might also be contextualised within the continuum of disc distortion stages ranging from lamellar to annular rupture (Adams and Hutton, 1985). In contrast, other bending directions, such as left and right lateral bending, stiffness and phase angle returned to baseline levels post-recovery. This is likely because lateral bending does not exert as much stress on the lateral annulus fibrosus as flexion does on the anterior annulus. Flexion involves high stress on

the anterior annulus due to the FSU's extreme flexion angle while the high strain of compressive repetitive loading is applied. Therefore, the more evenly distributed load in lateral bending facilitates more efficient recovery.

In occupational scenarios, breaks are typically short and intermittent during the workday and unlikely to amount to 3 hours in total, the minimum duration that literature indicates is required for the disc to reach a steady state when hydrated (Costi et al., 2002, Bezci et al., 2015) . The current study findings, which are based on a 7-hour recovery period representing typical overnight sleep, focus on an effective break rather than shorter breaks during the workday. The study's findings suggest that even with a full rest equivalent to sleep, the disc may not fully recover from the mechanical changes induced by such repetitive lifting. These findings call into question the current occupational health guidelines that recommend rest breaks and adequate recovery periods during work to prevent spinal disorders and whether the emphasis of these guidelines ought to be on proper lifting techniques, reducing the number of lifts, and interventions such as mechanical lifting aids and supportive equipment, to reduce the mechanical load exerted on the spine.

While animal FSUs were carefully selected for their anatomical and mechanical similarities to human counterparts, it was crucial to recognise and account for inherent interspecies differences, which potentially contributed to the divergent results between these findings and previous ones. The ovine FSUs in the present study inherently differed from the porcine FSUs (Drake et al., 2005), and both, in turn, varied from the human FSUs (Amin, 2019a). Moreover, additional variability was introduced by the different loading protocols used in simulating repetitive lifting, such as combining flexion with extension (Drake et al., 2005) or compression with axial rotation (Amin, 2019a), in contrast to the present study, which applied compression combined with flexion. Furthermore, these variations in species and loading protocols might explain the diverse impacts of repetitive lifting observed in the latter study (Amin, 2019a), with mechanical changes found in compression, extension, left axial rotation, and lateral shear directions, in addition to flexion. However, the 6DOF mechanical testing of the current

study did not find such an impact. A critical methodological distinction to consider in the previous study was that half of the FSUs (N=6) were previously employed in measuring internal disc strain, during which grids were inserted into the discs using an 18G needle. This prior modification, while demonstrating no statistically significant effects on the disc mechanics and offering valuable insights into internal disc strain, introduced an additional variable that differed from the current study, where no grid was made.

The present study simulated 1,000 cycles of repetitive lifting under combined compression and high flexion, which was possible to perform in a day's workload, offering a contrast to studies involving 6,000 (Drake et al., 2005) and 20,000 (Amin, 2019a) cycles. While these relatively high-cycle conditions provided mechanical insights into the endurance limits of disc tissues, they did not specifically address the aspect of inter-day recovery, an aspect that is crucial in real-world scenarios. The current approach, by not exceeding one-day's workload, was more reflective of typical daily activities, though it came with its limitations. In addition to the limitation associated with using ovine FSUs, the study's testing protocol applied a high flexion angle to these FSUs, potentially causing significant disc damage. This risk was especially pronounced under the combined effect of repetitive loading, equivalent to the intradiscal pressure experienced when carrying a 20 kg weight. The observed decrease in stiffness and increase in phase angle in the FSUs might be attributed to the combined effects of repetitive lifting with compression and the high flexion angle.

4.6 Conclusion

This study evaluated the biomechanical changes in 6DOF stiffness and phase angle of FSUs due to simulated repetitive lifting. The investigation revealed substantial biomechanical alterations, particularly in flexion, where stiffness significantly decreased, and phase angle increased both immediately after repetitive lifting and following a recovery period. The study offered initial insights for future studies to build upon, further exploring the impact of

repetitive lifting and investigating whether recovery duration and adequate recovery periods in workplaces can moderate these effects.

Chapter 5 Assessing the Combined Impact of Needle Injuries and Repetitive Lifting on Lumbar Disc Mechanics: Immediate and Post-Recovery Changes in 6DOF Stiffness and Phase Angle of Ovine FSUs

5.1 Abstract

Needle injuries have been linked to disc degeneration, and *in vitro* studies have contributed to the understanding of the mechanical effects of such injuries. However, these investigations have focused solely on the mechanical impacts of needle injuries on intervertebral discs without considering the combined mechanical conditions, like repetitive lifting, known to affect the intervertebral disc significantly. Individuals might continue working in repetitive lifting jobs after undergoing needle injuries, a risk highlighted by observing that subjects with such injuries, which could result in disc herniation, engaged in occupations that required repetitive lifting. This study aimed to bridge this gap by assessing the combined effects on six degrees of freedom (6DOF) mechanical stiffness and phase angle using twenty ovine functional spinal units (FSUs), previously adapted to a recovery state following simulated repetitive activities (**Chapter 4**). The FSUs were divided into control and injury groups, each of which consisted of 10 FSUs. The injury group was subjected to 25G needle injuries in the posterolateral region. As detailed in **Chapter 4**, mechanical testing was replicated in three stages: before lifting, immediately after lifting, and after a recovery period. The findings showed an impact of needle injuries immediately after repetitive lifting contralaterally, showing an increase in stiffness in right lateral bending (27.27%, $P=0.01$) despite the needle injury being inflicted on the left posterolateral side. The increase in contralateral stiffness highlighted a compensatory response of the disc to potential vulnerability at the needle injury

side, provoked immediately after repetitive lifting. However, the increase in stiffness diminished after the recovery period, which underlined the disc's capability to recover from biomechanical stress. One main benefit highlighted by these findings is the potential advantage of incorporating recovery periods in occupational scenarios to alleviate these effects.

5.2 Introduction

Low back pain (LBP) and other back disorders are significant health issues both in Australia and around the world, resulting in substantial economic costs (Hartvigsen et al., 2018, Vos et al., 2017, Davis, 2012, Penm et al., 2006). Essential treatment methods for back disorders include electrothermal therapy and the diagnostic technique of discography, which is acknowledged and accepted by professional spine societies for its effectiveness (Hunt et al., 2019, Centerville et al., 2018, Bogduk, 2004, Gilbert et al.). The use of needles is fundamental in these clinical procedures and plays a pivotal role in administering biological therapies aimed at addressing disc degeneration (Buckley et al., 2018, Cho et al., 2013, Ren et al., 2013, Tam et al., 2014, Wei et al., 2023). The effectiveness of discography has been the subject of debate due to varying insights from studies (Carragee et al., 2009, Hur et al., 2016) regarding its association with disc degeneration. Nonetheless, discography remains the primary method for identifying discogenic pain (Chen and Gao, 2023).

Insights into the effects of needle injuries on intervertebral discs have been examined using animal models. *In vivo* studies (Cunha et al., 2017, Keorochana et al., 2010, Hsieh et al., 2009, Kim et al., 2005, Masuda et al., 2006, Fazzalari et al., 2001a) revealed that needle injuries could accelerate disc degeneration over time. However, *in vitro* studies testing on functional spinal units (FSUs) showed that while needle injuries did not alter disc height in a bovine model (Michalek and Iatridis, 2012), they could disrupt the inner annulus under sudden overload in ovine FSUs (van Heeswijk et al., 2018). Several *in vitro* studies exploring the mechanical effects of needle injuries on discs using rat FSUs revealed a reduction in disc stiffness, predominantly in torsion (Torre et al., 2019) and

compression (Michalek et al., 2010b). However, these changes in rat model studies were evident when using needles that constituted 40% of the disc height, a proportion that previously recognised as significant in altering the mechanical behaviour of the discs (Elliott et al., 2008). In contrast, other *in vitro* studies using bovine FSUs with needle sizes below this threshold indicated that such injuries did not significantly impact the disc's stiffness or phase angle in movements including compression, flexion-extension, lateral bending, and torsion (Michalek and Iatridis, 2012). Nevertheless, in studies using bovine-isolated discs, additional effects of needle injuries were observed, including a decrease in dynamic modulus and an increase in creep (Korecki et al., 2008). Furthermore, in bovine annulus explants, these injuries caused varied increases and decreases in circumferential shear strain within different regions (Michalek et al., 2010a) and caused a decrease in intra-bundle shear (Vergari et al., 2017). Despite these alterations in fibre bundles, the linear strain between bundles and intra-bundle shear remained consistent (Vergari et al., 2017).

Studies examining the mechanical effects of needle injuries on intervertebral discs have focused on these injuries in isolation, often not accounting for the impact of repetitive lifting, which previous studies have shown can cause effects on the disc (Chapter 4). After needle injuries, individuals might continue to engage in occupational activities involving repetitive lifting. This potential risk was identified by noting that subjects in a 10-year cohort clinical study, which linked needle injuries to disc herniation, had lifting occupations (Carragee et al., 2009). The current study aimed to build upon the assessment of FSUs previously adapted to a recovery state following simulated repetitive lifting without any needle injury (Chapter 4). Using the same FSUs, this study randomly assigned the FSUs to either control or injury groups. Both groups would undergo a three-stage mechanical assessment: before repetitive lifting, immediately after repetitive lifting, and after a recovery period. It is hypothesised that FSUs in the injury group will exhibit a reduction in 6DOF stiffness and an increase in phase angle at all stages compared to the control group, with the greatest changes to occur immediately after the lifting. The hypothesis is based on the compromised structural integrity and increased fluid loss due to the needle disc ruptures,

which can potentially result in decreased stiffness and increased phase angle, more pronounced after the lifting as a contributing factor.

5.3 Materials and Methods

5.3.1 FSU Preparation

The FSUs used in this chapter are the same as the ones prepared and subjected to simulated repetitive lifting in **Chapter 4**. The preparation procedures, including thawing, dissection to isolate the L4-L5 FSUs, and potting in polymethyl methacrylate (PMMA), followed the protocols previously outlined. The FSUs were kept hydrated throughout the preparation process, with regular applications of saline spray and saline-moistened paper towels. Further details on the preparation steps are provided in **Chapter 4**.

5.3.2 Creation of Needle Injury

For the creation of needle injuries, the twenty FSUs were divided into two groups, control and injury, each of which consisted of 10 randomly assigned FSUs. A 25G needle with a diameter of 0.5 mm was selected to simulate the needle-to-disc height ratio seen in human discs. This choice achieved a 12.8% ratio relative to the average ovine disc height (3.9 mm), thereby closely approximating the scale used in humans. This ratio was the nearest equivalent to that in humans, where an 18G needle (1.3 mm diameter) corresponded to a 11.5% ratio against the average human disc height (11.3 mm) ([O'Connell et al., 2007](#)). Briefly, as previously detailed (**Section 3.3**), needle injuries were inflicted in the posterolateral region using a custom-designed apparatus to ensure reproducible needle insertion into the disc. The needle insertion level was set at approximately the top quarter of the disc's height with measurements taken by a calliper, and the location was chosen to avoid needle hitting the ovine concave bottom vertebra during insertion. The apparatus included a needle holder equipped with a calliper-calibrated stopper to maintain the needle's insertion depth at approximately 17 mm from the annulus edge, thereby ensuring full penetration of the annulus. Prior to insertion, each needle was marked with a

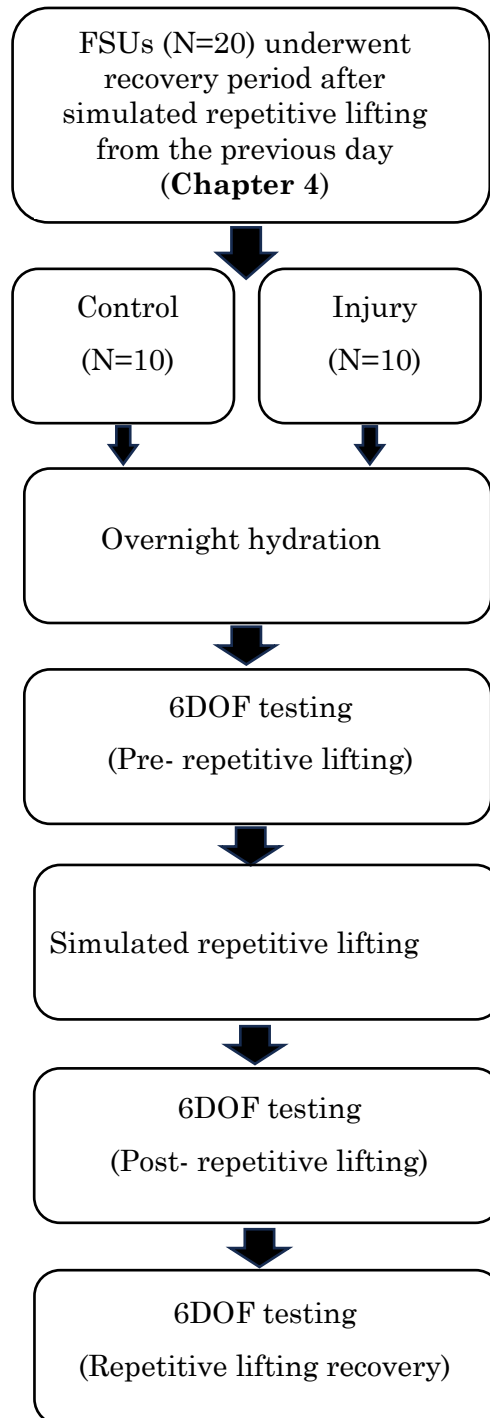
water-safe green marker (Staedtler Lumocolor 317 Permanent M), enabling tracing of the injury site during subsequent structural evaluation (**Section 3.5**) for later study (**Chapter 6**). Meanwhile, the control group of FSUs did not undergo this injury process and remained intact to provide a baseline for comparison.

5.3.3 Mechanical Testing

Mechanical testing procedures followed the protocol described in Chapter 4 (**Section 4.3.2**), with the addition of needle injuries for the injury group. The same 6DOF mechanical testing and repetitive lifting simulations were employed, except for the introduction of the needle injury procedure in the injury group.

Prior to mechanical testing, each FSU from the injury group was removed from the hexapod immediately following the recovery period after the previous day's repetitive lifting session (**Chapter 4**). The injury group FSUs then underwent needle injury creation using the injury creation apparatus (**Section 3.3**). The control group FSUs, treated to maintain consistent handling and avoid any treatment-related bias, were similarly removed from the hexapod and placed in the apparatus, but they did not undergo the needle injury procedure. Subsequently, FSUs from both groups were remounted into the hexapod to begin replicating the previous day's mechanical testing (**Figure 5.1**).

Figure 5.1 An overview of the mechanical testing sequence for each FSU, following the recovery period from the previous day's repetitive lifting. Two randomly assigned groups, 'Control' (N=10) and 'Injury' (N=10), with the 'Injury' group undergoing needle injury creation, while both groups proceeded to overnight hydration. The sequence advanced with 6DOF testing both before (pre-) and after (post-) simulated repetitive lifting, concluding with a final 6DOF test following the recovery period after the repetitive lifting.

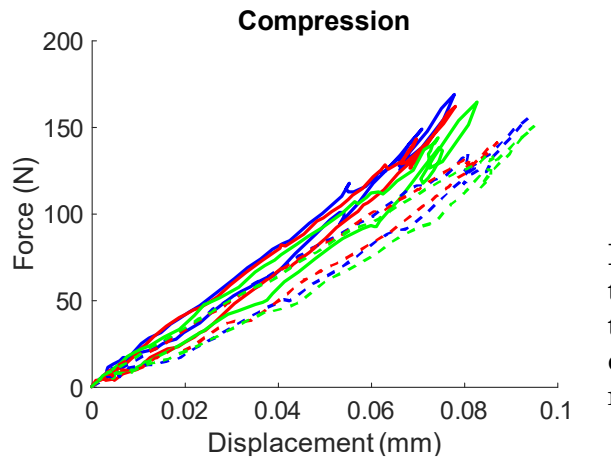
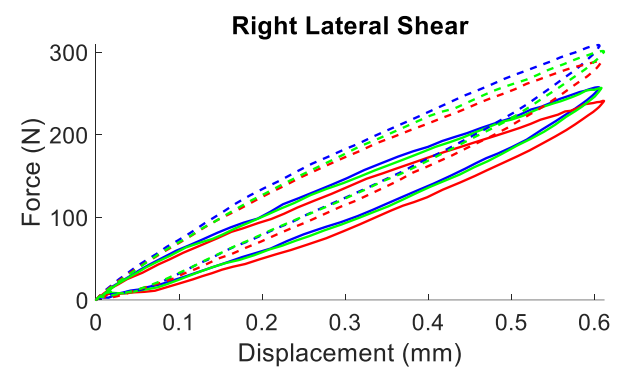
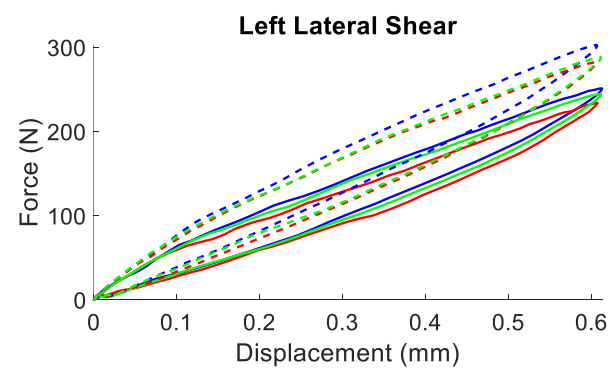
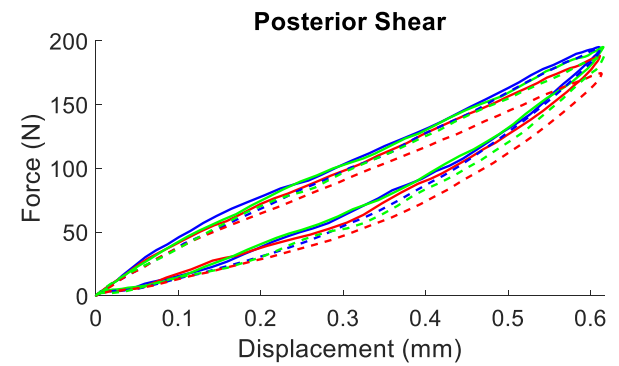
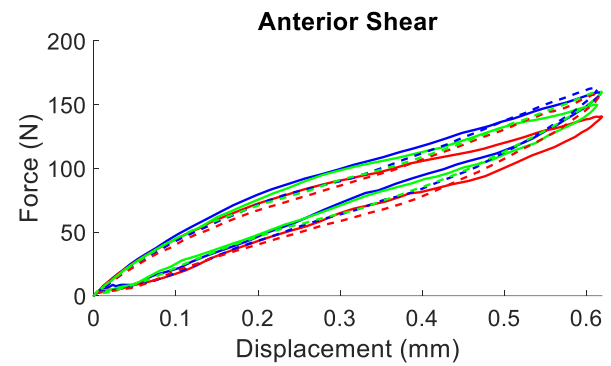


5.3.4 Data Analysis

The analysis of load-displacement curves and calculations of stiffness and phase angle were performed as previously detailed (**Chapter 4**). For the statistical analysis, separate Analyses of Covariance (ANCOVA) were conducted using IBM SPSS Statistics (version 25.0.0.2) for each DOF to investigate the effects of needle injuries on disc stiffness and phase angle. The analyses were conducted to identify significant differences in these measures between the control and injury groups across three loading conditions: before (pre-) and after (post-) repetitive lifting, as well as during the recovery phase following repetitive lifting. The ANCOVA was employed to control for baseline differences, using measurements from repetitive lifting recovery recorded on the previous day as the covariate. Post hoc analyses were conducted using the Least Significant Difference (LSD) method, with a predefined alpha level of 0.05 to determine statistical significance.

5.4 Results

The quality of data from the 6DOF mechanical tests performed on FSUs of the control and injury groups was assessed following the successful completion of the mechanical testing. Exceptions included one 6DOF test after repetitive lifting and a compression test, both in the control group. Furthermore, one phase angle compression test from the control group was excluded from each of the post-repetitive lifting and recovery stages, as it was classified as an outlier (**Appendix B.1**). The load-displacement curves, including all loading directions in both the control and injury groups, revealed similar mechanical behaviour at each mechanical stage: before (pre-) repetitive lifting, after (post-) repetitive lifting, and after repetitive lifting recovery (**Figure 5.2** and **Figure 5.3**).



Solid — Control Dashed- - - Injury

Blue — Pre-repetitive lifting

Red — Post-repetitive

Green — Repetitive lifting recovery

Figure 5.2 Load-displacement curves for averaged shear and compression tests. Solid lines represent the control group, whereas dashed lines represent the injury group. Both groups were subjected to mechanical testing at three different loading stages: before (pre-, in blue) repetitive lifting, after (post-, in red) repetitive lifting, and following repetitive lifting recovery (in green).

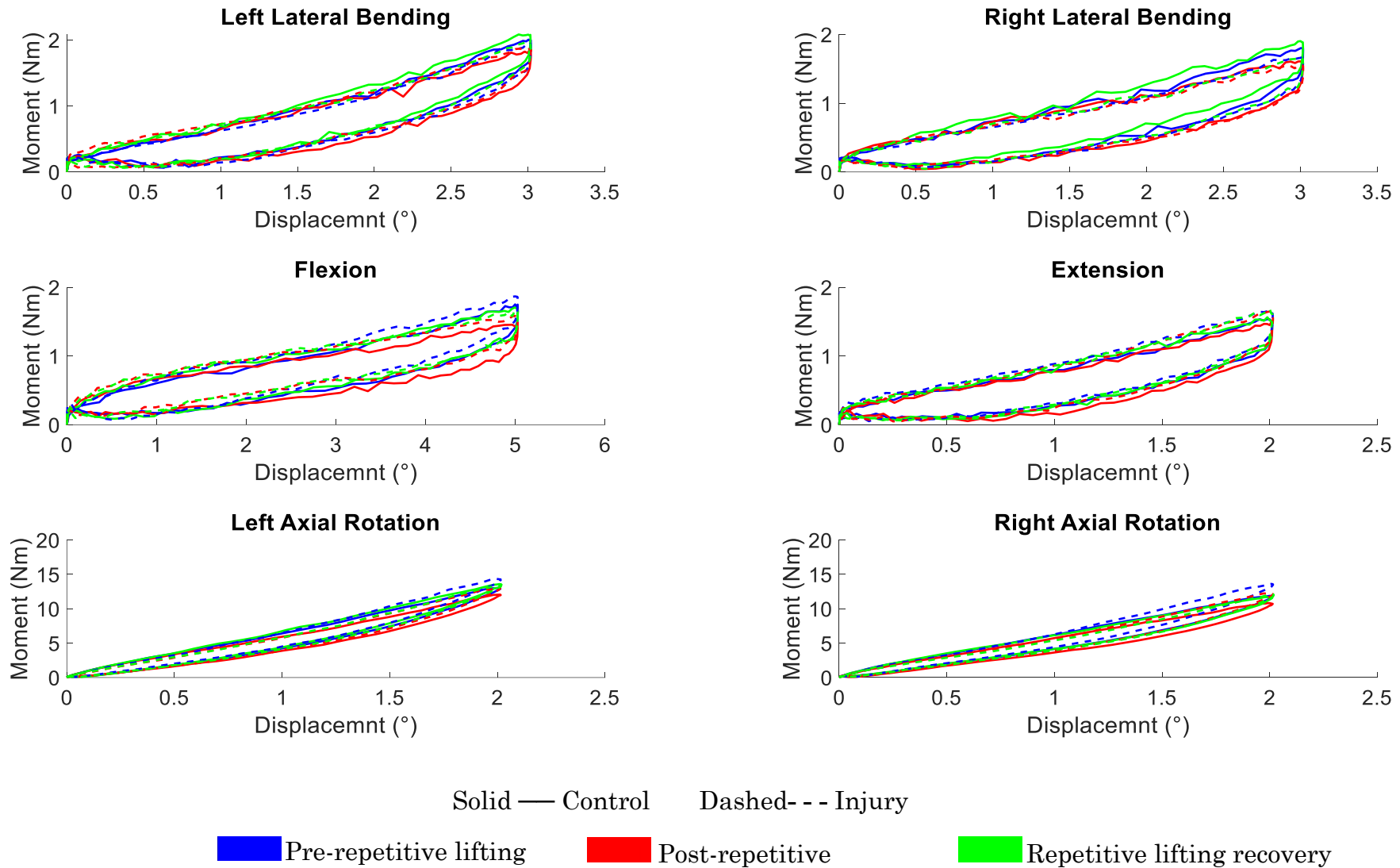


Figure 5.3 Averaged load-displacement curves for rotational loading directions. Solid lines represent the control group, whereas dashed lines represent the injury group. Both groups were subjected to mechanical testing at three different loading stages: before (pre-, in blue) repetitive lifting, after (post-, in red) repetitive lifting, and following repetitive lifting recovery (in green).

5.4.1 Stiffness and Phase Angle

This section presents a comprehensive view of the analysis, including the initial data before refining it by applying a conservative threshold that considers only changes of 25% or above as significant. Details addressing the determination of this threshold are included in the discussion section of this chapter, where the refined data is discussed after applying the threshold.

5.4.1.1 Translational and Shear DOFs

The analyses showed no significant differences ($P > 0.05$) in stiffness and phase angle across almost all loading conditions in both groups. However, an exception was observed in the injury group, with an 8.69% increase in the left lateral shear phase angle ($P = 0.02$) after repetitive lifting (**Table 5-1**, **Figure 5.4**, and **Figure 5.5**).

Table 5-1 Percent differences (%) and p-values (P) for averaged changes in stiffness and phase angle in the injury group compared to the control group across different directions: compression (Comp), right lateral shear (RLS), left lateral shear (LLS), anterior shear (AS), and posterior shear (PS). Values indicating significance ($P < 0.05$) are highlighted in bold and underlined. The table includes data from mechanical testing conducted before (pre-) repetitive, after (post-) repetitive lifting, and following repetitive lifting recovery.

DOF	Pre-repetitive lifting				Post-repetitive lifting				Repetitive lifting recovery			
	Stiffness		Phase		Stiffness		Phase		Stiffness		Phase	
	(%)	P	(%)	P	(%)	P	(%)	P	(%)	P	(%)	P
Comp	-13.0	0.260	7.43	0.325	-16.5	0.150	-1.50	0.902	-12.7	0.224	-3.66	0.640
AS	22.72	0.187	-0.48	0.914	37.4	0.112	-6.93	0.287	25.45	0.228	0.84	0.891
PS	5.29	0.555	0.08	0.988	-7.3	0.442	8.26	0.292	-0.46	0.954	5.10	0.405
RLS	1.81	0.657	0.00	0.994	1.33	0.814	0.80	0.882	-5.86	0.250	-0.09	0.985
LLS	-0.07	0.988	-0.786	0.79	-3.35	0.554	8.69	<u>0.025</u>	-3.08	0.664	5.14	0.179

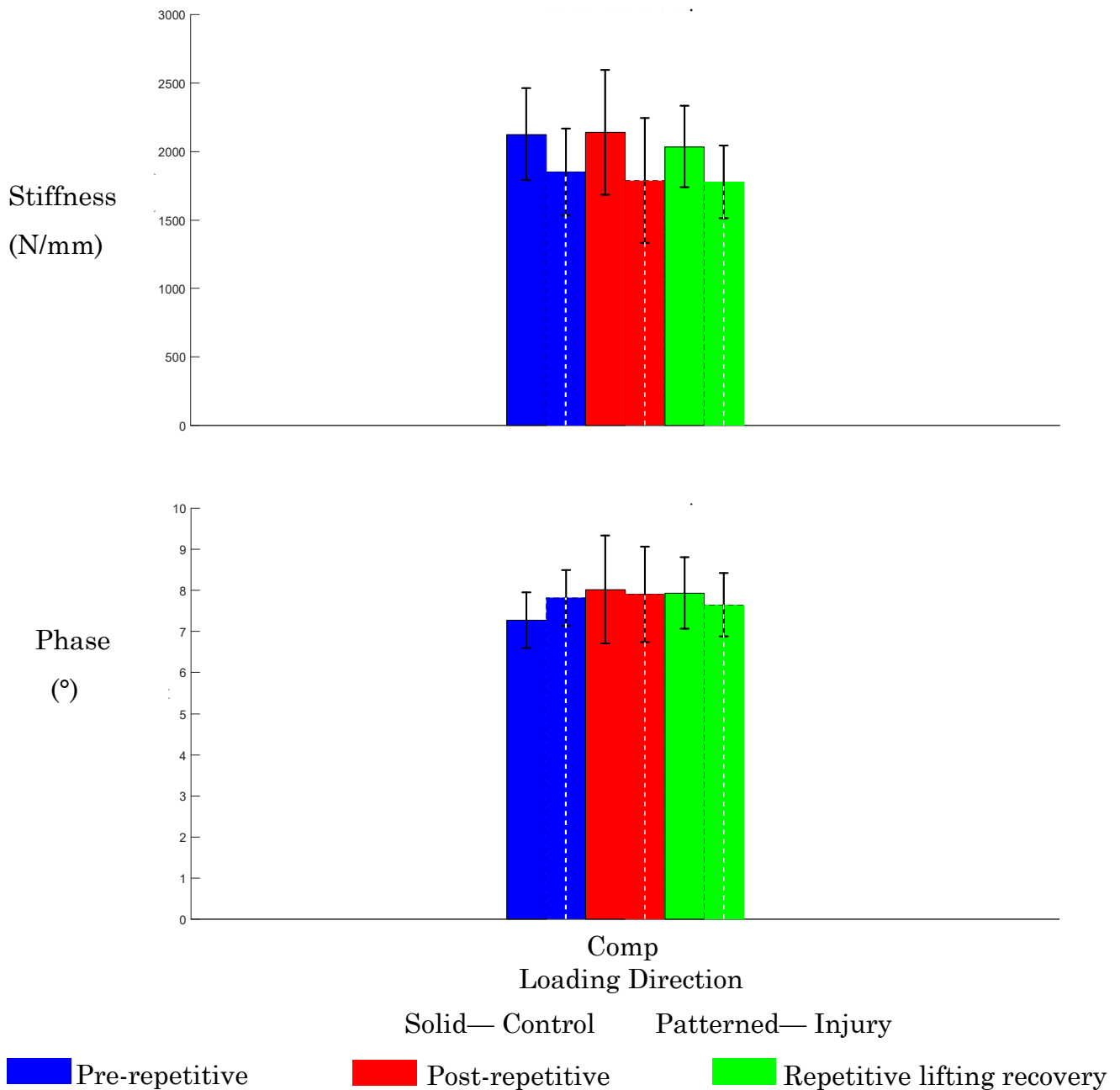


Figure 5.4 Averaged stiffness (N/mm) and phase angle (°) with a 95% CI for compression (Comp). Solid bars represent the control group, while patterned bars indicate the injury group. Both groups underwent mechanical testing at three stages: before (pre-, in blue), after (post-, in red), and following (in green) repetitive lifting. Significant findings, marked with an asterisk (*), indicate $p < 0.05$, suggesting statistical significance between the groups within each loading stage. Sample sizes: control - pre-repetitive lifting (stiffness=9, phase=9), post-repetitive lifting (stiffness=8, phase=8), recovery (stiffness=8, phase=8). Injury - consistent counts of 10 for stiffness and phase across all stages.

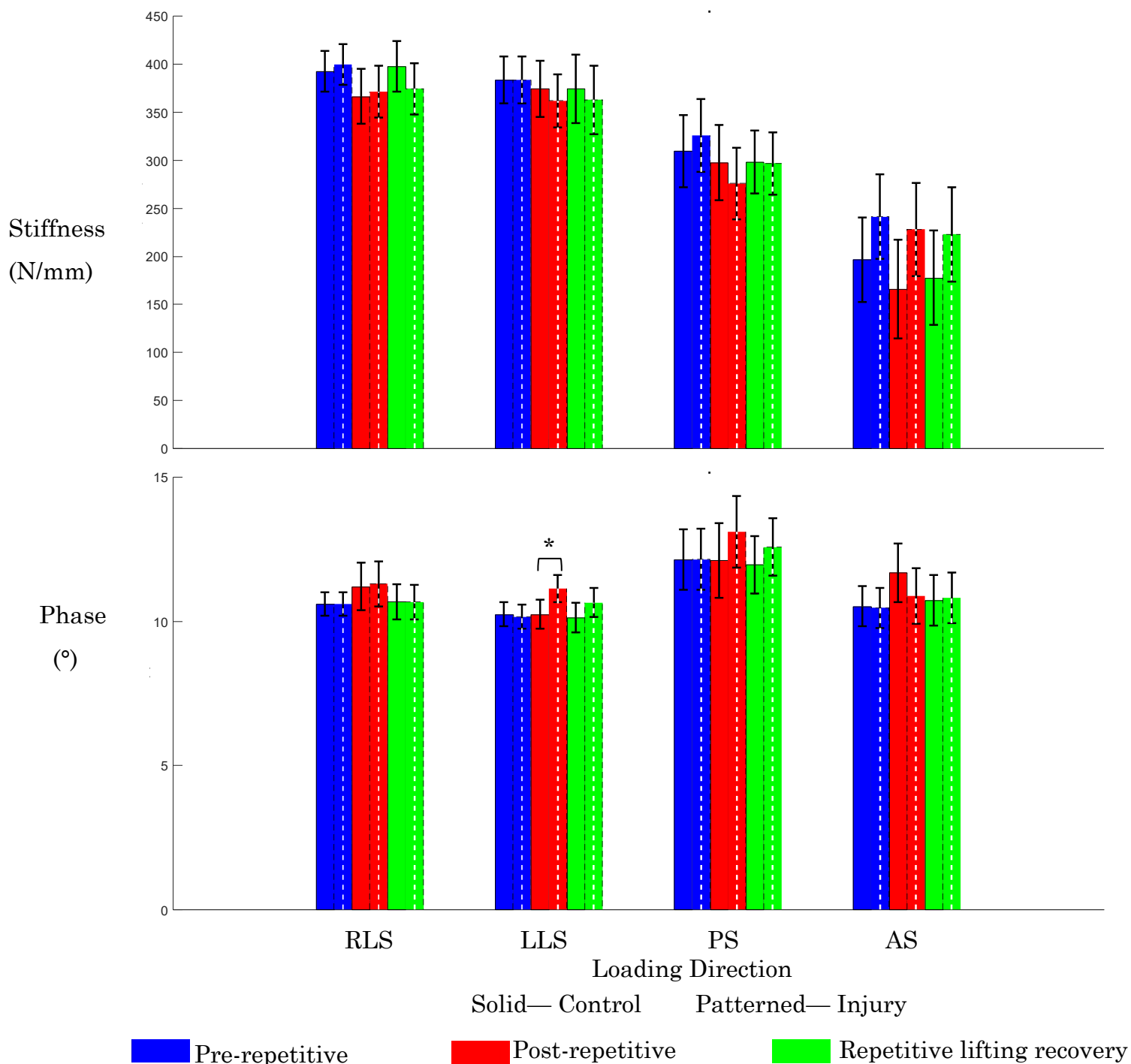


Figure 5.5 Averaged stiffness (N/mm) and phase angle (°) with a 95% CI for all shear directions, including right and left lateral shear (RLS, LLS, respectively), anterior shear (AS), and posterior shear (PS). Solid bars represent the control group, while patterned bars indicate the injury group. Both groups underwent mechanical testing at three stages: before (pre-, in blue), after (post-, in red), and following (in green) repetitive lifting. Significant findings, marked with an asterisk (*), indicate $p < 0.05$, suggesting statistical significance between the groups under all loading conditions. Sample sizes: control - pre-repetitive lifting (stiffness=10, phase=10), post-repetitive lifting (stiffness=9, phase=9), recovery (stiffness=10, phase=10). Injury - consistent counts of 10 for stiffness and phase across all stages.

5.4.1.2 Rotational and Bending DOFs

The data analysis, comparing stiffness and phase angle measurements between the control and injury groups, exhibited no significant differences ($P > 0.05$) across all three loading conditions. However, in the injury group, there were two exceptions: a 27.27% increase in stiffness ($P = 0.01$) in right lateral bending after repetitive lifting and a 10.52% decrease in phase angle ($P = 0.01$) in right axial rotation following recovery from repetitive lifting (**Table 5-2** and **Figure 5.6**).

Table 5-2 Percent differences (%) and p-values (P) for averaged changes in stiffness and phase angle in the injury group compared to the control group in extension (EXT), flexion (FLEX), left axial rotation (LAR), right axial rotation (RAR), left lateral bending (LLB), and right lateral bending (RLB). Values with significance (P < 0.05) are highlighted in bold and underlined. This comparative analysis includes mechanical testing conducted before (pre-) repetitive lifting, after (post-) repetitive lifting, and following repetitive lifting recovery.

DOF	Pre-repetitive lifting				Post-repetitive lifting				Repetitive lifting recovery			
	Stiffness		Phase		Stiffness		Phase		Stiffness		Phase	
	(%)	P	(%)	P	(%)	P	(%)	P	(%)	P	(%)	P
EXT	-7.06	0.482	-0.37	0.871	3.80	0.868	-1.42	0.759	7.89	0.477	-2.74	0.575
FLEX	2.94	0.820	-6.42	0.262	-4.17	0.795	-8.17	0.234	7.14	0.676	-0.99	0.881
LAR	0.27	0.962	-1.51	0.774	-1.42	0.803	1.50	0.823	-6.62	0.102	-4.49	0.426
RAR	3.69	0.443	0.20	0.965	3.38	0.469	0.77	0.872	-7.65	0.124	-10.52	<u>0.014</u>
LLB	14.49	0.130	-3.21	0.60	13.56	0.183	-5.66	0.33	10.45	0.275	9.38	0.06
RLB	16.36	0.058	-4.49	0.18	27.27	<u>0.013</u>	-7.48	0.06	11.54	0.375	-3.98	0.38

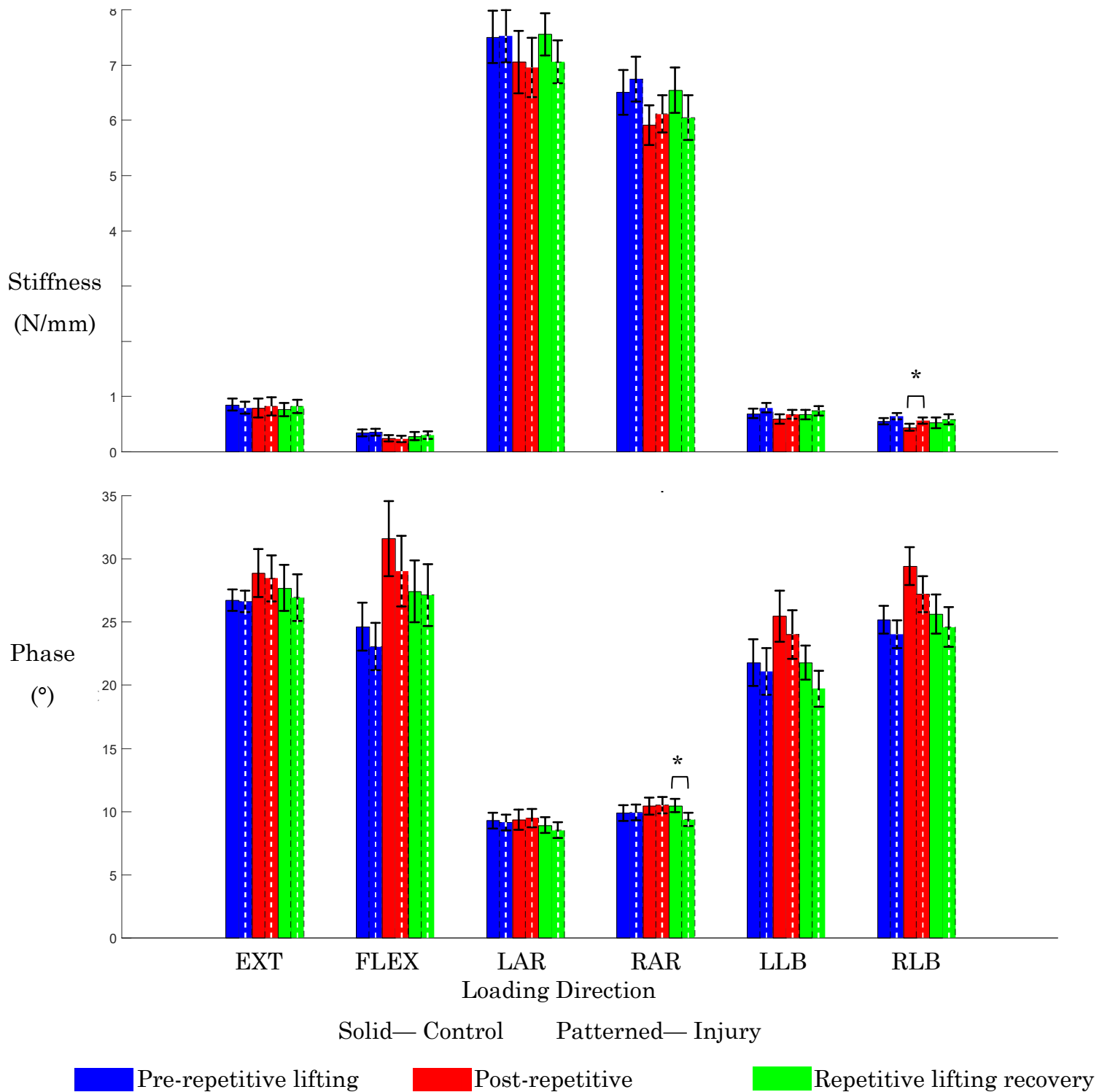


Figure 5.6 Averaged stiffness (N/mm) and phase angle (°) with a 95% CI for all rotational directions including extension (EXT), flexion (FLEX), left and right axial rotation (LAR, RAR), and left and right lateral bending (LLB, RLB). Solid bars represent the control group, while dashed bars indicate the injury group. Both groups underwent mechanical testing at three stages: before (pre-, in blue), after (post-, in red), and following (in green) repetitive lifting. Significant findings, marked with an asterisk (*), indicate $p < 0.05$. Sample sizes: control - pre-repetitive lifting (stiffness=10, phase=10), post-repetitive lifting (stiffness=9, phase=9), recovery (stiffness=10, phase=10). Injury - consistent counts of 10 for stiffness and phase across all stages.

5.5 Discussion

For the first time, this study has evaluated the 6DOF mechanical effects of combined needle injuries and simulated repetitive lifting on FSUs, likely to occur in a standard workday. The mechanical assessment was performed using ovine FSUs at three mechanical stages: before repetitive lifting, immediately after repetitive lifting, and following a recovery period.

As previously indicated (Amin et al., 2016a) and established (Chapter 4), interpreting significant changes required considering statistical and practical significance, biological variability, and potential systematic errors in experimental settings. A conservative threshold was set in this context, with changes below 25% being considered within laboratory environments' possible variability and error margins. Consequently, according to this threshold, the statistical analysis indicated that only right lateral bending experienced a significant biomechanical change by the needle injury after repetitive lifting, exhibiting a 27.27% ($p = 0.01$) increase in stiffness (Table 5-1 and Table 5-2). This change exceeded the conservative threshold, suggesting a substantial biomechanical response.

Considering this change, it was critical to address the pre-existing irreversible mechanical alterations inherited from the previous day's repetitive lifting (Chapter 4). The alterations were evident in FSU's flexion, by a significant decrease in stiffness of 77.19% and an 89.01% increase in phase angle, providing a crucial baseline for understanding the subsequent mechanical changes induced by the creation of needle injury in this study.

The findings mostly diverged from the hypothesis, which predicted a reduction in 6DOF stiffness and an increase in phase angle at all stages in the injury group compared to the control group. An impact of needle injuries after repetitive lifting contralaterally was observed, showing a 27.27% increase in stiffness ($p = 0.01$) in right lateral bending despite the needle injury being inflicted on the left posterolateral side. However, consistent with the hypothesis, after repetitive lifting, there was an 8.69% rise in phase angle ($p = 0.02$) in left lateral shear, and

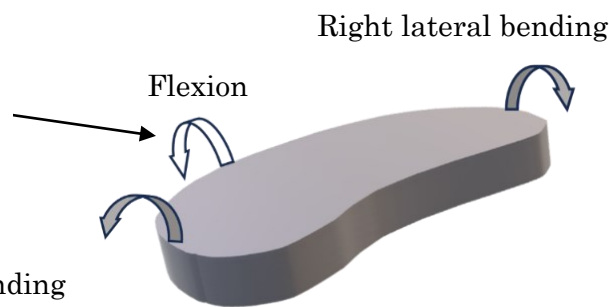
a 10.52% decrease in stiffness ($p = 0.01$) was noted in right axial rotation following the recovery period.

The increase in right lateral bending stiffness observed in this study after repetitive lifting could be attributed to a compensatory mechanism (**Figure 5.7**). The mechanism responded to the injury and weakness on the left lateral side, which was affected by a posterolateral needle injury and further compromised by a pre-existing irreversible reduction in flexion stiffness from the previous day's repetitive lifting (**Chapter 4**). Furthermore, the emergence of increased stiffness in right lateral bending, absent before the lifting, suggested a distinctive response of the disc specifically triggered by repetitive lifting to counteract the pre-existing stiffness reduction in flexion, a forward bending intrinsically related to lateral bending. However, the increased stiffness was found to be reversible after a recovery period.

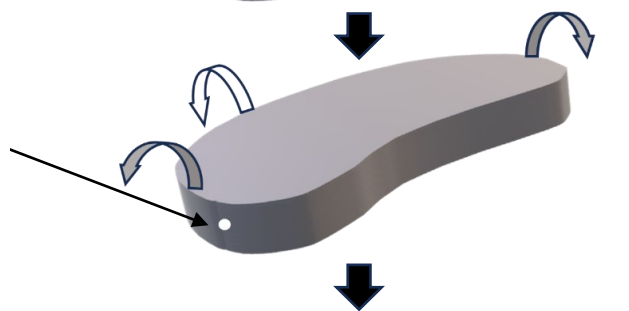
The compensatory mechanism can be further understood as the disc's passive response to maintain overall balance and stability. The response is reflected in the increased stiffness on the contralateral side (right lateral bending), which distributes the mechanical loads more evenly across the disc, reducing stress on the injured left side. The increase in stiffness suggests a biomechanical response of the disc aimed at maintaining equilibrium in bending movements and perhaps preventing further injury or stress on the left side by making the right side of the disc more resistant to bending and distributing the loads more evenly across the disc. Moreover, the stiffness increased in right lateral bending diminished after the recovery period and this indicates a reversible response of the disc to the imposed stress and suggests the disc's inherent resilience and ability to recover from biomechanical stress. However, a similar compensatory response was not observed when the FSUs were subjected to repetitive lifting alone in the previous day (**Chapter 4**), where no injury was present which highlights how the context of repetitive lifting (with and without needle injury) significantly influences recovery dynamics. For instance, in the scenario without injury, repetitive lifting alone caused significant and irreversible changes in flexion stiffness, though they were substantial, they might have been insufficient to trigger a compensatory

mechanism similar to that observed when repetitive lifting was combined with needle injury. Another aspect that may relate to the recovery dynamics is that the presence of a needle injury could potentially cause uneven load distribution across the disc, which triggers a compensatory response to maintain balance and stability.

a) Initial condition of the disc with pre-existing irreversible decreased flexion stiffness after repetitive lifting and recovery period (**Chapter 4**).

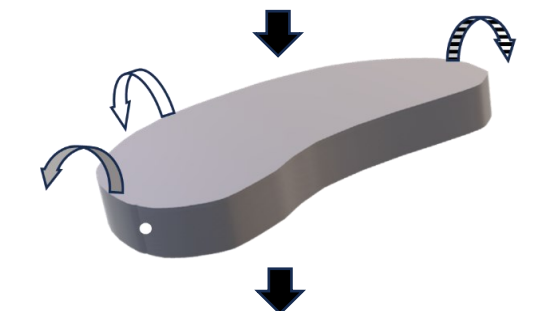


b) The disc now incorporates a posterolateral needle injury to the left side, combined with the previous condition from (a). Despite this injury, there is no change in lateral bending stiffness.



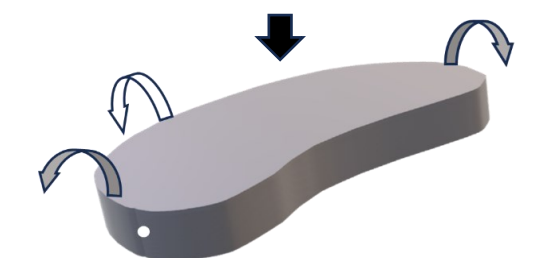
Simulated repetitive lifting

c) Immediately after repetitive lifting, the disc with the condition of (b) exhibits a compensatory biomechanical reaction, reflected as a stiffness increase in right lateral bending, contralateral to the injury.



Repetitive lifting recovery

d) After the recovery period, the increased stiffness in right lateral bending observed in (c) is reversible, diminishing after the recovery period.



Stiffness condition:  No change  Decrease  Increase

Figure 5.7 Diagram illustrating the mechanistic theory of an intervertebral disc's response to simulated repetitive lifting, considering a pre-existing irreversible decrease in flexion stiffness before injury (**Chapter 4**) (a). This initial state is compounded with a posterolateral needle injury to the left side, with no change in lateral bending stiffness observed (b). The subsequent compensatory biomechanical response immediately following the simulated repetitive lifting is characterised by an increase in right lateral bending stiffness on the side contralateral to the injury (c), serving to balance bending movements and potentially prevent further injury or stress on the left side. This increased stiffness was shown to be reversible, diminishing after a recovery period (d), which indicates the disc's inherent resilience and ability to recover from such biomechanical stress.

Considering the 29% incidence of disc herniation previously observed in cases of repetitive lifting at 2000 cycles (Drake et al., 2005), which was twice the magnitude examined in the current study, the vulnerability of the left side annulus to needle injuries could be anticipated. Despite variations in the conditions that produced herniation compared to the current study, such as the use of porcine FSUs and the incorporation of flexion-extension movements in the repetitive lifting rather than solely flexion, the herniation observed suggested a high potential of disruption to occur in at least the inner annulus at an earlier stage, as in the 1000-cycle loading employed in this study. This implication could become even more significant when considering the additional strain on the annulus by the needle injury. The predicted vulnerability of the inner annulus, observed under the combined conditions of repetitive lifting and needle injury in this study, also aligned with the disruption seen in 75% of the lateral inner annulus due to needle-induced damage following sudden overload on ovine FSUs (van Heeswijk et al., 2018). Despite their loading differences, with repetitive lifting causing gradual injury through prolonged low-intensity loading and sudden overload leading to abrupt, high-intensity impact, both might result in a similar injury profile and cause vulnerability within the annulus but with varying levels of interaction with needle injuries. Additionally, the previous study investigating the effects of needle injuries under sudden overload conditions also identified an asymmetrical response (van Heeswijk et al., 2018), yet this response was structural. In this instance, nuclear material penetrated and tracked circumferentially in a direction contralateral to the needle injury site following a disruption. This asymmetrical structural response aligned with and reflected the asymmetrical mechanical responses observed in the current study, exhibited as an increase in lateral bending stiffness on the contralateral side of the needle injury. This pattern revealed the potential for an asymmetric response within the disc, enduring across various loading conditions. It also showed the inherent tendency of disc biomechanics to respond asymmetrically to localised stress, such as that caused by needle injury, whether the stress was structural or mechanical.

These present findings suggest that future revisions to current occupational health guidelines for repetitive lifting may be necessary to account for the additional strain imposed by needle injuries. Such guidelines should consider scenarios where employees continue working after sustaining such injuries, as lifters might undergo extreme lifting tasks, require a clinical procedure involving a needle injury, and then continue their work. While the findings in the previous chapter indicate that occupational guidelines for those engaged in extreme repetitive lifting without injury may benefit more by increasing emphasis on proper lifting posture and reducing the number of lifts during the day to prevent irreversible mechanical changes to the disc, this chapter's findings additionally emphasise extending rest breaks to no less than three hours to allow for sufficient disc recovery. Such extended break durations, which may be more feasible by granting a day off, can accommodate those engaged in repetitive lifting who have sustained needle injuries. Furthermore, incorporating interventions such as mechanical lifting aids and supportive equipment can help reduce the mechanical load exerted on the spine. However, further research is necessary to confirm these recommendations, particularly in human models, before definitive changes to guidelines are made.

It is also important to consider the limitations of this study. In addition to the use of ovine FSUs instead of human ones, the application of a high flexion angle based on human FSU ranges ([Pearcy and Tibrewal, 1984](#), [Adams and Hutton, 1983](#), [Stokes and Frymoyer, 1987](#)) is a significant factor. Such an angle, combined with 1,000 cycles of repetitive loading, may lead to disc damage, a consideration that needs to be accounted for in future research. Such an angle, combined with 1,000 cycles of repetitive loading, may lead to significant disc damage, a factor that requires consideration.

5.6 Conclusion

This study offers new insights into the biomechanical effects of needle injuries on discs under simulated repetitive lifting, assessed at stages before and after repetitive lifting and following a recovery period. The observed increase in

stiffness, found in lateral bending after the lifting, indicated a distinctive response of the disc to such loading with such localised injury. This reaction might act as a compensatory mechanism to the mechanical changes induced by the needle injury, thereby highlighting the disc's complex biomechanical response mechanisms. While the mechanical changes observed, including those that were not statistically significant, and the reversible increase in stiffness following recovery, suggest that needle injuries may be well tolerated in ovine models, further research is needed to assess in human models, before broader conclusions can be drawn. These findings could contribute to future discussions on occupational health guidelines for repetitive lifting tasks involving needle injuries, including considerations for extended rest breaks and the use of mechanical aids to alleviate additional strain and improve recovery, particularly for workers who continue lifting after sustaining such injuries.

Chapter 6 Does Repetitive Lifting Increase Annulus Fibrosus Structural Disruption After Needle Insertion Injury?

6.1 Abstract

The effects of needle injuries on disc mechanics and structure have been investigated by previous research, providing insights into these impacts. However, the structural impact of needle injuries on the annulus fibrosus under simulated repetitive lifting has remained unknown. This study aimed to address this gap by investigating the morphology of needle injuries in the annulus fibrosus of functional spinal units (FSUs) subjected to simulated repetitive lifting before and after the injury (n=3) (**Chapter 5**), comparing outcomes with control injuries in FSUs that underwent no mechanical loading (n=3). Sections were collected from injuries in both groups, perpendicular to the injury axis, where microscope images were taken, and injury area, length, solidity, and aspect ratio were quantified. The results did not show significant effects of repetitive lifting on the quantified parameters. However, notable variability in the measurements, especially in injury area and solidity, suggested the presence of hidden effects from repetitive lifting, potentially concealed by the inherent variability in needle injury forms in the AF. The study data revealed previously known forms of needle injury: the parallel form aligning with the oblique fibres of the annulus fibrosus and the cross form intersecting adjacent fibres, both reflecting their natural occurrence and intrinsic manifestation. Additionally, this study introduced, for the first time, a hybrid form of needle injury featuring characteristics of both the parallel and the cross forms. The study findings, along with the incorporated preliminary analysis, could encourage future studies to explore the potential for differential responses to repetitive lifting among needle injuries based on their form. This direction could also promote research aimed at a better understanding of the structural effects on the annulus fibrosus under

repetitive lifting and different mechanical loading scenarios, ultimately targeting insights into the interplay between disc mechanics and injuries.

6.2 Introduction

Back disorders, including low back pain (LBP), have been a prevalent health problem in Australia and worldwide, leading to significant disability (Hartvigsen et al., 2018, Vos et al., 2017, Davis, 2012, Penm et al., 2006). The economic burden of these disorders has been substantial over the years, with the annual cost in Australia exceeding 605 million AUD (Penm et al., 2006), and in the United States surpassing 50 billion USD (Hartvigsen et al., 2018, Vos et al., 2017, Davis, 2012, Penm et al., 2006, AIHW, 2023). In treatments for back disorders, needles have been used for both therapeutic and diagnostic purposes. Procedures such as electrothermal therapy involve inserting needles into the disc to deliver heat to specific tissues, a method that aids in pain relief and healing. For diagnosis, in discography, needles have been used to inject a contrast dye into the disc to assist in imaging and evaluating the disc structure to identify any pain sources. Needles offer precision and minimal invasiveness, making them suitable for back treatments and diagnosis applications. Although some cohort studies have presented conflicting results concerning the use of needles in discography's link to disc degeneration (Carragee et al., 2009, Hur et al., 2016), it is still an acceptable intervention by professional spine societies (Hunt et al., 2019, Centerville et al., 2018, Bogduk, 2004, Gilbert et al.) and is considered the gold standard for diagnosing discogenic pain (Chen and Gao, 2023). Furthermore, needles have been increasingly viewed as avenues for delivering biological treatments of disc degeneration (Buckley et al., 2018, Cho et al., 2013, Ren et al., 2013, Tam et al., 2014).

In vivo studies using animal models have indicated that needle injuries may accelerate disc degeneration over time (Cunha et al., 2017, Keorochana et al., 2010, Hsieh et al., 2009, Kim et al., 2005, Masuda et al., 2006). *In vitro* research on animal models has further explored the effects of needle injuries on spinal discs using annulus explants (Michalek et al., 2010a, Vergari et al., 2017) and

isolated discs (Korecki et al., 2008) under various mechanical testing protocols. In isolated bovine discs needle injuries, even of small size, could cause immediate and progressive changes in disc height, stiffness, and viscoelastic properties, including a reduced dynamic modulus and increased creep, which do not recover. However, testing on bovine annulus explants showed that needle injuries led to slight changes in fibre bundle shearing, yet despite these changes, the linear strain within and between fibre bundles remained relatively stable (Vergari et al., 2017). Further study using bovine annulus explants found that while needle injuries led to changes in the distribution of annulus shear strain, they did not exacerbate these annulus disruptions (Michalek et al., 2010a).

In vitro studies focusing on rat FSUs highlighted a decline in disc stiffness found in torsion and compression, following needle injuries (Torre et al., 2019, Michalek et al., 2010b). These changes were pronounced when the needle size was at least 40% of the disc height, a ratio previously identified as a critical factor in altering disc mechanics (Elliott et al., 2008). Additionally, similar study but using bovine FSUs with smaller needles indicated minimal impact on the disc's stiffness or phase angle across various movements, including compression, flexion-extension, lateral bending, and torsion. Furthermore, the study showed discs maintained their height despite needle injuries (Michalek and Iatridis, 2012). Yet, when needle injury was combined with sudden overload, noticeable disruptions in the inner annulus were evident (Table 2-3) (van Heeswijk et al., 2018).

Earlier studies have contributed to the understanding of how needle injuries affect the intervertebral disc's mechanics and structure. However, there remains a crucial need for further investigation into these structural effects within the annulus fibrosus in the context of simulated repetitive lifting, commonly experienced in various work environments. The importance of such research is crucial considering that individuals with needle injuries are likely involved in tasks that require repetitive lifting. Comprehending the implications of needle injuries on the annulus fibrosus during repetitive lifting is key to a more

comprehensive evaluation of disc health and an accurate determination of injury risks (**Chapter 4**).

Previous studies have provided insights into the effects of needle injuries on the disc mechanics and structure, but there remains a notable gap in understanding their structural impacts on the annulus fibrosus under simulated repetitive lifting. This scenario is relevant, given that individuals in lifting occupations who have experienced needle injuries were shown to have an increased risk of disc herniation, as evidenced by a 10-year clinical cohort study ([Carragee et al., 2009](#)). Addressing this gap is crucial for the health and safety of workers in physically demanding roles, as lifting is typical in labour scenarios and can significantly affect the disc's health in the long term. This study aims to bridge this gap by investigating needle-induced ruptures in the annulus fibrosus using ovine FSUs that have undergone a day of simulated repetitive lifting before the injury (**Chapter 4**) and after the injury (**Chapter 5**). It is hypothesised that needle-induced ruptures in the annulus fibrosus will show significant structural changes under simulated repetitive lifting. These changes are expected to manifest as an increase in injury area, length, and aspect ratio, along with a decrease in the solidity of the annulus fibrosus (the ratio of the injury area to its convex hull, the smallest convex polygon containing the injury). The hypothesis is founded on the compromised structural integrity caused by the ruptures, with exacerbation expected due to mechanical stress from repetitive lifting.

6.3 Materials and Methods

6.3.1 FSU Preparation

The methods of this study were designed to investigate needle injuries of ovine FSUs, which were randomly divided into two groups: mechanical injury and control injury. All FSUs had 25G needle injuries inflicted in their left posterolateral annulus. The mechanical injury group, which included the ten FSUs identified in **Chapter 5**, was subjected to a one-day simulated repetitive lifting conducted before (**Chapter 4**) and after (**Chapter 5**) the injuries, with an intervening period of overnight hydration. The lifting involved 1000 cycles,

combining compression (1.1 MPa) and flexion (13°). A control group was added to the present study, providing a comparative analysis baseline. This group consisted of seven ovine FSUs (comprising two L45 and five L23 levels) that underwent procedures similar to those of the mechanical injury group, including FSU preparation and the creation of needle injuries in the left posterolateral annulus fibrosus (**Chapter 5**). However, a key difference was the absence of mechanical testing with overnight hydration, as this hydration was integrated into the mechanical loading simulation and was not applicable to the control group. This preserved the integrity of the control specimens' needle injuries, thereby facilitating a clear comparison with the mechanical injury group.

6.3.2 Needle Injury Sectioning

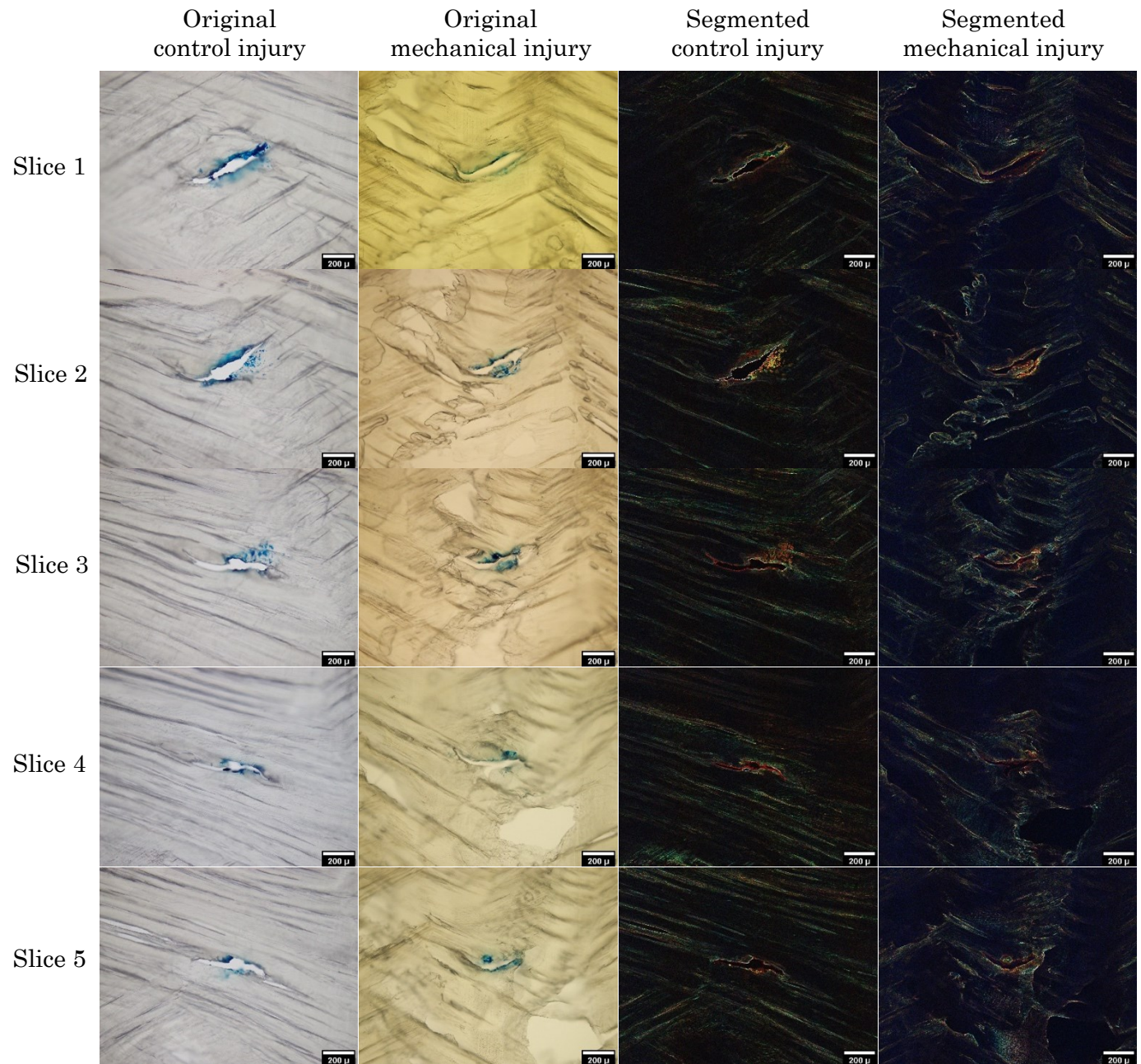
After the control group FSUs underwent the same injury creation protocols as the mechanical group FSUs, both groups proceeded with identical needle injury sectioning as detailed earlier (**Section 3.5**). Briefly, upon removal from -20 °C storage, each FSU underwent careful excision of the upper vertebra using a feather blade, followed by a three-day fixation in a 10% buffered formalin solution. This duration was chosen to represent the median within the range of literature-reported fixation durations, varying from 24 to 48 hours ([Wilke et al., 1997](#), [Fazzalari et al., 2001c](#), [Veres et al., 2008](#)) to one week ([van Heeswijk et al., 2018](#)). After fixation, the disc-bottom vertebra segments were repositioned in the apparatus used for needle injury creation, which allowed for precise extraction of the needle injury track within the annulus. A cut was initially made perpendicular to the needle injury axis at the nucleus-annulus interface using a feather blade, followed by the careful isolation of the needle injury track at the lower disc endplate junction. This extraction was performed with precision as it was crucial to align the needle injury track properly for subsequent microtome sectioning. The extracted segment was then embedded in an optimal cutting temperature (OCT) compound and frozen below -20°C, followed by sectioning from the outer annulus to the inner, perpendicularly to the injury axis, using a microtome (Leica Biosystems, CM3050, Germany). This sectioning maintained a consistent thickness of 60 µm per section, continuing until a depth of 1200 µm

into the annulus was reached, at which five consecutive slices were collected. Each slice was immediately imaged at 10X magnification using a Brightfield BX50 light microscope (Olympus, Japan) for the analysis of the injury slices.

6.3.3 Injury Quantification and Data Analysis

In a brief overview, and as extensively detailed previously (**Section 3.5.2**), the analysis of images was conducted using ImageJ software (version 1.53s) for quantifying the injury's area and length (elongated axis), and MATLAB software (R2018b, MathWorks, USA) for additional morphometric quantification of injury solidity (injury area to convex hull area) and aspect ratio. Specifically, injury quantification from each group using ImageJ involved processing the original images for segmentation and mask creation, while MATLAB was used to evaluate the solidity and aspect ratio using these injury masks (**Figure 6.1** and **Figure 6.2**). The mean values for each injury parameter were calculated by averaging measurements obtained from five slices for every injury in each group, with each slice treated as an individual representation of the injury. This approach accounted for minor variations while ensuring a comprehensive view of each injury's profile. Statistical differences in injury parameters between the control and mechanical injury groups were assessed using IBM SPSS Statistics software (version 25.0.0.2), wherein independent t-tests were performed for each parameter.

Figure 6.1 Representative injury images from each group, organised by sequential injury slices (1-5) along the rows, with each slice being 60 μm thick. Columns 1 and 2 display original brightfield images from the control and mechanical groups both with green ink outlines marking the injuries. Columns 3 and 4 show these images processed using ImageJ for injury segmentation.



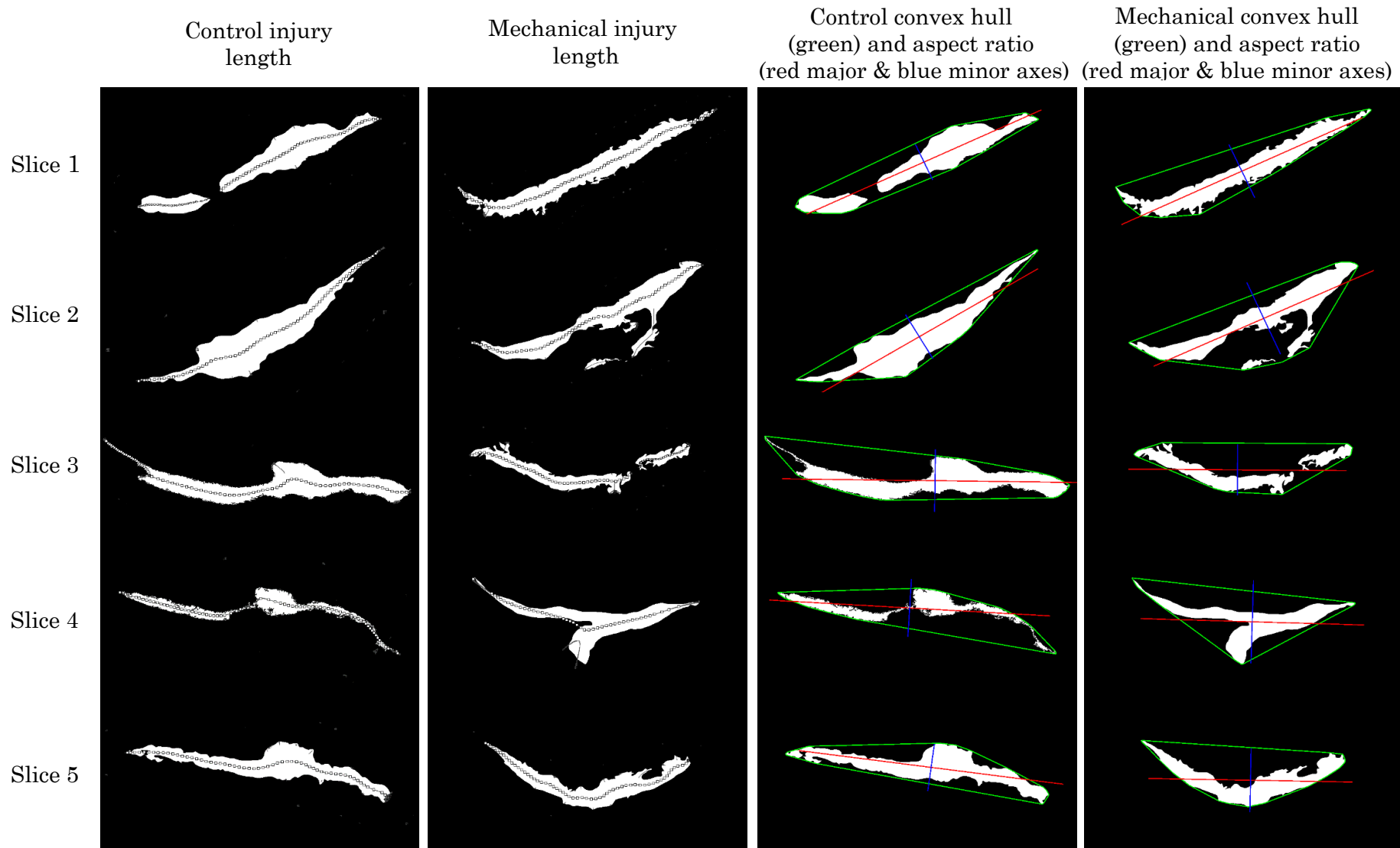


Figure 6.2 Injury masks of the representative injuries of each group (**Figure 6.1**), organised by sequential injury slices (1-5) along the rows. Columns 1 and 2 display injury mask images from the control and mechanical groups, both highlighting injury lengths using ImageJ. Columns 3 and 4 show these images with the convex hull area (green), and principal major (red) and minor (blue) axes plotted by MATLAB for aspect ratio calculations.

6.4 Results

The study initially began with a total of 10 FSUs for the mechanical injury group and 7 FSUs for the control group. Due to various challenges, a final sample size of three injuries per group was achieved. Unexpected logistical challenges influenced the final sample size. During a period of freezer maintenance, two FSUs from the mechanical injury group were inadvertently misplaced and could not be located. Furthermore, an error encountered during the microtome slicing process necessitated the exclusion of one mechanical injury FSU. Technical difficulties encountered while slicing also resulted in predominantly unsuccessful sectioning across five slices in four injuries from each group (**Appendix D**). These issues led to the exclusion of several samples, ultimately resulting in a final sample size of three injuries per group.

Due to these challenges, a final sample size of three injuries per group was achieved, with each injury consisting of five consecutive slices. From these slices, mean values for each injury parameter (area, length, solidity, and aspect ratio) were averaged for each group. The original and processed images, related measurements, tables, and bar charts of these injuries are presented in **Appendix C**.

The mechanical injury group exhibited no significant differences in all injury parameters compared to the control group. The observed differences included a 17.6% decrease in injury area ($p=0.704$), a 1.4% decrease in length ($p=0.661$), a 1.8% decrease in solidity ($p=0.935$), and an 11.5% increase in aspect ratio ($p=0.796$) in the mechanical group (**Figure 6.3**). However, despite the non-significant p -values, effect sizes were considered crucial due to the small sample size ($n=3$ per group). The use of Hedges' g for effect size estimation was considered appropriate, as it provided more conservative and less biased estimates in small sample conditions, correcting Cohen's d ([Hedges and Olkin, 1985](#), [Cohen, 2013](#)). This choice was informed by the need for an accurate representation of the effect size despite the limited sample. As a result, small effect sizes and 95% confidence intervals were observed for all parameters

(Table 6-1). Additionally, a GPower analysis (GPower Version 3.1.9.6) was conducted to assess the adequacy of the current sample size in achieving reliable statistical power. The analysis was based on a desired statistical power of 0.80, an alpha level of 0.05, and a two-tailed test. The results indicated the need for substantially larger sample sizes to achieve the desired power level: approximately 652 samples for the area, 506 for length, 8724 for solidity, and 1398 for aspect ratio.

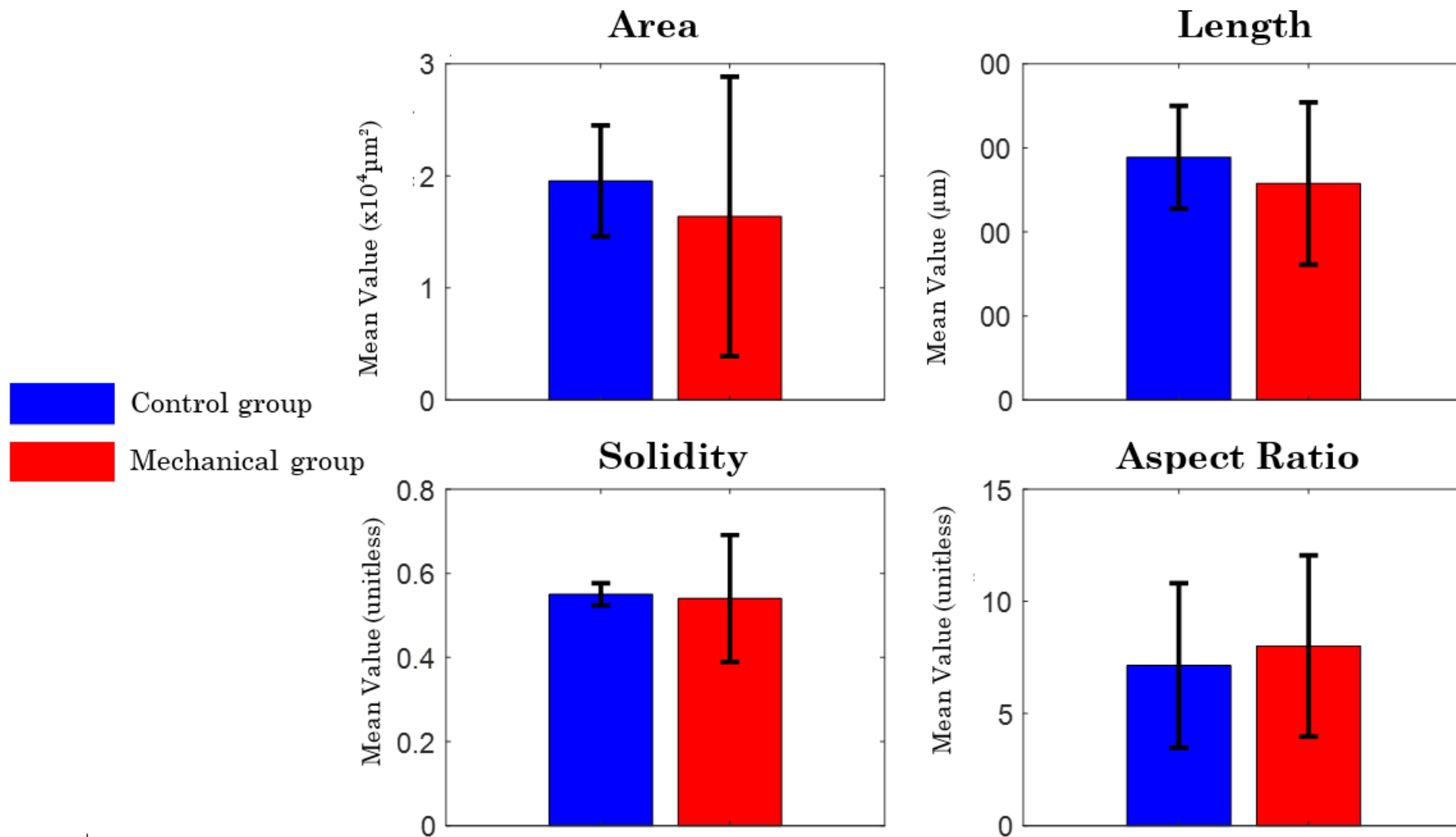


Figure 6.3 Mean values for the control group (blue, n=3) and the mechanical injury group (red, n=3) for all measured parameters: area (μm^2), length (μm), solidity (unitless), and aspect ratio (unitless). Each bar represents the group mean, calculated by averaging the mean values of the three injuries in the respective group. The error bars signify the 95% confidence intervals.

Table 6-1 T-test p-value' of independent t-test. '95% Confidence Interval' presents the range of values for the difference between control and mechanical groups. 'Hedges' g' shows the effect size, with the negative sign suggesting that the mechanical group has a lower mean than the control group for the respective parameters, and a positive value indicates the opposite. 'Effect Size Interpretation' provides a general interpretation of the magnitude of the effect size (Small for $0.2 < |Hedges' g| < 0.5$, Medium for $0.5 \leq |Hedges' g| < 0.8$, and Large for $|Hedges' g| \geq 0.8$).

Parameter	T-Test p-Value	95% Confidence Interval	Hedges' g Value	Effect Size Interpretation
Area	0.704	[-24664, 18338]	-0.22	Small ($0.2 \leq$)
Length	0.661	[-428, 304]	-0.25	Small ($0.2 \leq$)
Solidity	0.935	[-0.26, 0.24]	-0.06	Negligible
Aspect ratio	0.796	[-7.88, 9.62]	0.15	Negligible

6.5 Discussion

This study investigated needle injuries in the annulus fibrosus for the first time using ovine FSUs with a unique approach. The FSUs were subjected to a simulated repetitive lifting equivalent to 1000 cycles of compression and flexion before and on the following day after the injury to replicate real-life labour scenarios. Significant structural changes were hypothesised for the injuries under repetitive lifting compared to the control injuries in FSUs that underwent no mechanical loading. The changes were expected to appear as an increase in injury area, length, and aspect ratio with a decrease in solidity. However, while the findings revealed a decreasing trend in all parameters for the mechanical injury group, except for the aspect ratio these changes were insignificant. Furthermore, the analysis of effect sizes, conducted in the context of the study's small sample size, supported these findings, revealing only a small or negligible effect of the mechanical group. However, the 17.6% lower injury area and 11.5% higher aspect ratio of the injury were still notable in magnitude compared to a 1.8% lower solidity and 1.4% lower length. In the current study, despite the small sample size and associated small effect size, the changes observed suggest potential mechanistic trends that become more pronounced under extended periods of repetitive lifting beyond 1,000 cycles, equivalent to one day after the injury. Supporting this notion, a previous study investigated the effects of repetitive loading equivalent to 20,000 cycles or a year's duration and found a

decrease in disc height (Amin et al., 2019b). It is important to consider, however, that this study did not account for the inter-day recovery period simulating fluid re-equilibration during sleep. Despite this limitation, the findings are still relevant as they emphasise the potential long-term worst-case effects of repetitive lifting on disc morphology. These effects, particularly the reduction in disc height, could provide insights into how extended repetitive lifting might further influence injury parameters like area, length, solidity, and aspect ratio in the annulus fibrosus.

Nevertheless, the injury area and solidity measurements (**Figure 6.3**) showed distinguishably higher variability in the mechanical group compared to the control group, which might indicate differential responses among the mechanical injuries, which in turn could be an indicator of influencing combined factors such as intrinsic variations due to the specific nature of the injuries incurred. Moreover, while this study employed a reproducible technique to standardise the insertion of needles for creating injuries and ensured consistent depth for collecting injury slices within the annulus, the intrinsic manifestation of these injuries — specifically their form within the collagen fibres of the annular layer — appeared to be less controllable. Parallel form injuries, aligned with the orientation of the oblique annular fibres, were observed in both control and mechanical injuries in this study (**Figure 6.4a**). This observation aligns with a hypothesis from a previous study (van Heeswijk, 2017), which suggested that when the needle tip is approximately aligned with the oblique fibres, it tends to separate them, facilitating the needle's passage through the annular layer and forming what was termed as a 'slit-like injury' (**Figure 6.4b**). Similarly, the previous study hypothesised that in the case of cross injuries, which intersect the fibre orientation, the counter-oblique fibres act as a barrier and are severed by the needle, leading to injuries defined as a 'hole' (**Figure 6.4d**). However, consistent with this hypothesis, the present study revealed hybrid injuries, a new form featuring both parallel and cross forms, in the layer adjacent with counter-oblique fibres (**Figure 6.4c**).

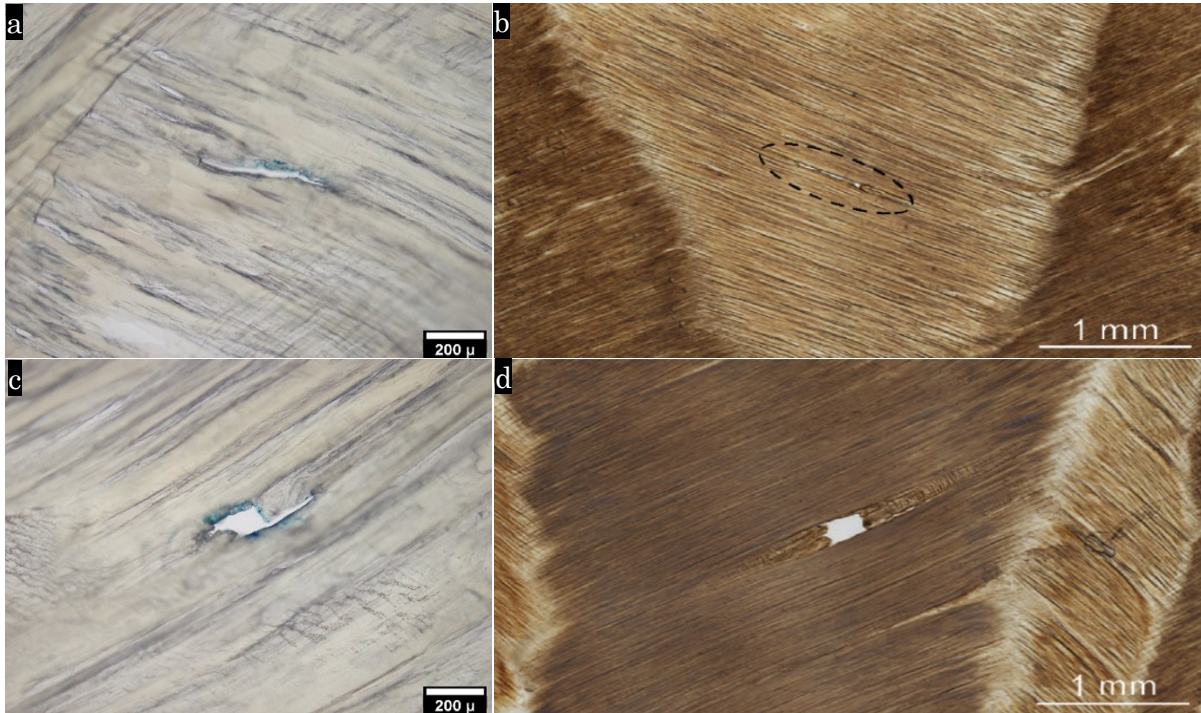


Figure 6.4 Comparison of 25G needle injuries in adjacent annulus layers as observed in the current (a, c) and previous (b, d) studies (van Heeswijk, 2017), each illustrating distinct forms of injuries. Parallel injuries from both studies appeared within annular layers in images (a) and (b). Notably, in the counter-oblique adjacent layers (c and d), the higher Brightfield magnification (200 μm scale bar) from the current study reveals a hybrid (parallel and cross) form injury (c). In contrast, the previous study, using lower DIC magnification (1 mm scale bar), the injury manifested in cross form (d).

In this study, classifying control and mechanical injuries based on their injury form was challenging. While some injuries could be distinctly categorised as either parallel or hybrid, the majority exhibited a merging of different proportions between parallel and cross forms and across two annular layers, thereby complicating their clear classification. However, a preliminary evaluation was conducted by comparing one distinguishable parallel injury and one hybrid injury within a single annular layer, using two consecutive slices from both control and mechanical injuries. This approach aimed to assess how injury parameters might vary between these distinct injury forms compared to their respective controls. The representation of these injuries (**Figure 6.5**) was compared quantitatively in relation to differences in the parameters of area, length, solidity, and aspect ratio in the mechanical injuries, averaging across the two consecutive slices and comparing each injury form to its respective form of control injury (**Table 6-2**). While this evaluation identified notable differences in

all parameters across consecutive slices of both parallel and hybrid forms in both groups (**Table 6-3**), the primary focus on mechanical injuries within this evaluation also revealed pronounced differences (**Table 6-2**). In the mechanical injuries, the area increased by 49.1% in parallel injury and decreased by 9.9% in hybrid injury, while solidity increased by 45.8% for parallel injury but only by 8.2% for hybrid injury. These changes were accompanied by similar trends in length and aspect ratio; both injury forms exhibited decreases in length (20.8% in parallel and 24.8% in hybrid) and aspect ratio (38.3% in parallel and 39.7% in hybrid injuries) (**Table 6-2**). Although preliminary, these findings underline the consistent notion of variability in injury area and solidity measurements (**Figure 6.3**), as indicated earlier. They suggest that the absence of significant effects in all injury parameters of the primary results might be concealed by the heterogeneous nature of injury forms seen in data of both groups, which could potentially mask any uniform trends. The findings further raise the question whether the repetitive lifting imposed on the mechanical injuries has significant impacts on injury parameters dependent on the form of injury. For instance, the effects on solidity and area are more pronounced in parallel injuries than in hybrid injuries. The 49.1% increase in area for parallel injuries and the 9.9% decrease in hybrid injuries suggest that repetitive lifting may have a more notable effect on parallel injuries, potentially due to greater fibre separation as hypothesised ([van Heeswijk, 2017](#)), compared to the more confined separation in hybrid injuries. While highlighting the heterogeneity nature of the injuries forms as limitation of the present study, these observations suggest future studies with large sample size to investigate the effects of repetitive lifting among injuries within consistent injury form and within a single annular layer. Additionally, the potential role of repetitive lifting in transforming one injury form into another, for example, from a hybrid to a parallel form, may require further attention. Future research may also assess the notable changes in injury parameters that appeared across consecutive slices within one annular layer in both injury forms and groups (**Table 6-3**). This could provide a deeper insight into the dynamic nature of these injuries and how they evolve and respond to mechanical loadings, such as repetitive lifting.

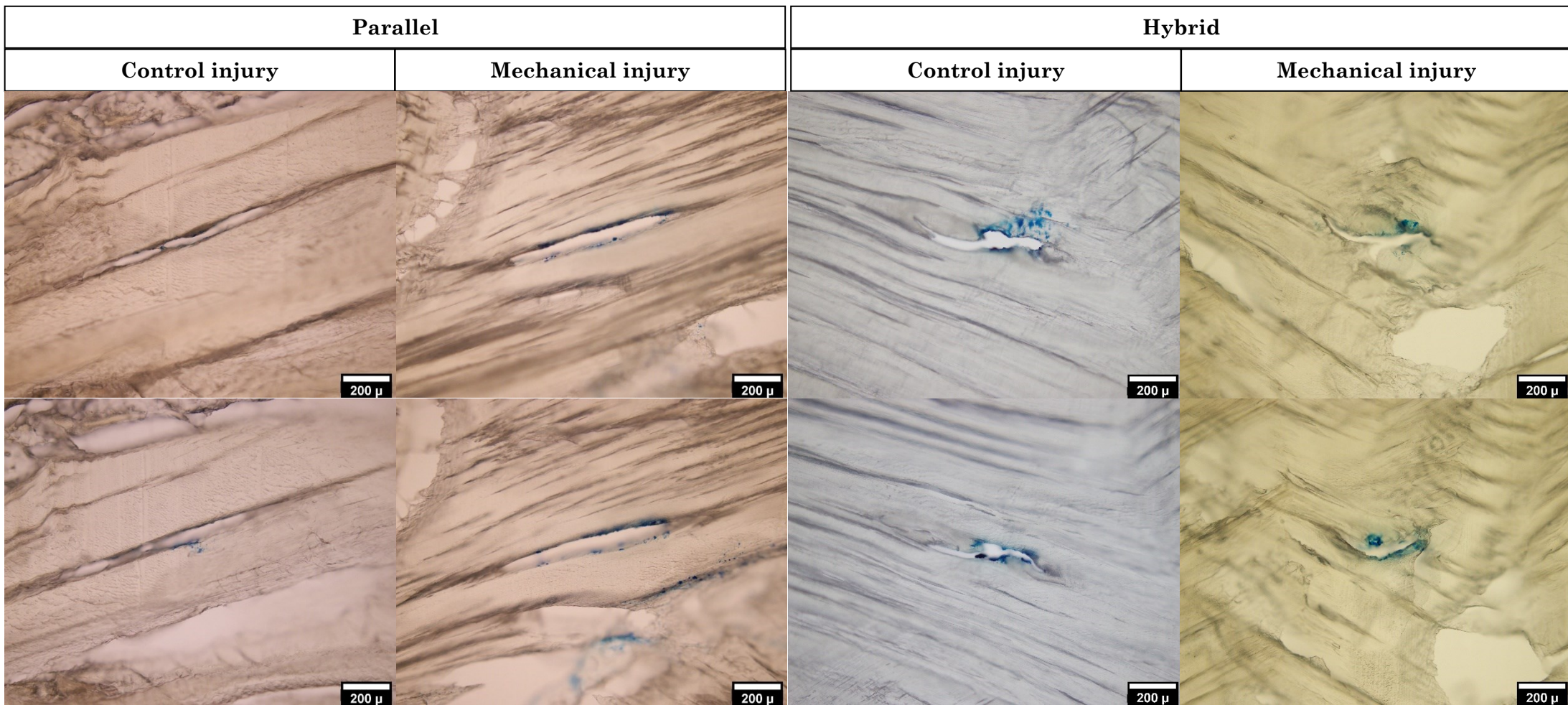


Figure 6.5 Comparison of parallel and hybrid injury forms in two consecutive slices. The parallel and hybrid injury forms are within a single annular layer, presented in two consecutive slices: the top slice and the bottom slice with each slice shown in both control and mechanical injuries.

Table 6-2 (Left) and **Table 6-3** (Right) quantify changes in injury area, length, solidity, and aspect ratio within a single annular layer for the parallel and hybrid injury forms in both the control (cont) and mechanical (mech) injuries (**Figure 6.5**). Table 6-2 quantifies changes in the parameters in the mechanical group, averaging across slices and comparing each injury form to its respective control. Table 6-3 quantifies changes in injury parameters across the consecutive slices, comparing the bottom slice to the top.

Parameter	Difference in mechanical group injuries compared to its respective control (Averaging the top and bottom slices)				Parameter	Change across two consecutive slices of injury in one annular layer (Bottom slice to top slice change)			
	Parallel		Hybrid			Parallel		Hybrid	
	cont (%)	mech (%)	cont (%)	mech (%)		cont (%)	mech (%)	cont (%)	mech (%)
Area	—	+49.1%	—	-9.9%	Area	-54.8	3.8	-19.5	42.4
Length	—	-20.8%	—	-24.8%	Length	-6.0	-3.8	-15.6	18.7
Solidity	—	+45.8%	—	+8.2%	Solidity	-37.8	13.5	-18.6	-9.8
Aspect	—	-38.3%	—	-39.7%	Aspect	-0.4	17.8	-28.2	-13.7

Technical difficulties encountered during sectioning, which led to predominantly unsuccessful sectioning of the needle injuries, resulted in a reduced final sample size of three injuries per group. This reduction might have influenced the overall findings. Moreover, the limitations posed by this smaller sample size, highlighted by the GPower analysis recommending larger sample sizes for adequate statistical power, suggest that the observed non-significant effects and minimal effect sizes may be attributed to limited sample power. For instance, achieving the desired statistical power (0.80) with an alpha level of 0.05 would require significantly larger sample sizes for all parameters (506–8724 samples). These requirements present logistical challenges in terms of both resources and time, given the technical difficulties encountered in this study.

In terms of practicality, performing future studies with such large sample sizes may not be feasible in typical experimental conditions without technical improvements and refinements to the study design. Potential solutions could include improving sectioning techniques and using non-invasive imaging technologies. These approaches might assist in overcoming the resource burden by allowing larger data sets to be collected more efficiently and reducing specimen loss, thereby ensuring a higher yield of usable samples. However, even with significant improvements in these methods, the large sample sizes required for adequate statistical power would still present a challenge, as the magnitude of the necessary sample sizes remains substantial. Therefore, alternative approaches may be necessary, such as the use of finite element analysis (FEA) to complement experimental findings and reduce the need for large physical samples.

6.6 Conclusion

This study investigated the effects of simulated repetitive lifting on needle injury morphology in the annulus fibrosus using ovine FSUs. The results did not show significant effects of repetitive lifting on the injury area, length, solidity, and aspect ratio. However, while the results do not directly suggest hidden effects, the inherent variability in needle injury forms may have concealed them. This

evaluation also revealed, for the first time, a hybrid form of needle injury which features characteristics of both the known parallel form, aligned with the orientation of the oblique annular fibres, and the cross form, which intersects the fibre orientation. The preliminary analysis, which also compared the effects of repetitive lifting on two distinct injury forms, one parallel and one hybrid, raises questions for future studies to investigate further the potential effects of repetitive lifting on both injury forms. This assessment and suggested future investigations are crucial for understanding the development and exacerbation of annulus fibrosus injuries due to occupational lifting. Insights from such research are key to developing effective prevention and treatment strategies in occupational health, particularly for improving therapeutic needle interventions in the intervertebral discs.

Chapter 7 Concluding Insights and Future Directions

Ovine functional spinal units (FSUs) were used in this research to evaluate the impact of simulated repetitive lifting on the intervertebral disc. The overall aims were (i) to evaluate the sole effects of simulated repetitive lifting on the six degrees of freedom (6DOF) stiffness and phase angle of the FSUs and (ii) to assess the combined impact of needle injuries and repetitive lifting on these properties. For both aims, evaluations were conducted immediately after the lifting and following a recovery period. The third aim of the research was to investigate the impact of repetitive lifting on the morphology of needle injuries within the annulus fibrosus, quantifying the injury area, length, aspect ratio, and solidity.

7.1 Overview of Key Findings

7.1.1 Repetitive Lifting Irreversibly Alters FSU Flexion Stiffness and Viscoelastic Properties

This study explored the biomechanical changes in 6DOF stiffness and phase angle of FSUs due to simulated repetitive lifting. The 6DOF mechanical properties were evaluated immediately after the lifting session and following a recovery period. The assessment showed that the mechanical effects were confined to flexion without impacting other directions, likely due to repetitive lifting being performed at high flexion. The changes in flexion mechanics, characterised by a reduction in FSU stiffness and an increase in phase angle, indicated microstructural alterations within the disc tissues. The alterations, possibly associated with increased internal strain, substantially modified the disc's viscoelastic properties, resulting in decreased stiffness and an increased phase angle that persisted even after a period of recovery. Furthermore, these biomechanical changes might be contextualised within the continuum of disc

distortion stages, ranging from lamellar disruption to annular rupture, showing the progressive nature of tissue damage.

7.1.2 Immediately after Lifting, the Combined Effects of Needle Injuries and Repetitive Lifting on FSU Stiffness Trigger a Compensatory Response in the Disc

This study investigated the 6DOF mechanical impact of needle injuries on FSUs stiffness and phase angle under conditions of simulated repetitive lifting, with assessments conducted both immediately after lifting and following a recovery period. It was found that an increase in right lateral bending stiffness immediately after lifting acted as a passive compensatory response to a weakened contralateral side due to a posterolateral needle injury, compounded by a pre-existing permanent reduction in flexion stiffness, a forward bending intrinsically related to lateral bending. The vulnerability of the left side annulus to needle injuries could be due to disruption likely in the inner annulus as a consequence of cumulative damage from the repetitive lifting. The right side's increased stiffness during lateral bending, previously not present, suggested a distinctive biomechanical response of the disc to counteract the reduced flexion stiffness, thereby maintaining equilibrium in bending movements and potentially preventing further injury or stress to the injured left side. The increase in stiffness was temporary, diminishing after a recovery period, which depicted the disc's inherent resilience and capability to recover from biomechanical stress. This pattern of response to and recovery from localised needle injuries combined with repetitive lifting revealed the disc's complex biomechanical mechanisms, further highlighting its resilience.

7.1.3 Different Forms of Needle Injuries in the Annulus Fibrosus May Exhibit Different Morphological Responses to Repetitive Lifting: Preliminary Analysis

This study investigated needle injuries in the annulus fibrosus, in FSUs subjected to simulated repetitive lifting before and after the injury, comparing outcomes with control injuries that underwent no mechanical loading. The effect of repetitive lifting was assessed on the morphometric parameters of these injuries, such as injury area, length, solidity, and aspect ratio, involving the analysis of sectioned slices perpendicular to the needle injury axis and averaging measurements across the slices. However, the distinguished variability seen in the measurements of injury area and solidity could indicate the presence of hidden effects from repetitive lifting, potentially concealed by the inherent variability in needle injury forms in the AF. Two forms of injury were identified within the AF, reflecting their natural occurrence, and highlighting an intrinsic manifestation that was less controllable in the sectioning depth of the study, which extended beyond a singular annular layer. These forms included the parallel form, aligned with the orientation of the oblique annular fibres in one layer, and the cross form, which intersected the counter-oblique fibre orientation in the adjacent layer. The study, for the first time, identified a hybrid form injury featuring characteristics of both parallel and cross forms. The majority of the study injuries exhibited this hybrid form with the merging of different proportions between parallel and cross forms. However, one parallel injury and one hybrid injury within a single annular layer were distinctly categorised, allowing for the preliminary quantification of injury morphology across a consistent injury form within one annular layer. The preliminary analysis raises questions about potential differential responses among needle injuries depending on their form, providing a direction for future studies to investigate.

7.2 Significance

While conducted using an animal model, this thesis presents novel findings on the impact of simulated repetitive lifting on FSU mechanics, both as an isolated factor and in combination with disc needle injuries, likely required by clinical interventions for conditions resulting from such lifting. It further explores how repetitive lifting may have an injury form-dependent impact on the morphology of needle-induced disruptions in the disc's annulus, laying the groundwork for future research and additional investigation. The research findings on the biomechanical effects of repetitive lifting contribute to the foundational research required for developing safety guidelines for workers involved in repetitive lifting tasks. Additionally, the insightful examination of the interplay between repetitive lifting and disc needle injuries provides a foundation for future studies aimed at advancing the diagnosis and treatment techniques of disc issues. The research outcomes not only inform clinical practice but also show key areas that have the potential to impact rehabilitation and the development of specific preventative strategies within workplace environments, particularly for individuals with disc needle injuries. Moreover, the preliminary analysis of changes in needle injury morphology due to repetitive lifting sets the stage for future studies to explore how needle injuries in the disc annulus potentially develop and worsen not only within the context of repetitive lifting but also under mechanical loading scenarios.

7.3 Future Directions

Future research using human FSUs could provide more relevant insights into human FSU biomechanics than this research's use of ovine FSUs despite their structural and mechanical similarities. Building on this research's examination of the mechanical impact of day-long repetitive lifting in the primary direction (flexion + compression) characterised by high levels of repetitions, weight, and flexion, the effects in less severe scenarios need to be explored. This investigation could be achieved by reducing the level of replicated lifting repetitions, carried weight or degree of flexion or by investigating the effects of varying combinations

of these factors. Further research could deepen insights by examining the mechanical impact of replicating additional postures likely to be associated with repetitive lifting. These postures could be mimicked by combining axial rotation or lateral bending with compression and flexion. Understanding the intrinsic effects of variables related to the severity of repetitive lifting tasks and associated motions is critical for developing safety guidelines for workers and, more specifically, for developing recommendations to suit a day's lifting activities.

Given that repetitive lifting likely necessitates the creation of needle injuries for diagnostic or therapeutic purposes, this research's examination of repetitive lifting's impact on the morphology of needle injuries within the annulus fibrosus encountered limitations due to the inherent variability in forms of needle injuries. This variability posed a significant challenge, as it could cause the variability noticed in measurements, potentially concealing hidden effects. This issue presented a challenge in drawing definitive conclusions about the morphology of injuries and their evolution under conditions of repetitive lifting. The preliminary analysis, which identified parallel, cross, and novel hybrid forms of injuries, suggests that each injury form may respond differently to repetitive lifting. Although this variability poses a challenge, it suggests a methodological refinement, limiting the depth of perpendicular sectioning to the injury axis and confining morphological measurements to a single annular layer where the form of injury remains consistent across sectioned slices. Further, the technical difficulties encountered during the sectioning of injuries, which caused a significant reduction in sample size, likely impacted the overall findings and statistical power. Future studies will require improved sectioning techniques, non-invasive imaging technology to reduce specimen loss, and substantially larger sample sizes (506 to 8724 samples), though obtaining such samples will present logistical challenges. This in turn highlights the potential utility of simulations like finite element analysis (FEA) as an alternative approach to complement experimental data and reduce reliance on large physical samples. By overcoming the limitations of this research, future research could provide more definitive insights into the differential responses of needle injury forms to

repetitive lifting, ultimately contributing to improved disc diagnostic and therapeutic strategies.

7.4 Conclusion

This research adds to the knowledge of the mechanical effects of repetitive lifting on the intervertebral disc and its interaction with needle injuries, which may arise due to demanding clinical intervention. The most important finding of this research showed that the sole impact of repetitive lifting under combined flexion and compression led to an irreversible decrease in FSU flexion stiffness. Compounded by disc needle injury and further simulated repetitive lifting, the disc adjusted its mechanical response with a compensatory mechanism to maintain bending stiffness equilibrium to protect the injured side from more injury. This phenomenon suggests an inherent resilience of the disc and highlights the importance of recognising these responses for developing effective injury management and prevention strategies. The research further highlighted the intrinsic heterogeneity in needle injury forms, which is essential for consideration in future studies on the impact of mechanical loading on their morphological development. Beyond the parallel form, aligning with oblique annular fibres, and the cross form, intersecting fibre orientations, this study presented a hybrid form combining both characteristics for the first time. This observation underlines the importance of considering varied injury forms in studies of disc mechanics and their implications for the development of injury morphology, not limited to needle injuries but also including annulus injuries in general, as a broader potential.

Chapter 8 References

- ADAMS, M., BOGDUK, N., BURTON, K. & DOLAN, P. 2002. *The Biomechanics of Back Pain*, Churchill Livingstone, Edinburgh, London, New York. Oxford, Philadelphia.
- ADAMS, M. & DOLAN, P. 1995. Recent advances in lumbar spinal mechanics and their clinical significance. *Clinical Biomechanics*, 10, 3-19.
- ADAMS, M. & HUTTON, W. 1982. Prolapsed intervertebral disc: a hyperflexion injury. *Spine*, 7, 184-191.
- ADAMS, M. & HUTTON, W. 1983. The effect of posture on the fluid content of lumbar intervertebral discs. *Spine*, 8, 665-671.
- ADAMS, M., MCNALLY, D. & DOLAN, P. 1996. 'STRESS'DISTRIBUTIONS INSIDE INTERVERTEBRAL DISCS: THE EFFECTS OF AGE AND DEGENERATION. *The Journal of bone and joint surgery. British volume*, 78, 965-972.
- ADAMS, M. A. 2004. Biomechanics of back pain. *Acupuncture in medicine*, 22, 178-188.
- ADAMS, M. A., FREEMAN, B. J., MORRISON, H. P., NELSON, I. W. & DOLAN, P. 2000. Mechanical initiation of intervertebral disc degeneration. *Spine*, 25, 1625-1636.
- ADAMS, M. A. & HUTTON, W. 1985. Gradual disc prolapse. *Spine*, 10, 524-531.
- ADAMS, M. A. & ROUGHLEY, P. J. 2006a. What is intervertebral disc degeneration, and what causes it? *Spine*, 31, 2151-2161.
- ADAMS, M. A. & ROUGHLEY, P. J. 2006b. What is intervertebral disc degeneration, and what causes it? *Spine (Phila Pa 1976)*, 31, 2151-61.
- ADAMS, P. & MUIR, H. 1976. Qualitative changes with age of proteoglycans of human lumbar discs. *Annals of the rheumatic diseases*, 35, 289-296.
- AIHW 2023. Chronic musculoskeletal conditions. Canberra.
- ALI, A., KHAN, S. A., AURANGZEB, A., AHMED, E., ALI, G., MUHAMMAD, G. & MEHMOOD, S. 2013. Lumbar disc herniation in patients with chronic backache. *Journal of Ayub Medical College Abbottabad*, 25, 68-70.
- AMIN, D. 2019a. *Analysis of Internal Strains and Mechanics During Simulated Repetitive Lifting Motions in Human Lumbar Spinal Segments*. Flinders University, College of Science and Engineering.
- AMIN, D., MOAWAD, C. & COSTI, J. 2019b. New Findings Confirm Regional Internal Disc Strain Changes During Simulation of Repetitive Lifting Motions. *Annals of biomedical engineering*, 47, 1378-1390.
- AMIN, D. B., LAWLESS, I. M., SOMMERFELD, D., STANLEY, R. M., DING, B. & COSTI, J. J. 2016a. The effect of six degree of freedom loading sequence on the in-vitro compressive properties of human lumbar spine segments. *Journal of biomechanics*, 49, 3407-3414.
- AMIN, D. B., SOMMERFELD, D., LAWLESS, I. M., STANLEY, R. M., DING, B. & COSTI, J. J. 2016b. Effect of degeneration on the six degree of freedom mechanical properties of human lumbar spine segments. *Journal of Orthopaedic Research*, 34, 1399-1409.

- AMIN, D. B., TAVAKOLI, J., FREEMAN, B. J. & COSTI, J. J. 2020. Mechanisms of Failure Following Simulated Repetitive Lifting: A Clinically Relevant Biomechanical Cadaveric Study. *Spine*, 45, 357-367.
- ANDERSON, D. G., LI, X., TANNOURY, T., BECK, G. & BALIAN, G. 2003. A fibronectin fragment stimulates intervertebral disc degeneration in vivo. *Spine*, 28, 2338-2345.
- ANDERSSON, G. B. 1999. Epidemiological features of chronic low-back pain. *The lancet*, 354, 581-585.
- ANKEL-SIMONS, F. 2010. *Primate anatomy: an introduction*, Elsevier.
- ANTONIOU, J., STEFFEN, T., NELSON, F., WINTERBOTTOM, N., HOLLANDER, A. P., POOLE, R. A., AEBI, M. & ALINI, M. 1996. The human lumbar intervertebral disc: evidence for changes in the biosynthesis and denaturation of the extracellular matrix with growth, maturation, ageing, and degeneration. *The Journal of clinical investigation*, 98, 996-1003.
- ASANO, S., KANEDA, K., UMEHARA, S. & TADANO, S. 1992. The mechanical properties of the human L4–5 functional spinal unit during cyclic loading: the structural effects of the posterior elements. *Spine*, 17, 1343-1352.
- ASHTON-MILLER, J. A. & SCHULTZ, A. B. 1997. Biomechanics of the human spine. *Basic Orthopaedic Biomechanics*. Philadelphia: Lippincott–Raven, 353-93.
- BEAUCHEMIN, P., BAYLY, P., GARBOW, J., SCHMIDT, J., OKAMOTO, R., CHÉRIET, F. & PÉRIÉ, D. 2018. Frequency-dependent shear properties of annulus fibrosus and nucleus pulposus by magnetic resonance elastography. *NMR in Biomedicine*, 31, e3918.
- BEN-ABRAHAM, E. I., CHEN, J., FELMLEE, J. P., ROSSMAN, P., MANDUCA, A., AN, K.-N. & EHMAN, R. L. 2017. Feasibility of MR elastography of the intervertebral disc. *Magnetic resonance imaging*, 39, 132-137.
- BERGER-ROSCHE, N., CASAROLI, G., RASCHE, V., VILLA, T., GALBUSERA, F. & WILKE, H.-J. 2017. Influence of complex loading conditions on intervertebral disc failure. *Spine*, 42, E78-E85.
- BETEGÓN-PUTZE, I., GONZALEZ, A., SEVILLANO, X., BLASCO-ESCÁMEZ, D. & CAÑO-DELGADO, A. I. 2019. My ROOT: a method and software for the semiautomatic measurement of primary root length in Arabidopsis seedlings. *The Plant Journal*, 98, 1145-1156.
- BEZCI, S. E., NANDY, A. & O'CONNELL, G. D. 2015. Effect of Hydration on Healthy Intervertebral Disk Mechanical Stiffness. *Journal of Biomechanical Engineering*, 137.
- BOGDUK, N. 2004. International Spine Intervention Society & Standards Committee. *Practice guidelines for spinal diagnostic and treatment procedures*.
- BOOS, N., WEISSBACH, S., ROHRBACH, H., WEILER, C., SPRATT, K. F. & NERLICH, A. G. 2002. Classification of age-related changes in lumbar intervertebral discs: 2002 Volvo Award in basic science. *Spine*, 27, 2631-2644.
- BRUEHLMANN, S. B., HULME, P. A. & DUNCAN, N. A. 2004a. In situ intercellular mechanics of the bovine outer annulus fibrosus subjected to biaxial strains. *Journal of biomechanics*, 37, 223-231.

- BRUEHLMANN, S. B., MATYAS, J. R. & DUNCAN, N. A. 2004b. ISSLS prize winner: Collagen fibril sliding governs cell mechanics in the annulus fibrosus: an in situ confocal microscopy study of bovine discs. *Spine*, 29, 2612-2620.
- BUCKLEY, C. T., HOYLAND, J. A., FUJII, K., PANDIT, A., IATRIDIS, J. C. & GRAD, S. 2018. Critical aspects and challenges for intervertebral disc repair and regeneration—Harnessing advances in tissue engineering. *Jor Spine*, 1, e1029.
- CALLAGHAN, J. P. & MCGILL, S. M. 2001. Intervertebral disc herniation: studies on a porcine model exposed to highly repetitive flexion/extension motion with compressive force. *Clinical biomechanics*, 16, 28-37.
- CARRAGEE, E. J., DON, A. S., HURWITZ, E. L., CUELLAR, J. M., CARRINO, J. & HERZOG, R. 2009. 2009 ISSLS prize winner: does discography cause accelerated progression of degeneration changes in the lumbar disc: a ten-year matched cohort study. *Spine*, 34, 2338-2345.
- CASSIDY, J., HILTNER, A. & BAER, E. 1989. Hierarchical structure of the intervertebral disc. *Connective tissue research*, 23, 75-88.
- CENTERVILLE, O., NIAGARA, W., SPINE, A., CENTER, I. P., WOODBINE, D., MANCHIKANTI, L., MEDTRONIC, S. & STRYKER, N. 2018. An update of the systematic appraisal of the accuracy and utility of discography in chronic spinal pain. *Pain physician*, 21, 91-110.
- CHAN, D. D. & NEU, C. P. 2014. Intervertebral disc internal deformation measured by displacements under applied loading with MRI at 3T. *Magnetic resonance in medicine*, 71, 1231-1237.
- CHAO, S., PACELLA, M. J. & TORG, J. S. 2010. The pathomechanics, pathophysiology and prevention of cervical spinal cord and brachial plexus injuries in athletics. *Sports medicine*, 40, 59-75.
- CHEN, Y. & GAO, Z. 2023. Progress in Discography. *Spine Surgery and Related Research*, 7, 129-135.
- CHEUNG, J. P. Y. & LUK, K. D. K. 2019. The relevance of high-intensity zones in degenerative disc disease. *International orthopaedics*, 43, 861-867.
- CHO, H., LEE, S., PARK, S.-H., HUANG, J., HASTY, K. A. & KIM, S.-J. 2013. Synergistic effect of combined growth factors in porcine intervertebral disc degeneration. *Connective tissue research*, 54, 181-186.
- COHEN, J. 2013. *Statistical power analysis for the behavioral sciences*, Academic press.
- COHEN, N. P., FOSTER, R. J. & MOW, V. C. 1998. Composition and dynamics of articular cartilage: structure, function, and maintaining healthy state. *Journal of Orthopaedic & Sports Physical Therapy*, 28, 203-215.
- COOPER, S. 2018. Lifting, pushing and pulling (manual handling). Safe Work Australia.
- CORTES, D. H., MAGLAND, J. F., WRIGHT, A. C. & ELLIOTT, D. M. 2014. The shear modulus of the nucleus pulposus measured using magnetic resonance elastography: a potential biomarker for intervertebral disc degeneration. *Magnetic resonance in medicine*, 72, 211-219.
- COSTI, J. J., HEARN, T. C. & FAZZALARI, N. L. 2002. The effect of hydration on the stiffness of intervertebral discs in an ovine model. *Clinical biomechanics*, 17, 446-455.

- COSTI, J. J., STOKES, I. A., GARDNER-MORSE, M. G. & IATRIDIS, J. C. 2008a. Frequency-dependent behavior of the intervertebral disc in response to each of six degree of freedom dynamic loading: solid phase and fluid phase contributions. *Spine*, 33, 1731.
- COSTI, J. J., STOKES, I. A., GARDNER-MORSE, M. G. & IATRIDIS, J. C. 2008b. Frequency-dependent behavior of the intervertebral disc in response to each of six degree of freedom dynamic loading: solid phase and fluid phase contributions. *Spine*, 33, 1731-1738.
- CUNHA, C., LAMAS, S., GONÇALVES, R. M. & BARBOSA, M. A. 2017. Joint analysis of IVD herniation and degeneration by rat caudal needle puncture model. *Journal of Orthopaedic Research*, 35, 258-268.
- DALL'ARA, E., PEÑA-FERNÁNDEZ, M., PALANCA, M., GIORGI, M., CRISTOFOLINI, L. & TOZZI, G. 2017. Precision of digital volume correlation approaches for strain analysis in bone imaged with micro-computed tomography at different dimensional levels. *Frontiers in Materials*, 4, 31.
- DAVIS, M. A. 2012. Where the United States spends its spine dollars: expenditures on different ambulatory services for the management of back and neck conditions. *Spine*, 37, 1693.
- DEYO, R. A. & MIRZA, S. K. 2016. Herniated lumbar intervertebral disk. *New England Journal of Medicine*, 374, 1763-1772.
- DING, B., CAZZOLATO, B. S., STANLEY, R. M., GRAINGER, S. & COSTI, J. J. 2014. Stiffness analysis and control of a stewart platform-based manipulator with decoupled sensor-actuator locations for ultrahigh accuracy positioning under large external loads. *Journal of Dynamic Systems, Measurement, and Control*, 136, 061008.
- DING, B., STANLEY, R. M., CAZZOLATO, B. S. & COSTI, J. J. Real-time FPGA control of a hexapod robot for 6-DOF biomechanical testing. IECON 2011-37th Annual Conference on IEEE Industrial Electronics Society, 2011. IEEE, 252-257.
- DISNEY, C., ECKERSLEY, A., MCCONNELL, J., GENG, H., BODEY, A., HOYLAND, J., LEE, P., SHERRATT, M. & BAY, B. 2019. Synchrotron tomography of intervertebral disc deformation quantified by digital volume correlation reveals microstructural influence on strain patterns. *Acta biomaterialia*, 92, 290-304.
- DOLAN, P. & ADAMS, M. 1998. Repetitive lifting tasks fatigue the back muscles and increase the bending moment acting on the lumbar spine. *Journal of biomechanics*, 31, 713-721.
- DRAKE, J. D., AULTMAN, C. D., MCGILL, S. M. & CALLAGHAN, J. P. 2005. The influence of static axial torque in combined loading on intervertebral joint failure mechanics using a porcine model. *Clinical Biomechanics*, 20, 1038-1045.
- E SILVA, J. M. D. S., UTSCH, J., KIMM, M. A., ALLNER, S., EPPLE, M. F., ACHTERHOLD, K. & PFEIFFER, F. 2017. Dual-energy micro-CT for quantifying the time-course and staining characteristics of ex-vivo animal organs treated with iodine-and gadolinium-based contrast agents. *Scientific reports*, 7, 17387.

- EDWARDS, W. T., ORDWAY, N., ZHENG, Y., MCCULLEN, G., HAN, Z. & YUAN, H. A. 2001. Peak stresses observed in the posterior lateral annulus. *Spine*, 26, 1753-1759.
- ELLIOTT, D. M., YERRAMALLI, C. S., BECKSTEIN, J. C., BOXBERGER, J. I., JOHANNESSEN, W. & VRESILOVIC, E. J. 2008. The effect of relative needle diameter in puncture and sham injection animal models of degeneration. *Spine*, 33, 588-596.
- ERNST, C., STADNIK, T., PEETERS, E., BREUCQ, C. & OSTEAX, M. 2005. Prevalence of annular tears and disc herniations on MR images of the cervical spine in symptom free volunteers. *European journal of radiology*, 55, 409-414.
- FAVERLY, D. R., HENDRIKS, J. H. & HOLLAND, R. 2001. Breast carcinomas of limited extent: frequency, radiologic-pathologic characteristics, and surgical margin requirements. *Cancer*, 91, 647-659.
- FAZZALARI, L. N., COSTI, J. J., HEARN, C. T., FRASER, D. R., VERNON-ROBERTS, A. B., HUTCHINSON, H. J., MANTHEY, H. B., PARKINSON, H. I. & SINCLAIR, H. C. 2001a. Mechanical and Pathologic Consequences of Induced Concentric Annular Tears in an Ovine Model. *Spine*, 26, 2575-2581.
- FAZZALARI, N. L., COSTI, J. J., HEARN, T. C., FRASER, R. D., VERNON-ROBERTS, B., HUTCHINSON, J., MANTHEY, B. A. & PARKINSON, I. H. 2001b. Mechanical and pathologic consequences of induced concentric annular tears in an ovine model. *Spine*, 26, 2575-2581.
- FAZZALARI, N. L., COSTI, J. J., HEARN, T. C., FRASER, R. D., VERNON-ROBERTS, B., HUTCHINSON, J., MANTHEY, B. A., PARKINSON, I. H. & SINCLAIR, C. 2001c. Mechanical and pathologic consequences of induced concentric annular tears in an ovine model. *Spine*, 26, 2575-2581.
- FERGUSON, S. J. & STEFFEN, T. 2003. Biomechanics of the aging spine. *European Spine Journal*, 12, S97-S103.
- FRYMOYER, J. W. & WIESEL, S. W. 2004. *The adult and pediatric spine*, Lippincott Williams & Wilkins.
- GADD, M. & SHEPHERD, D. 2011. Viscoelastic properties of the intervertebral disc and the effect of nucleus pulposus removal. *Proceedings of the Institution of Mechanical Engineers, Part H: Journal of Engineering in Medicine*, 225, 335-341.
- GALANTE, J. O. 1967. Tensile properties of the human lumbar annulus fibrosus. *Acta Orthopaedica Scandinavica*, 38, 1-91.
- GILBERT, T., KREINER, D. S., RESNICK, D., O'NEILL, C., REITMAN, C., SHAFFER, W. O. & SUMMERS, J. NASS Clinical Guidelines Committee William C. Watters III, MD, Committee Chair Jamie Baisden, MD, Surgical Treatment Chair.
- GONZÁLEZ, A., SEVILLANO, X., BETEGÓN-PUTZE, I., BLASCO-ESCÁMEZ, D., FERRER, M. & CAÑO-DELGADO, A. I. 2020. MyROOT 2.0: An automatic tool for high throughput and accurate primary root length measurement. *Computers and electronics in agriculture*, 168, 105125.
- GORDON, S. J., YANG, K. H., MAYER, P. J., MACE JR, A. H., KISH, V. L. & RADIN, E. L. 1991. Mechanism of disc rupture. A preliminary report. *Spine*, 16, 450-456.

- GOTH, W., LESICKO, J., SACKS, M. S. & TUNNELL, J. W. 2016. Optical-based analysis of soft tissue structures. *Annual review of biomedical engineering*, 18, 357-385.
- GREENWALD, R. A., MOY, W. W. & SEIBOLD, J. Functional properties of cartilage proteoglycans. *Seminars in arthritis and rheumatism*, 1978. Elsevier, 53-67.
- HADLEY, L. 1961. Anatomico-roentgenographic studies of the posterior spinal articulations. *The American journal of roentgenology, radium therapy, and nuclear medicine*, 86, 270-276.
- HAEFELI, M., KALBERER, F., SAEGESSER, D., NERLICH, A. G., BOOS, N. & PAESOLD, G. 2006. The course of macroscopic degeneration in the human lumbar intervertebral disc. *Spine*, 31, 1522-1531.
- HAN, B., ZHU, K., LI, F.-C., XIAO, Y.-X., FENG, J., SHI, Z.-L., LIN, M., WANG, J. & CHEN, Q.-X. 2008. A simple disc degeneration model induced by percutaneous needle puncture in the rat tail. *Spine*, 33, 1925-1934.
- HANSSON, T., KELLER, T. & SPENGLER, D. 1987. Mechanical behavior of the human lumbar spine. II. Fatigue strength during dynamic compressive loading. *Journal of Orthopaedic Research*, 5, 479-487.
- HARTVIGSEN, J., HANCOCK, M. J., KONGSTED, A., LOUW, Q., FERREIRA, M. L., GENEVAY, S., HOY, D., KARPPINEN, J., PRANSKY, G. & SIEPER, J. 2018. What low back pain is and why we need to pay attention. *The Lancet*, 391, 2356-2367.
- HARVEY-BURGESS, M. & GREGORY, D. E. 2019. The Effect of Axial Torsion on the Mechanical Properties of the Annulus Fibrosus. *Spine*, 44, E195-E201.
- HEALTH, A. I. O. & WELFARE 2019. Back problems. Canberra: AIHW.
- HEDGES, L. & OLKIN, I. 1985. Parametric estimation of effect size from a series of experiments. *Statistical methods for meta-analysis*, 107-145.
- HENEWEER, H., STAES, F., AUFDEM KAMPE, G., VAN RIJN, M. & VANHEES, L. 2011. Physical activity and low back pain: a systematic review of recent literature. *European Spine Journal*, 20, 826-845.
- HILTON, R. C., BALL, J. & BENN, R. T. 1976. Vertebral end-plate lesions (Schmorl's nodes) in the dorsolumbar spine. *Annals of the Rheumatic Diseases*, 35, 127-132.
- HIRSCH, C. & SCHAJOWICZ, F. 1952. Studies on Structural Changes in the Lumbar Annulus Fibrosus. *Acta Orthopaedica Scandinavica*, 22, 184-231.
- HOY, D. 2010. The global burden of low back pain: estimates from the Global Burden of Disease 2010 study [published online ahead of print March 24, 2014]. *Ann Rheum Dis*. doi, 10.
- HSIEH, A. H., HWANG, D., RYAN, D. A., FREEMAN, A. K. & KIM, H. 2009. Degenerative anular changes induced by puncture are associated with insufficiency of disc biomechanical function. *Spine*, 34, 998-1005.
- HUANG, Y.-C., URBAN, J. P. & LUK, K. D. 2014. Intervertebral disc regeneration: do nutrients lead the way? *Nature Reviews Rheumatology*, 10, 561.
- HUNT, C. L., LAW, L. A. & QU, W. 2019. Regenerative Therapies for Chronic Intradiscal Pain. *Deer's Treatment of Pain*. Springer.

- HUR, J.-W., RYU, K.-S., KIM, J.-S. & SEONG, J.-H. 2016. Long-Term Follow-up of Disc Degeneration after Discography: Minimum 5-Year Follow-Up at a Single Center Experience. *Global Spine Journal*, 6, s-0036-1582645-s-0036-1582645.
- IATRIDIS, J. C. & AP GWYNN, I. 2004. Mechanisms for mechanical damage in the intervertebral disc annulus fibrosus. *Journal of biomechanics*, 37, 1165-1175.
- IATRIDIS, J. C., WEIDENBAUM, M., SETTON, L. A. & MOW, V. C. 1996. Is the nucleus pulposus a solid or a fluid? Mechanical behaviors of the nucleus pulposus of the human intervertebral disc. *Spine*, 21, 1174-1184.
- IJIMA, H., TADA, T., KUMADA, T., KOBAYASHI, N., YOSHIDA, M., AOKI, T., NISHIMURA, T., NAKANO, C., ISHII, A. & TAKASHIMA, T. 2019. Comparison of liver stiffness assessment by transient elastography and shear wave elastography using six ultrasound devices. *Hepatology Research*.
- INOUE, H. & TAKEDA, T. 1975. Three-dimensional observation of collagen framework of lumbar intervertebral discs. *Acta Orthopaedica Scandinavica*, 46, 949-956.
- JI, Y., LITAO, R., REN, W., DUN, G., LIU, J., ZHANG, Y. & WAN, Q. 2019. Stiffness of prostate gland measured by transrectal Real-Time shear wave elastography for detection of prostate cancer: A feasibility study. *The British journal of radiology*, 92, 20180970.
- JORDAN, J. L., KONSTANTINOU, K. & O'DOWD, J. 2011. Herniated lumbar disc. *BMJ clinical evidence*, 2011.
- KAIGLE, A. M., HOLM, S. H. & HANSSON, T. H. 1997. 1997 volvo award winner in biomechanical studies: Kinematic behavior of the porcine lumbar spine: A chronic lesion model. *Spine*, 22, 2796-2806.
- KAZARIAN, L. E. & KALEPS, I. 1979. *Mechanical and physical properties of the human intervertebral joint*, Aerospace Medical Research Laboratories.
- KELSEY, J. L. 1975. An epidemiological study of the relationship between occupations and acute herniated lumbar intervertebral discs. *International Journal of Epidemiology*, 4, 197-205.
- KELSEY, J. L., GITHEENS, P. B., WHITE III, A. A., HOLFORD, T. R., WALTER, S. D., O'CONNOR, T., OSTFELD, A. M., WEIL, U., SOUTHWICK, W. O. & CALOGERO, J. A. 1984. An epidemiologic study of lifting and twisting on the job and risk for acute prolapsed lumbar intervertebral disc. *Journal of orthopaedic research*, 2, 61-66.
- KEOROCHANA, G., JOHNSON, J. S., TAGHAVI, C. E., LIAO, J.-C., LEE, K.-B., YOO, J. H., NGO, S. S. & WANG, J. C. 2010. The effect of needle size inducing degeneration in the rat caudal disc: evaluation using radiograph, magnetic resonance imaging, histology, and immunohistochemistry. *The spine journal*, 10, 1014-1023.
- KERR, G. J., VERAS, M. A., KIM, M. K. M. & SÉGUIN, C. A. Decoding the intervertebral disc: Unravelling the complexities of cell phenotypes and pathways associated with degeneration and mechanotransduction. *Seminars in cell & developmental biology*, 2017. Elsevier, 94-103.
- KHALAF, K., NIKKHOO, M., KARGAR, R. & NAJAFZADEH, S. The effect of needle puncture injury on the biomechanical response of intervertebral

- discs. *Orthopaedic Proceedings*, 2017. The British Editorial Society of Bone & Joint Surgery, 122-122.
- KIM, K. S., YOON, S. T., LI, J., PARK, J. S. & HUTTON, W. C. 2005. Disc degeneration in the rabbit: a biochemical and radiological comparison between four disc injury models. *Spine*, 30, 33-37.
- KIRKALDY-WILLIS, W. H. & FARFAN, H. F. 1982. Instability of the lumbar spine. *Clin Orthop Relat Res*, 110-23.
- KOELLER, W., MEIER, W. & HARTMANN, F. 1984. Biomechanical properties of human intervertebral discs subjected to axial dynamic compression: a comparison of lumbar and thoracic discs. *Spine*, 9, 725-733.
- KOELLER, W., MUEHLHAUS, S., MEIER, W. & HARTMANN, F. 1986. Biomechanical properties of human intervertebral discs subjected to axial dynamic compression—influence of age and degeneration. *Journal of Biomechanics*, 19, 807-816.
- KOO, T. K. & LI, M. Y. 2016. A guideline of selecting and reporting intraclass correlation coefficients for reliability research. *Journal of chiropractic medicine*, 15, 155-163.
- KOPPENHAVER, S. L., SCUTELLA, D., SORRELL, B. A., YAHALOM, J., FERNÁNDEZ-DE-LAS-PEÑAS, C., CHILDS, J. D., SHAFFER, S. W. & SHINOHARA, M. 2019. Normative parameters and anthropometric variability of lumbar muscle stiffness using ultrasound shear-wave elastography. *Clinical Biomechanics*, 62, 113-120.
- KORECKI, C. L., COSTI, J. J. & IATRIDIS, J. C. 2008. Needle puncture injury affects intervertebral disc mechanics and biology in an organ culture model. *Spine*, 33, 235.
- KRAEMER, J., KOLDITZ, D. & GOWIN, R. 1985. Water and electrolyte content of human intervertebral discs under variable load. *Spine*, 10, 69-71.
- LAMA, P., LE MAITRE, C., DOLAN, P., TARLTON, J., HARDING, I. & ADAMS, M. 2013. Do intervertebral discs degenerate before they herniate, or after? *The bone & joint journal*, 95, 1127-1133.
- LANGLAIS, T., DESPRAIRIES, P., PIETTON, R., ROHAN, P.-Y., DUBOUSSET, J., MEAKIN, J. R., WINLOVE, P. C., VIALLE, R., SKALLI, W. & VERGARI, C. 2019. Microstructural characterization of annulus fibrosus by ultrasonography: a feasibility study with an in vivo and in vitro approach. *Biomechanics and Modeling in Mechanobiology*, 1-8.
- LAWLESS, I., DING, B., CAZZOLATO, B. & COSTI, J. 2014. Adaptive velocity-based six degree of freedom load control for real-time unconstrained biomechanical testing. *Journal of biomechanics*, 47, 3241-3247.
- LI, X., ZHANG, C., HAGGERTY, A. E., YAN, J., LAN, M., SEU, M., YANG, M., MARLOW, M. M., MALDONADO-LASUNCIÓN, I. & CHO, B. 2020. The effect of a nanofiber-hydrogel composite on neural tissue repair and regeneration in the contused spinal cord. *Biomaterials*, 245, 119978.
- LIVSHITS, G., POPHAM, M., MALKIN, I., SAMBROOK, P. N., MACGREGOR, A. J., SPECTOR, T. & WILLIAMS, F. M. 2011. Lumbar disc degeneration and genetic factors are the main risk factors for low back pain in women: the UK Twin Spine Study. *Annals of the rheumatic diseases*, 70, 1740-1745.

- LOMBARDI, S., SCOLA, E., IPPOLITO, D., ZAMBELLI, V., BOTTA, G., CUTTIN, S., TRIULZI, F. & LOMBARDI, C. M. 2019. Micro-computed tomography: a new diagnostic tool in postmortem assessment of brain anatomy in small fetuses. *Neuroradiology*, 1-10.
- LU, M. Y., HUTTON, W. C. & GHARPURAY, V. M. 1996. Can variations in intervertebral disc height affect the mechanical function of the disc? *Spine*, 21, 2208-2216.
- LU, W. W., LUK, K. D., HOLMES, A. D., CHEUNG, K. M. & LEONG, J. C. 2005. Pure shear properties of lumbar spinal joints and the effect of tissue sectioning on load sharing. *Spine*, 30, E204-E209.
- MAERZ, T., NEWTON, M., KRISTOF, K., MOTOVYLYAK, O., FISCHGRUND, J., PARK, D. & BAKER, K. 2014. Three-dimensional characterization of in vivo intervertebral disc degeneration using EPIC- μ CT. *Osteoarthritis and cartilage*, 22, 1918-1925.
- MARCHAND, F. & AHMED, A. M. 1990. Investigation of the laminate structure of lumbar disc anulus fibrosus. *Spine*, 15, 402-410.
- MARGARITONDO, G. & HWU, Y. 2021. Imaging with coherent X-rays: From the early synchrotron tests to SYNAPSE. *Journal of Imaging*, 7, 132.
- MARRAS, W. S., LAVENDER, S. A., LEURGANS, S. E., FATHALLAH, F. A., FERGUSON, S. A., GARY ALLREAD, W. & RAJULU, S. L. 1995. Biomechanical risk factors for occupationally related low back disorders. *Ergonomics*, 38, 377-410.
- MARSHALL, L. W. & MCGILL, S. M. 2010. The role of axial torque in disc herniation. *Clinical Biomechanics*, 25, 6-9.
- MARTIN, J. T., GORTH, D. J., BEATTIE, E. E., HARFE, B. D., SMITH, L. J. & ELLIOTT, D. M. 2013. Needle puncture injury causes acute and long-term mechanical deficiency in a mouse model of intervertebral disc degeneration. *Journal of Orthopaedic Research*, 31, 1276-1282.
- MASUDA, K., AOTA, Y., MUEHLEMAN, C., IMAI, Y., OKUMA, M., THONAR, E. J., ANDERSSON, G. B. & AN, H. S. 2005. A novel rabbit model of mild, reproducible disc degeneration by an anulus needle puncture: correlation between the degree of disc injury and radiological and histological appearances of disc degeneration. *Spine*, 30, 5-14.
- MASUDA, K., IMAI, Y., OKUMA, M., MUEHLEMAN, C., NAKAGAWA, K., AKEDA, K., THONAR, E., ANDERSSON, G. & AN, H. S. 2006. Osteogenic protein-1 injection into a degenerated disc induces the restoration of disc height and structural changes in the rabbit anular puncture model. *Spine*, 31, 742-754.
- MEHTA, J. P., LAVENDER, S. A. & JAGACINSKI, R. J. 2014. Physiological and biomechanical responses to a prolonged repetitive asymmetric lifting activity. *Ergonomics*, 57, 575-588.
- MICHALEK, A., GARDNER-MORSE, M. & IATRIDIS, J. 2012. Large residual strains are present in the intervertebral disc annulus fibrosus in the unloaded state. *Journal of biomechanics*, 45, 1227-1231.
- MICHALEK, A. J., BUCKLEY, M. R., BONASSAR, L. J., COHEN, I. & IATRIDIS, J. C. 2009. Measurement of local strains in intervertebral disc annulus fibrosus tissue under dynamic shear: contributions of matrix fiber orientation and elastin content. *Journal of biomechanics*, 42, 2279-2285.

- MICHALEK, A. J., BUCKLEY, M. R., BONASSAR, L. J., COHEN, I. & IATRIDIS, J. C. 2010a. The effects of needle puncture injury on microscale shear strain in the intervertebral disc annulus fibrosus. *The Spine Journal*, 10, 1098-1105.
- MICHALEK, A. J., BUCKLEY, M. R., BONASSAR, L. J., COHEN, I. & IATRIDIS, J. C. 2010a. The effects of needle puncture injury on microscale shear strain in the intervertebral disc annulus fibrosus. *The Spine Journal*, 10, 1098-1105.
- MICHALEK, A. J., FUNABASHI, K. L. & IATRIDIS, J. C. 2010b. Needle puncture injury of the rat intervertebral disc affects torsional and compressive biomechanics differently. *European Spine Journal*, 19, 2110-2116.
- MICHALEK, A. J., FUNABASHI, K. L. & IATRIDIS, J. C. 2010b. Needle puncture injury of the rat intervertebral disc affects torsional and compressive biomechanics differently. *European Spine Journal*, 19, 2110-2116.
- MICHALEK, A. J. & IATRIDIS, J. C. 2011. Penetrating annulus fibrosus injuries affect dynamic compressive behaviors of the intervertebral disc via altered fluid flow: an analytical interpretation. *Journal of biomechanical engineering*, 133.
- MICHALEK, A. J. & IATRIDIS, J. C. 2012. Height and torsional stiffness are most sensitive to annular injury in large animal intervertebral discs. *The Spine Journal*, 12, 425-432.
- MIZUTANI, R., TAKEUCHI, A., UESUGI, K., TAKEKOSHI, S., OSAMURA, R. Y. & SUZUKI, Y. 2008. X-ray microtomographic imaging of three-dimensional structure of soft tissues. *Tissue Engineering Part C: Methods*, 14, 359-363.
- MÖLLER, B. & SCHATTAT, M. Quantification of Stromule Frequencies in Microscope Images of Plastids Combining Ridge Detection and Geometric Criteria. *BIOIMAGING*, 2019. 38-48.
- MUNDT, D. J., KELSEY, J. L., GOLDEN, A. L., PASTIDES, H., BERG, A. T., SKLAR, J., HOSEA, T. & PANJABI, M. M. 1993. An epidemiologic study of non-occupational lifting as a risk factor for herniated lumbar intervertebral disc. *Spine*, 18, 595-602.
- NACHEMSON, A. & MORRIS, J. M. 1964. In vivo measurements of intradiscal pressure: discometry, a method for the determination of pressure in the lower lumbar discs. *JBJ*, 46, 1077-1092.
- NATARAJAN, R. N. & ANDERSSON, G. B. 1999. The influence of lumbar disc height and cross-sectional area on the mechanical response of the disc to physiologic loading. *Spine*, 24, 1873.
- NELISSEN, J. L., SINKUS, R., NICOLAY, K., NEDERVEEN, A. J., OOMENS, C. W. & STRIJKERS, G. J. 2019. Magnetic resonance elastography of skeletal muscle deep tissue injury. *NMR in Biomedicine*, e4087.
- NEWELL, N., LITTLE, J. P., CHRISTOU, A., ADAMS, M. A., ADAM, C. J. & MASOUIROS, S. D. 2017. Biomechanics of the human intervertebral disc: A review of testing techniques and results. *Journal of the Mechanical Behavior of Biomedical Materials*, 69, 420-434.

- NIKKHOO, M., KARGAR, R. & KHALAF, K. Biphasic Rheology of Different Artificial Degenerated Intervertebral Discs. World Congress on Medical Physics and Biomedical Engineering 2018, 2019. Springer, 671-674.
- O'CONNELL, G. D., JOHANNESSEN, W., VRESILOVIC, E. J. & ELLIOTT, D. M. 2007. Human internal disc strains in axial compression measured noninvasively using magnetic resonance imaging. *Spine*, 32, 2860-2868.
- OSTI, O., VERNON-ROBERTS, B., MOORE, R. & FRASER, R. 1992. Annular tears and disc degeneration in the lumbar spine. A post-mortem study of 135 discs. *The Journal of bone and joint surgery. British volume*, 74, 678-682.
- OSTI, O. L., VERNON-ROBERTS, B. & FRASER, R. D. 1990. 1990 Volvo Award in experimental studies. Anulus tears and intervertebral disc degeneration. An experimental study using an animal model. *Spine (Phila Pa 1976)*, 15, 762-7.
- PANSARE, V. J., HEJAZI, S., FAENZA, W. J. & PRUD'HOMME, R. K. 2012. Review of long-wavelength optical and NIR imaging materials: contrast agents, fluorophores, and multifunctional nano carriers. *Chemistry of materials*, 24, 812-827.
- PEARCY, M. & TIBREWAL, S. 1984. Axial rotation and lateral bending in the normal lumbar spine measured by three-dimensional radiography. *Spine*, 9, 582-587.
- PEARCY, M. J. 1985. Stereo radiography of lumbar spine motion. *Acta Orthopaedica Scandinavica*, 56, 1-45.
- PEARCY, M. J. & BOGDUK, N. 1988. Instantaneous axes of rotation of the lumbar intervertebral joints. *Spine*, 13, 1033-1041.
- PELLE, D. W., PEACOCK, J. D., SCHMIDT, C. L., KAMPFSCHULTE, K., SCHOLTEN, D. J., RUSSO, S. S., EASTON, K. J. & STEENSMA, M. R. 2014. Genetic and functional studies of the intervertebral disc: a novel murine intervertebral disc model. *PloS one*, 9, e112454.
- PENM, E., DIXON, T. & BHATIA, K. 2006. *Health Expenditure for Arthritis and Musculoskeletal Conditions in Australia, 2000-01*, Australian Institute of Health and Welfare.
- PEZOWICZ, C. A., ROBERTSON, P. A. & BROOM, N. D. 2006. The structural basis of interlamellar cohesion in the intervertebral disc wall. *Journal of anatomy*, 208, 317-330.
- PUNNETT, L., FINE, L. J., KEYSERLING, W. M., HERRIN, G. D. & CHAFFIN, D. B. 1991. Back disorders and nonneutral trunk postures of automobile assembly workers. *Scandinavian journal of work, environment & health*, 337-346.
- RACE, A., BROOM, N. D. & ROBERTSON, P. 2000. Effect of loading rate and hydration on the mechanical properties of the disc. *Spine*, 25, 662-669.
- RAJ, P. P. 2008. Intervertebral disc: anatomy-physiology-pathophysiology-treatment. *Pain Pract*, 8, 18-44.
- RAJASEKARAN, S., BAJAJ, N., TUBAKI, V., KANNA, R. M. & SHETTY, A. P. 2013. ISSLS Prize Winner: The Anatomy of Failure in Lumbar Disc Herniation An In Vivo, Multimodal, Prospective Study of 181 Subjects. *Spine*, 38, 1491-1500.

- RAWLS, A. & FISHER, R. E. 2018. Developmental and functional anatomy of the spine. *The genetics and development of scoliosis*. Springer.
- REN, S., LIU, Y., MA, J., LIU, Y., DIAO, Z., YANG, D., ZHANG, X., XI, Y. & HU, Y. 2013. Treatment of rabbit intervertebral disc degeneration with co-transfection by adeno-associated virus-mediated SOX9 and osteogenic protein-1 double genes in vivo. *International journal of molecular medicine*, 32, 1063-1068.
- RIIHIMÄKI, H. 1991. Low-back pain, its origin and risk indicators. *Scandinavian journal of work, environment & health*, 81-90.
- ROBERTS, S., MENAGE, J. & URBAN, J. 1989. Biochemical and structural properties of the cartilage end-plate and its relation to the intervertebral disc. *Spine*, 14, 166-174.
- RODRIGUES, S. A., THAMBYAH, A. & BROOM, N. D. 2017. How maturity influences annulus-endplate integration in the ovine intervertebral disc: a micro-and ultra-structural study. *Journal of anatomy*, 230, 152-164.
- RUSSO, M. P. 2017. *Effects of Needle Insertion on Six Degree of Freedom Disc Mechanics*. Bachelor of Engineering (Biomedical)(Honours) thesis, Flinders University.
- SAPIEE, N. H., THAMBYAH, A., ROBERTSON, P. A. & BROOM, N. D. 2019. New evidence for structural integration across the cartilage-vertebral endplate junction and its relation to herniation. *The Spine Journal*, 19, 532-544.
- SCHMIDT, H., KETTLER, A., ROHLMANN, A., CLAES, L. & WILKE, H.-J. 2007. The risk of disc prolapses with complex loading in different degrees of disc degeneration—a finite element analysis. *Clinical biomechanics*, 22, 988-998.
- SCHMORL, G., GOIN, L.S., JUNGHANNS, H. AND WILK, S.P., 1959. The human spine in health and disease: anatomicopathologic studies. *Grune & Stratton*.
- SCHOLLUM, M. L., ROBERTSON, P. A. & BROOM, N. D. 2008. ISSLS prize winner: microstructure and mechanical disruption of the lumbar disc annulus: part I: a microscopic investigation of the translamellar bridging network. *Spine*, 33, 2702-2710.
- SCHOLLUM, M. L., ROBERTSON, P. A. & BROOM, N. D. 2009. A microstructural investigation of intervertebral disc lamellar connectivity: detailed analysis of the translamellar bridges. *Journal of anatomy*, 214, 805-816.
- SCHOLLUM, M. L., ROBERTSON, P. A. & BROOM, N. D. 2010. How age influences unravelling morphology of annular lamellae—a study of interfibre cohesivity in the lumbar disc. *Journal of anatomy*, 216, 310-319.
- SCHWAN, S., LUDTKA, C., FRIEDMANN, A., HEILMANN, A., BAERTHEL, A., BREHM, W., WIESNER, I., MEISEL, H. J. & GOEHRE, F. 2019. Long-term Pathology of Ovine Lumbar Spine Degeneration following Injury via Percutaneous Minimally Invasive Partial Nucleotomy. *Journal of Orthopaedic Research®*.
- SHARABI, M., WADE, K. R., GALBUSERA, F., RASCHE, V., HAJ-ALI, R. & WILKE, H.-J. 2018. Three-dimensional microstructural reconstruction of

- the ovine intervertebral disc using ultrahigh field MRI. *The Spine Journal*, 18, 2119-2127.
- SHARMA, A., PILGRAM, T. & WIPPOLD, F. 2009. Association between annular tears and disk degeneration: a longitudinal study. *American Journal of Neuroradiology*, 30, 500-506.
- SHU, C. C., SMITH, M. M., SMITH, S. M., DART, A. J., LITTLE, C. B. & MELROSE, J. 2017. A histopathological scheme for the quantitative scoring of intervertebral disc degeneration and the therapeutic utility of adult mesenchymal stem cells for intervertebral disc regeneration. *International journal of molecular sciences*, 18, 1049.
- SIVAN, S. S., WACHTEL, E. & ROUGHLEY, P. 2014. Structure, function, aging and turnover of aggrecan in the intervertebral disc. *Biochimica et Biophysica Acta (BBA)-General Subjects*, 1840, 3181-3189.
- SOBAJIMA, S., KOMPEL, J. F., KIM, J. S., WALLACH, C. J., ROBERTSON, D. D., VOGT, M. T., KANG, J. D. & GILBERTSON, L. G. 2005a. A slowly progressive and reproducible animal model of intervertebral disc degeneration characterized by MRI, X-ray, and histology. *Spine*, 30, 15-24.
- SOBAJIMA, S., SHIMER, A. L., CHADDERDON, R. C., KOMPEL, J. F., KIM, J. S., GILBERTSON, L. G. & KANG, J. D. 2005b. Quantitative analysis of gene expression in a rabbit model of intervertebral disc degeneration by real-time polymerase chain reaction. *The Spine Journal*, 5, 14-23.
- STOKES, I. & FRYMOYER, J. W. 1987. Segmental motion and instability. *Spine*, 12, 688-691.
- STRAKER, L. 1999. An overview of manual handling injury statistics in western Australia. *International Journal of Industrial Ergonomics*, 24, 357-364.
- STRASSER, J., HAINDL, M. T., STOLLBERGER, R., FAZEKAS, F. & ROPELE, S. 2019. Magnetic resonance elastography of the human brain using a multiphase DENSE acquisition. *Magnetic resonance in medicine*.
- STREITBERGER, K. J., DIEDERICHS, G., GUO, J., FEHLNER, A., HAMM, B., BRAUN, J. & SACK, I. 2015. In vivo multifrequency magnetic resonance elastography of the human intervertebral disk. *Magnetic resonance in medicine*, 74, 1380-1387.
- TAM, V., ROGERS, I., CHAN, D., LEUNG, V. Y. & CHEUNG, K. M. 2014. A comparison of intravenous and intradiscal delivery of multipotential stem cells on the healing of injured intervertebral disk. *Journal of Orthopaedic Research*, 32, 819-825.
- TAMPIER, C., DRAKE, J. D., CALLAGHAN, J. P. & MCGILL, S. M. 2007. Progressive disc herniation: an investigation of the mechanism using radiologic, histochemical, and microscopic dissection techniques on a porcine model. *Spine*, 32, 2869-2874.
- TANAKA, M. 2018. Biomechanical investigation on the influence of the regional material degeneration of an intervertebral disc in a lower lumbar spinal unit: A finite element study. *Computers in biology and medicine*, 98, 26-38.
- TAVAKOLI, J. & COSTI, J. J. 2018a. New findings confirm the viscoelastic behaviour of the inter-lamellar matrix of the disc annulus fibrosus in radial and circumferential directions of loading. *Acta biomaterialia*, 71, 411-419.

- TAVAKOLI, J. & COSTI, J. J. 2018b. Ultrastructural organization of elastic fibres in the partition boundaries of the annulus fibrosus within the intervertebral disc. *Acta biomaterialia*, 68, 67-77.
- TAVAKOLI, J., ELLIOTT, D. & COSTI, J. 2017. The ultra-structural organization of the elastic network in the intra-and inter-lamellar matrix of the intervertebral disc. *Acta biomaterialia*, 58, 269-277.
- TAVAKOLI, J., ELLIOTT, D. M. & COSTI, J. J. 2016. Structure and mechanical function of the inter-lamellar matrix of the annulus fibrosus in the disc. *Journal of Orthopaedic Research*, 34, 1307-1315.
- THOMPSON, J. P., PEARCE, R. H., SCHECHTER, M., ADAMS, M. E., TSANG, I. & BISHOP, P. B. 1990. *Preliminary Evaluation of a Scheme for Grading the Gross Morphology of the Human Intervertebral Disc*.
- THOMPSON, R. E., PEARCY, M. J., DOWNING, K. J., MANTHEY, B. A., PARKINSON, I. H. & FAZZALARI, N. L. 2000. Disc lesions and the mechanics of the intervertebral joint complex. *Spine (Phila Pa 1976)*, 25, 3026-35.
- TORG, J. S., GUILLE, J. T. & JAFFE, S. 2002. Injuries to the cervical spine in American football players. *JBJS*, 84, 112-122.
- TORRE, O. M., EVASHWICK-ROGLER, T. W., NASSER, P. & IATRIDIS, J. C. 2019. Biomechanical test protocols to detect minor injury effects in intervertebral discs. *Journal of the mechanical behavior of biomedical materials*, 95, 13-20.
- URBAN, J. P. & ROBERTS, S. 2003a. Degeneration of the intervertebral disc. *Arthritis Res Ther*, 5, 120.
- URBAN, J. P. G. & ROBERTS, S. 2003b. Degeneration of the intervertebral disc. *Arthritis Research & Therapy*, 5, 120-130.
- VAN HEESWIJK, V. 2017. *The regional susceptibility of the intervertebral disc to mechanically induced disruption and herniation*. ResearchSpace@Auckland.
- VAN HEESWIJK, V. M., THAMBYAH, A., ROBERTSON, P. A. & BROOM, N. D. 2018. Does an Annular Puncture Influence the Herniation Path? *Spine*, 43, 467-476.
- VERES, S. P., ROBERTSON, P. A. & BROOM, N. D. 2008. ISSLS prize winner: microstructure and mechanical disruption of the lumbar disc annulus: part II: how the annulus fails under hydrostatic pressure. *Spine*, 33, 2711-2720.
- VERES, S. P., ROBERTSON, P. A. & BROOM, N. D. 2009. The morphology of acute disc herniation: a clinically relevant model defining the role of flexion. *Spine*, 34, 2288-2296.
- VERES, S. P., ROBERTSON, P. A. & BROOM, N. D. 2010. ISSLS prize winner: how loading rate influences disc failure mechanics: a microstructural assessment of internal disruption. *Spine*, 35, 1897-1908.
- VERGARI, C., DUBOIS, G., VIALLE, R., GENNISSON, J.-L., TANTER, M., DUBOUSSET, J., ROUCH, P. & SKALLI, W. 2016a. Lumbar annulus fibrosus biomechanical characterization in healthy children by ultrasound shear wave elastography. *European radiology*, 26, 1213-1217.

- VERGARI, C., MANSFIELD, J., MEAKIN, J. R. & WINLOVE, P. C. 2016b. Lamellar and fibre bundle mechanics of the annulus fibrosus in bovine intervertebral disc. *Acta biomaterialia*, 37, 14-20.
- VERGARI, C., MANSFIELD, J. C., CHAN, D., CLARKE, A., MEAKIN, J. R. & WINLOVE, P. C. 2017. The effects of needle damage on annulus fibrosus micromechanics. *Acta biomaterialia*, 63, 274-282.
- VERGARI, C., ROUCH, P., DUBOIS, G., BONNEAU, D., DUBOUSSET, J., TANTER, M., GENNISSON, J.-L. & SKALLI, W. 2014a. Intervertebral disc characterization by shear wave elastography: An in vitro preliminary study. *Proceedings of the Institution of Mechanical Engineers, Part H: Journal of Engineering in Medicine*, 228, 607-615.
- VERGARI, C., ROUCH, P., DUBOIS, G., BONNEAU, D., DUBOUSSET, J., TANTER, M., GENNISSON, J.-L. & SKALLI, W. 2014b. Non-invasive biomechanical characterization of intervertebral discs by shear wave ultrasound elastography: a feasibility study. *European radiology*, 24, 3210-3216.
- VERNON-ROBERTS, B., FAZZALARI, N. L. & MANTHEY, B. A. 1997. Pathogenesis of tears of the anulus investigated by multiple-level transaxial analysis of the T12-L1 disc. *Spine*, 22, 2641-2646.
- VERNON-ROBERTS, B., MOORE, R. J. & FRASER, R. D. 2007. The natural history of age-related disc degeneration: the pathology and sequelae of tears. *Spine*, 32, 2797-2804.
- VITAL, J. M., DIMEGLIO, A., PETIT, M. & BOISSIÈRE, L. 2020. The Growth Cartilages of the Spine and Pelvic Vertebra. *Spinal Anatomy: Modern Concepts*, 53-74.
- VOS, T., ABAJOBIR, A. A., ABATE, K. H., ABBAFATI, C., ABBAS, K. M., ABD-ALLAH, F., ABDULKADER, R. S., ABDULLE, A. M., ABEBO, T. A. & ABERA, S. F. 2017. Global, regional, and national incidence, prevalence, and years lived with disability for 328 diseases and injuries for 195 countries, 1990–2016: a systematic analysis for the Global Burden of Disease Study 2016. *The Lancet*, 390, 1211-1259.
- WADE, K. R., ROBERTSON, P. A. & BROOM, N. D. 2011. A fresh look at the nucleus-endplate region: new evidence for significant structural integration. *European Spine Journal*, 20, 1225-1232.
- WADE, K. R., ROBERTSON, P. A. & BROOM, N. D. 2012a. On how nucleus-endplate integration is achieved at the fibrillar level in the ovine lumbar disc. *Journal of anatomy*, 221, 39-46.
- WADE, K. R., ROBERTSON, P. A. & BROOM, N. D. 2012b. On the extent and nature of nucleus-annulus integration. *Spine*, 37, 1826-1833.
- WALTER, B. A., MAGESWARAN, P., MO, X., BOULTER, D. J., MASHALY, H., NGUYEN, X. V., PREVEDELLO, L. M., THOMAN, W., RATERMAN, B. D. & KALRA, P. 2017. MR Elastography-derived Stiffness: A Biomarker for Intervertebral Disc Degeneration. *Radiology*, 285, 167-175.
- WATANABE, A., BENNEKER, L. M., BOESCH, C., WATANABE, T., OBATA, T. & ANDERSON, S. E. 2007. Classification of intervertebral disk degeneration with axial T2 mapping. *American Journal of Roentgenology*, 189, 936-942.

- WEI, Q., LIU, D., CHU, G., YU, Q., LIU, Z., LI, J., MENG, Q., WANG, W., HAN, F. & LI, B. 2023. TGF- β 1-supplemented decellularized annulus fibrosus matrix hydrogels promote annulus fibrosus repair. *Bioactive Materials*, 19, 581-593.
- WILKE, H.-J., KETTLER, A. & CLAES, L. E. 1997. Are sheep spines a valid biomechanical model for human spines? *Spine*, 22, 2365-2374.
- WILKE, H.-J., KIENLE, A., MAILE, S., RASCHE, V. & BERGER-ROSCHE, N. 2016. A new dynamic six degrees of freedom disc-loading simulator allows to provoke disc damage and herniation. *European Spine Journal*, 25, 1363-1372.
- WILKE, H. J., NEEF, P., CAIMI, M., HOOGLAND, T. & CLAES, L. E. 1999a. New in vivo measurements of pressures in the intervertebral disc in daily life. *Spine*, 24, 755-762.
- WILKE, H. J., NEEF, P., CAIMI, M., HOOGLAND, T. & E. CLAES, L. 1999b. *New In Vivo Measurements of Pressures in the Intervertebral Disc in Daily Life*.
- WIRTH, M. A. 2004. Shape analysis and measurement. *Image Processing Group*, 1-49.
- WRIGHT, A. C., YODER, J. H., VRESILOVIC, E. J. & ELLIOTT, D. M. 2016. Theory of MRI contrast in the annulus fibrosus of the intervertebral disc. *Magnetic Resonance Materials in Physics, Biology and Medicine*, 29, 711-722.
- WU, Q., SHI, D., CHENG, T., LIU, H., HU, N., CHANG, X., GUO, Y. & WANG, M. 2019. Improved display of cervical intervertebral discs on water (iodine) images: incidental findings from single-source dual-energy CT angiography of head and neck arteries. *European Radiology*, 29, 153-160.
- XIANG, L., MA, F., YAO, M., XU, G., PU, H., LIU, H., FANG, Y. & WU, R. 2019. Benign lesion evaluation: Factors causing the “stiff rim” sign in breast tissues using shear-wave elastography. *The British journal of radiology*, 92, 20180602.
- YAMAGUCHI, J. T. & HSU, W. K. 2019. Intervertebral disc herniation in elite athletes. *International orthopaedics*, 43, 833-840.
- YANG, C.-H., CHIANG, Y.-F., CHEN, C.-H., WU, L.-C., LIAO, C.-J. & CHIANG, C.-J. 2016. The effect of annular repair on the failure strength of the porcine lumbar disc after needle puncture and punch injury. *European Spine Journal*, 25, 906-912.
- YIN, Z., MURPHY, M. C., LI, J., GLASER, K. J., MAUER, A. S., MOUNAJJED, T., THERNEAU, T. M., LIU, H., MALHI, H. & MANDUCA, A. 2019. Prediction of nonalcoholic fatty liver disease (NAFLD) activity score (NAS) with multiparametric hepatic magnetic resonance imaging and elastography. *European radiology*, 1-9.
- ZEHR, J. D. & CALLAGHAN, J. P. 2023. Towards the estimation of ultimate compression tolerance as a function of cyclic compression loading history: implications for lifting-related low back injury risk assessment. *Theoretical Issues in Ergonomics Science*, 24, 547-563.
- ZHANG, H., LA MARCA, F., HOLLISTER, S. J., GOLDSTEIN, S. A. & LIN, C.-Y. 2009. Developing consistently reproducible intervertebral disc

degeneration at rat caudal spine by using needle puncture. *Journal of Neurosurgery: Spine*, 10, 522-530.

Appendices

Appendix A

A.1 Excluded stiffness and phase angle measurements from the mechanical testing of chapter 4

A.1.1 Noisy signal at the last compression cycle

A.1.1.1 Before (pre-) repetitive lifting

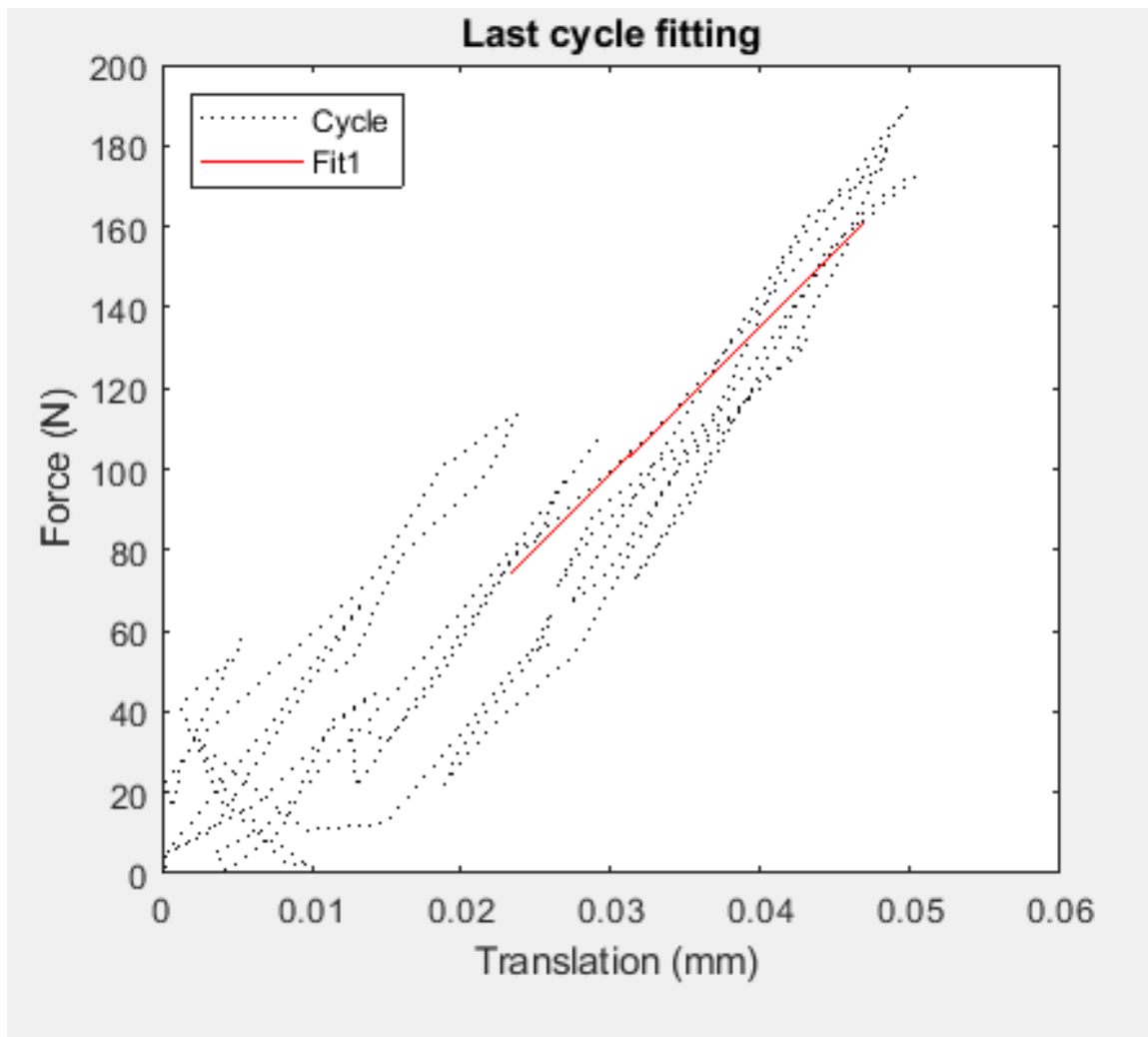


Figure A- 1 Noisy signal at the last compression cycle before (pre-) repetitive lifting leading to the omission of the stiffness measurement from this cycle (FSU 08ID50).

A.1.1.2 Before (pre-) repetitive lifting

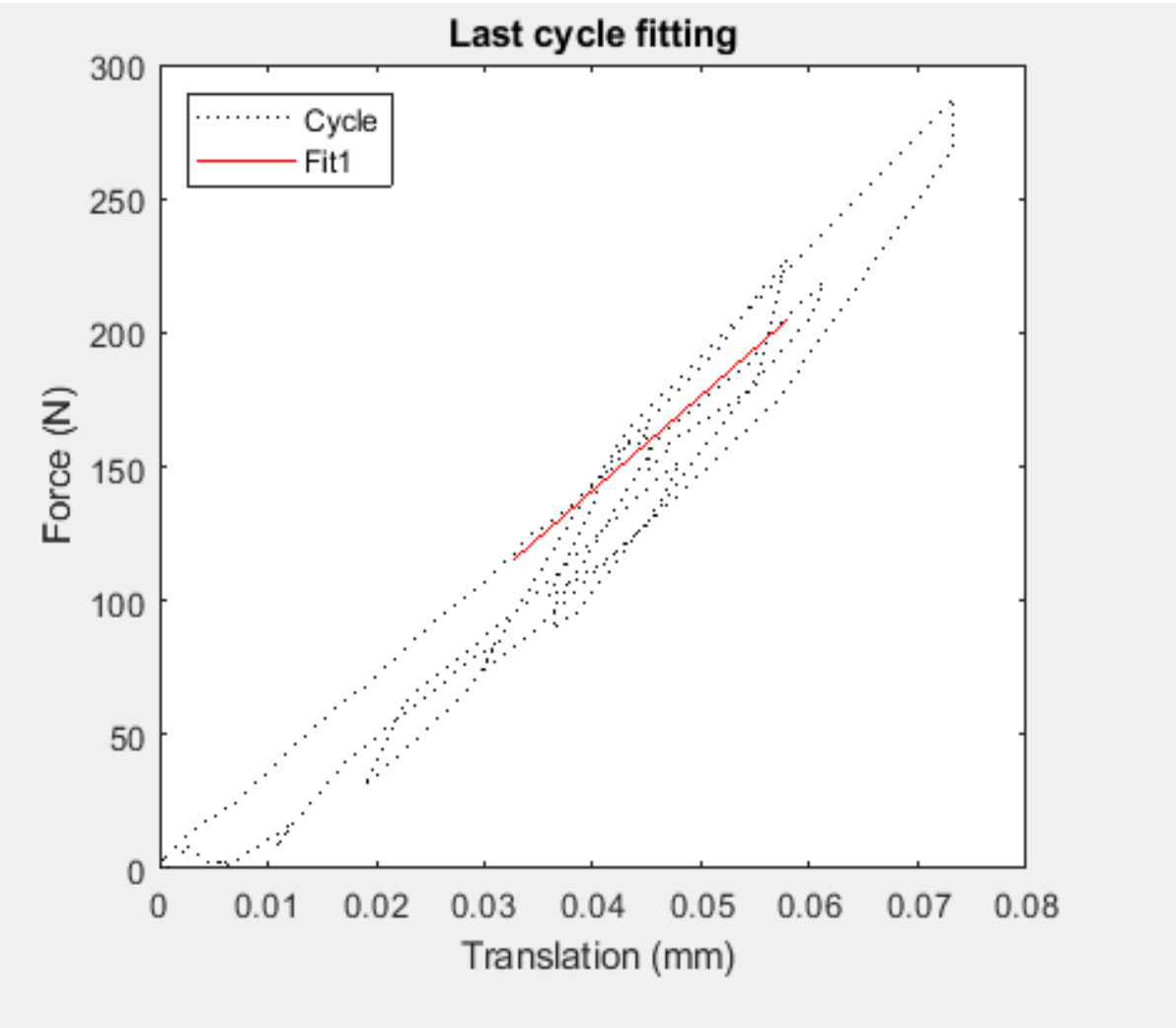


Figure A- 2 Noisy signal at the last compression cycle after (post-) repetitive lifting leading to the omission of the stiffness measurement from this cycle (FSU 10ID20).

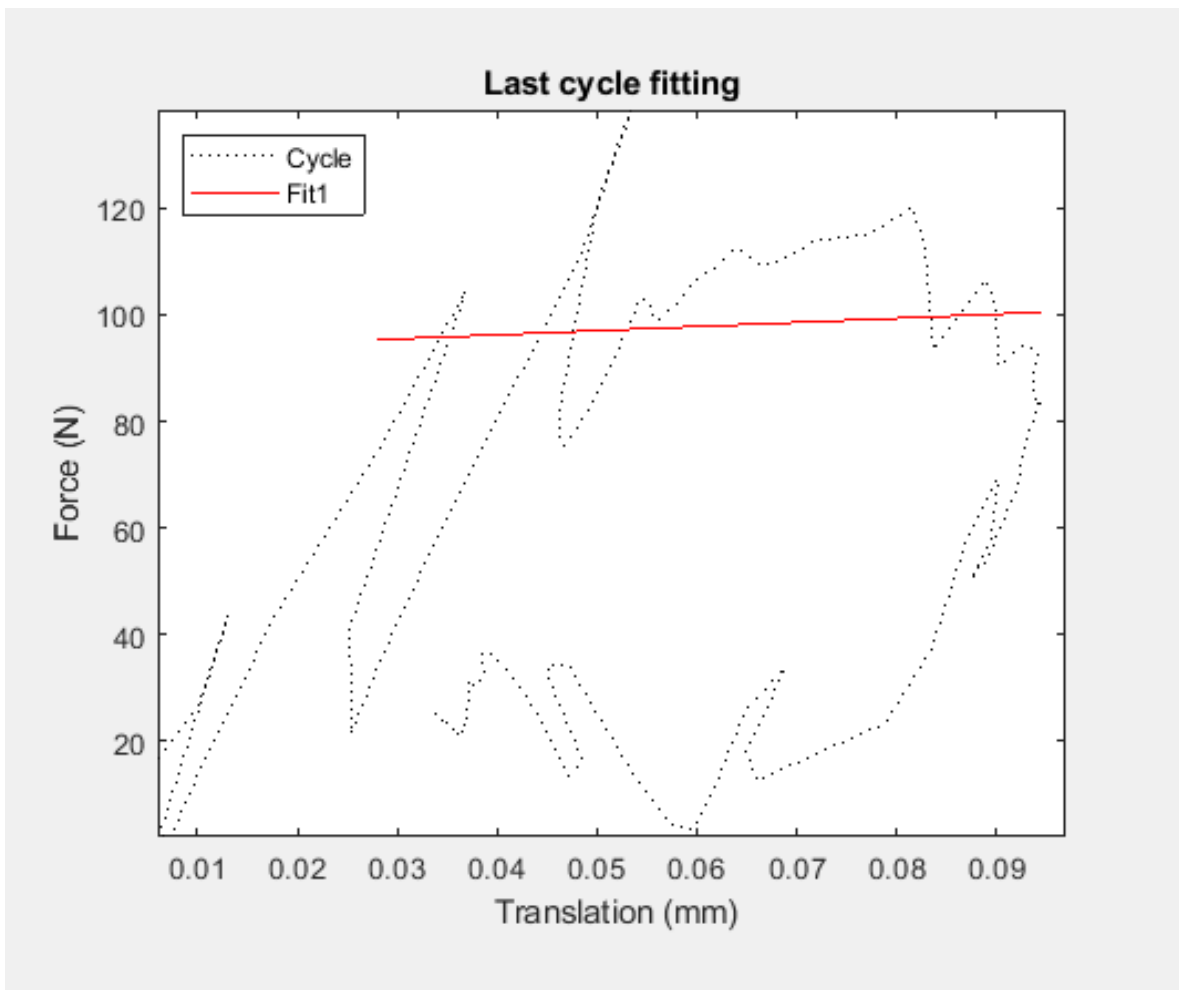


Figure A- 3 Noisy signal at the last compression cycle after (post-) repetitive lifting leading to the omission of the stiffness measurement from this cycle (FSU 12ID24).

A.1.2 Outlier measurements based on statistical analysis

A.1.2.1 Before (pre-) repetitive lifting

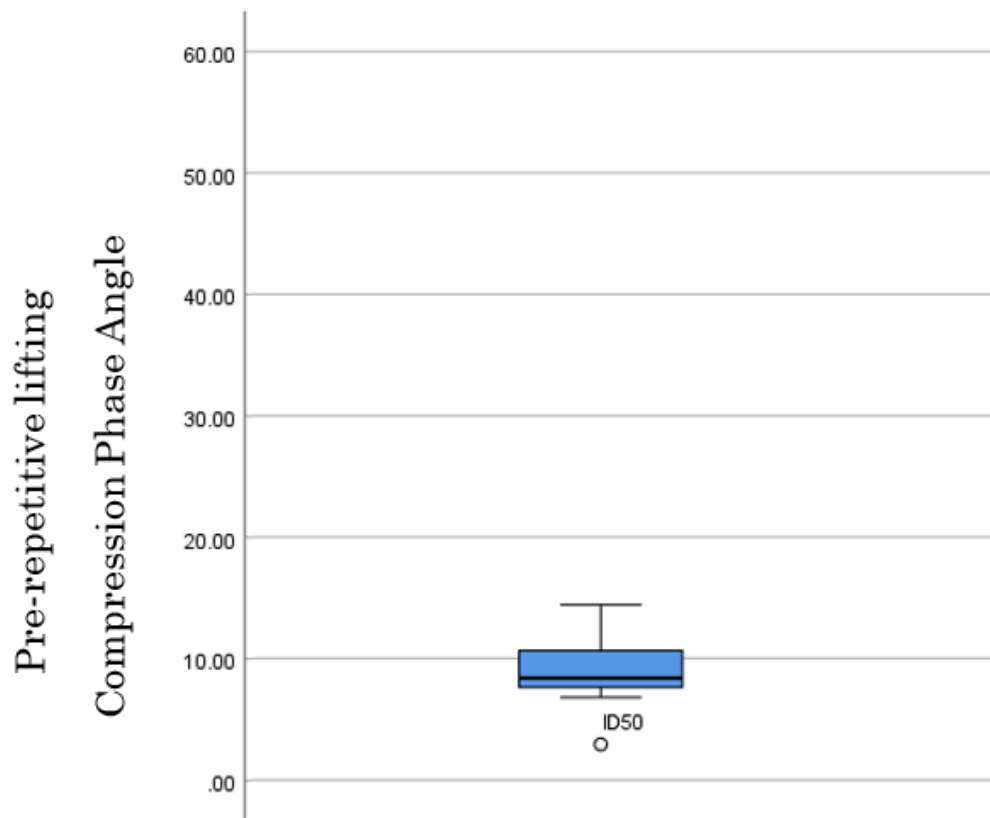


Figure A- 4 Outlier of one compression phase angle measurement before (pre-repetitive lifting) leading to the omission of this measurement (FSU ID50).



Figure A- 5 Outlier of one compression phase angle measurement before (pre-repetitive lifting) leading to the omission of this measurement (FSU ID24).

A.1.2.2 After (post-) repetitive lifting

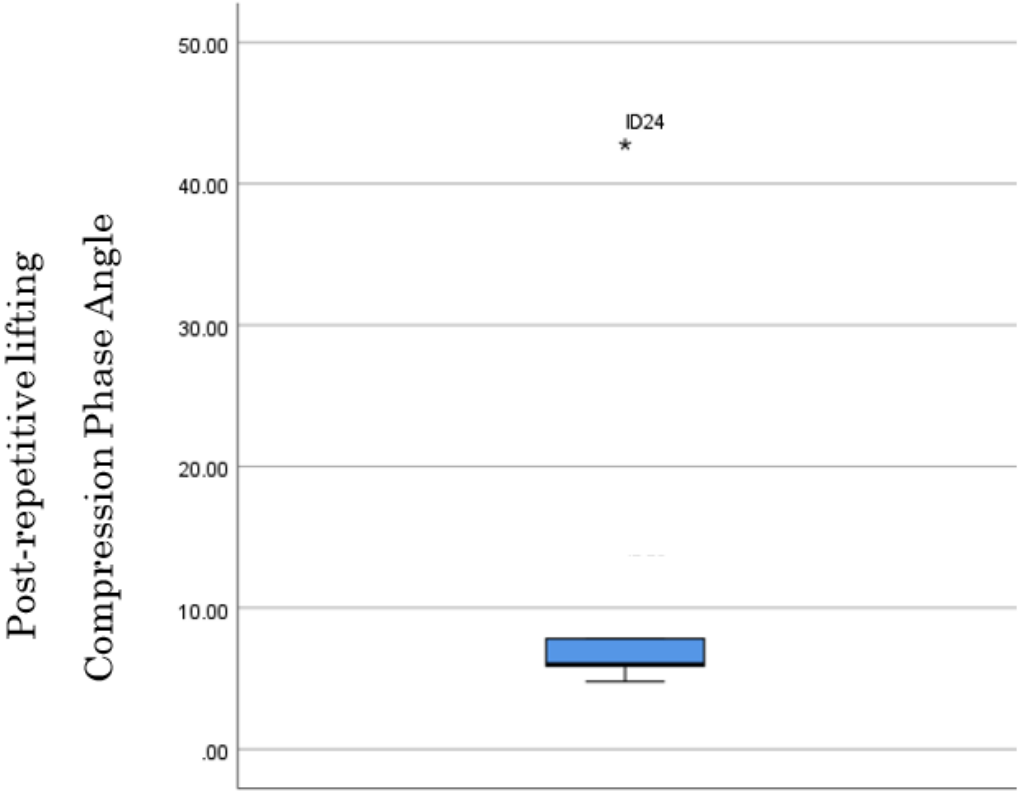


Figure A- 6 Outlier of one compression phase angle measurement after (post-repetitive lifting) leading to the omission of this measurement (FSU ID24).

A.1.2.3 After recovering period

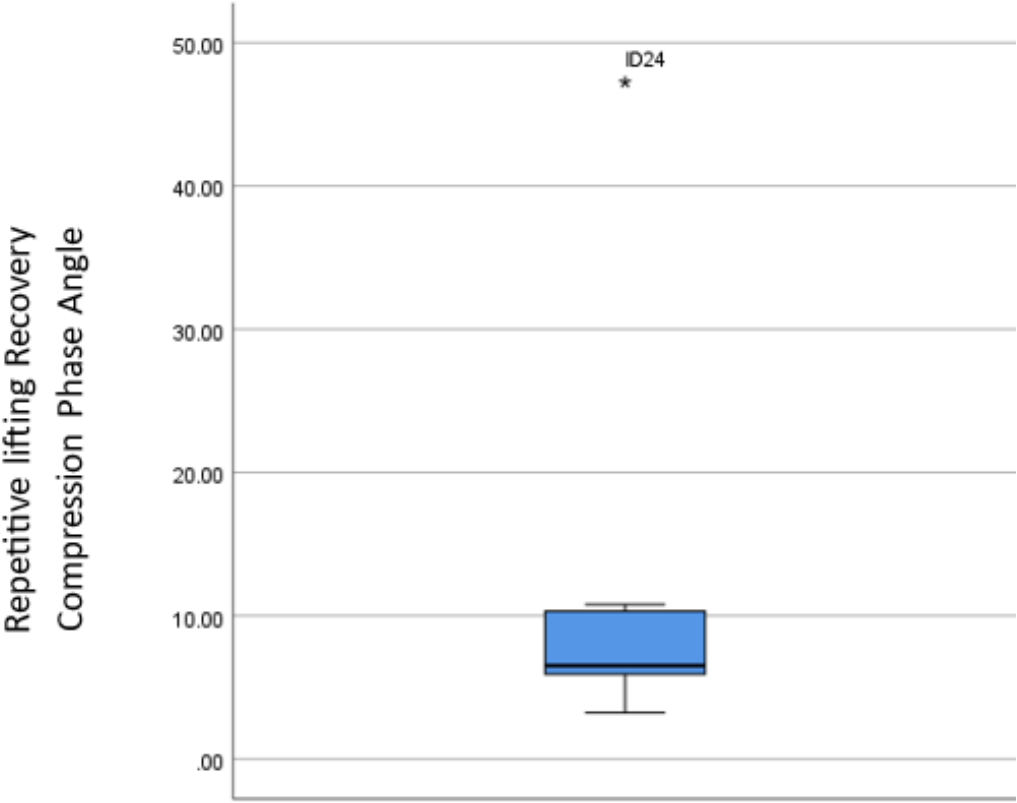


Figure A- 7 Outlier of one compression phase angle measurement following recovery period leading to the omission of this measurement (FSU ID24).

Appendix B

B.1 Excluded stiffness and phase angle measurements from the mechanical testing of Chapter 5

B.1.1 Noisy signal at the last compression cycle

B.1.1.1 Before (pre-) repetitive lifting

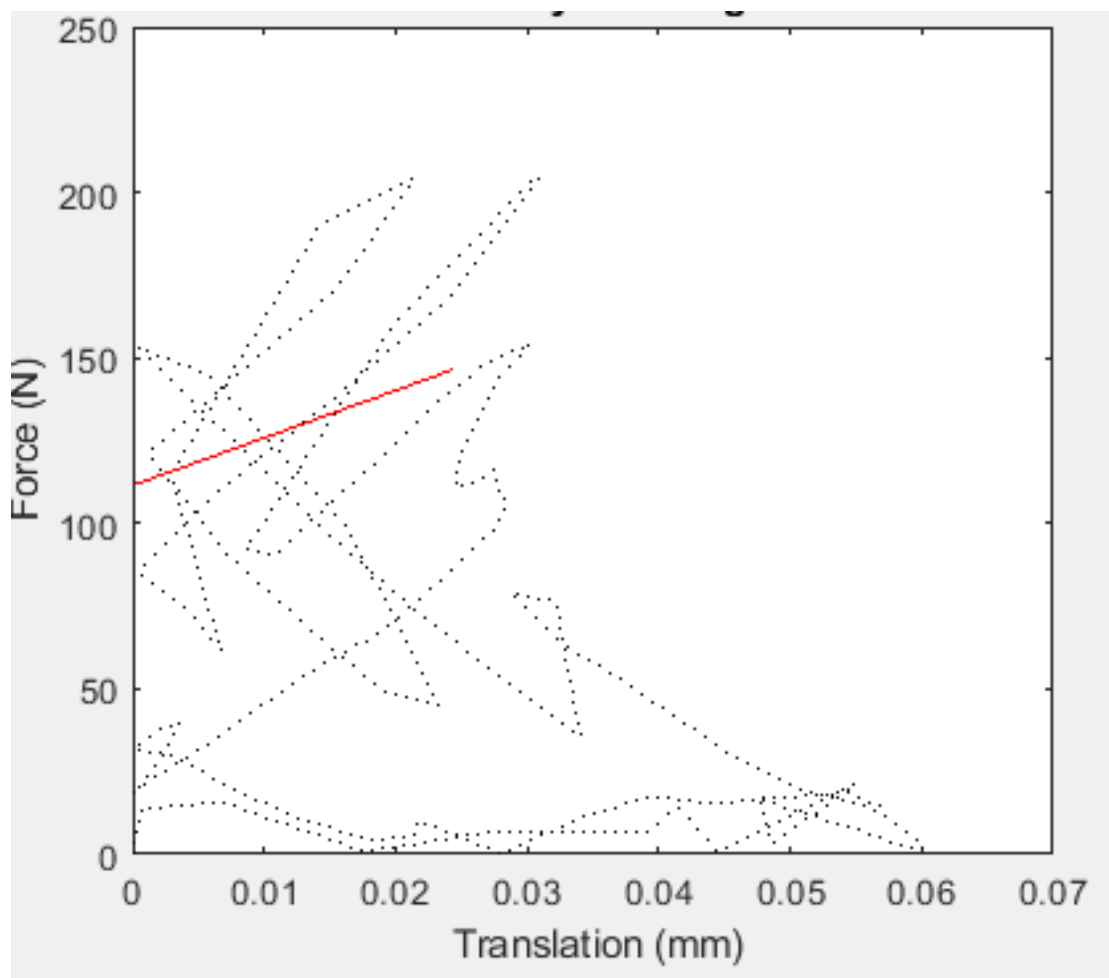


Figure B- 1 Noisy signal at the last compression cycle before (pre-)repetitive lifting leading to the omission of the stiffness measurement from this cycle in the control group data (FSU 12ID24).

B.1.1.2 After (post-) repetitive lifting

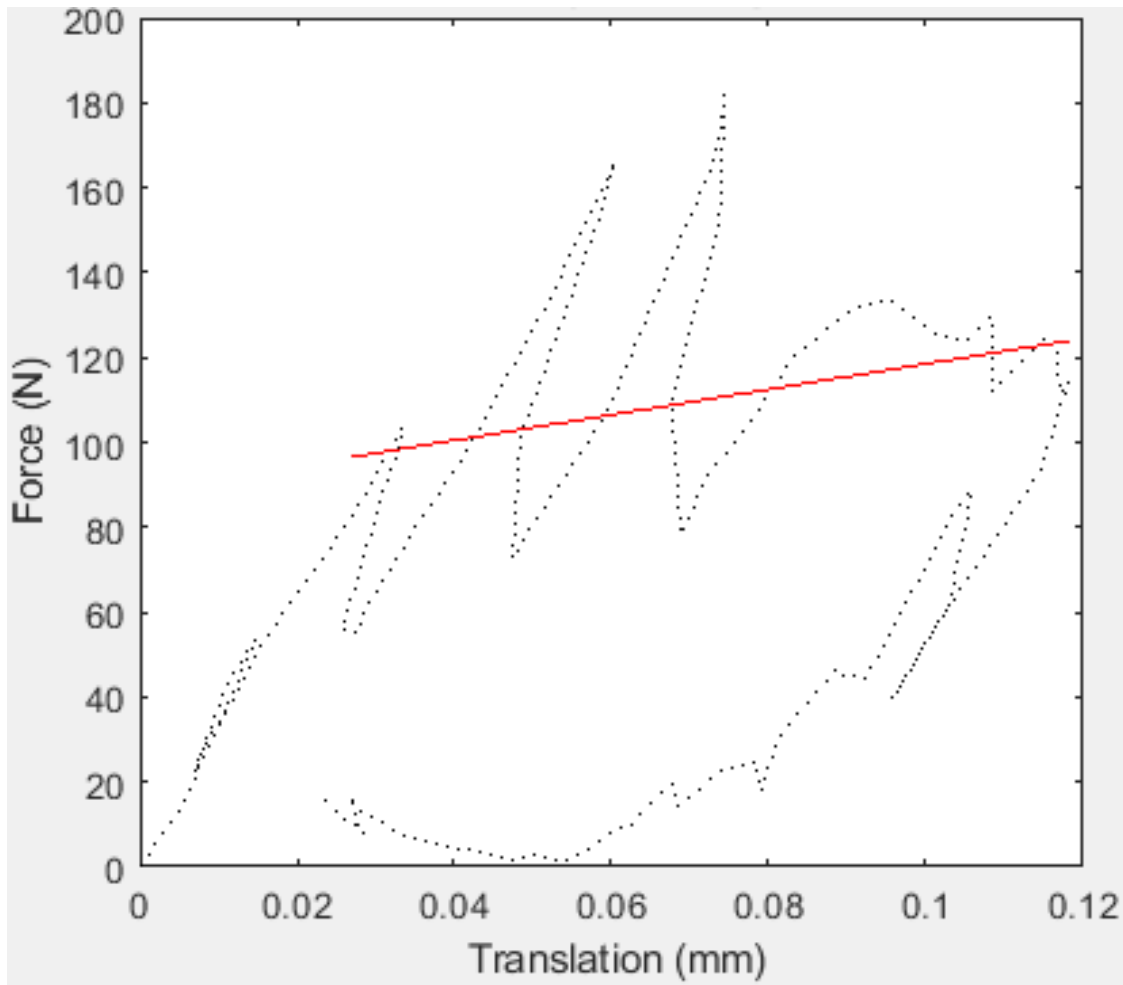


Figure B- 2 Noisy signal at the last compression cycle after (post-)repetitive lifting leading to the omission of the stiffness measurement from this cycle in the control group data (FSU 12ID24).

B.1.1.3 After recovery period

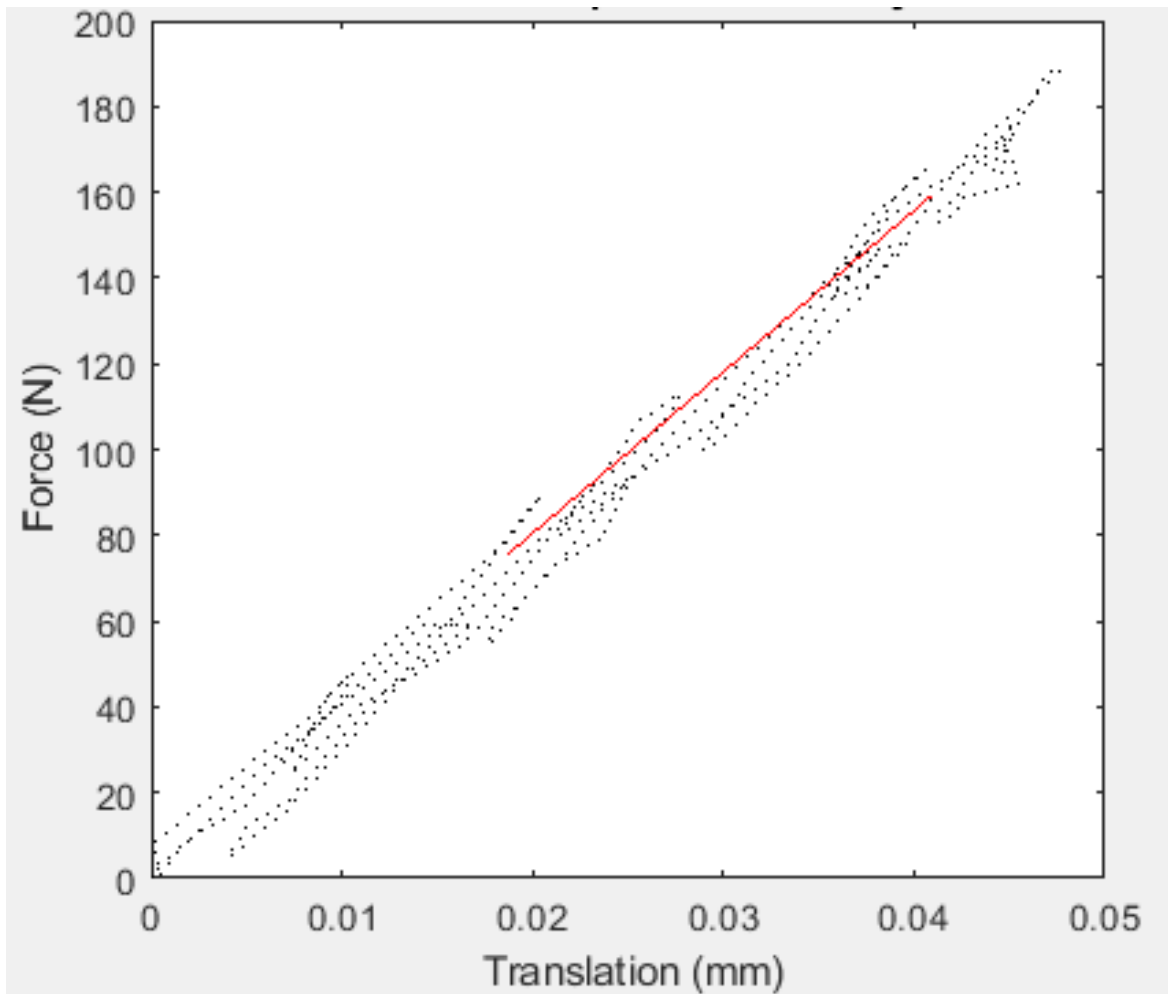


Figure B- 3 Noisy signal at the last compression cycle after recovery period leading to the omission of the stiffness measurement from this cycle in the control group data (FSU 11ID12).

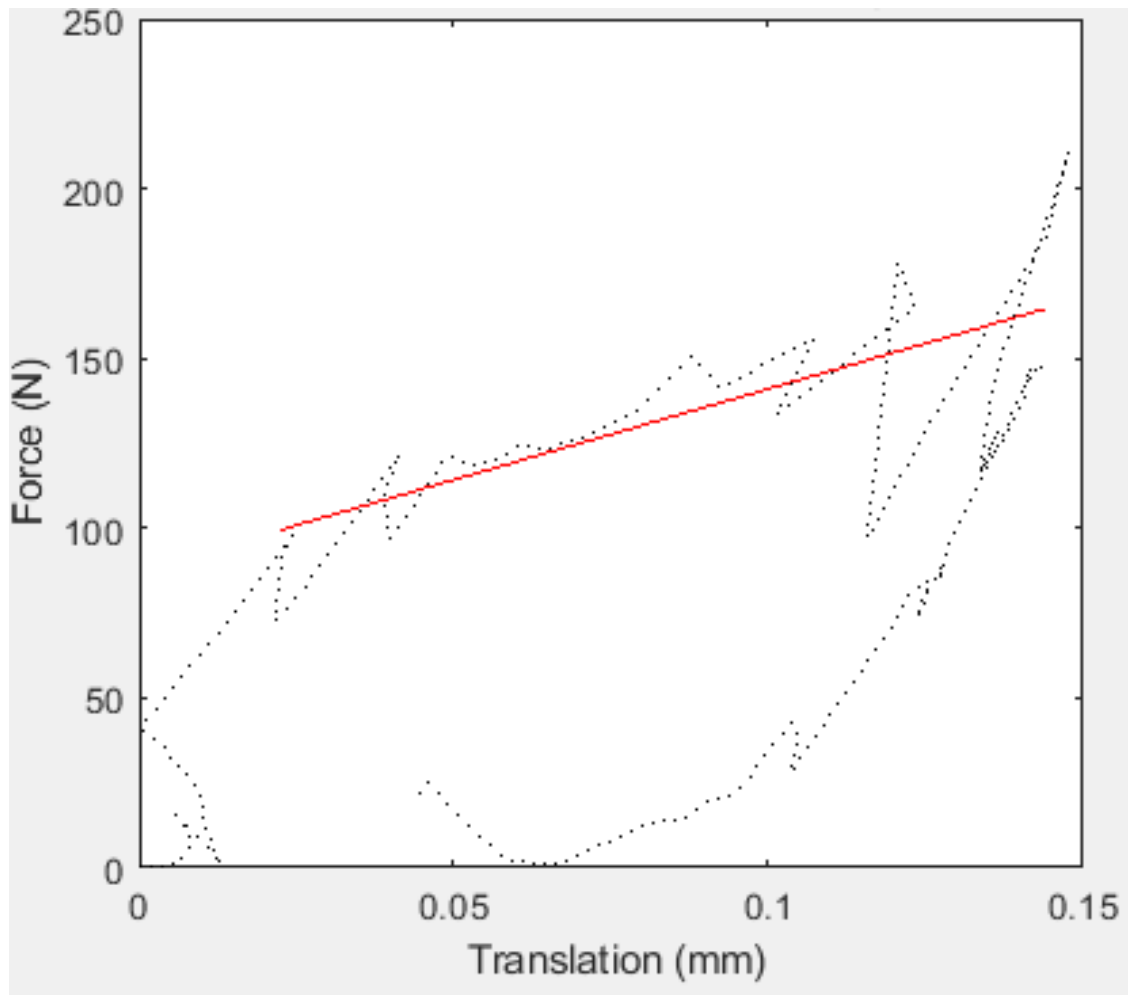


Figure B- 4 Noisy signal at the last compression cycle after recovery period leading to the omission of the stiffness measurement from this cycle in the control group data (FSU 12ID24).

B.1.2 Outlier measurements based on statistical analysis

B.1.2.1 Before (pre-) repetitive lifting

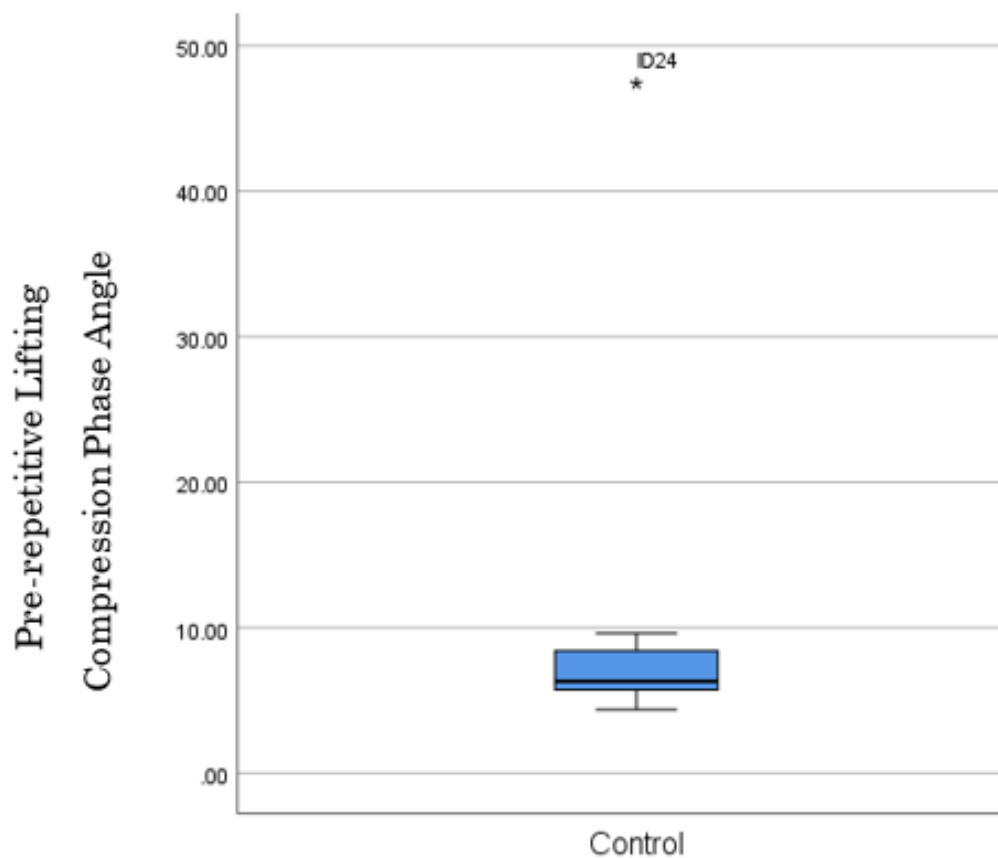


Figure B- 5 Outlier of one compression phase angle measurement before (Pre-Repetitive Lifting) leading to the omission of this measurement in the control group data (FSU 12ID24).

B.1.2.2 After (post-) repetitive lifting

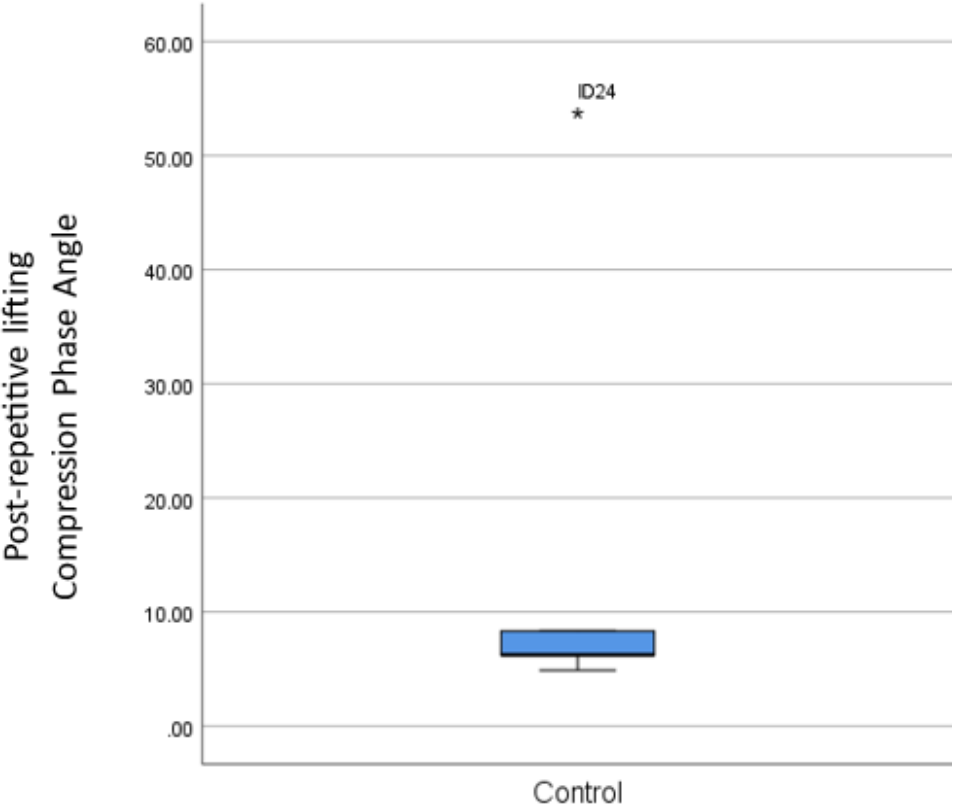


Figure B- 6 Outlier of one compression phase angle measurement after (post-) Repetitive Lifting) leading to the omission of this measurement in the control group data (FSU 12ID24).

B.1.2.3 After recovery period

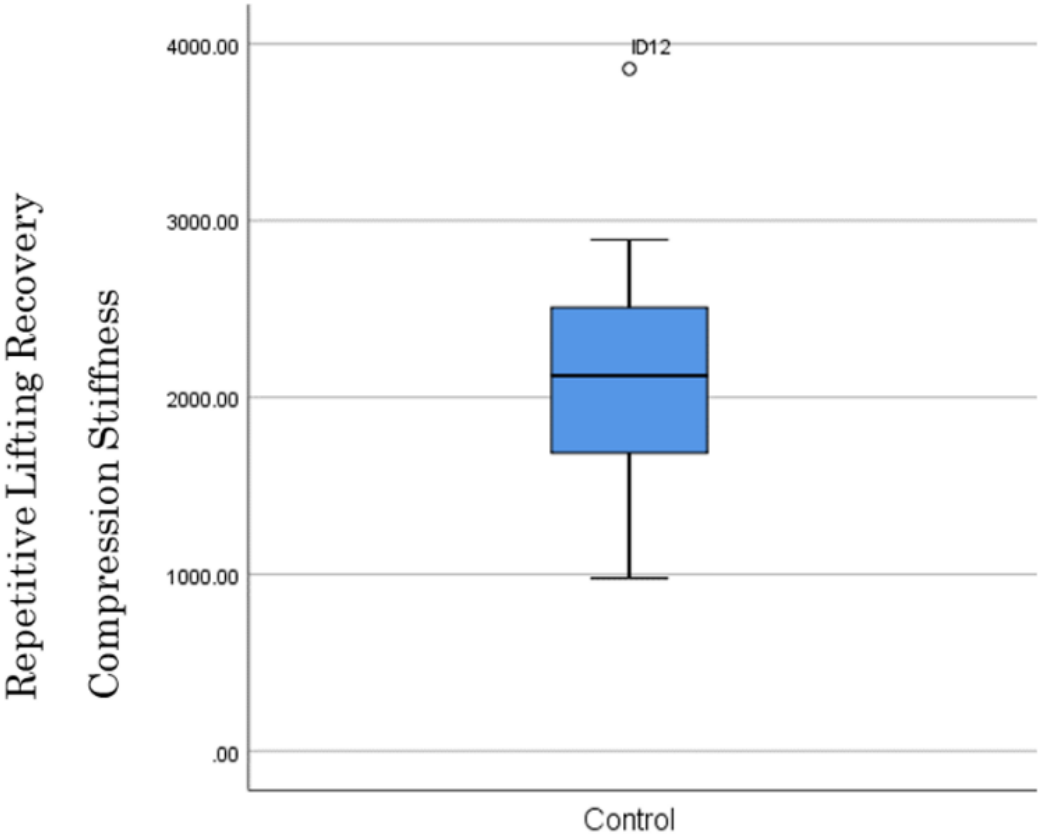


Figure B- 7 Outlier of one compression phase angle measurement after recovery period leading to the omission of this measurement in the control group data (FSU 11ID12).

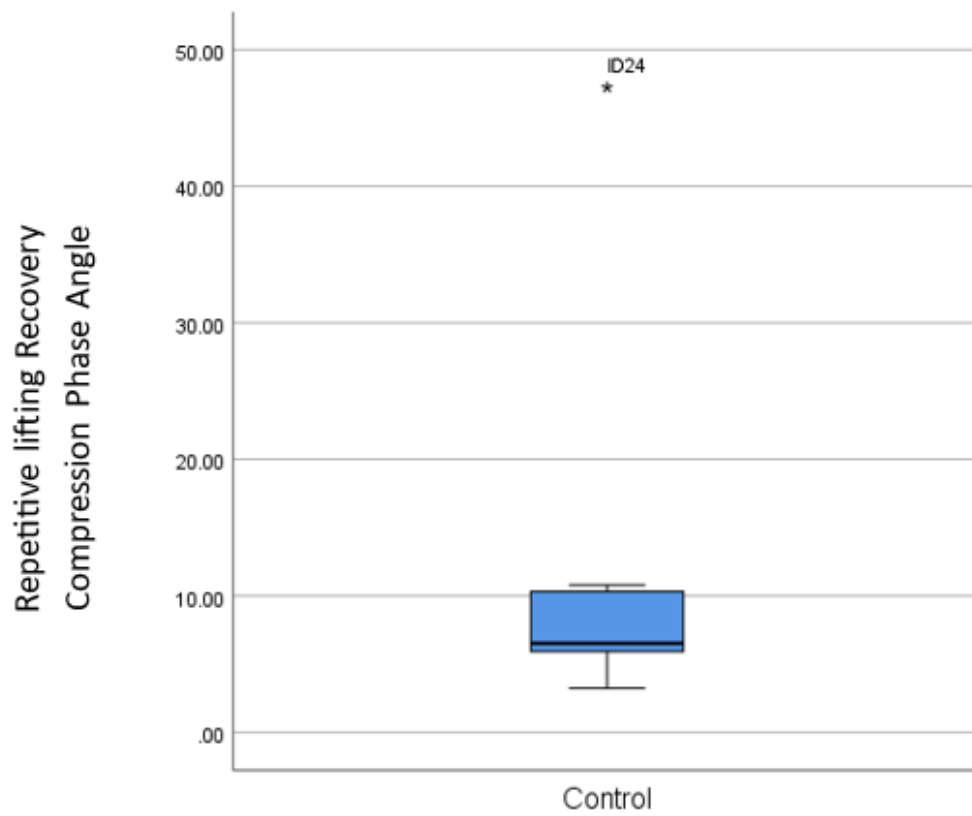


Figure B- 8 Outlier of one compression phase angle measurement following recovery period leading to the omission of this measurement (FSU ID24).

Appendix C

C.1 Original and processed images of control and mechanical needle injuries with segmentation and measurements of area, length, solidity, and aspect ratio across slices 1 through 5

C.1.1 Injury slice 1

C.1.1.1 Original images

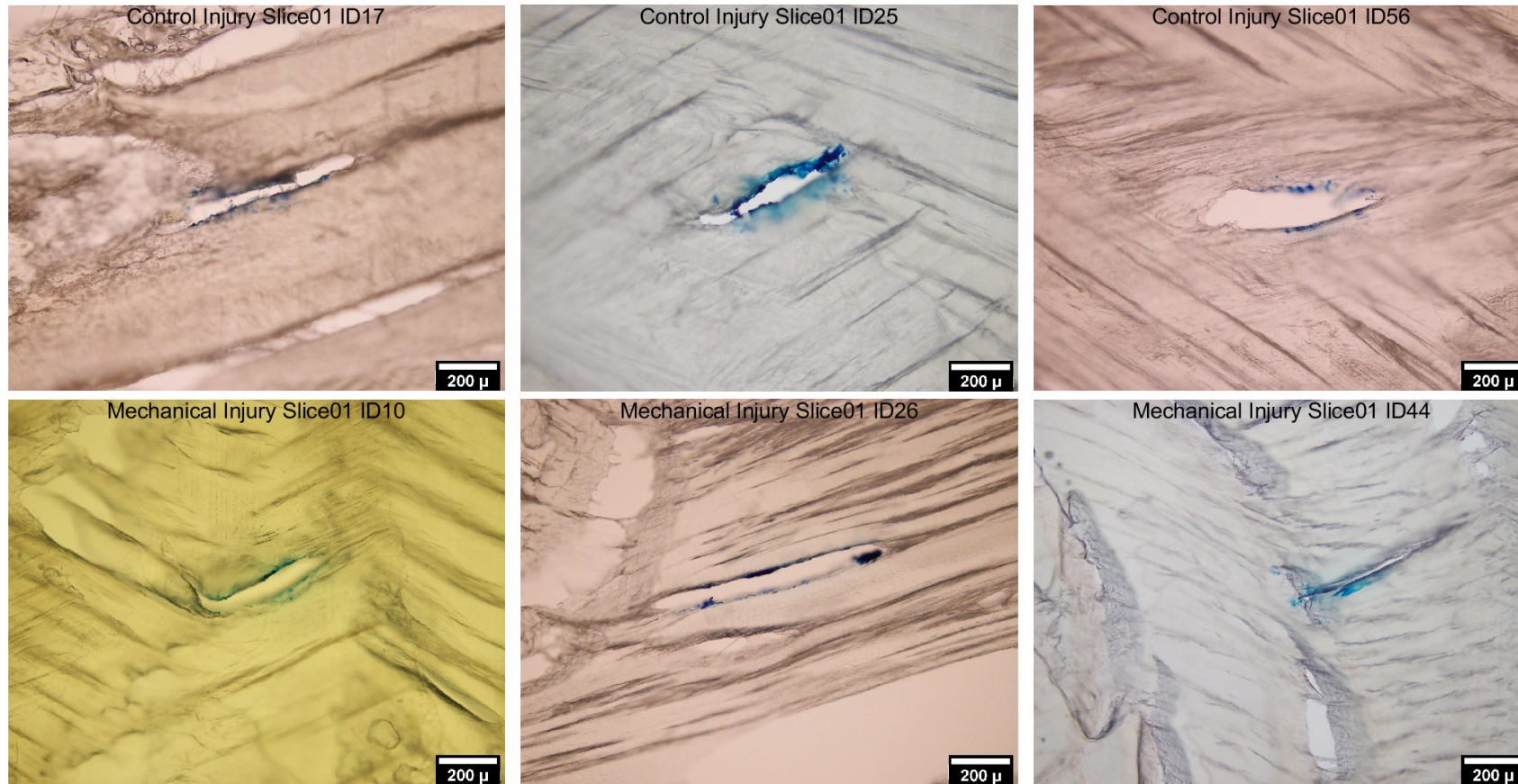


Figure C- 1 Original images of needle injuries in Slice 1. Each image is annotated with labels indicating control or mechanical injuries, along with the slice number and specific injury IDs. The top row displays control injuries, labelled as ID17, ID25, and ID56, respectively. The bottom row shows mechanical injuries, with labels ID10, ID26, and ID44, respectively.

C.1.1.2 Segmentation and area measurements

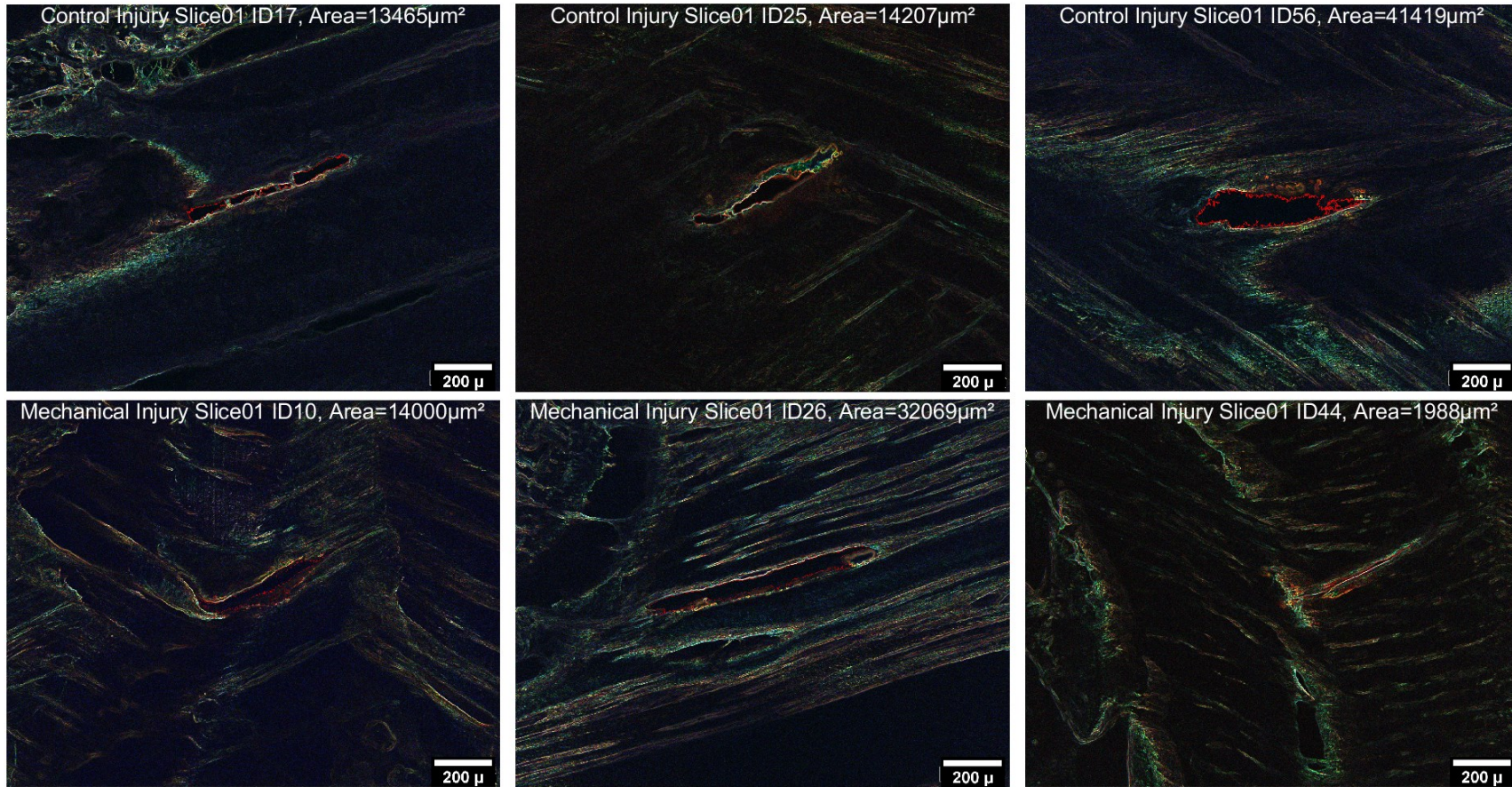


Figure C- 2 Segmentation of needle injuries in slice 1. Each image is annotated with labels indicating control or mechanical injuries, along with the slice number and specific injury IDs, each with its respective area measurement. The top row displays control injuries, labelled as ID17, ID25, and ID56, respectively. The bottom row shows mechanical injuries, with labels ID10, ID26, and ID44, respectively.

C.1.1.3 Length measurements

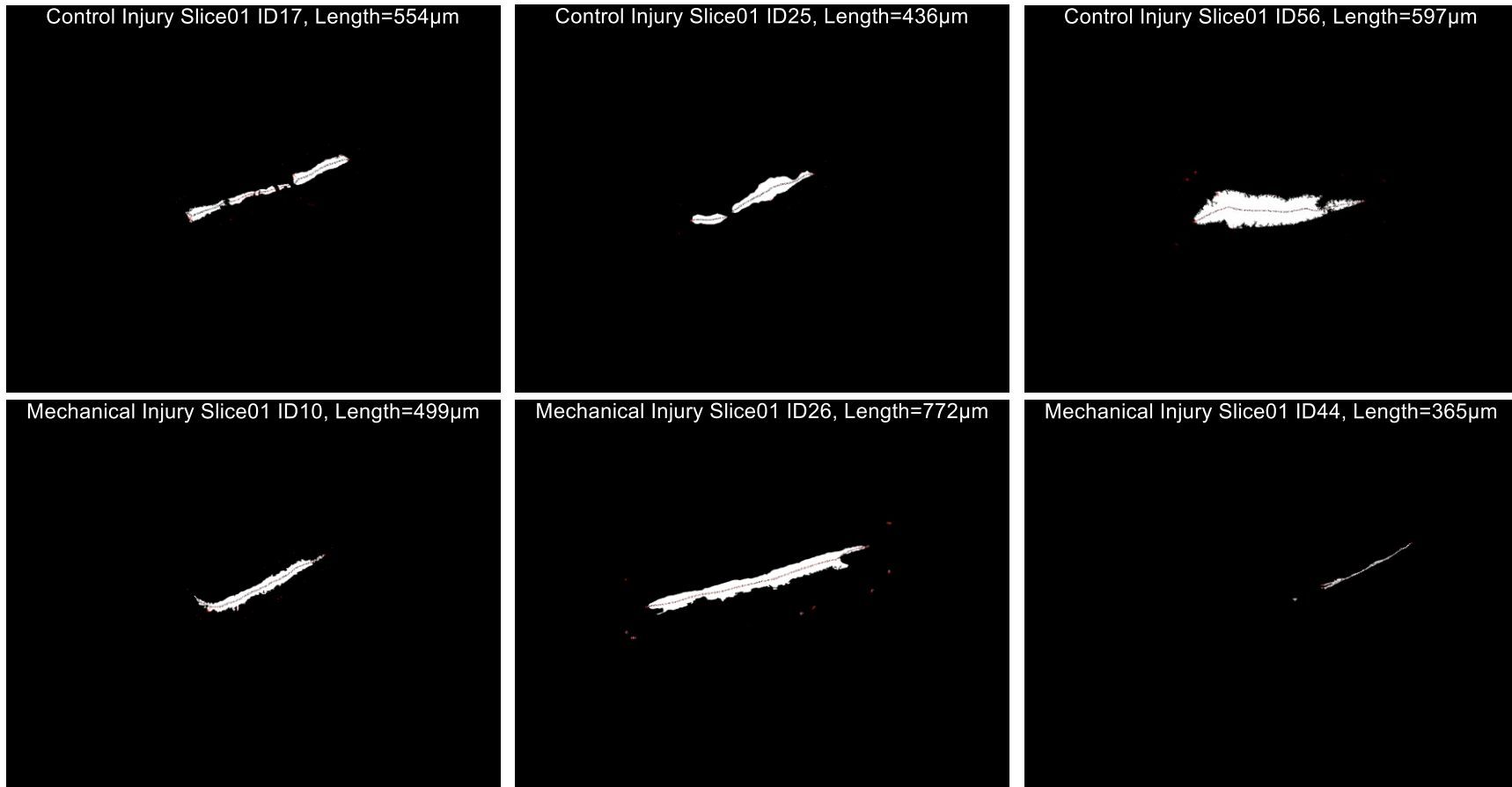


Figure C- 3 Length of needle injuries in slice 1. Each image is annotated with labels indicating control or mechanical injuries, along with the slice number and specific injury IDs, each with its respective length measurement. The top row displays control injuries, labelled as ID17, ID25, and ID56, respectively. The bottom row shows mechanical injuries, with labels ID10, ID26, and ID44, respectively.

C.1.1.4 Solidity measurements

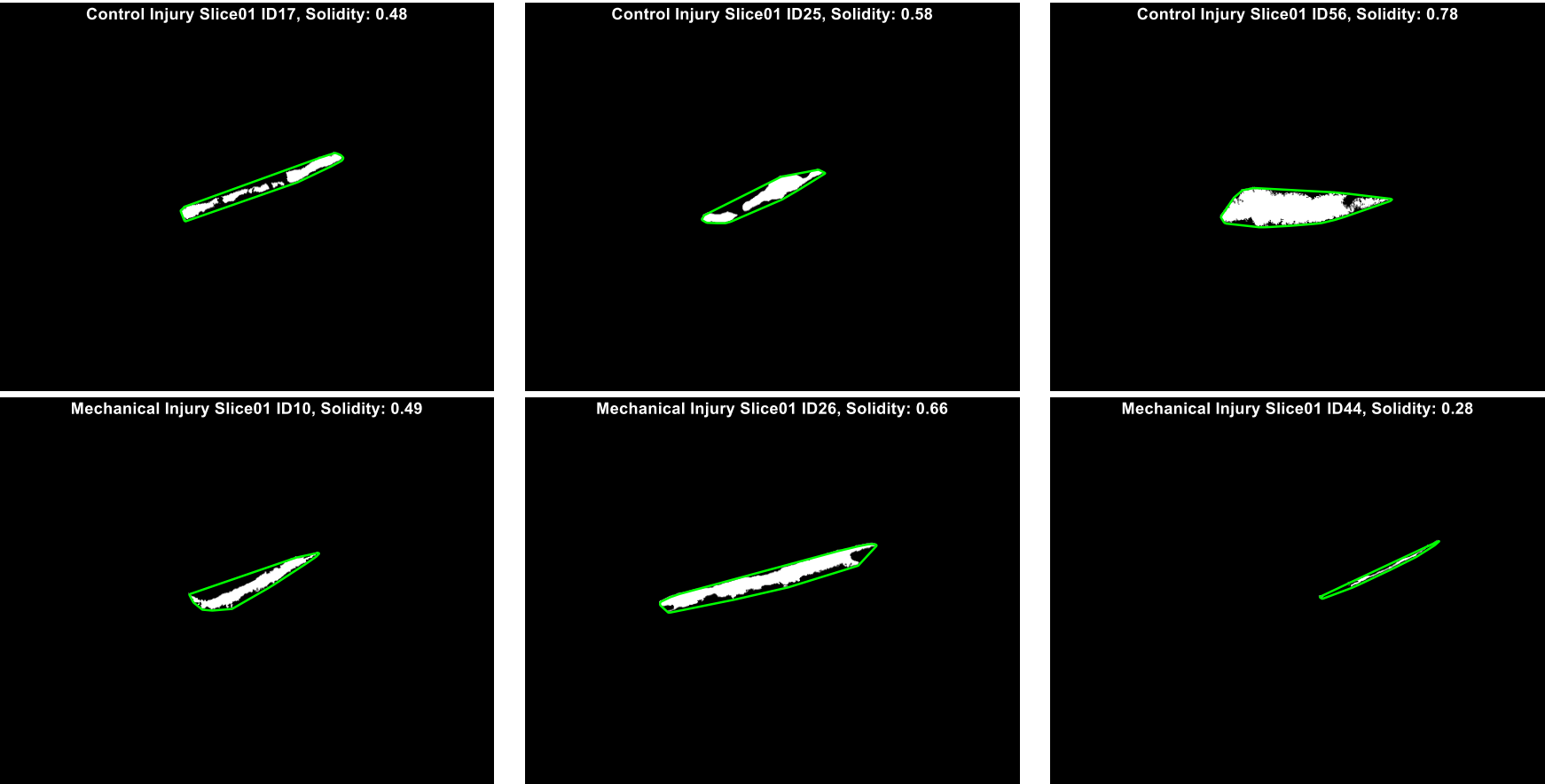


Figure C- 4 Solidity of needle injuries in slice 1. Each image is annotated with labels indicating control or mechanical injuries, along with the slice number and specific injury IDs, each with its respective solidity measurement. The top row displays control injuries, labelled as ID17, ID25, and ID56, respectively. The bottom row shows mechanical injuries, with labels ID10, ID26, and ID44, respectively.

C.1.1.5 Aspect ratio measurements

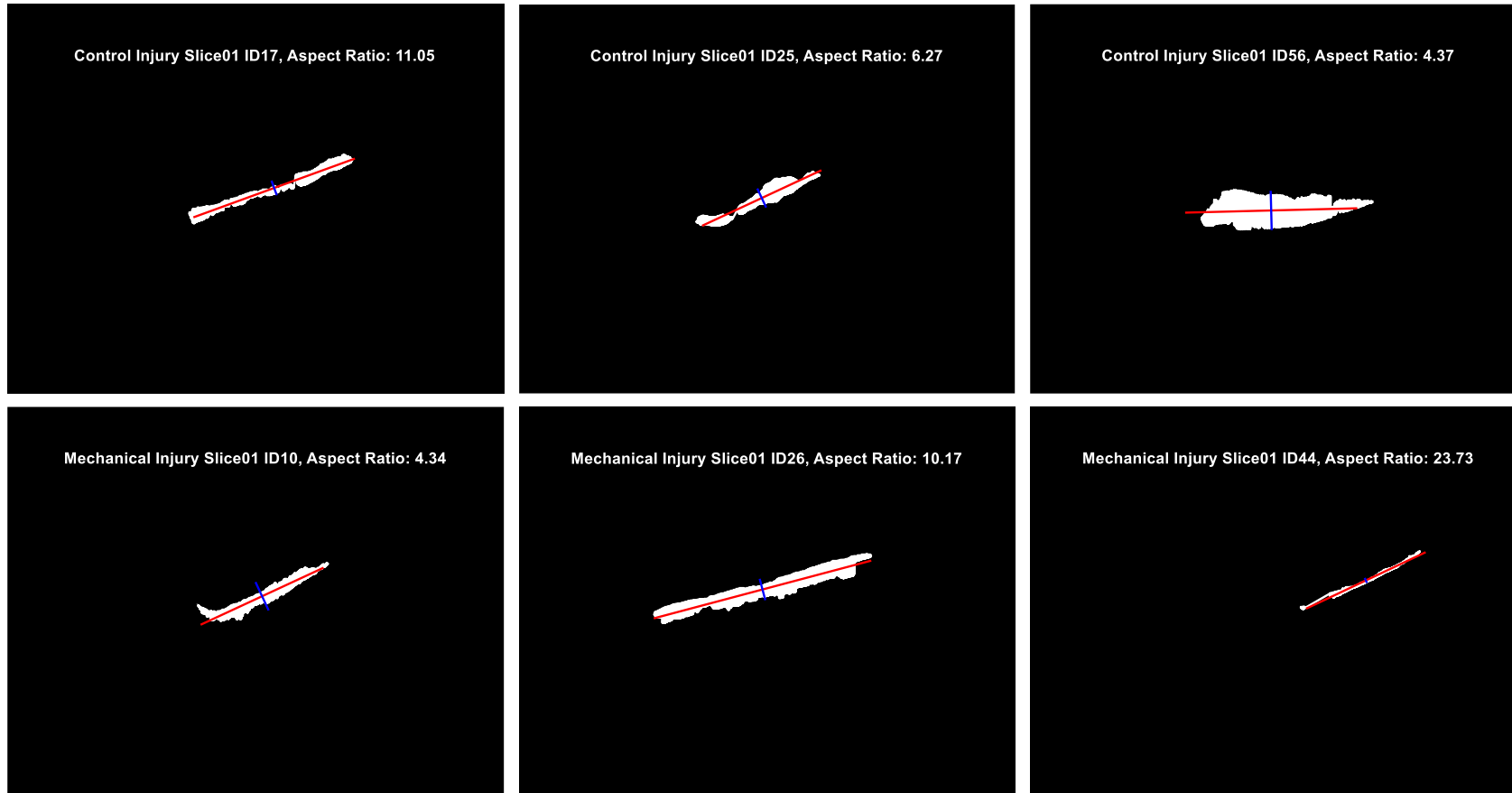


Figure C- 5 Aspect ratio of needle injuries in slice 1. Each image is annotated with labels indicating control or mechanical injuries, along with the slice number and specific injury IDs, each with its respective aspect ratio measurement. The top row displays control injuries, labelled as ID17, ID25, and ID56, respectively. The bottom row shows mechanical injuries, with labels ID10, ID26, and ID44, respectively.

C.1.2 Injury slice 2

C.1.2.1 Original images

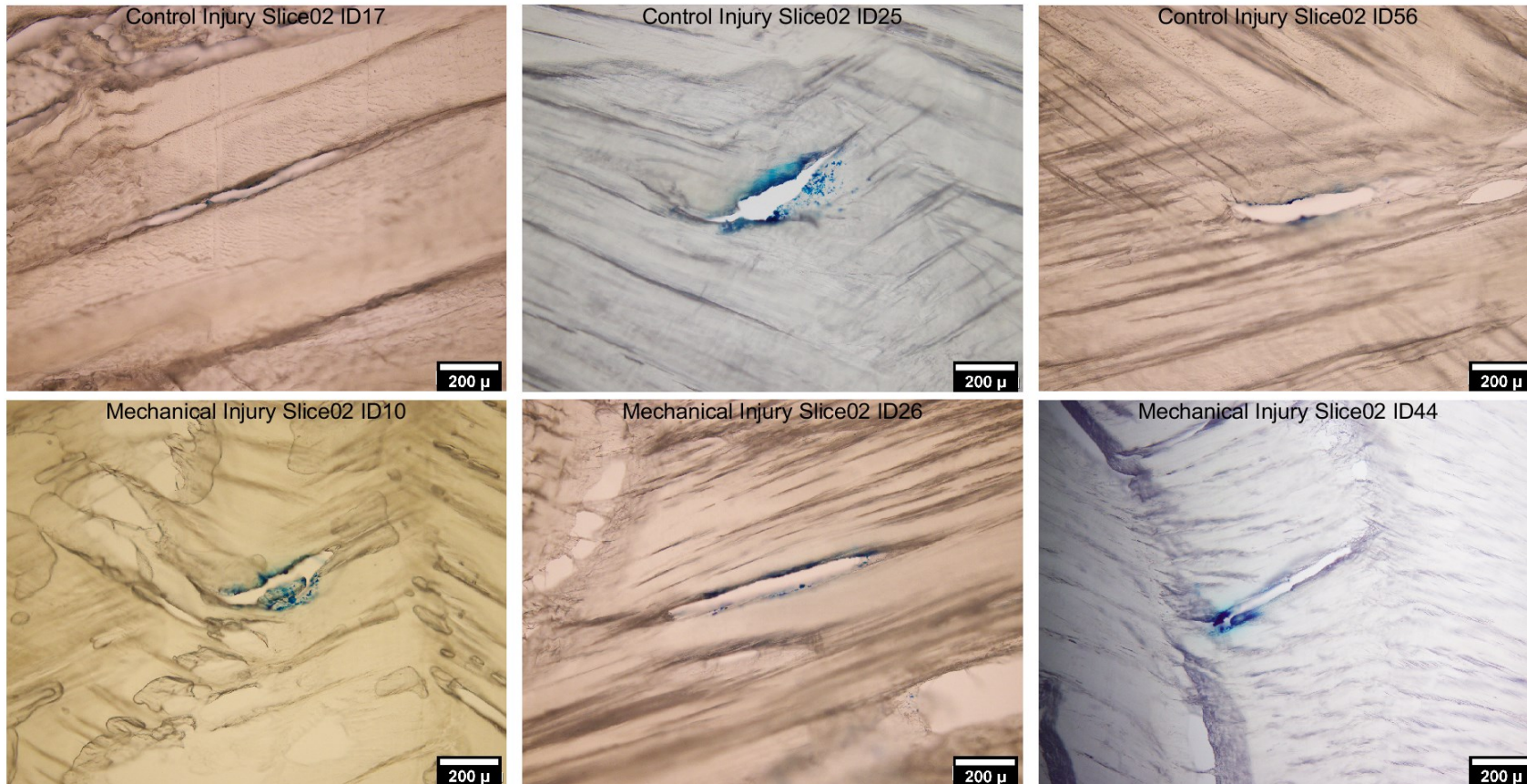


Figure C- 6 Original images of needle injuries in slice 2. Each image is annotated with labels indicating control or mechanical injuries, along with the slice number and specific injury IDs. The top row displays control injuries, labelled as ID17, ID25, and ID56, respectively. The bottom row shows mechanical injuries, with labels ID10, ID26, and ID44, respectively.

C.1.2.2 Segmentation and area measurements

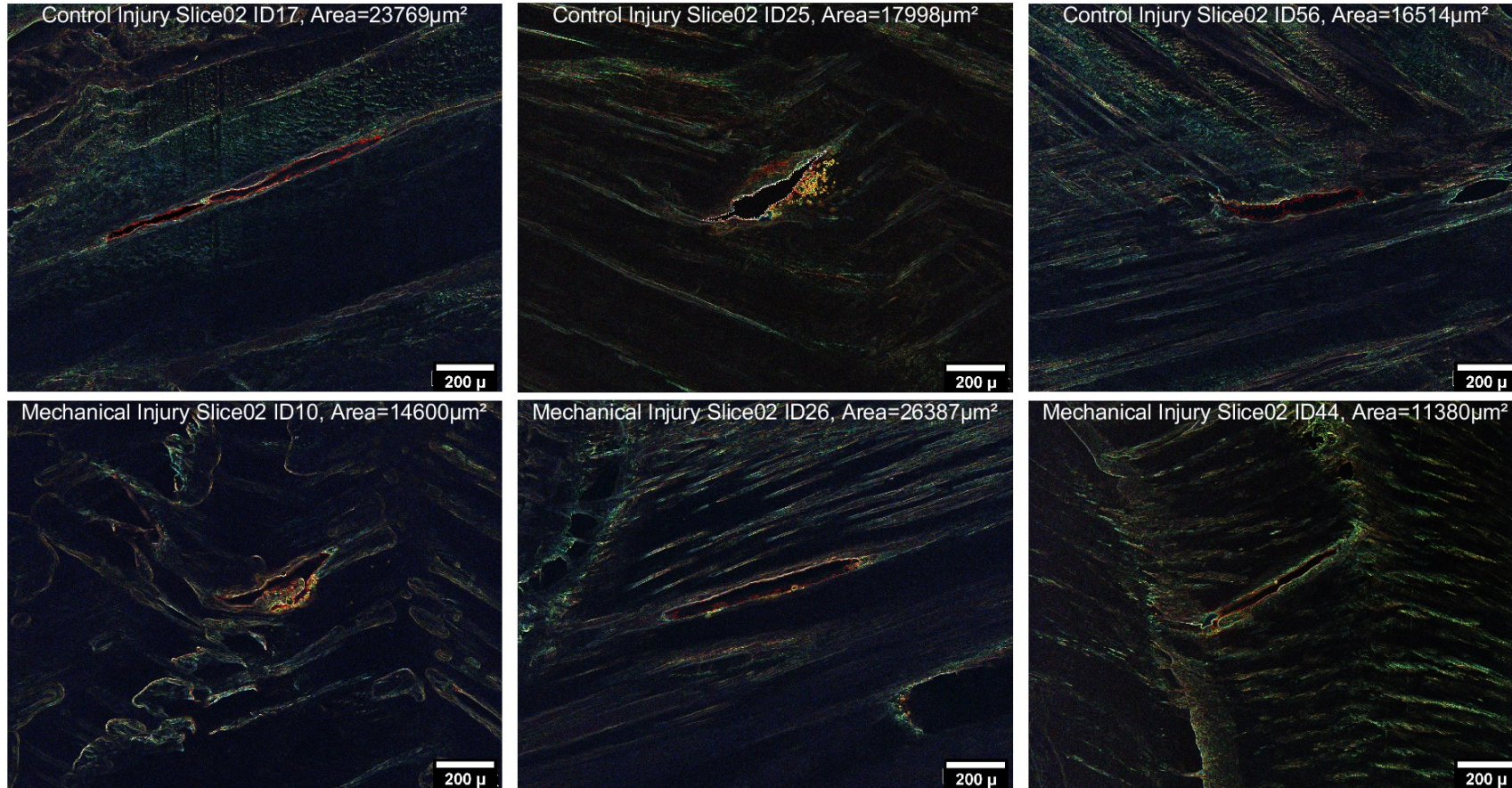


Figure C- 7 Segmentation of needle injuries in slice 2. Each image is annotated with labels indicating control or mechanical injuries, along with the slice number and specific injury IDs, each with its respective area measurement. The top row displays control injuries, labelled as ID17, ID25, and ID56, respectively. The bottom row shows mechanical injuries, with labels ID10, ID26, and ID44, respectively.

C.1.2.3 Length measurements

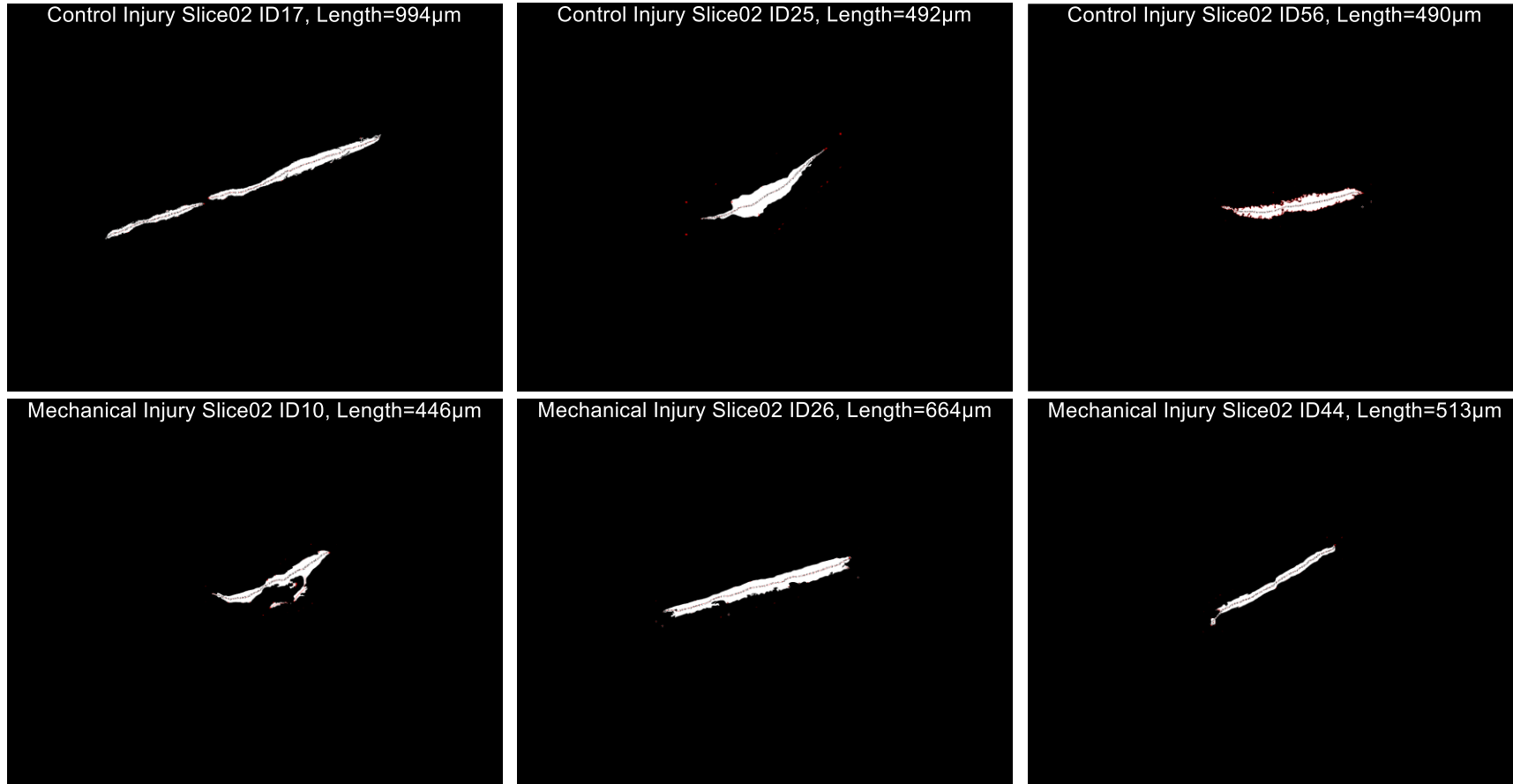


Figure C- 8 Length of needle injuries in slice 2. Each image is annotated with labels indicating control or mechanical injuries, along with the slice number and specific injury IDs, each with its respective length measurement. The top row displays control injuries, labelled as ID17, ID25, and ID56, respectively. The bottom row shows mechanical injuries, with labels ID10, ID26, and ID44, respectively.

C.1.2.4 Solidity measurements

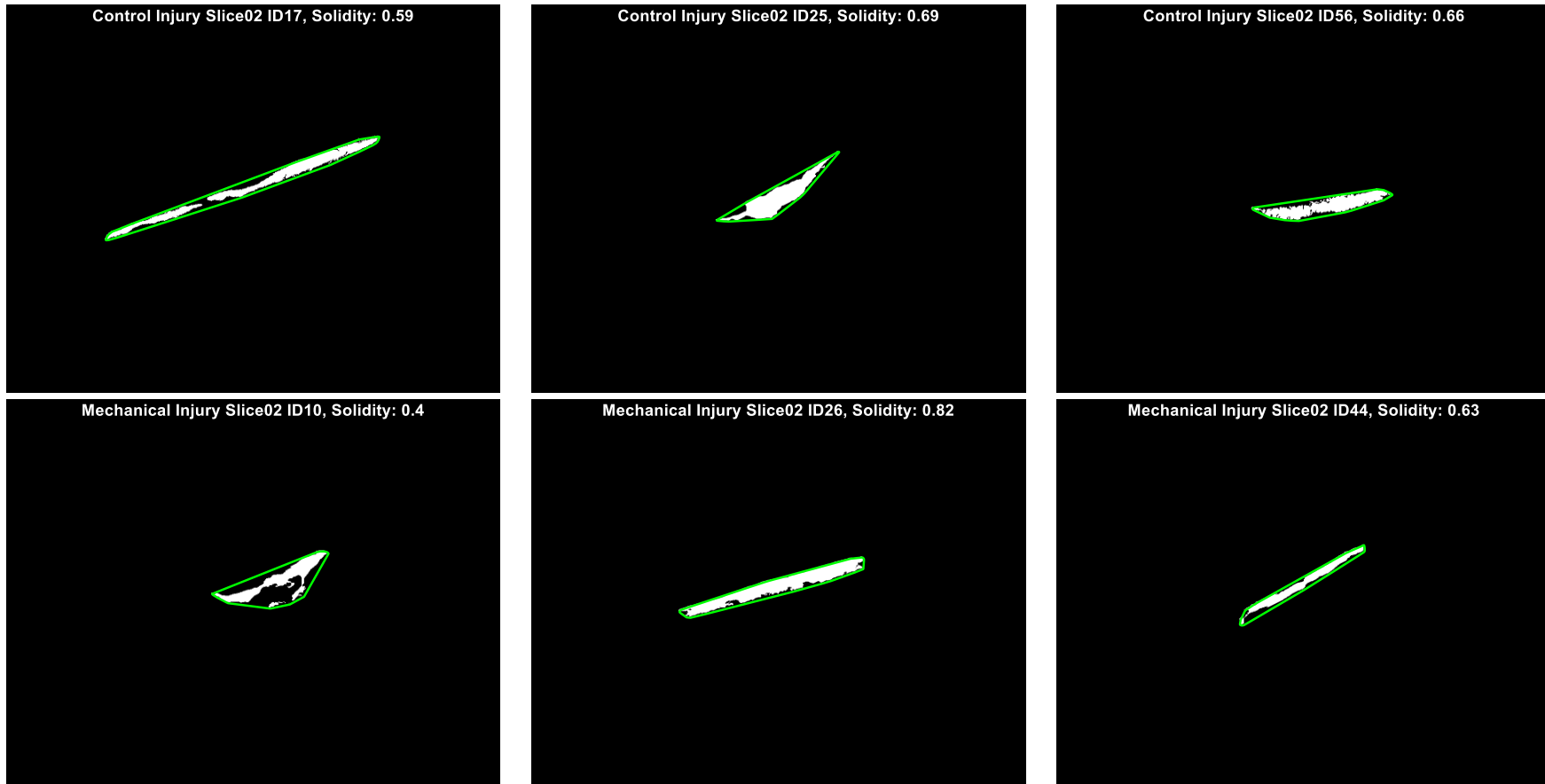


Figure C- 9 Solidity of needle injuries in slice 2. Each image is annotated with labels indicating control or mechanical injuries, along with the slice number and specific injury IDs, each with its respective solidity measurement. The top row displays control injuries, labelled as ID17, ID25, and ID56, respectively. The bottom row shows mechanical injuries, with labels ID10, ID26, and ID44, respectively.

C.1.2.5 Aspect ratio measurements

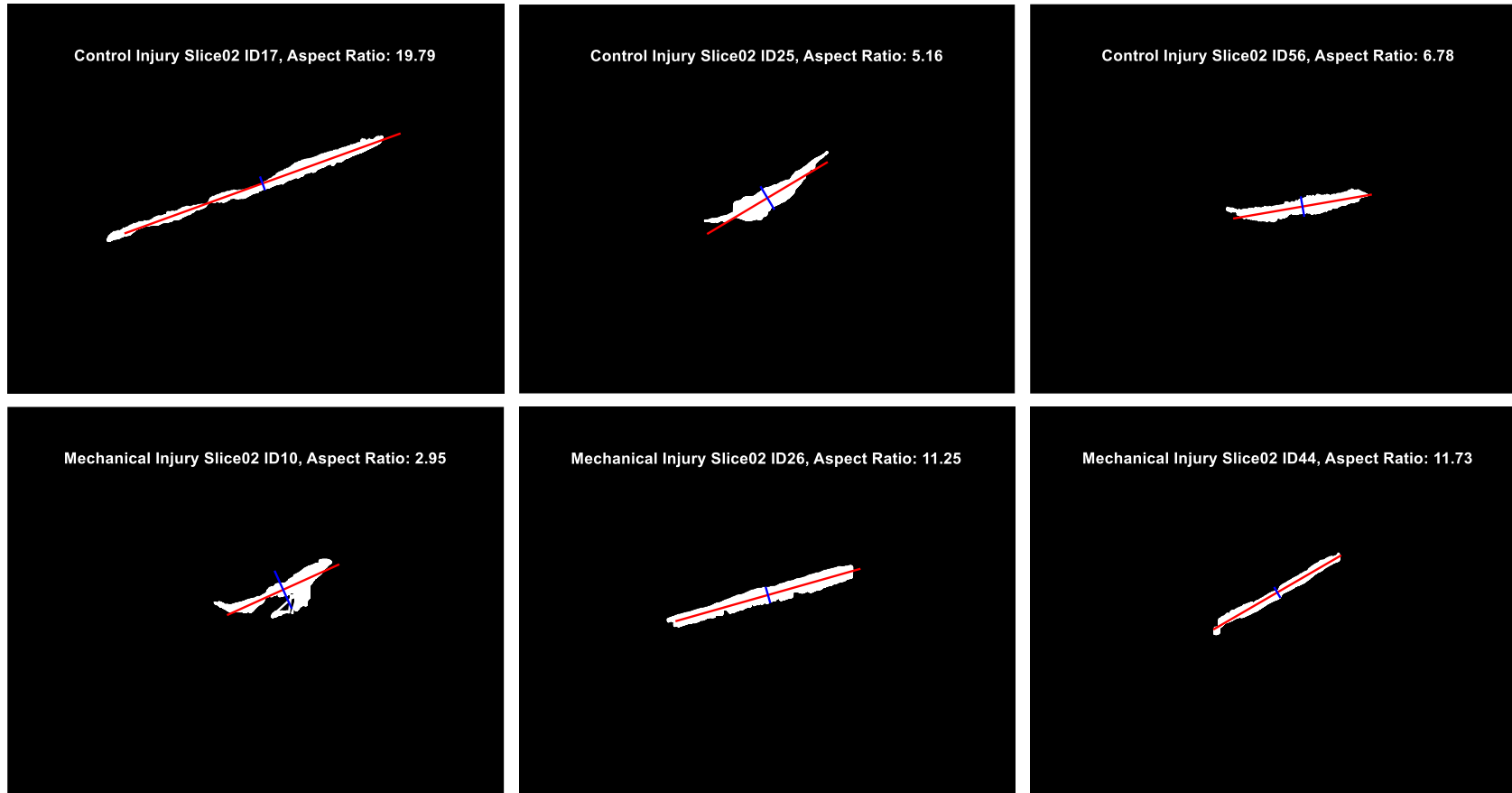


Figure C- 10 Aspect ratio of needle injuries in slice 2. Each image is annotated with labels indicating control or mechanical injuries, along with the slice number and specific injury IDs, each with its respective aspect ratio measurement. The top row displays control injuries, labelled as ID17, ID25, and ID56, respectively. The bottom row shows mechanical injuries, with labels ID10, ID26, and ID44, respectively.

C.1.3 Injury slice 3

C.1.3.1 Original images

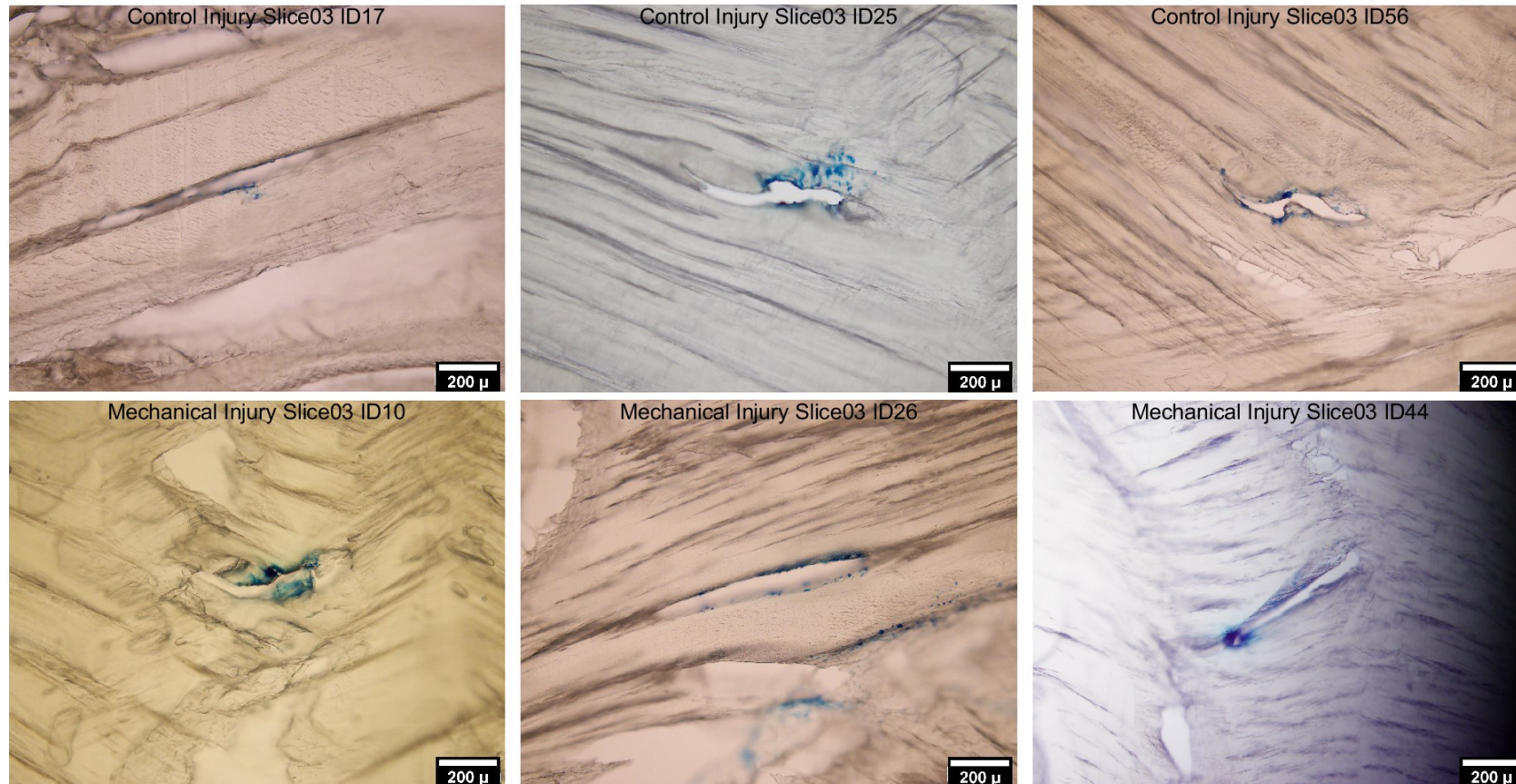


Figure C- 11 Original images of needle injuries in slice 3. Each image is annotated with labels indicating control or mechanical injuries, along with the slice number and specific injury IDs. The top row displays control injuries, labelled as ID17, ID25, and ID56, respectively.

C.1.3.2 Segmentation and area measurements

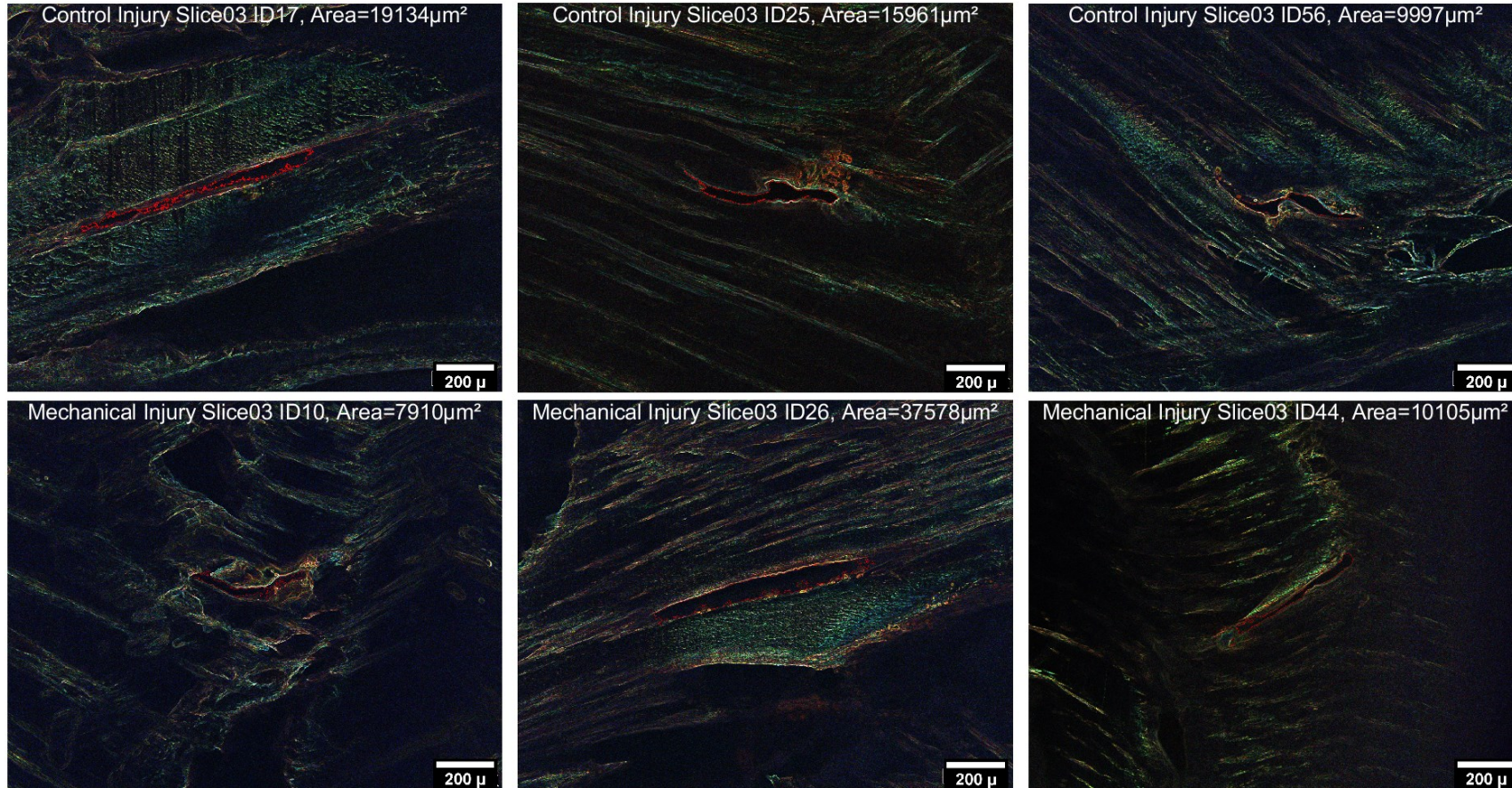


Figure C- 12 Segmentation of needle injuries in slice 3. Each image is annotated with labels indicating control or mechanical injuries, along with the slice number and specific injury IDs, each with its respective area measurement. The top row displays control injuries, labelled as ID17, ID25, and ID56, respectively. The bottom row shows mechanical injuries, with labels ID10, ID26, and ID44, respectively.

C.1.3.3 Length measurements



Figure C- 13 Length of needle injuries in slice 3. Each image is annotated with labels indicating control or mechanical injuries, along with the slice number and specific injury IDs, each with its respective length measurement. The top row displays control injuries, labelled as ID17, ID25, and ID56, respectively. The bottom row shows mechanical injuries, with labels ID10, ID26, and ID44, respectively.

C.1.3.4 Solidity measurements

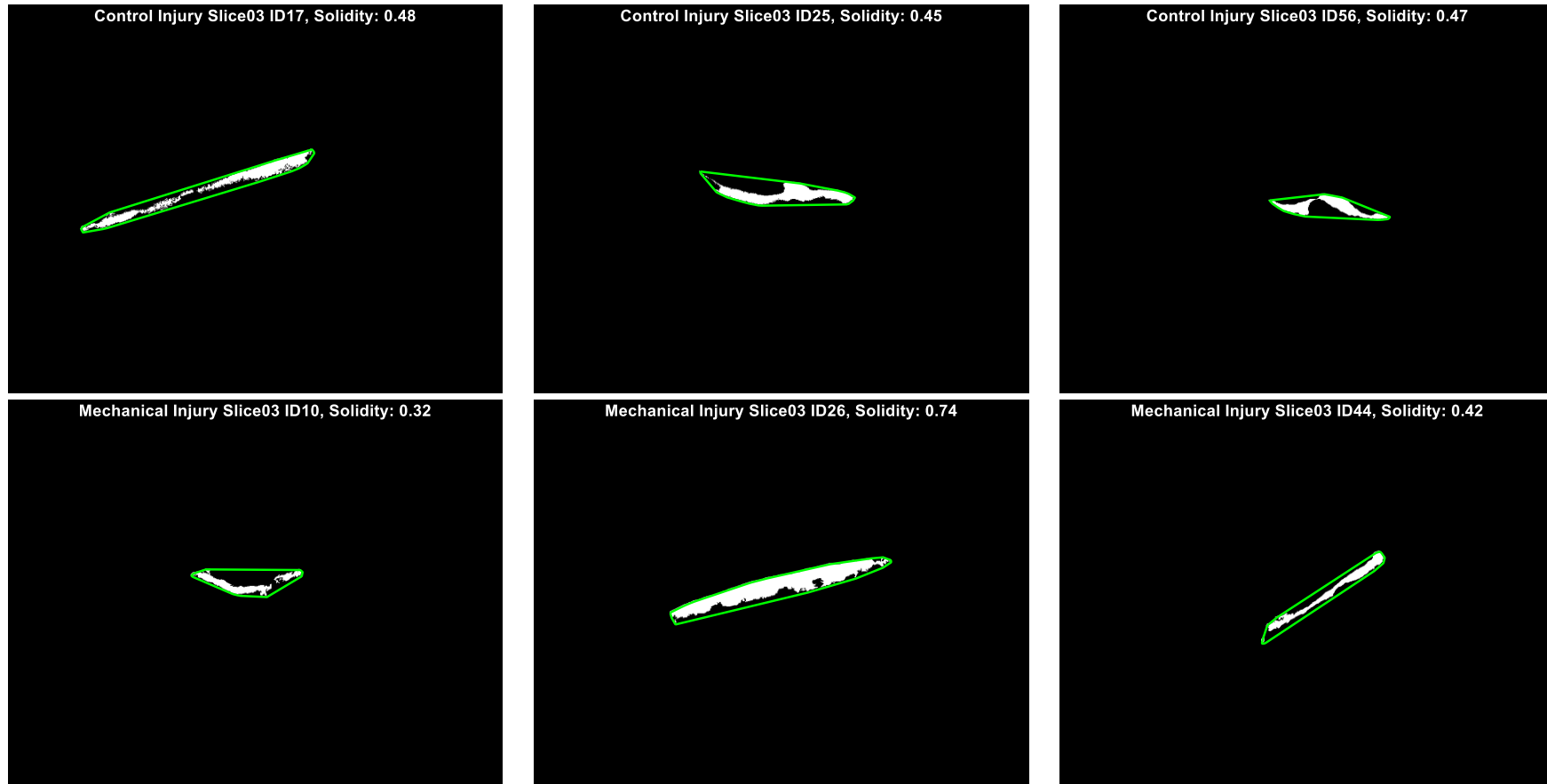


Figure C- 14 Solidity of needle injuries in slice 3. Each image is annotated with labels indicating control or mechanical injuries, along with the slice number and specific injury IDs, each with its respective solidity measurement. The top row displays control injuries, labelled as ID17, ID25, and ID56, respectively. The bottom row shows mechanical injuries, with labels ID10, ID26, and ID44, respectively.

C.1.3.5 Aspect ratio measurements

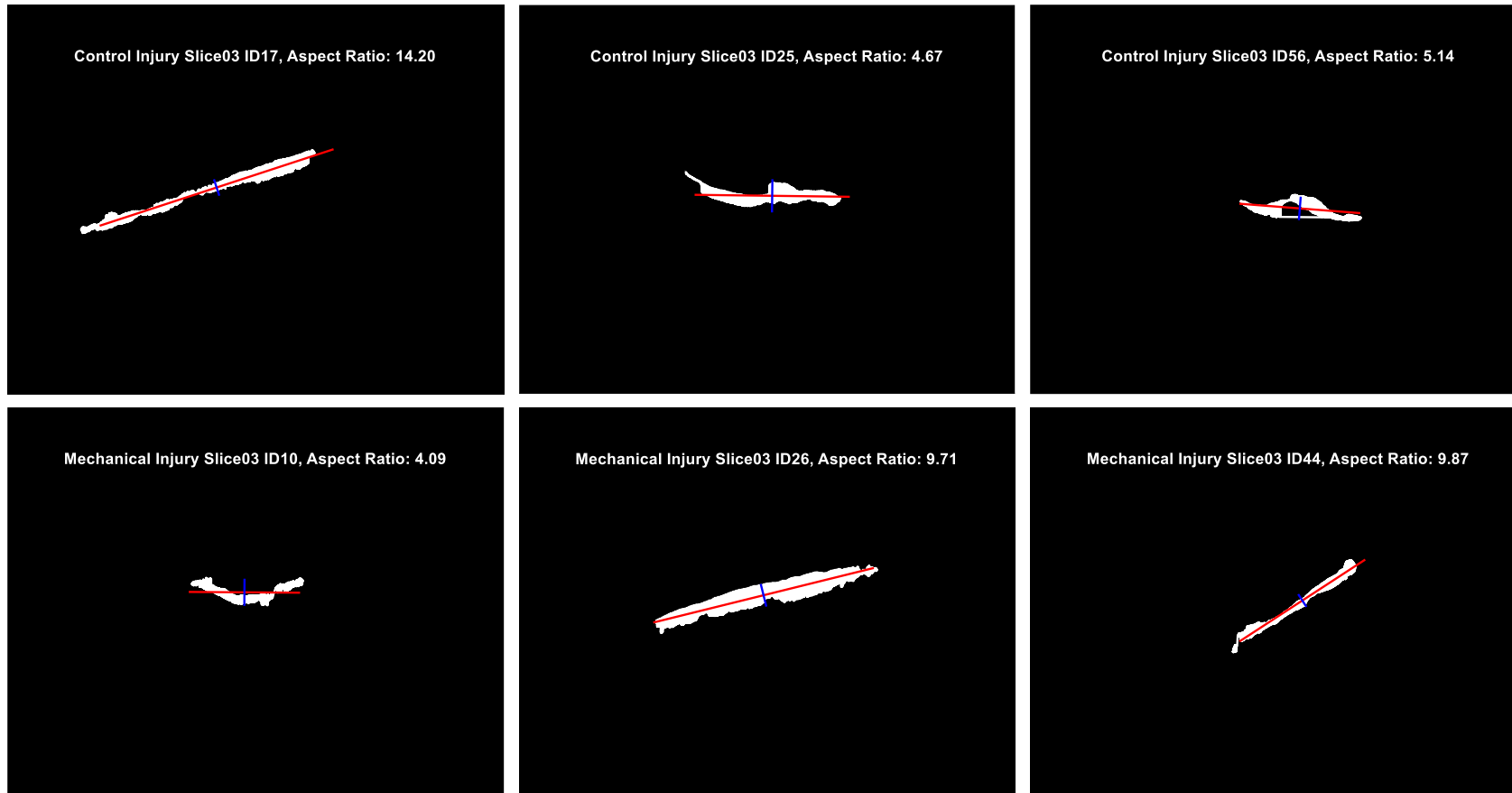


Figure C- 15 Aspect ratio of needle injuries in slice 3. Each image is annotated with labels indicating control or mechanical injuries, along with the slice number and specific injury IDs, each with its respective aspect ratio measurement. The top row displays control injuries, labelled as ID17, ID25, and ID56, respectively. The bottom row shows mechanical injuries, with labels ID10, ID26, and ID44, respectively.

C.1.4 Injury slice 4

C.1.4.1 Original images

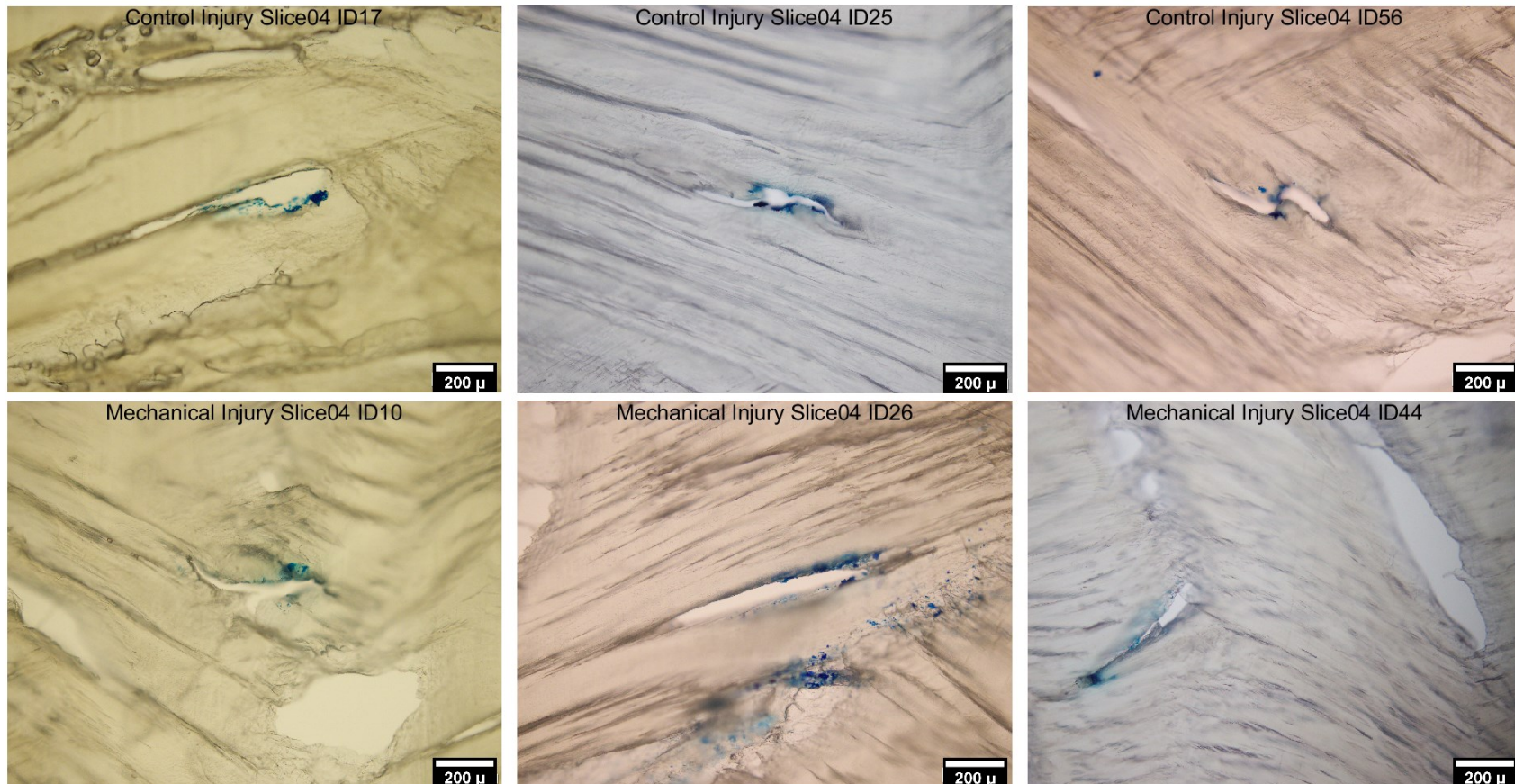


Figure C- 16 Original images of needle injuries in slice 4. Each image is annotated with labels indicating control or mechanical injuries, along with the slice number and specific injury IDs. The top row displays control injuries, labelled as ID17, ID25, and ID56, respectively. The bottom row shows mechanical injuries, with labels ID10, ID26, and ID44, respectively.

C.1.4.2 Segmentation and area measurements

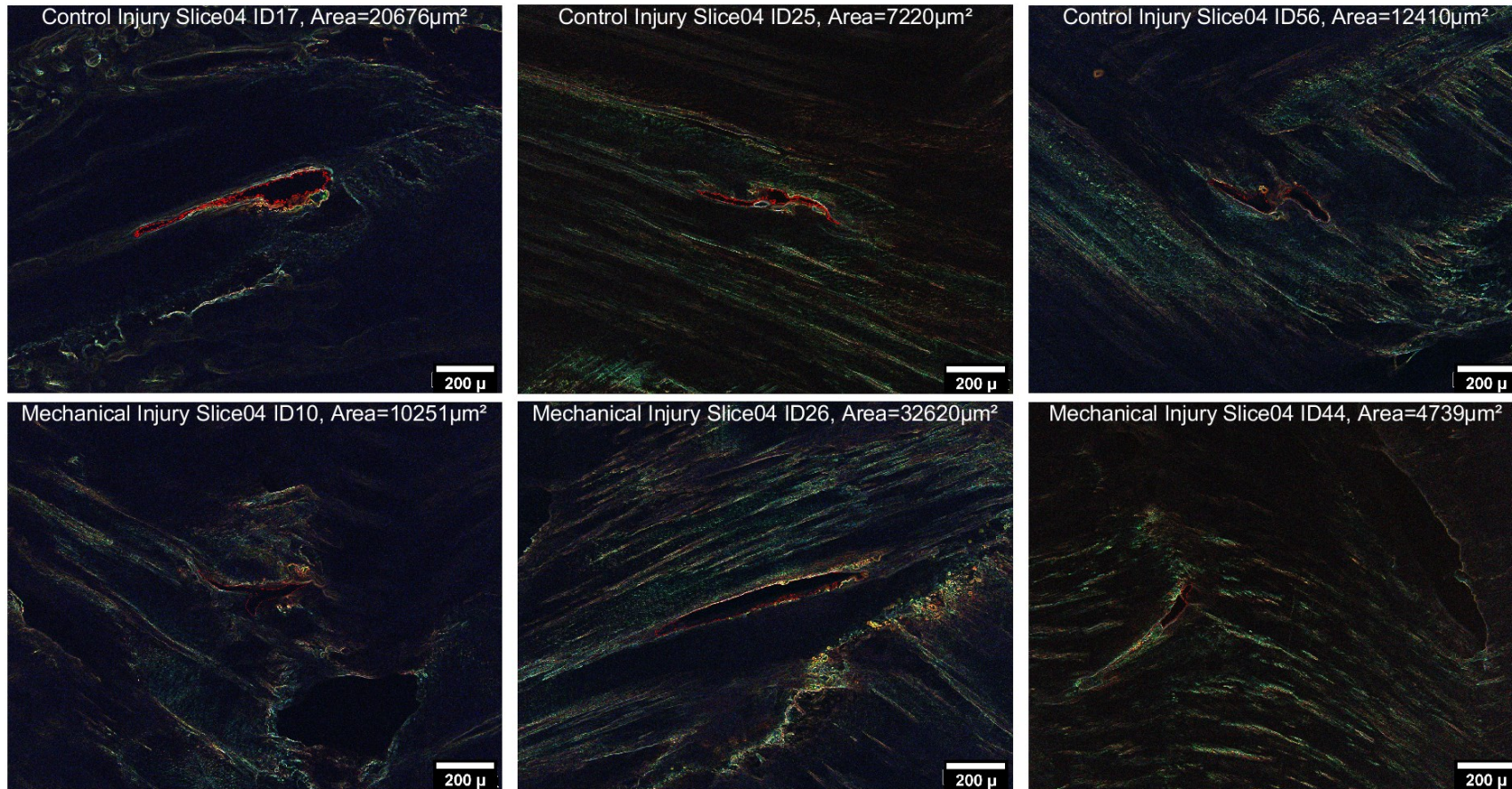


Figure C- 17 Segmentation of needle injuries in slice 4. Each image is annotated with labels indicating control or mechanical injuries, along with the slice number and specific injury IDs, each with its respective area measurement. The top row displays control injuries, labelled as ID17, ID25, and ID56, respectively. The bottom row shows mechanical injuries, with labels ID10, ID26, and ID44, respectively.

C.1.4.3 Length measurements



Figure C- 18 Length of needle injuries in slice 4. Each image is annotated with labels indicating control or mechanical injuries, along with the slice number and specific injury IDs, each with its respective length measurement. The top row displays control injuries, labelled as ID17, ID25, and ID56, respectively. The bottom row shows mechanical injuries, with labels ID10, ID26, and ID44, respectively.

C.1.4.4 Solidity measurements

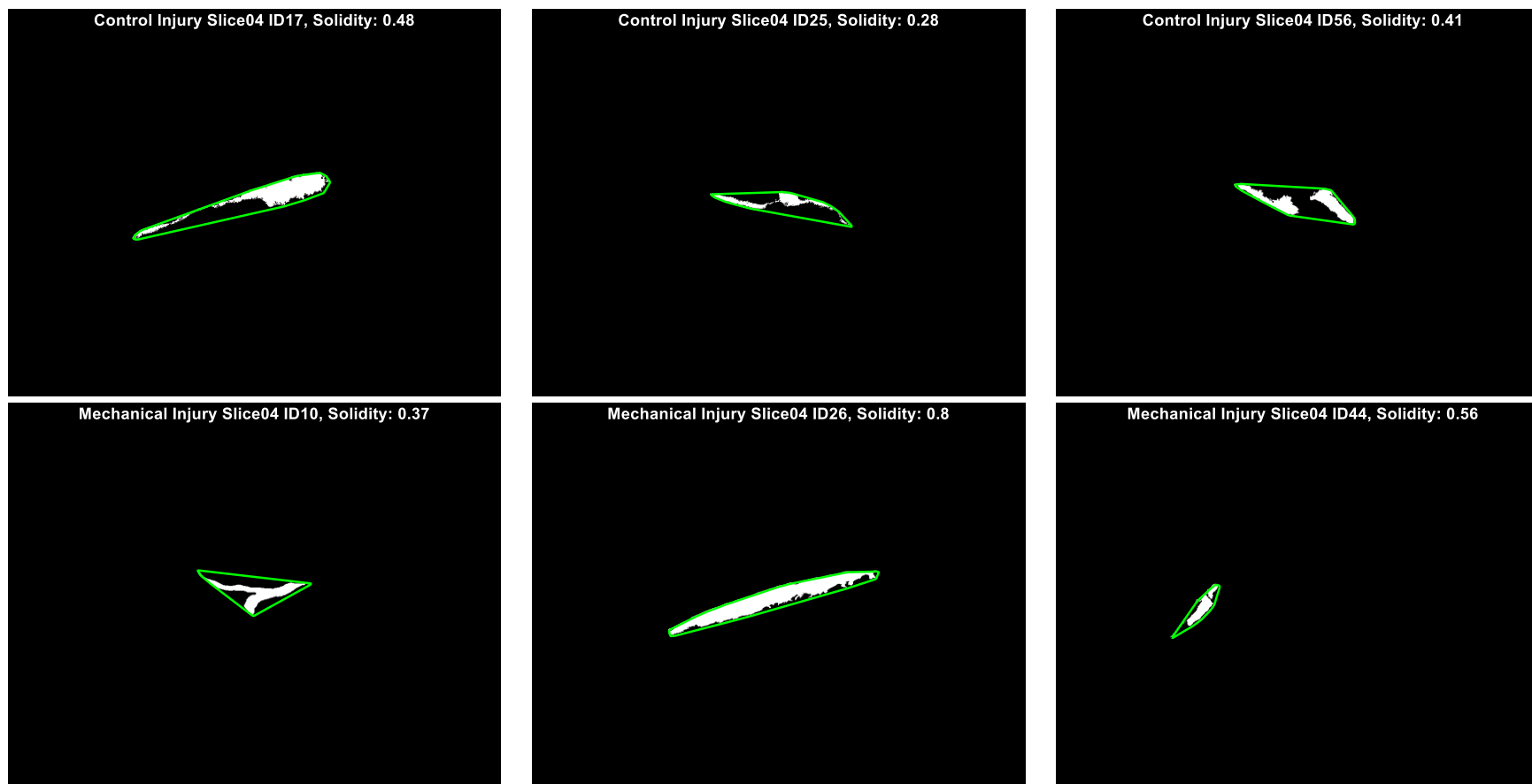


Figure C- 19 Solidity of needle injuries in slice 4. Each image is annotated with labels indicating control or mechanical injuries, along with the slice number and specific injury IDs, each with its respective solidity measurement. The top row displays control injuries, labelled as ID17, ID25, and ID56, respectively. The bottom row shows mechanical injuries, with labels ID10, ID26, and ID44, respectively.

C.1.4.5 Aspect ratio measurements

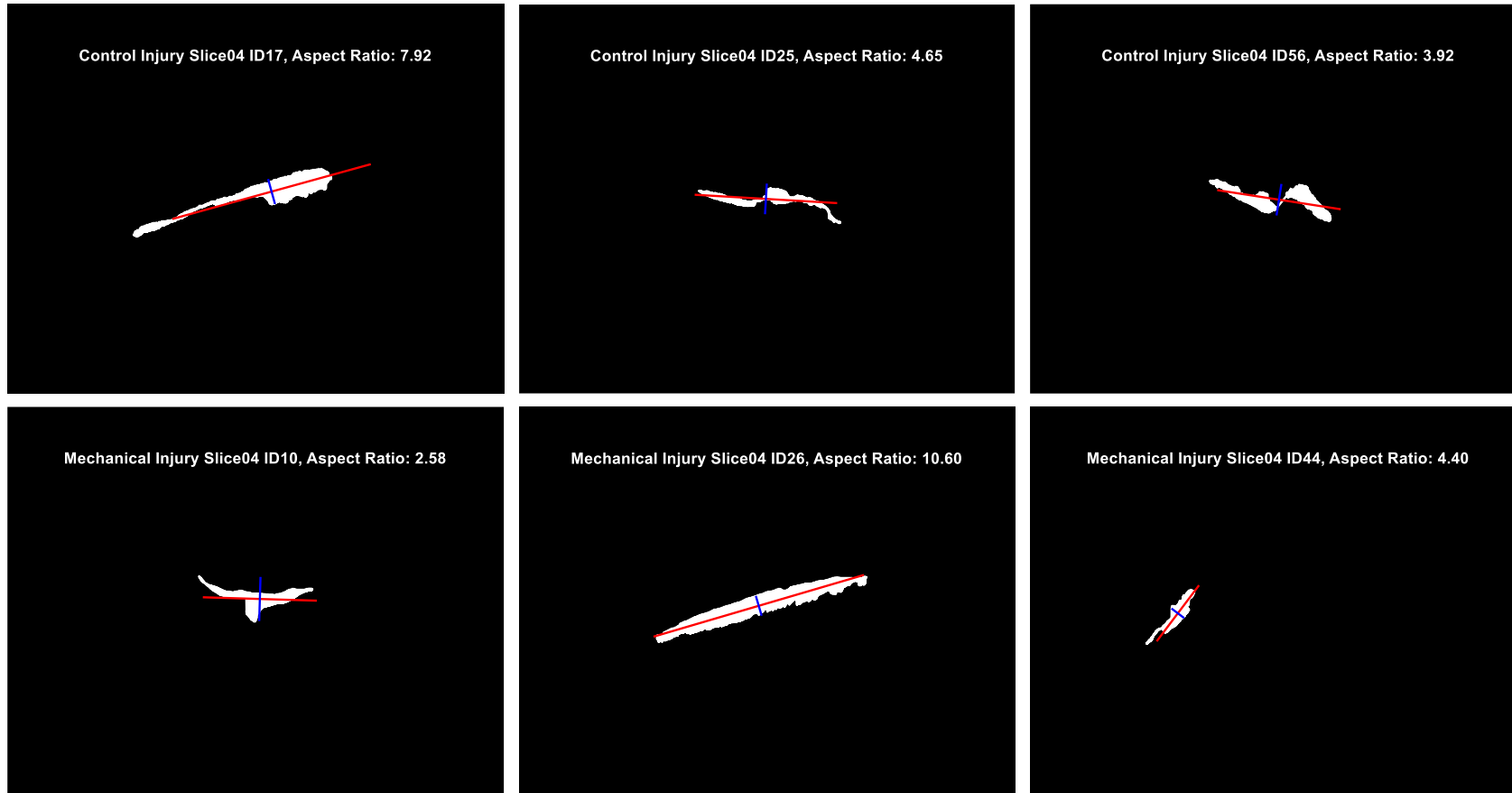


Figure C- 20 Aspect ratio of needle injuries in slice 4. Each image is annotated with labels indicating control or mechanical injuries, along with the slice number and specific injury IDs, each with its respective aspect ratio measurement. The top row displays control injuries, labelled as ID17, ID25, and ID56, respectively. The bottom row shows mechanical injuries, with labels ID10, ID26, and ID44, respectively.

C.1.5 Injury slice 5

C.1.5.1 Original images

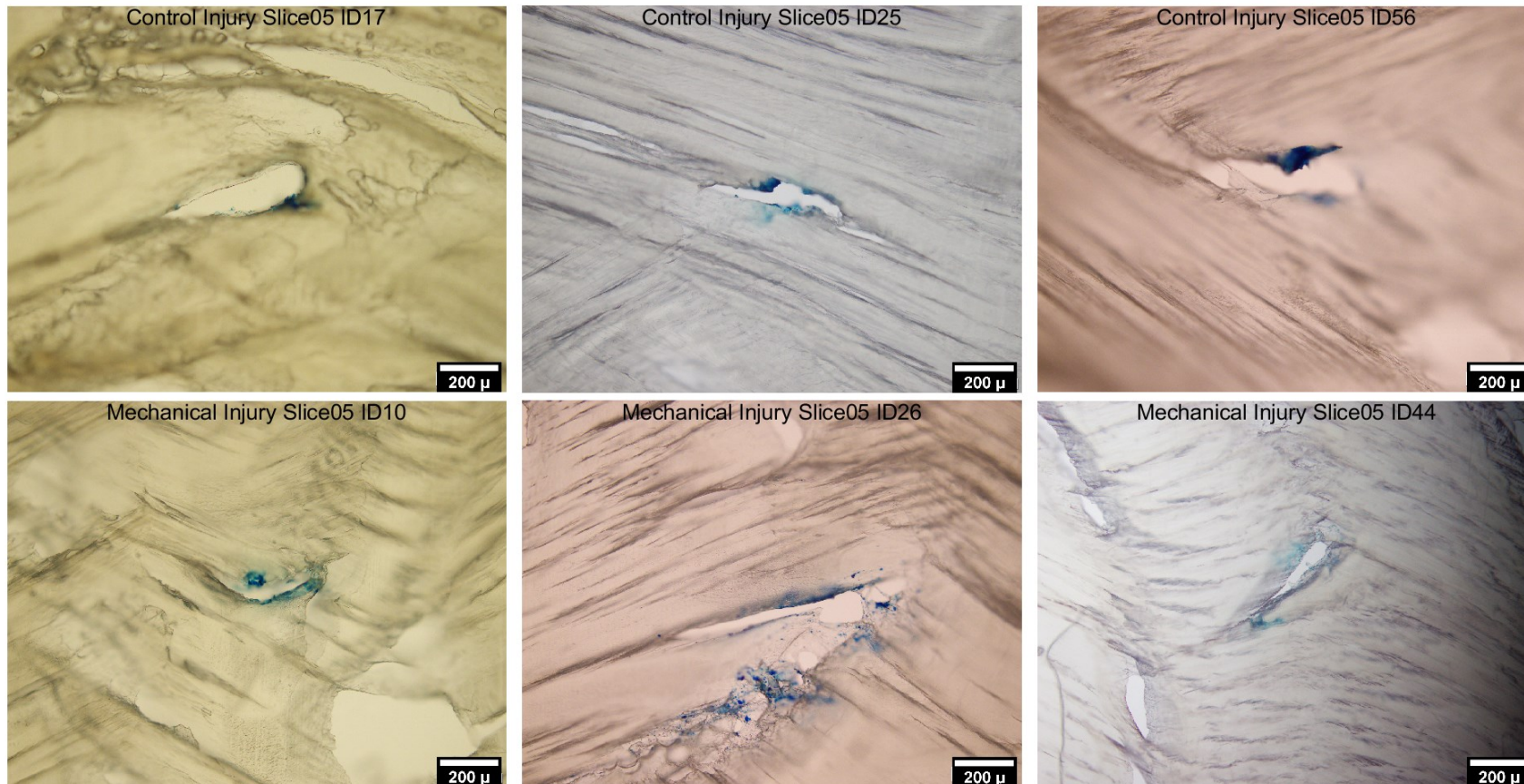


Figure C- 21 Original images of needle injuries in slice 5. Each image is annotated with labels indicating control or mechanical injuries, along with the slice number and specific injury IDs. The top row displays control injuries, labelled as ID17, ID25, and ID56, respectively. The bottom row shows mechanical injuries, with labels ID10, ID26, and ID44, respectively.

C.1.5.2 Segmentation and area measurements

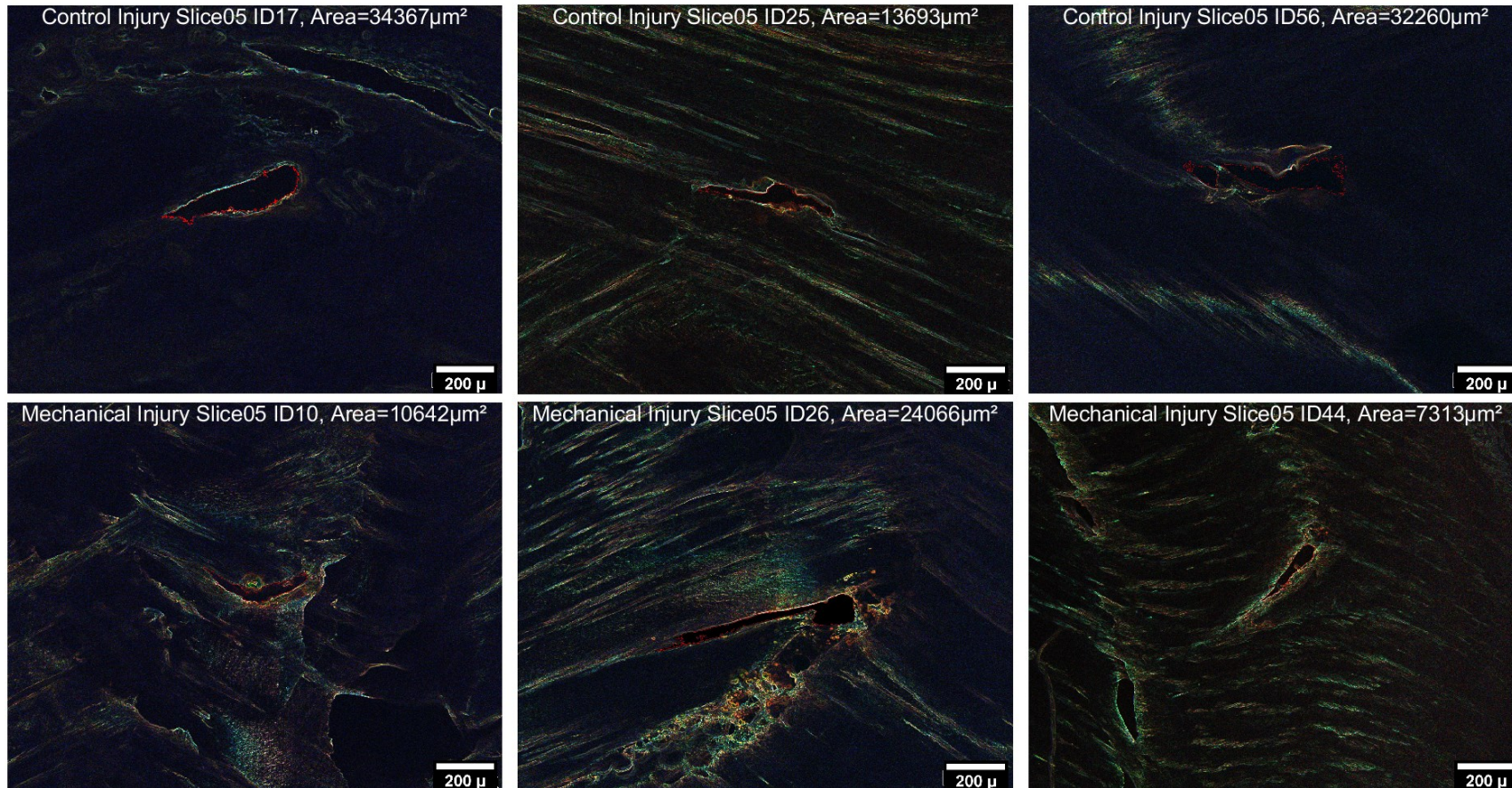


Figure C- 22 Segmentation of needle injuries in slice 5. Each image is annotated with labels indicating control or mechanical injuries, along with the slice number and specific injury IDs, each with its respective area measurement. The top row displays control injuries, labelled as ID17, ID25, and ID56, respectively. The bottom row shows mechanical injuries, with labels ID10, ID26, and ID44, respectively.

C.1.5.3 Length measurements



Figure C- 23 Length of needle injuries in slice 5. Each image is annotated with labels indicating control or mechanical injuries, along with the slice number and specific injury IDs, each with its respective length measurement. The top row displays control injuries, labelled as ID17, ID25, and ID56, respectively. The bottom row shows mechanical injuries, with labels ID10, ID26, and ID44, respectively.

C.1.5.4 Solidity measurements

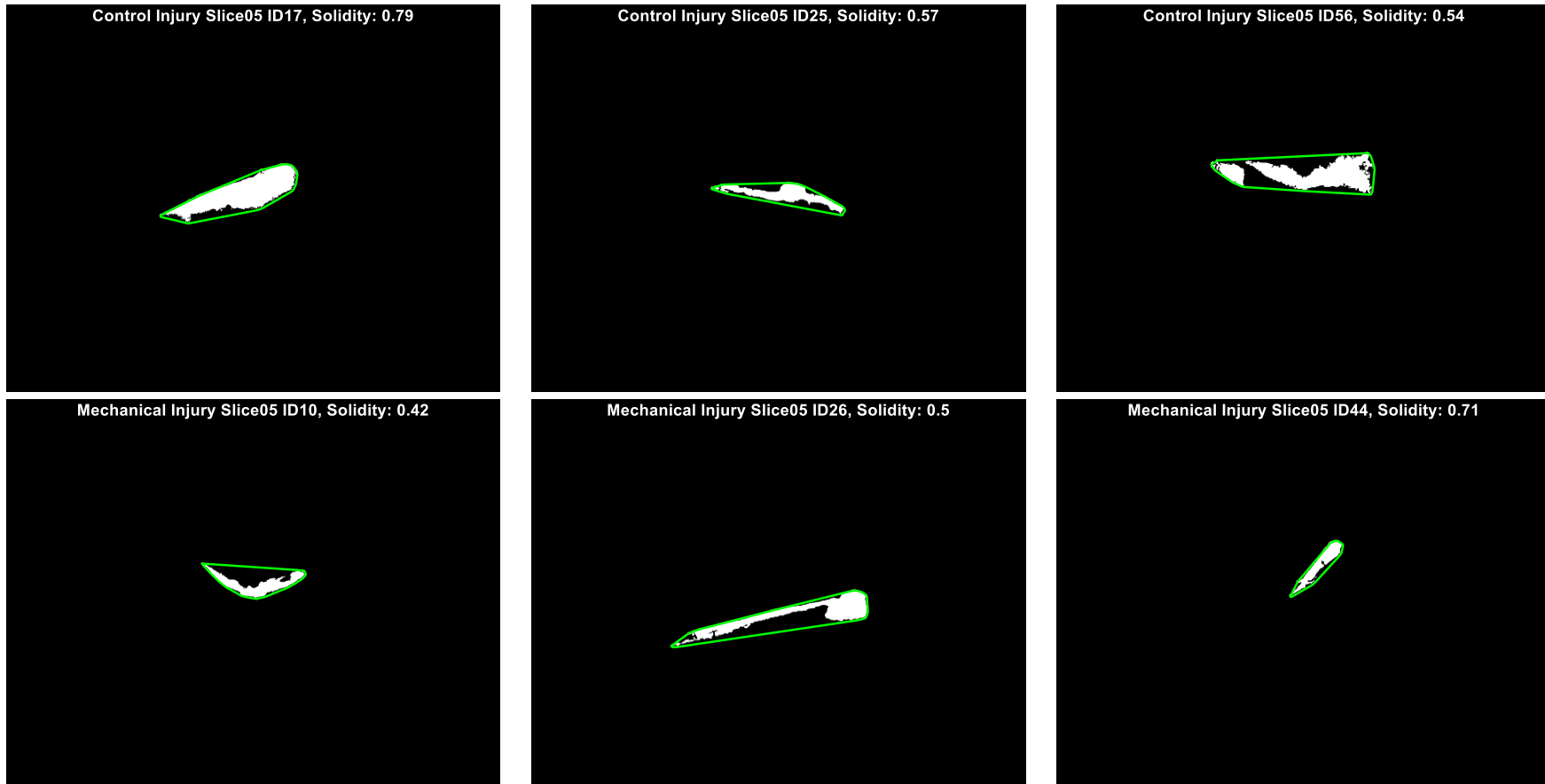


Figure C- 24 Solidity of needle injuries in slice 5. Each image is annotated with labels indicating control or mechanical injuries, along with the slice number and specific injury IDs, each with its respective solidity measurement. The top row displays control injuries, labelled as ID17, ID25, and ID56, respectively. The bottom row shows mechanical injuries, with labels ID10, ID26, and ID44, respectively.

C.1.5.5 Aspect ratio measurements

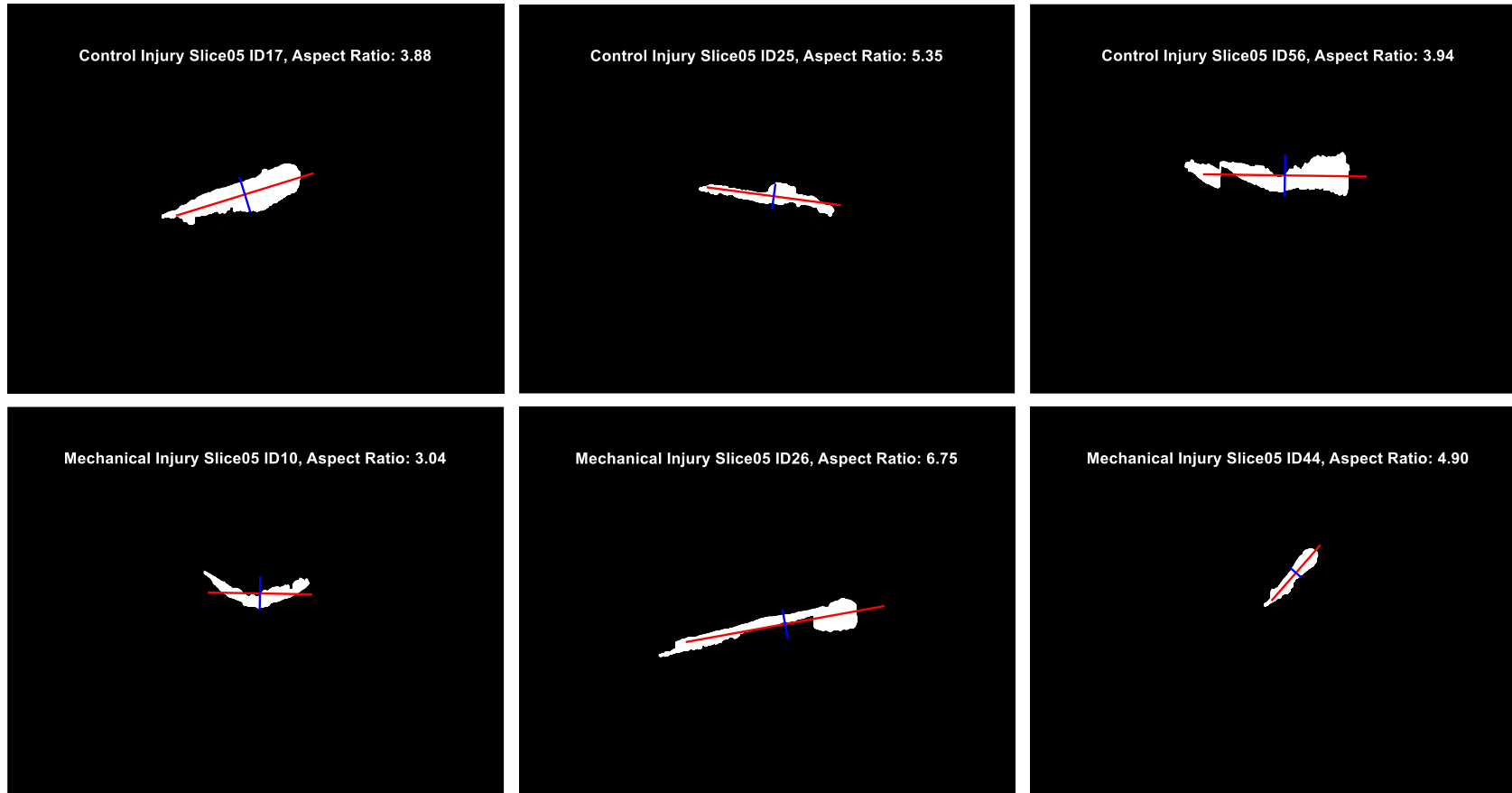


Figure C- 25 Aspect ratio of needle injuries in slice 5. Each image is annotated with labels indicating control or mechanical injuries, along with the slice number and specific injury IDs, each with its respective aspect ratio measurement. The top row displays control injuries, labelled as ID17, ID25, and ID56, respectively. The bottom row shows mechanical injuries, with labels ID10, ID26, and ID44, respectively.

C.2 Tables of measurements and mean values for each injury parameter (area, length, solidity, and aspect ratio) of control and mechanical injury groups

C.2.1 Area (μm^2)

Table C- 1 Area measurements (μm^2) across five slices for each injury within control and mechanical groups along with the mean values.

Group	Injury	Slice 1	Slice 2	Slice 3	Slice 4	Slice 5	Mean
Control	ID17	13465	23769	19134	20676	34367	22282.20
Control	ID25	14207	17998	15961	7220	13693	13815.80
Control	ID56	41419	16514	9997	12410	32260	22520.00
Mechanical	ID10	14000	14600	7910	10251	10642	11480.60
Mechanical	ID26	32069	26387	37578	32620	24066	30544.00
Mechanical	ID44	1988	11380	10105	4739	7313	7105.00

C.2.2 Length (μm)

Table C- 2 Length measurements (μm) across five slices for each injury within control and mechanical groups along with the mean values.

Group	Injury	Slice 1	Slice 2	Slice 3	Slice 4	Slice 5	Mean
Control	ID17	554	994	839	708	497	718.40
Control	ID25	436	492	566	532	472	499.60
Control	ID56	597	490	445	430	610	514.40
Mechanical	ID10	499	446	395	421	405	433.20
Mechanical	ID26	772	664	788	750	704	735.60
Mechanical	ID44	365	513	506	244	256	376.80

C.2.3 Solidity (unitless)

Table C- 3 Solidity measurements (unitless) across five slices for each injury within control and mechanical groups along with the mean values.

Group	Injury	Slice 1	Slice 2	Slice 3	Slice 4	Slice 5	Mean
Control	ID17	0.48	0.59	0.48	0.48	0.79	0.56
Control	ID25	0.58	0.69	0.45	0.28	0.57	0.52
Control	ID56	0.78	0.66	0.47	0.41	0.54	0.57
Mechanical	ID10	0.49	0.40	0.32	0.37	0.42	0.40
Mechanical	ID26	0.66	0.82	0.74	0.80	0.50	0.70
Mechanical	ID44	0.28	0.63	0.42	0.56	0.71	0.52

C.2.4 Aspect ratio (unitless)

Table C- 4 Aspect ratio (unitless) across five slices for each injury within control and mechanical groups along with the mean values.

Group	Injury	Slice 1	Slice 2	Slice 3	Slice 4	Slice 5	Mean
Control	ID17	11.05	19.79	14.2	7.92	3.88	11.37
Control	ID25	6.27	5.16	4.67	4.65	5.35	5.22
Control	ID56	4.37	6.78	5.14	3.92	3.94	4.83
Mechanical	ID10	4.34	2.95	4.09	2.58	3.04	3.40
Mechanical	ID26	10.17	11.25	9.71	10.6	6.75	9.70
Mechanical	ID44	23.73	11.73	9.87	4.4	4.9	10.93

Bar charts of mean values for each injury parameter (area, length, solidity, and aspect ratio) of control and mechanical injury groups

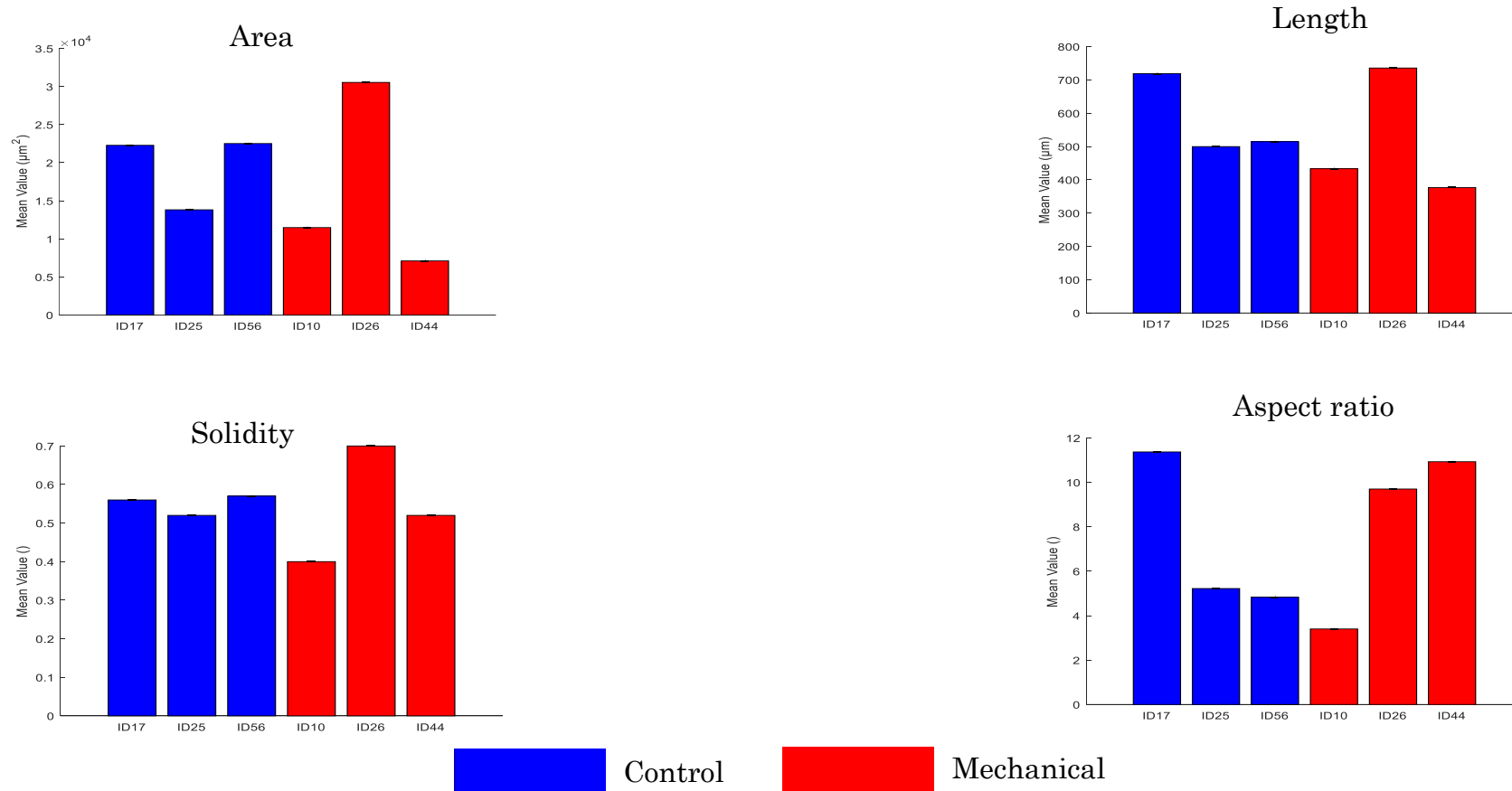


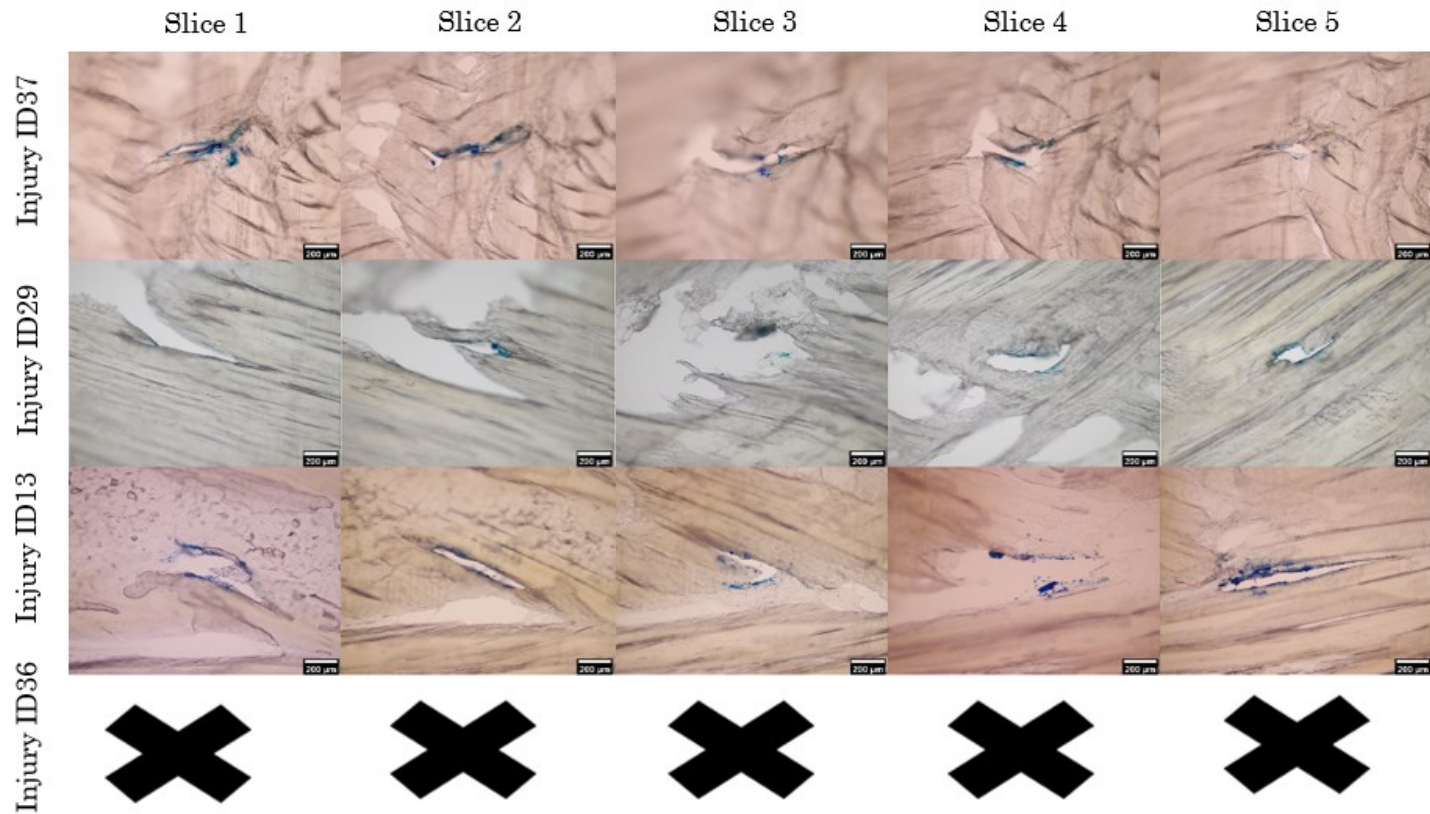
Figure C- 26 Mean values for each injury in the control (blue, n=3) and mechanical injury (red, n=3) groups for four measured parameters, as labelled above each chart: area (μm^2), length (μm), density (unitless), and aspect ratio (unitless). Each of the three bars per colour represents the average of measurements from the five slices for the respective injury.

Appendix D

D.1 Original images of control and mechanical groups with predominant unsuccessful sectioning across slices 1 through 5

D.1.1 Control injuries

Figure D- 1 Original images of control group with predominant unsuccessful sectioning across slices 1 through 5. Columns correspond to the respective slices, and rows represent individual injuries. "X" marks indicate instances where sectioning was entirely unsuccessful, resulting in no slices being collected for imaging.



D.1.2 Mechanical injuries

Figure D- 2 Original images of mechanical group with predominant unsuccessful sectioning across slices 1 through 5. Columns correspond to the respective slices, and rows represent individual injuries. "X" marks indicate instances where sectioning was entirely unsuccessful, resulting in no slices being collected for imaging.

